LIÈGE université
Sciences Appliquées

Thermomechanical modelling of the creep-fatigue behaviour and damage of Nickel-alloy receiver tubes used in Concentrated Solar Power plants

Thesis submitted in partial fulfilment of the requirements for the degree of Doctor of Philosophy (PhD) in Engineering Science

By

Hélène MORCH

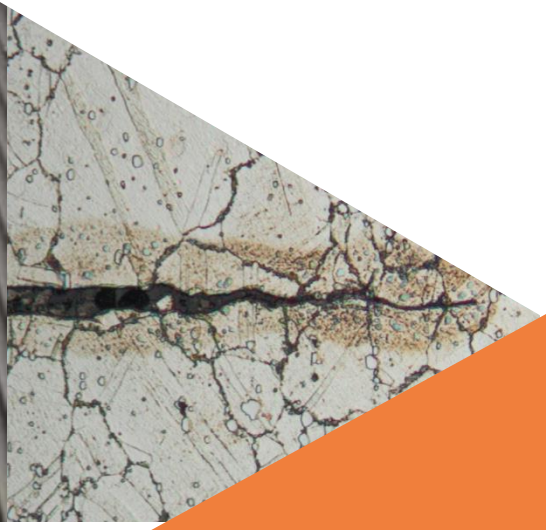

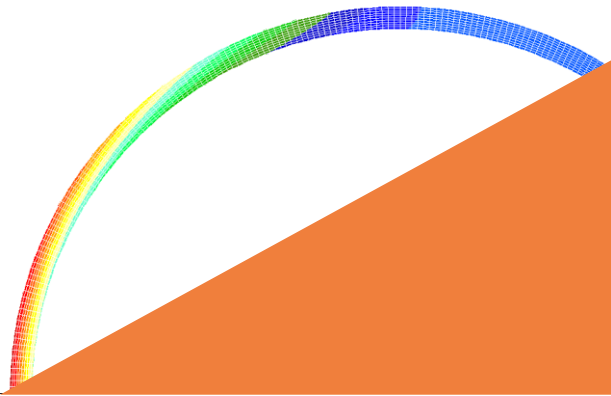

Supervisor: Pr. Laurent DUCHÊNE

Co-supervisor: Pr. Anne-Marie HABRAKEN

COLLEGE OF ARCHITECTURE, GEOLOGY AND CIVIL ENGINEERING

OCTOBER 2022

Thermomechanical modelling of the creep-fatigue behaviour and damage of Nickel-alloy receiver tubes used in Concentrated Solar Power plants

Thesis submitted in partial fulfilment of the requirements for the degree of Doctor of Philosophy (PhD) in Engineering Science

By

Hélène MORCH

Jury members

Prof. Anne Mertens (President)	University of Liège, Belgium
Prof. Laurent Duchêne (Supervisor)	University of Liège, Belgium
Prof. Anne-Marie Habraken (Co-supervisor)	University of Liège, Belgium
Dr Romain Boman	University of Liège, Belgium
Prof. Tasnim Hassan	North Carolina State University, USA
Dr Ridha Harzallah	John Cockerill Energy, Belgium
Dr Michael Bruyneel	University of Liège, Belgium/GDTech, Belgium

Abstract

The receivers in Concentrated Solar Power (CSP) plants of this study are made of vertical panels of metallic tubes in which molten salt flows. The salt is heated by the solar radiation hitting the surface of the tubes and the heat it carries is then used to produce electricity. The daily thermal loading/unloading of the solar receivers causes a combination of high temperature creep and fatigue in the receiver tubes. Additionally, the presence of molten salt inside the tubes can lead to severe corrosion. For this technology to be profitable, the lifetime of the solar receiver should be at least of 25 years. The objective of this thesis is the modelling of the thermomechanical behaviour of receiver tubes made of nickel alloy 230 and the prediction of their lifetime under the conditions encountered in the field of CSP.

In a first stage, an extensive experimental campaign was launched to assess the mechanical behaviour of alloy 230 at different temperatures and under various loading conditions. Additionally, a metallographic analysis of part of the tested samples was conducted to understand the micro-scale phenomena responsible for the macroscopic behaviour of alloy 230. In a second stage, based on the results of the experimental campaign and on results found in the scientific literature, a behaviour model based on the Chaboche framework was selected and implemented in the finite-element code Lagamine developed at the University of Liège. A specific formulation was proposed for the temperature-dependence of the model parameters. Consecutively, a damage model was associated to the behaviour model to predict the lifetime of the tubes under fatigue and creep, and the combination of both. This damage model is based on the unified Lemaitre damage model which is compatible with the Chaboche framework. In a third stage, the modelling of corrosion was added, for which a simplified model was created based on limited experimental data from the literature to simulate uniform corrosion. The resulting full model (behaviour, damage, and corrosion) is highly complex and requires long computational times for the precise modelling of the receiver tubes. In this respect, two methods were developed to make calculations faster using simplifying hypotheses. Both methods proved to be efficient for the reduction of computational time, but only one of the methods is really reliable in terms of accuracy of the results.

Finally, one receiver tube was modelled using the finite-element model and its lifetime was evaluated for a specific loading case. The results showed that the estimated lifetime exceeded the target of 25 years, and that uniform corrosion did not have a significant impact on the lifetime and behaviour.

Résumé

Les récepteurs des centrales solaires thermiques à concentration de cette étude sont constitués de panneaux de tubes métalliques verticaux dans lesquels circule du sel fondu. Ce sel est réchauffé par le rayonnement solaire concentré sur la surface des tubes, et la chaleur ainsi emmagasinée est ensuite utilisée pour la production d'électricité. Le chargement/déchargement thermique journalier des récepteurs solaires provoque à la fois du fluage à haute température et de la fatigue. Par ailleurs, la présence de sel fondu à l'intérieur des tubes peut créer d'importants problèmes de corrosion. Pour que ce type de technologie soit rentable, on estime qu'une durée de vie minimale de 25 ans est nécessaire pour le récepteur solaire. L'objectif de cette thèse est de modéliser le comportement thermomécanique des tubes de récepteurs solaires en alliage 230 (alliage de nickel) et de prédire leur durée de vie.

Dans un premier temps, une campagne expérimentale a été lancée pour étudier le comportement thermomécanique de l'alliage 230 à différentes températures et sous divers chargements. En outre, une analyse métallographique a été menée sur une partie des éprouvettes testées pour comprendre les phénomènes microscopiques responsables du comportement macroscopique de l'alliage. Dans un second temps, à partir des résultats expérimentaux et de résultats de la littérature, un modèle de comportement basé sur la loi constitutive de Chaboche a été choisi et implémenté dans le code éléments finis Lagamine développé à l'université de Liège. Une formulation spécifique a été proposée pour exprimer la dépendance à la température des paramètres du modèle. Ensuite, un modèle d'endommagement a été associé au modèle de comportement pour prédire la durée de vie sous fatigue, fluage, ou une combinaison des deux. Ce modèle est basé sur le modèle unifié de Lemaitre, qui s'intègre facilement à la loi de Chaboche. Dans un troisième temps, un modèle simplifié a été créé pour simuler la corrosion uniforme en se basant sur les données expérimentales disponibles dans la littérature. Le modèle complet (comportement, endommagement, et corrosion) est très complexe et nécessite de longs temps de calcul pour modéliser précisément les tubes de récepteur. Deux méthodes ont donc été mises en place pour réduire les temps de calcul en utilisant des hypothèses simplificatrices. Les deux méthodes ont permis de réduire significativement les temps de calcul, mais une seule des deux s'est avérée vraiment fiable et précise.

Enfin, un tube de récepteur a pu être modélisé en utilisant le code élément fini et sa durée de vie a été estimée pour un cas de charge particulier. Les résultats montrent que la durée de vie estimée est supérieure à l'objectif de 25 ans, et que la corrosion uniforme n'a pas d'impact significatif sur la durée de vie, ni sur le comportement mécanique du récepteur.

Acknowledgements

This work has been made possible thanks to two research programs led by John Cockerill Energy, with the participation of the CRM Group (Centre de Recherche Métallurgiques), and the financial support of the Walloon Region.

First and foremost, I would like to thank Pr. Laurent Duchêne (supervisor) for his valuable support and helpfulness along these six years of thesis, as well as Pr. Anne-Marie Habraken (co-supervisor) for her useful advice throughout the whole project.

I would also like to thank Ridha Harzallah for his availability and his constant effort at pushing the project forward.

From the CRM Group, I would especially like to thank Frédéric Novello, Olivier Lemaire, and Grégory Esser who oversaw the experimental campaign and gave valuable insight on the results.

Many thanks also to all the colleagues from the Materials and Solid Mechanics team at the University, who helped maintaining the code and improving it.

I would also like to address special thanks to Luc Papeleux and Romain Boman, who really helped improve the way the code was maintained and documented, and therefore made programming with Lagamine much more pleasant.

Finally, I would like to thank my family and all my friends who were there to provide moral support and helped me to stay motivated in difficult times.

Nomenclature

t	Time
T	Temperature
$\varepsilon/\underline{\varepsilon}/\boldsymbol{\varepsilon}$	Total strain (scalar/Voigt notation/tensorial notation)
$\varepsilon^{th}/\underline{\varepsilon}^{th}$	Thermal strain
$\varepsilon^{m}/\underline{\varepsilon}^{m}$	Mechanical strain
$\varepsilon^{p}/\underline{\varepsilon}^{p}$	Plastic/Viscoplastic strain
$\varepsilon^{e}/\underline{\varepsilon}^{e}$	Elastic strain
$\sigma/\underline{\sigma}/\boldsymbol{\sigma}$	Stress (scalar/Voigt notation/tensorial notation)
$\hat{\sigma}/\underline{\hat{\sigma}}$	Deviatoric stress
$\tilde{\sigma}/\underline{\tilde{\sigma}}$	Effective stress
σ_v	Viscous overstress
$\sigma^{d}/\underline{\sigma}^{d}$	Delayed stress
$\underline{\underline{E}}$	Elasticity tensor (Voigt notation)
G	Shear modulus
$\underline{\underline{C}}$	Consistent tangent matrix
$J(\underline{\sigma})$	Von Mises equivalent stress (scalar)
p	Plastic multiplier
R	Drag stress (scalar) – isotropic hardening
f	Von Mises yield surface
$\underline{X}/\underline{X}_i$	Back-stress (Voigt notation) – total backstress/partial back-stress
$\underline{Y}_i$	Mean stress evolution (Voigt notation)
q	Plastic strain memory surface radius
$\underline{\zeta}$	Plastic strain memory surface centre
$\underline{n}^*$	Normal to the plastic strain memory surface
$\underline{n}$	Normal to the yield surface
D	Total damage
D_f	Fatigue damage variable
D_c	Creep damage variable
D_u	Uniform corrosion damage variable
Y	Strain energy density release rate
w_s	Energy stored by hardening
r	Plastic multiplier with damage
$\underline{\underline{\mathcal{J}}}$	Jacobian matrix

Model parameters

Symbol	Parameter	Feature
E	Young modulus	Elasto-(visco)plasticity
ν	Poisson ratio	
σ_y	Yield strength	
b	Rate of isotropic hardening	Isotropic hardening
Q	Asymptotic value of R	
K	Norton-Hoff parameter	Viscosity
n	Norton-Hoff exponent parameter	
n_{AF}	Number of back-stresses	Kinematic hardening
C_i	Armstrong-Frederick parameter (asymptotic value)	
γ_i	Armstrong-Frederick parameter (rate)	
b_i	Static recovery parameter	Static recovery (in kinematic hardening)
r_i	Static recovery exponent	
$n_{AF,cyc}$	Number of back-stresses for cyclic hardening	Cyclic hardening (within kinematic hardening rule)
D_{γ_i}	Cyclic hardening rate	
a_{γ_i}	Cyclic hardening parameter for asymptotic value	
b_{γ_i}	Cyclic hardening parameter for asymptotic value	
c_{γ_i}	Cyclic hardening parameter for asymptotic value	
b_{D_γ}	Rate parameter for temperature evolution	
$n_{AF,Y}$	Number of back-stresses for mean stress evolution	Mean stress evolution (within kinematic hardening rule)
$\alpha_{b,i}$	Rate of mean stress evolution	
$Y_{st,i}$	Asymptotic value for mean stress evolution	
f_E	Weighing factor	Influence of the temperature history
f_E^S	Saturation value of the weighing factor	
D_{crit}	Critical damage value	Damage
S_f	Fatigue damage parameter	
s_f	Fatigue damage exponent parameter	
S_c	Creep damage parameter	
s_c	Creep damage exponent parameter	
k_c	Rabotnov creep damage exponent parameter	
K_u	Rate of corrosion (linear rule)	
K_p	Rate of corrosion (parabolic rule)	
L_e	Characteristic length of the element	

CONTENTS

Introduction

TABLE OF CONTENTS

1 CONTEXT

Over the past decades, the need for energy has been increasing steadily worldwide (see Figure 1). Up until the 19th century, the main energy source in use was biomass, i.e., wood that mostly served for domestic use (heating, cooking, …). The invention of the steam engine at the end of the 18th century led to the 1st industrial revolution: throughout the 19th century, coal-powered machines progressively replaced hand production methods and allowed the development of the industry. The progress of technology continued throughout the 20th century with the growth of the petroleum industry which allowed the development of faster and more efficient means of transport (automotive industry, aviation, cargo ships, …). Nowadays, our modern way of life is highly dependent on energy. On the other hand, most of the energy produced comes from highly polluting fuels such as coal, oil, and gas, which account for a quarter of the greenhouse gas emissions worldwide. Additionally, the available fuel supplies are decreasing sharply, leading to an increase in energy prices. In this context, it is essential to find and develop more sustainable and less polluting energies.

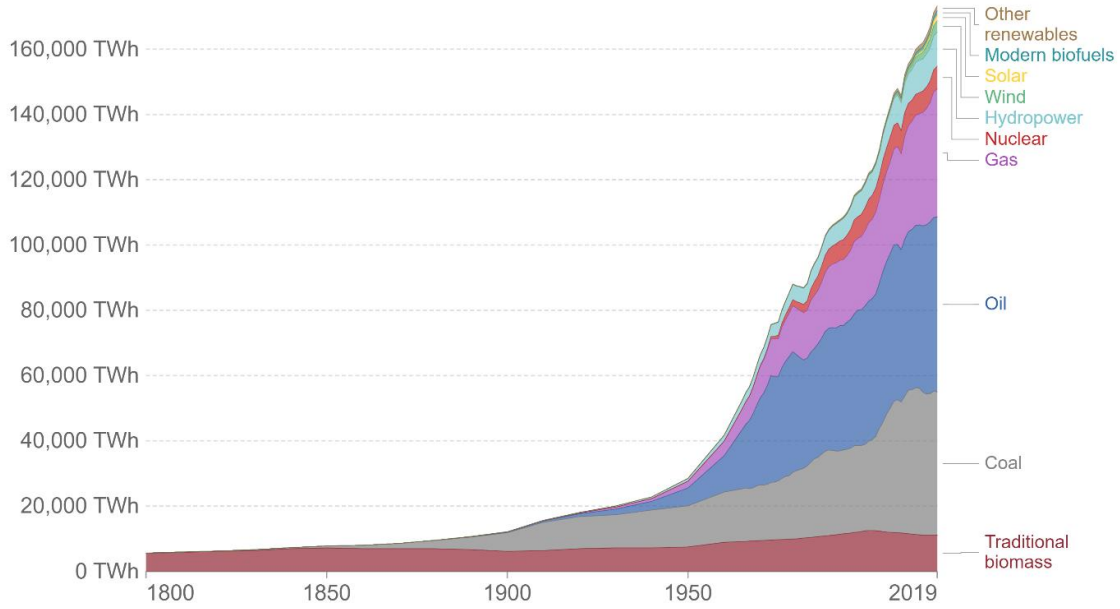

Figure 1 - Global primary energy consumption by source. Source: [1]; data from [2] and [3]

Solar energy, although it only represents about 1% of the current global energy consumption, is a very promising alternative to non-renewable energies as it is inexhaustible and available in large quantities: harvesting the solar energy on 25% of the surface of the Sahara desert would be enough to cover the whole world's energy consumption [4]. The main difficulty presented with solar energy – as with all renewable sources of energy in general – has long been the non-continuous availability. Indeed, whereas the functioning of a nuclear or a coal power plant can be adapted to the demand, energy from solar power can only be harvested during the day. Although electricity can

be stored using batteries, this is not a good solution on a large scale as the making of batteries is very energy-costly and their lifetime is limited (5 to 20 years).

Concentrated Solar Power (CSP) is a technology that allows the harvesting and storage of solar energy for the production of electricity. Figure 2 shows a CSP plant with thermal storage. The plant consists in a field of mirrors (heliostats) which reflect the sunlight towards a receiver placed on top of a tower. The receiver, shown in Figure 3 (a), is made of multiple panels of metallic tubes displayed in Figure 3 (b). A heat-transfer fluid, also called working fluid, is heated as it circulates inside the tubes. This fluid, once heated, can be stored or used for the direct production of electricity: the hot working fluid is used to heat water and turn it into steam, which is then used to put a turbine into motion, which in turn activates a generator. The first generation of CSP plants used water vapor as a heat-transfer fluid, which could not be stored. The second generation of CSP plants uses molten salt (usually solar salt: 60%$NaNO_3$, 40%KNO_3), which can be stored in insulated tanks thanks to its good capacity at retaining heat. The production of electricity is therefore made independent from the sun power harvesting. The main advantage of this type of CSP technology compared to other renewable energies is that the solar energy can easily be stored, and therefore electricity can be produced continually through night and day.

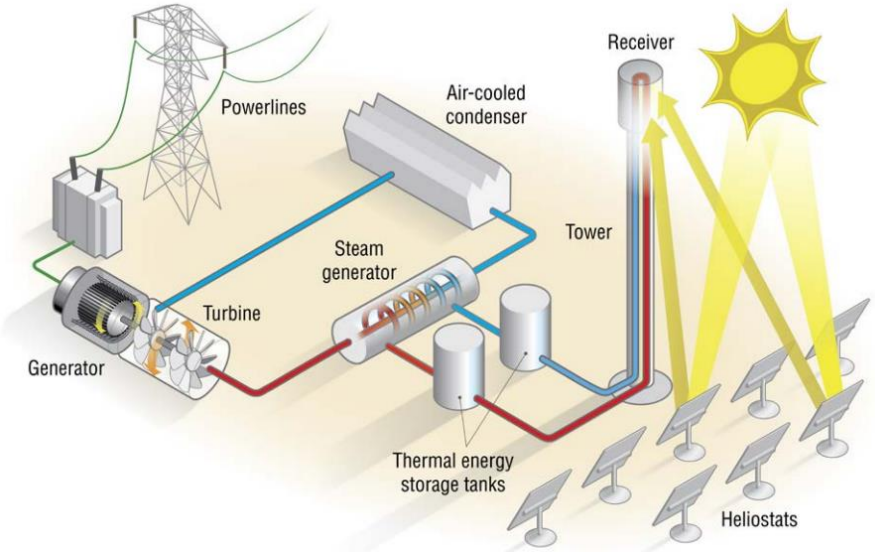

Figure 2 – Concentrated Solar Power plant (source: US Department of Energy)

Increasing the temperature of the working fluid is a good way to improve the efficiency of a CSP plant, however, solar salt is not stable above 565°C. The third generation of CSP plants, which is currently being developed, aims at using salts that can reach higher temperatures, such as chlorine salts which remain stable at temperatures as high as 730°C. However, increasing the temperature and changing the type of salt can lead to problems regarding the corrosion and the long-term resistance of the receiver.

(a) (b)

Figure 3 – (a) Installation of the solar receiver of the Cerro Dominador CSP plant, Chile; the receiver is about to be lifted at the top of the 220 m high tower - (b) Close-up of a panel of tubes. Source: John Cockerill (2019)

The tubes of the receiver are generally made of stainless steel or nickel-based alloy. These materials are known for their good mechanical properties at high temperature and high resistance to corrosion. However, the tubes are subjected to a complex loading which combines thermo-mechanical fatigue (cyclical loading with temperature changes), creep (several hours of continuous loading every day), and corrosion from the salt. The combined impact of these phenomena is difficult to estimate, especially over an expected lifetime of 25 to 30 years.

2 OBJECTIVES OF THE THESIS

John Cockerill (formerly CMI) has been working on the development of 2nd and 3rd generation CSP plants for several years. This thesis was realized as part of two projects conducted by John Cockerill: Solar Perform (2016-2019) and Solar GNext (2019-2023).

In 2016, the Solar Perform project was launched. The objectives of this first project were:

- The study of the thermo-mechanical durability of alloy 230, a nickel alloy used by John Cockerill to make their solar receiver. A large experimental campaign was conducted by the CRM Group (Centre de Recherches Métallurgiques). The Metallurgy and Materials Science (MMS) division of the University of Liège was also involved for the metallographic analysis of different samples.
- The development of a numerical model for the design of the solar receivers to predict the behaviour and lifetime of the tubes of the receiver.

- The development of a new coating to be applied on the receiver to maximize its absorbance (done by Lithcote Europe, a Belgian company specialized in coatings).

In 2019, the project Solar GNext, focusing on the development of 3rd generation CSP plants, was started. This second project centres around the impact of corrosion by the molten salts in receivers, the possibility to minimize the impact of corrosion through coatings or inhibitors, the research of new materials (nickel alloys) and new salts, and the longevity of these materials at higher temperatures. The same industrial partners were involved in this second project (CRM Group for the thermo-mechanical and corrosion testing, and Lithcote for the development of coatings).

To achieve the goals of these two projects in coordination with the different partners, this thesis sets the following objectives:

- The development and implementation of a thermo-mechanical creep-fatigue law within the finite-element code Lagamine [5] developed at the University of Liège.
- The development of a damage model adapted to thermo-mechanical creep-fatigue.
- The development of a corrosion damage model.
- The identification of the material parameters for nickel-based alloy 230 at different temperatures based on the results provided by the CRM Group and the validation of the behaviour and damage models.
- The development of tools to make the calculations faster and make the model an efficient design tool from an industrial point of view.
- The application of the developed model to the tubes of the receiver to estimate their lifetime.

3 OUTLINE

The body of this thesis is divided into six chapters.

The first chapter focuses on the thermo-mechanical study of alloy 230 at various temperatures. It contains a metallographic analysis of some samples tested in different conditions such as fatigue, creep, and combined creep-fatigue. In addition, the main results from the experimental campaign on alloy 230 are presented and analysed.

The second chapter details the behaviour model, based on the Chaboche model, and its implementation in the finite-element code Lagamine. A sensitivity analysis on the model parameters is also presented. This sensitivity analysis serves as a basis for a step-by-step method for the identification of the model parameters.

The third chapter deals with the damage model, which is based on the Lemaitre damage model. It covers the development and the numerical integration of the model, with and without coupling with the behaviour model of chapter 2.

In the fourth chapter, the subject of corrosion is tackled. An analysis of the experimental data available in the literature is detailed. Based on this analysis, a simple corrosion model is proposed and developed within the framework of the above-mentioned behaviour and damage models.

The fifth chapter deals with numerical efficiency and proposes tools to obtain numerical results rapidly and accurately. Two methods for reducing computational times are evaluated and compared.

Finally, in the sixth chapter, the tubes from the solar receivers are modelled to assess their lifetime. Different configurations are tested, using the methods developed in chapter 5 and testing the influence of corrosion.

4 REFERENCES

[1] H. Ritchie and M. Roser, “Our World in Data,” 2020. https://ourworldindata.org/energy-production-consumption.

[2] V. Smil, Energy Transitions: Global and National Perspectives. Praeger, 2016.

[3] BP, “Statistical Review of World Energy,” 2021. [Online]. Available: https://www.bp.com/en/global/corporate/energy-economics/statistical-review-of-world-energy.html.

[4] D. Mackay, Sustainable Energy — without the hot air. 2009.

[5] University of Liege, “Lagamine FE code.” http://www.lagamine.uliege.be/dokuwiki/doku.php/.

Chapter 1: Thermo-mechanical behaviour of alloy 230 and experimental campaign

TABLE OF CONTENTS

1 ALLOY 230

The material studied in this research is alloy 230 (UNS N06230), a nickel-chromium-tungsten-molybdenum alloy known to have a high strength and a good resistance to corrosion at high temperatures. The material tested by the CRM Group as part of the research was provided by Haynes® in the shape of bars. A small sample of tube was also provided to test for differences between bars and tubes.

1.1 COMPOSITION

The chemical composition of alloy 230 is given in Table 1.1 – Chemical composition in percentage by weight of alloy N06230 [2]. The presence of tungsten and molybdenum gives the alloy a good resistance at high temperatures as these elements diffuse slowly in nickel. Chromium, along with manganese, silicon and lanthanum, help improve the resistance to oxidation [1]. Alloy 230 has a density of 8.97g/cm^3.

Table 1.1 – Chemical composition in percentage by weight of alloy N06230 [2]

Ni	Cr	W	Co	Fe	Mo	Mn
Balance (47.49-65.19)	20-24	13-15	5.0 max.	3.0 max.	1-3	0.3-1
Si	Al	C	P	S	B	La
0.25-0.75	0.2-0.5	0.05-0.15	0.03 max.	0.015 max.	0.015 max.	0.005-0.05

In order to obtain its optimal mechanical properties, the alloy is heat-treated at temperatures between 1177°C and 1246°C before being rapidly cooled. This treatment limits carbide precipitation in the material to ensure a good ductility. The melting temperature of alloy 230 is between 1301°C and 1371°C.

1.2 THERMAL AND MECHANICAL PROPERTIES

1.2.1 Thermal properties

Alloy 230 has a relatively low thermal expansion coefficient compared to other similar materials (high-strength nickel alloys, stainless steels, etc.), as shown in Figure 1.1. For instance, the thermal expansion of alloy 230 being heated from room temperature to 700°C is around 1%. Since thermal deformation is the cause for the appearance of mechanical strains and stresses in the solar receiver, using a material with a low thermal expansion is advantageous.

The thermal conductivity of alloy 230 is not very high and varies from 8.9 W.m^{-1}.K^{-1} at room temperature to 26.4 W.m^{-1}.K^{-}1 at 900°C. For comparison, the thermal conductivity

of stainless steel 304, alloy 800H, and Hastelloy X are respectively 16.2, 11.5, and 9.2 $W.m^{-1}.K^{-1}$ at room temperature. The limited thermal conductivity of alloy 230 is however acceptable for the application to the solar receivers since the receiver tubes are very thin (around 1.5 mm).

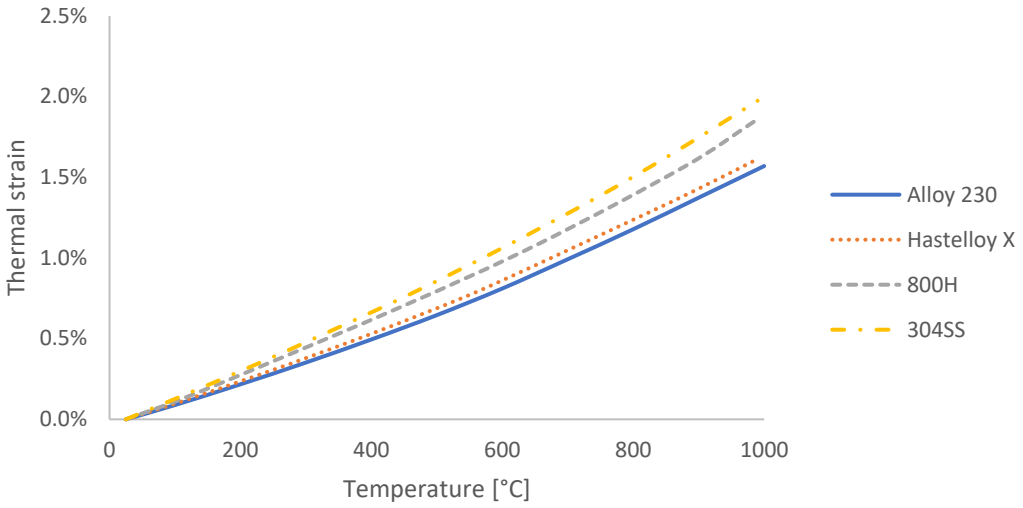

Figure 1.1 – Thermal expansion from room temperature of alloy 230, Hastelloy X, alloy 800H, and 304 stainless steel; data from Haynes [3]

1.2.2 Mechanical properties

Figure 1.2 shows the 0.2% yield strength and ultimate tensile strength (UTS) of alloy 230 at different temperatures. Both the 0.2% yield strength and the UTS decrease with temperature. The UTS starts to decrease more steeply after 650°C, while the 0.2% yield strength is rather stable between 500°C and 750°C. Overall, alloy 230 exhibits high tensile strength up to 750°C, with a 0.2% yield strength above 300 MPa and a UTS above 550 MPa.

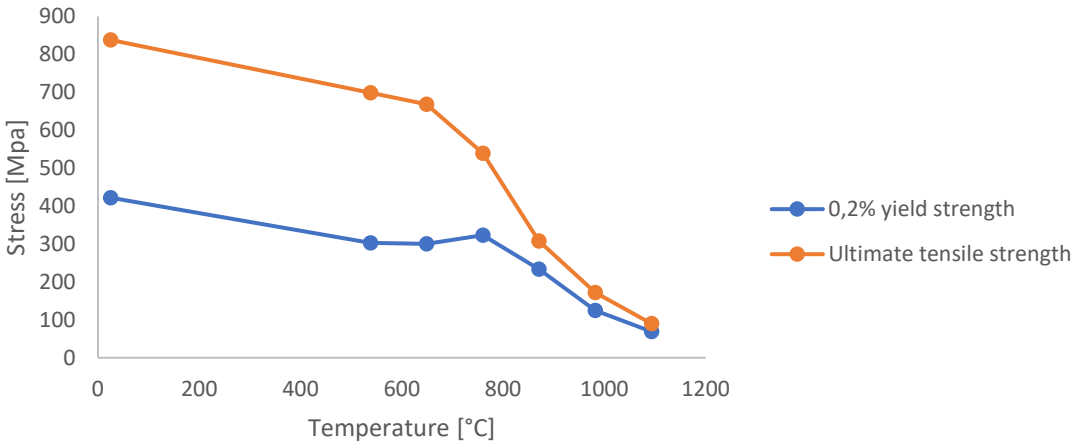

Figure 1.2 – 0.2% yield strength and ultimate tensile strength of alloy 230 at different temperatures [4]

At room temperature, the Young modulus of alloy 230 is about 212 GPa. The value of the Young modulus progressively decreases with temperature, as can be seen in Figure 1.3.

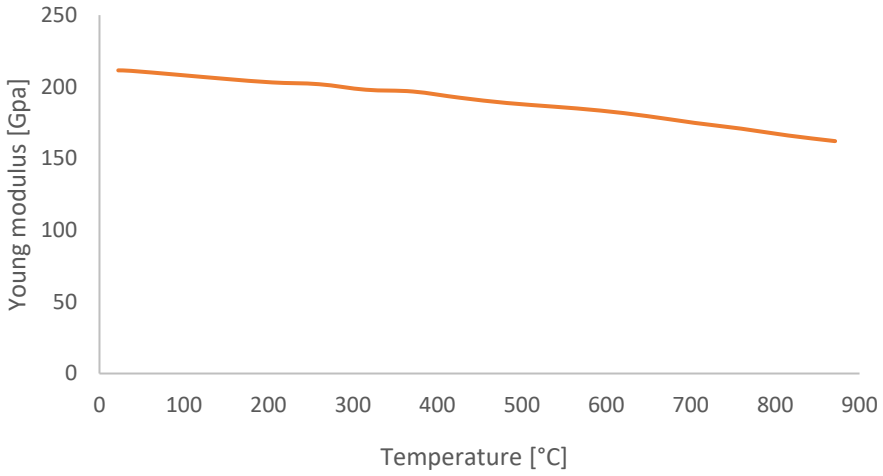

Figure 1.3 – Variation of the Young modulus of alloy 230 with temperature [2]

1.3 MICROSTRUCTURE

The microstructure of alloy 230 has been studied extensively in the literature. Additional analysis was performed by the CRM and by the Metallurgy and Material Science (MMS) lab of the University of Liège. All of the following analysis has been made on samples taken from bars, although the grain size was also measured on samples from tubes for comparison.

1.3.1 As-received microstructure

The ASTM (American Society for Testing and Materials) grain size is defined by Eq. (1.1), where n is the number of grains per inch at 100X magnification and G is the ASTM grain size.

$$n = 2^{G-1} \tag{1.1}$$

The ASTM grain size measured by CRM was of 4.5 for the bar. For the tube, the grain size was measured at 4.5 in the transversal direction and 5 in the longitudinal direction. These results are consistent with the data given by Haynes (grain size from 3 to 5 for bars, from 4 to 6.5 for sheets).

In its solution-annealed state, the material has a fully austenitic structure [1], [5], [6]. Despite the annealing process, uniformly distributed carbides can be observed, both on grain boundaries and inside grains, as shown in Figure 1.4. Those carbides are known to be tungsten-rich M_6C carbides which resist re-solution during the annealing process. Owing to their high stability, these carbides prevent grain-boundary migration and grain

growth when the material is exposed to very high temperatures [1], [7]. The presence of these carbides gives alloy 230 a good resistance to high-temperature creep and thermo-mechanical fatigue.

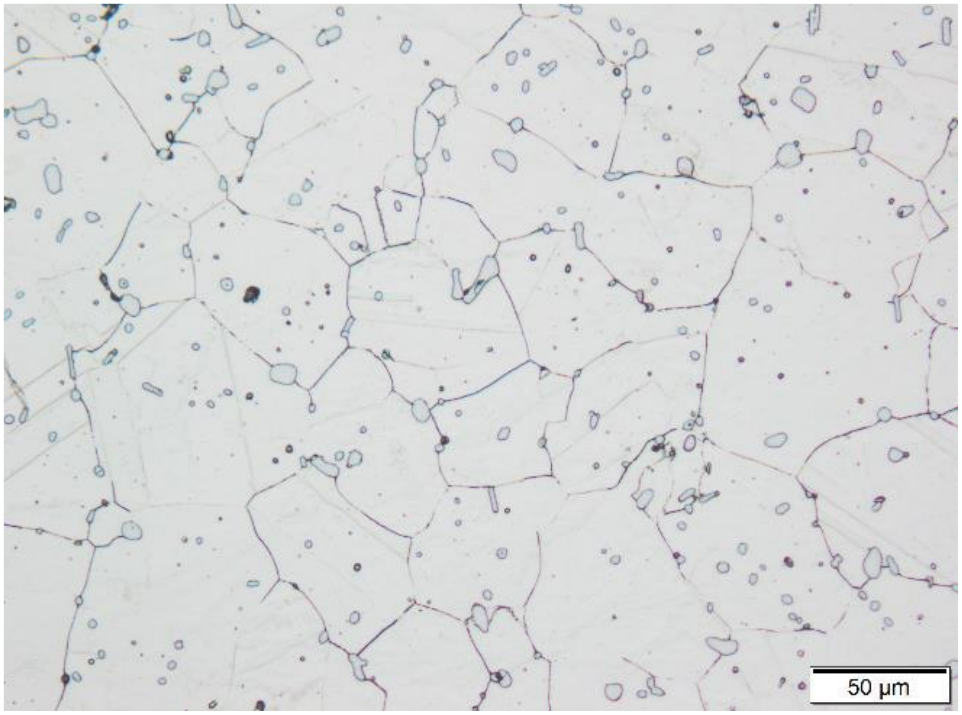

Figure 1.4 – Microstructure of as-received Haynes® 230 (bar) – MMS lab

In addition to these primary carbides, some smaller secondary $M_{23}C_6$ carbides can be found along grain boundaries [7]. These precipitates are known to form when the material is exposed to temperatures below 1150°C [8]. They form mainly at grain boundaries, pre-existing dislocations, and twin boundaries and are the only precipitates that have been found to form at temperatures between 650°C and 980°C [1], [5]. The amount of precipitation depends on the temperature, time, and loading of the material.

1.3.2 Microstructure after testing

As part of this research project, alloy 230 was tested at the CRM under different conditions. The experimental campaign is detailed in Section 2 below.

To get a better understanding of the changes of behaviour that can occur in the material when it is subjected to loading, several samples that had been tested were analysed by the Metallurgy and Materials Science lab at the University of Liège.

The samples were cut using wire electrical discharge machining or a cut-off wheel. They were then mounted within resin and finally polished using a 1-micron diamond suspension to achieve a mirror finish.

The microstructure of the specimens was observed using an Olympus BX60M microscope. After an observation of the material in the polished condition, the surface was chemically etched using a solution of HCl and HNO_2 to reveal the microstructural constituents of the specimen (grains and precipitates).

1.3.2.1 Fatigue at 700°C

Figure 1.5 shows the microstructure of alloy 230 after a fatigue test at 700°C with a strain amplitude $\Delta\varepsilon = \pm 0.3\%$ and a frequency of 0.5 Hz. The test was conducted to rupture, which occurred after around 8000 cycles, meaning the material was exposed to a temperature of 700°C for around 4,5 hours.

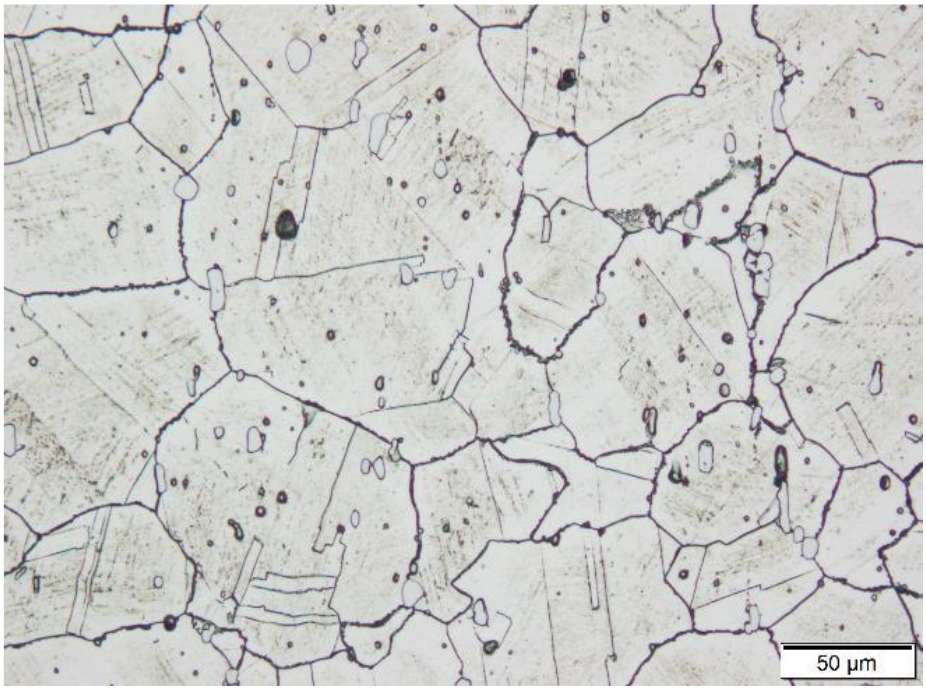

Figure 1.5 – Microstructure of alloy 230 after a fatigue test at 700°C with a strain amplitude $\Delta\varepsilon = \pm 0.3\%$

Compared to the reference state (Figure 1.4), the microstructure of the specimen after fatigue shows a recrystallised structure with twinning boundaries. The grain boundaries are more contrasted than in the reference, and some of them appear to be serrated, which is a sign of secondary precipitation taking place along the grain boundaries.

1.3.2.2 Creep at 700°C

Two creep samples were studied, both tested at 700°C:

- Sample ZC3 which was tested under a constant stress of 165 MPa for a duration of 7103h (rupture), shown in Figure 1.6.
- Sample ZC4 which was tested under a constant stress of 295 MPa for a duration of 172h (rupture), shown in Figure 1.7.

In both samples, the grains are elongated in the loading direction. In the ZC3 sample, the grain boundaries are more contrasted than in the reference (Figure 1.4), and some grain boundaries display serrations which indicate secondary precipitation. In the ZC4 sample, the grain boundaries are also more contrasted than the reference but less than the ZC3 sample. This can be explained from the difference in the duration of the tests. Sample ZC3 was exposed to a temperature of 700°C for more than 7000h, that is around 40 times longer than sample ZC4. Therefore, it is expected that more precipitation occurred in sample ZC3.

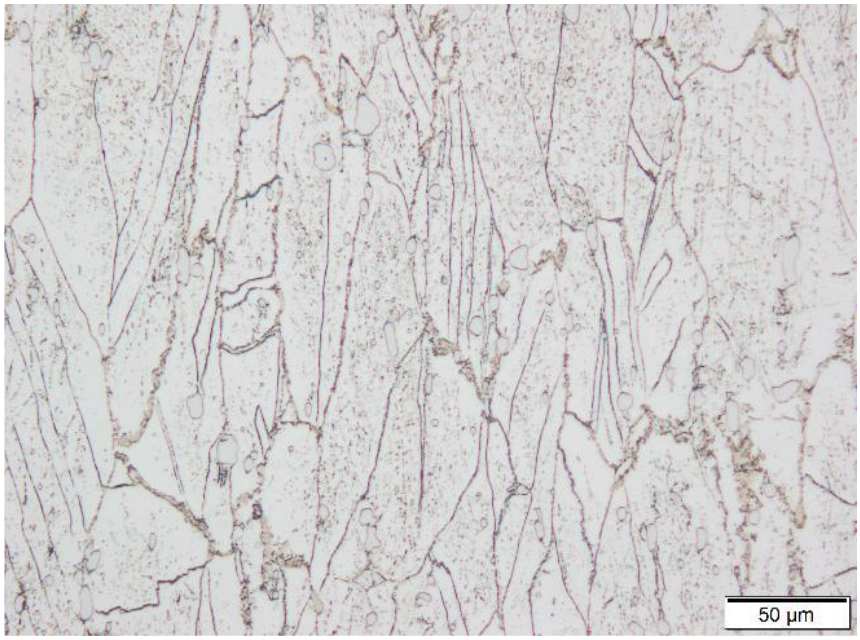

Figure 1.6 – Microstructure of alloy 230 after a creep test at 165 MPa (7103h)

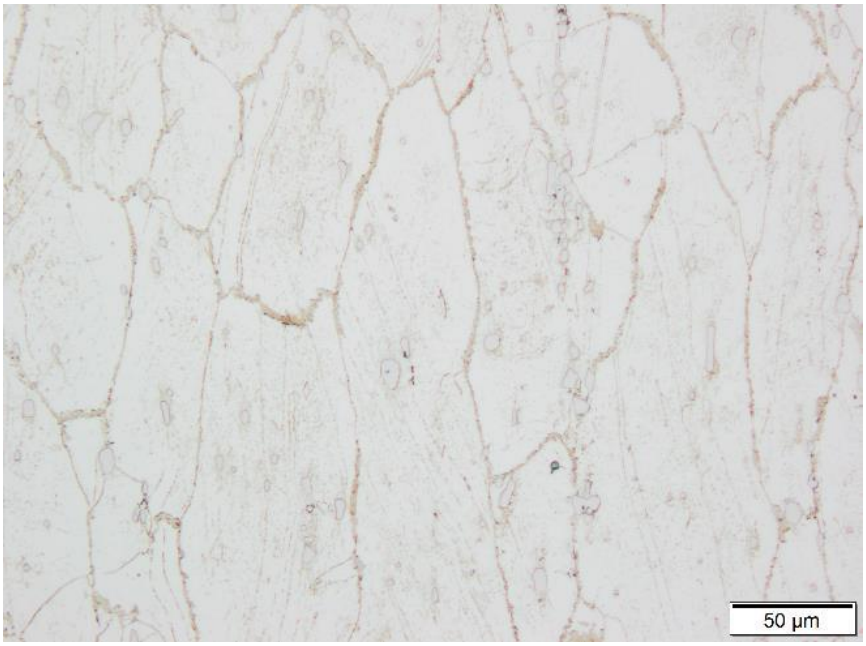

Figure 1.7 – Microstructure of alloy 230 after a creep test at 295 MPa (172h)

1.3.2.3 Creep-fatigue at 700°C

Creep-fatigue tests are strain-controlled cyclic tests which comprise hold times at maximum and/or minimum strain. Figure 1.8 shows the microstructure of the material after a creep-fatigue test at 700°C with a strain amplitude $\Delta\varepsilon = \pm 0.3\%$ and hold times of 120s at $\varepsilon = -0.3\%$ (compressive hold). The strain rate for loading and unloading is equal to 0.1%/s. The rupture occurred after 1378 cycles, corresponding to a total test time of 48 hours. The microstructure is similar to the microstructure obtained from the fatigue test (Section 1.3.2.1), with precipitates both inside grains and at grain boundaries, as well as twinning boundaries.

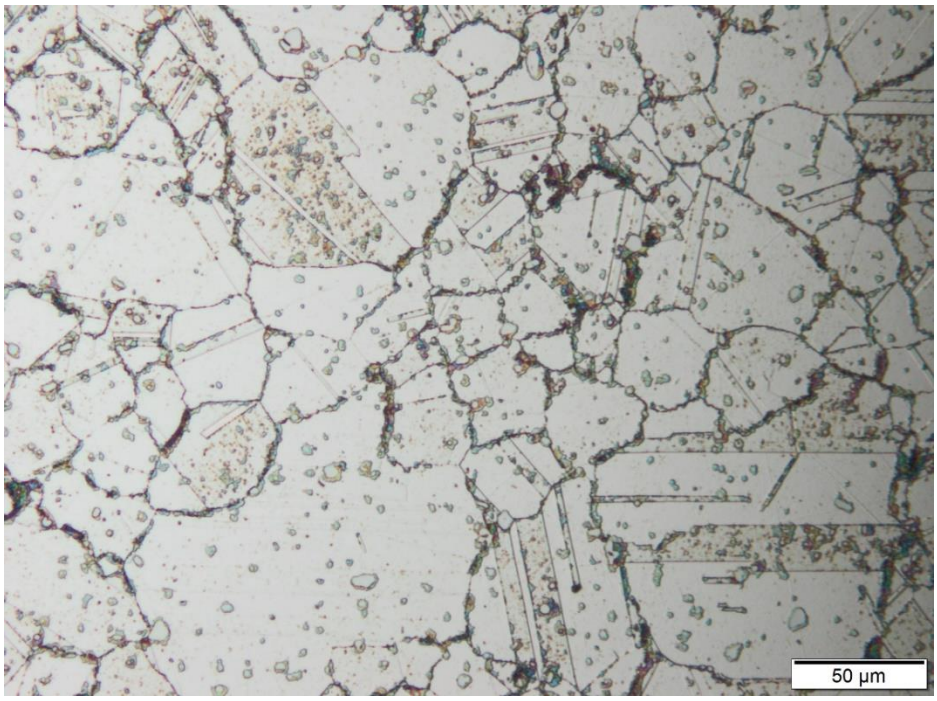

Figure 1.8 – Microstructure of alloy 230 after a creep-fatigue test at 700°C with a strain amplitude $\Delta\varepsilon = \pm 0.3\%$

Figure 1.9 shows the rupture plane and Figure 1.10 shows a secondary crack. Both pictures are evidence of a transgranular mode of cracking, usually associated with fatigue. In the literature, studies made on alloy 230 at 800°C and 850°C show that low-cycle fatigue testing result in transgranular cracking [9], while creep testing leads to intergranular cracking [6]. Mixed creep-fatigue loadings with hold times in tension led to mixed modes of cracking, with an increased influence of intergranular cracking with longer hold times [9], [10]. The fact that only transgranular cracking is observed in our case may be due to the fact that the hold times (where creep is likely to occur) are applied under compression, which is not favourable for the development of cracks. However, the lifetime under creep-fatigue is much shorter than the lifetime of the equivalent fatigue test studied above (same temperature, strain amplitude, and strain rate). This severe reduction of the lifetime does not seem to be linked directly to creep damage, which consists of grain boundary voiding and intergranular decohesion, but rather to

environmental factors. Indeed, thermal ageing causes significant precipitation and plays an important role in the lifetime reduction [11]. Additionally, oxidation was observed along the cracks and could have assisted the crack propagation. However, there is no sign that oxidation was responsible for crack initiation.

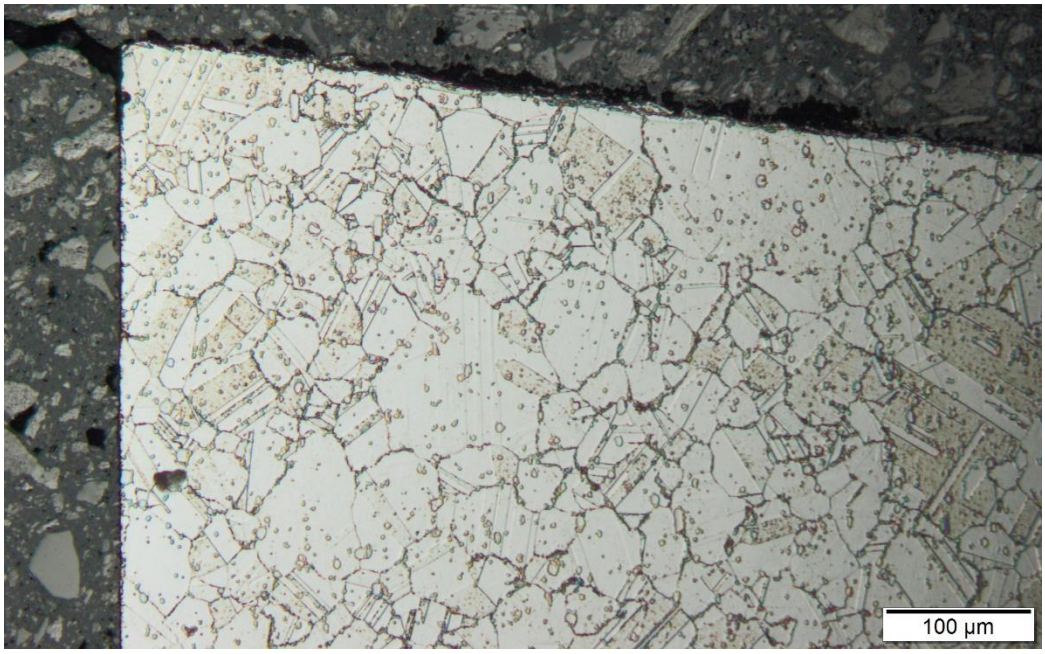

Figure 1.9 – Rupture surface of the tested sample after the creep-fatigue test at 700°C

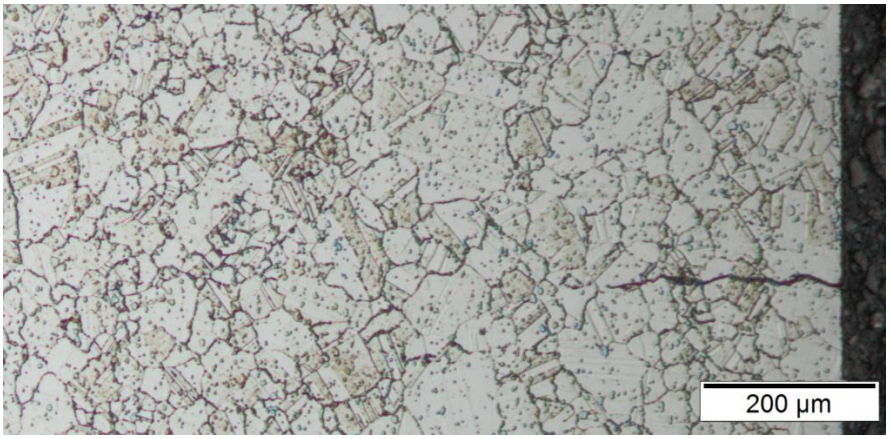

Figure 1.10 – Secondary crack in the material after creep-fatigue testing at 700°C

1.3.2.4 Anisothermal creep-fatigue between 300°C and 700°C

A test similar to the creep-fatigue test was performed with varying temperatures. In the anisothermal case, however, hold times of 120s were applied both in tension and compression. The temperature is varied along with the strain: compression phases correspond to the maximum temperature (700°C) and tensile phases to the minimum temperature (300°C). The strain rate is set to around 0.002% to match the temperature variation. Rupture occurred after 1549 cycles, corresponding to a total test duration of 330 hours.

Figure 1.11 shows the microstructure of the sample after testing. As for the fatigue and creep-fatigue tests, significant precipitation can be observed at grain boundaries and inside grains as well as twinning.

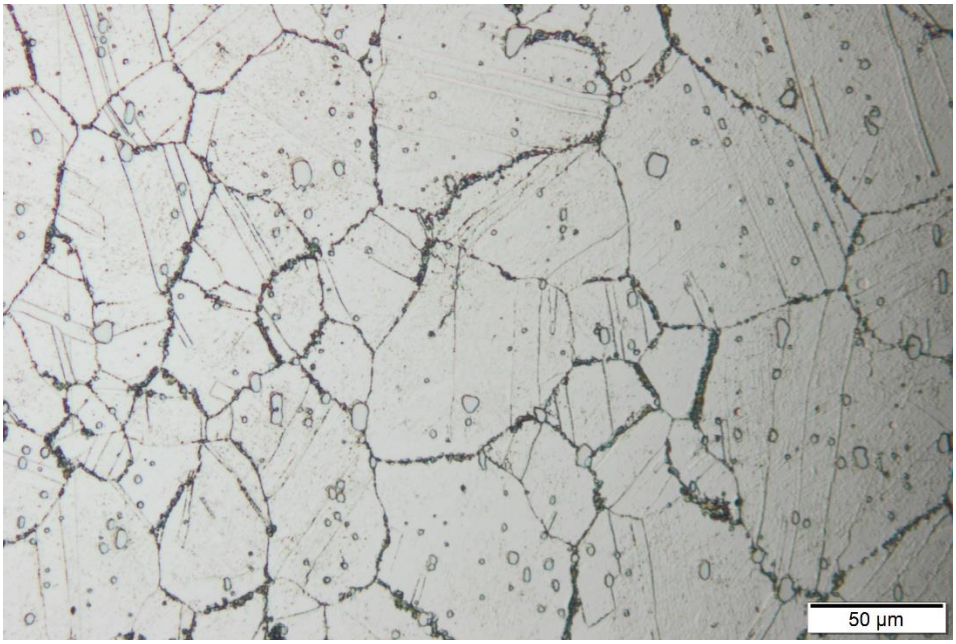

Figure 1.11 – Microstructure of alloy 230 after anisothermal creep-fatigue testing

The cracking mode is transgranular, as it was for the isothermal creep-fatigue tests. Figure 1.12 shows a close-up of a crack in the longitudinal plane. Once again, the effect of creep on the fracture mode may be less significant in these tests because the hold times at high temperature occur under compressive strain. The tensile hold times are done at 300°C, where little to no creep occurs.

Figure 1.12 – Transgranular crack in the sample after anisothermal creep-fatigue testing

2 EXPERIMENTAL CAMPAIGN

The following section summarizes the results of the mechanical experimental campaign performed on alloy 230 by the CRM for the Solar PERFORM and Solar GNEXT projects. All the samples tested were manufactured from bars of alloy 230.

For confidentiality reasons, all the test results are normalized, i.e., the values have been divided by an adequate factor for each type of test.

2.1 TENSILE TESTS

Tensile tests were performed at various temperatures to obtain the stress-strain relation of the material. The normalized results are shown in Figure 1.13. The maximum strain ε_{max} was chosen in a range from 1% to 5%. ε_{max} was used to normalize the strain in Figure 1.13 and the stress value at ε_{max} for the test at room temperature was used to normalize the stress. The strain range is limited to this maximum strain in the figure because large strain behaviour is not of interest for the application to solar receivers. The stress-strain curves are consistent with the general properties given by the manufacturer (see section 1.2.2): the stress is highest at room temperature and the behaviour remains more or less the same at temperatures ranging from 200°C to 700°C. Above 700°C, the stresses are lower and tend to decrease with increasing strain (softening of the material).

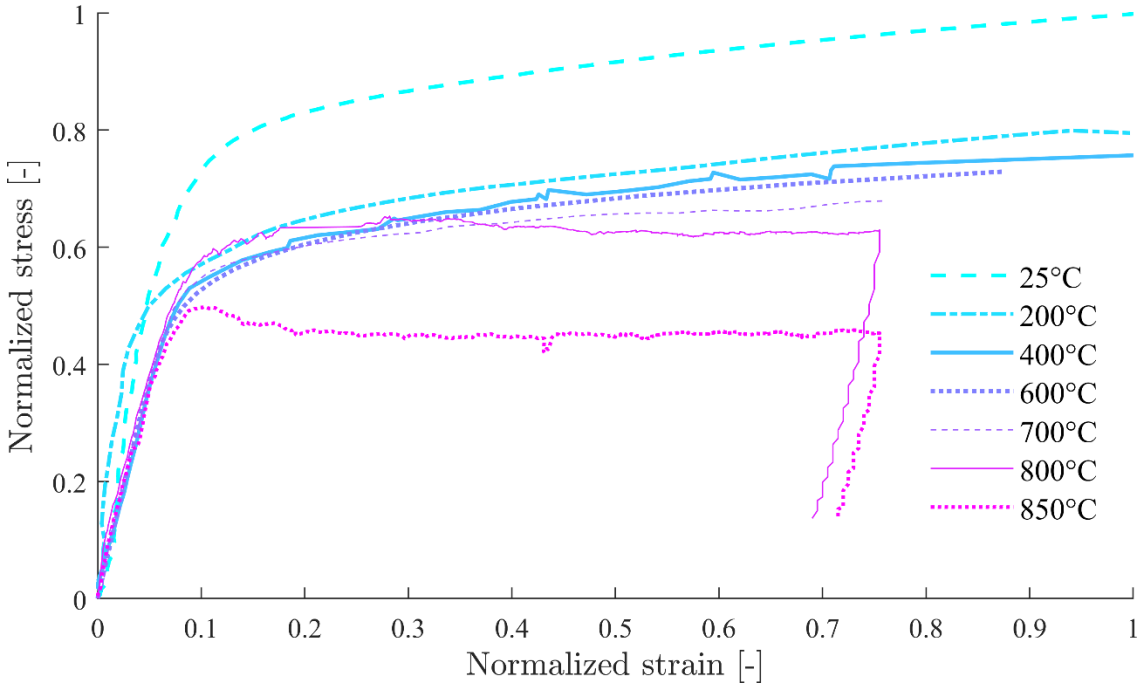

Figure 1.13 – Tensile test results at different temperatures. The stress is normalized with the value of the stress at a deformation ε_{max} at room temperature.

2.2 CREEP

Several creep tests were performed at temperatures ranging from 600°C to 850°C. Figure 1.14 shows the typical creep behaviour of alloy 230 at high temperature. Three stages can be distinguished:

- Primary creep, where the creep rate is initially high but decreases with time due to strain hardening. This stage is usually very short for alloy 230, particularly at higher temperatures.
- Secondary creep, where the creep rate remains constant due to a balance between strain hardening and thermal softening or recovery of dislocations.
- Tertiary creep, where the strain rate increases exponentially due to necking and coalescence of defects, leading to rupture.

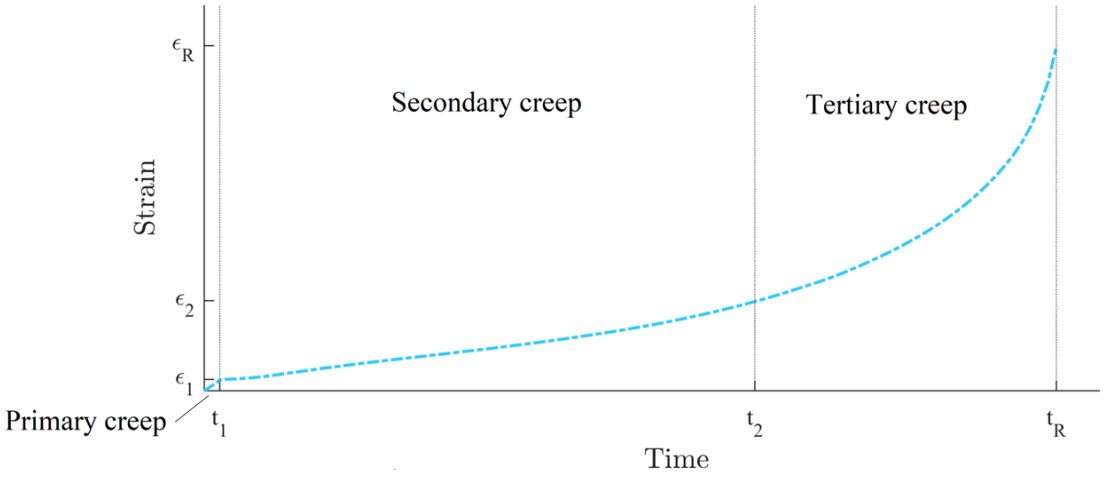

Figure 1.14 – Schematic of a typical creep test for alloy 230

The secondary creep phase is the most interesting for design purposes: primary creep is only a transitory state and tertiary creep corresponds to a highly damaged material, which should be avoided.

Figure 1.15 shows the secondary creep strain rate at different temperatures for three tested values of creep stress. The data comes from experiments done at the CRM and data provided by Haynes®. A logarithmic scale is used for the strain rate. For a given value of the creep stress, the evolution of creep strain rate with temperature is exponential. It can also be noted that the creep rate is relatively small at 600°C (10^{-4} $\%/h$), even for a high stress like 276 MPa, which corresponds to 92% of the yield stress.

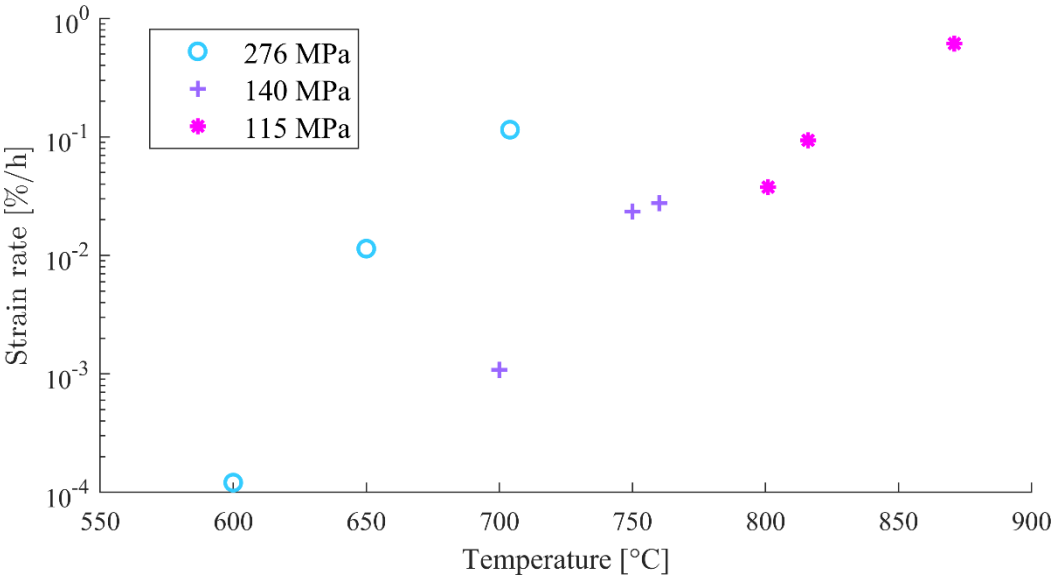

Figure 1.15 – Secondary creep strain rate as a function of temperature for different creep stress values

2.3 RELAXATION

Multiple hardening and relaxation (MHR) tests were performed at different temperatures. These tests consist in applying sequential strain holds and increasing the value of the strain at each new hold time, as shown in Figure 1.16. The sample is first maintained at a 0.1% strain for a duration t_{rel}, then the strain is increased to 0.2% and held at this strain for another period t_{rel}, then the strain is increased to 0.3%, etc… Relaxation is a phenomenon related to creep, and both are associated to the viscosity of the material at high temperature. The main mechanism is the diffusion of atoms which tend to eradicate dislocations, and therefore lower the mechanical resistance of the material. The stress curves shown in Figure 1.16 are normalized with the maximum stress obtained on the test at 600°C.

MHR tests show the relaxation behaviour of the material: at high temperature, the stress gradually decreases when the strain is kept constant. As can be seen in Figure 1.16, relaxation becomes more significant with increasing temperatures. At 600°C, there is little to no change in the stress level, which is coherent with the creep strain rate measured at 600°C (see Section 2.2 above). Starting from 700°C, there is a rapid and significant drop in the value of the stress. It can be noted that the rate of relaxation increases with temperature, i.e., the stress drops more rapidly at higher temperatures, which is expected because diffusion rates of atoms in metals become higher with increasing temperatures.

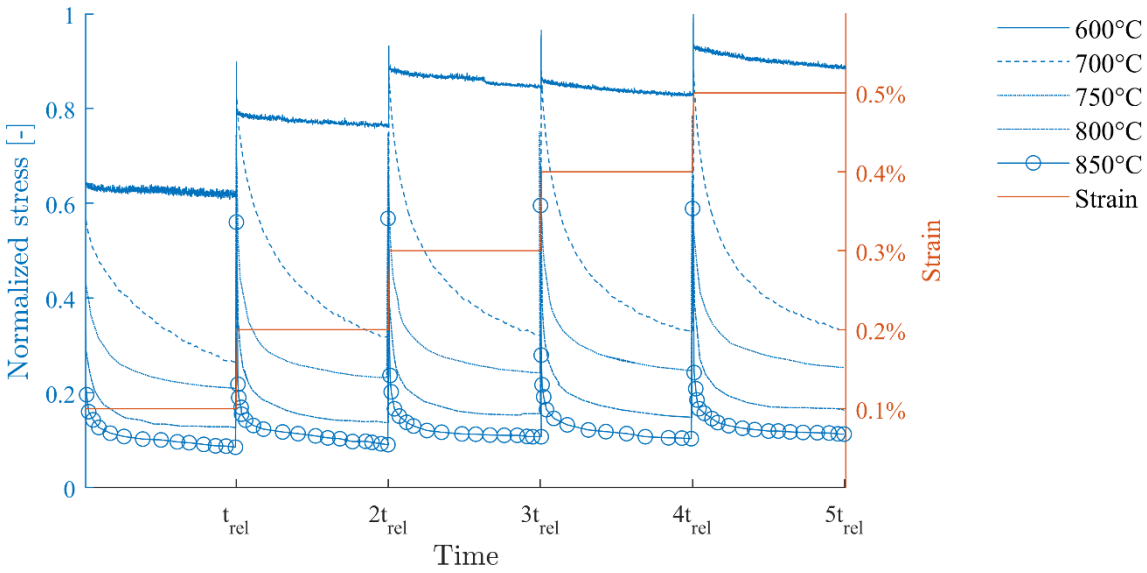

Figure 1.16 – Multiple hardening and relaxation tests at temperatures from 600°C to 850°C. The stress curves are normalized with the maximum stress at 600°C.

2.4 FATIGUE

Strain-controlled low-cycle fatigue (LCF) tests were performed at various temperatures with different strain amplitudes $\Delta\varepsilon$. Figure 1.17 represents the imposed strain for the low-cycle fatigue tests. The imposed strain has a triangular waveform and evolves between $-\Delta\varepsilon$ and $+\Delta\varepsilon$. Ahmed [12] showed that the value of the frequency has little to no effect on the LCF response of alloy 230 at temperatures below 871°C; therefore, the frequency of the loading was set to 0.5 s^{-1} for all tests as a compromise between an efficient control and a limited duration of the test. For tests above room temperature, the samples were heated with an inductor.

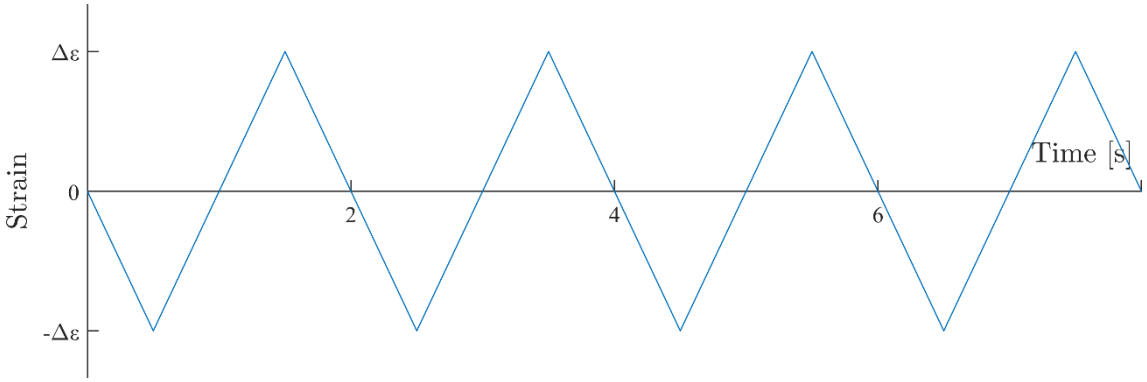

Figure 1.17 – Imposed strain for the low-cycle fatigue tests

Figure 1.18 and Figure 1.19 show the normalized stress amplitude from the LCF tests. The results are grouped by strain amplitude in Figure 1.18 and by temperature in Figure 1.19. For each graph, the stress amplitude σ_{amp} is normalized with the maximum stress of all LCF tests at that temperature or strain rate: for instance, at 0.2% strain amplitude in

Figure 1.18, the maximum stress amplitude $\sigma_{\max(0.2\%)}$ is obtained at the last cycle of the 400°C test. The curves plotted in the 0.2% graph correspond to $\sigma_{amp}/\sigma_{\max(0.2\%)}$.

From Figure 1.18, it can be observed that for a given strain amplitude, the stress levels are similar at high temperature. The room temperature stress amplitude is systematically above the other curves at low and intermediate cycle numbers, however, towards the end of the tests, stress amplitudes are often higher for medium temperatures (400 to 700°C). Above 700°C, cyclic hardening (i.e., an increase of the stress amplitude with cycles) is not as significant, and the final stress amplitude is lower than for temperatures ranging from 400°C to 700°C.

The change of behaviour with temperature is clearly not monotonous: for instance, with a 0.4% strain amplitude, the material exhibits cyclic softening at room temperature, significant cyclic hardening at temperatures from 400°C to 700°C, and a rapid stabilization at 800°C and 850°C.

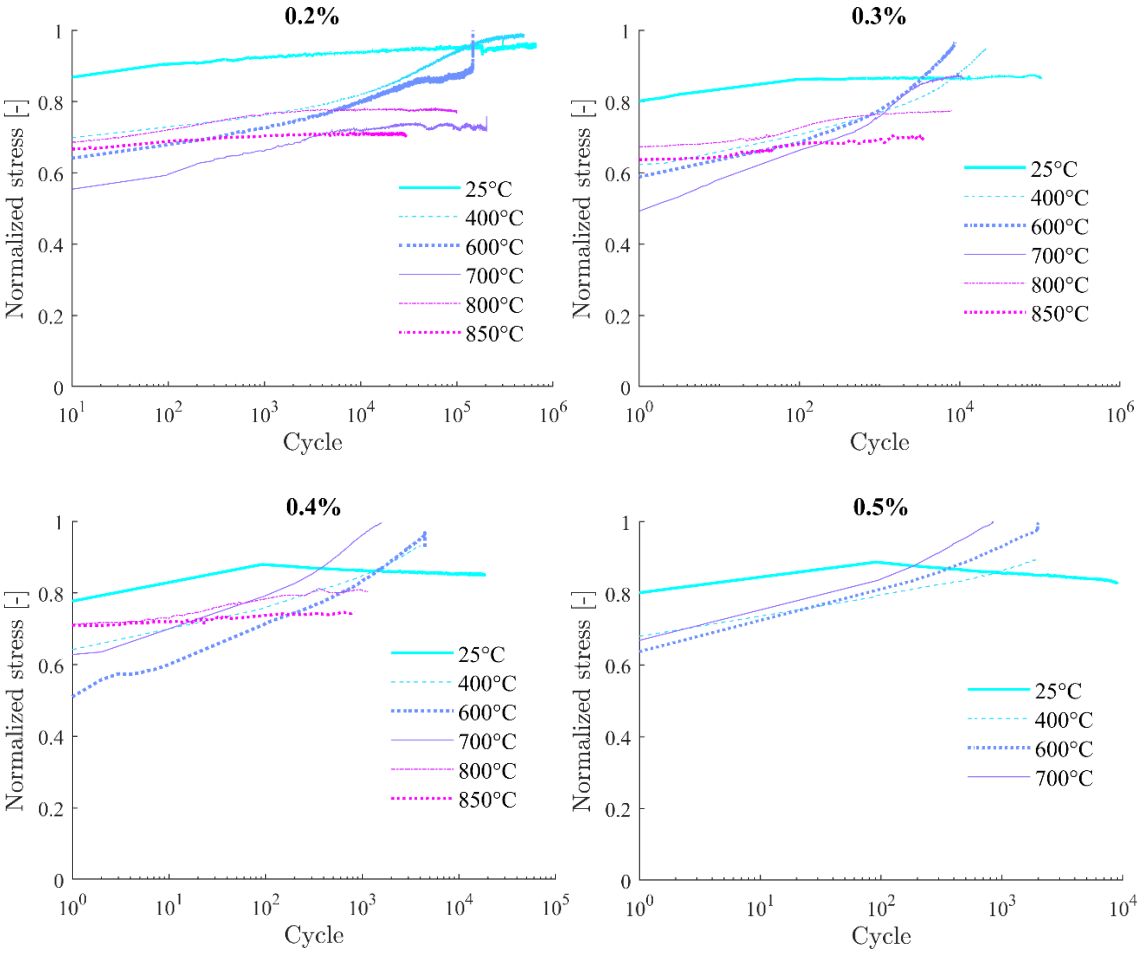

Figure 1.18 – Stress amplitude of LCF tests for strain amplitudes of 0.2%; 0.3%; 0.4%; 0.5%

Figure 1.19 shows that at every temperature the stress amplitude is higher for higher strain amplitudes. At room temperature, the stress amplitude increases in the first 100 cycles

and then decreases (cyclic softening for $\Delta\varepsilon = 0.5\%$ and 0.4%) or stabilizes. From 400°C to 700°C, the material exhibits significant cyclic hardening. For temperatures above 700°C, the stress amplitude tends to stabilize more rapidly.

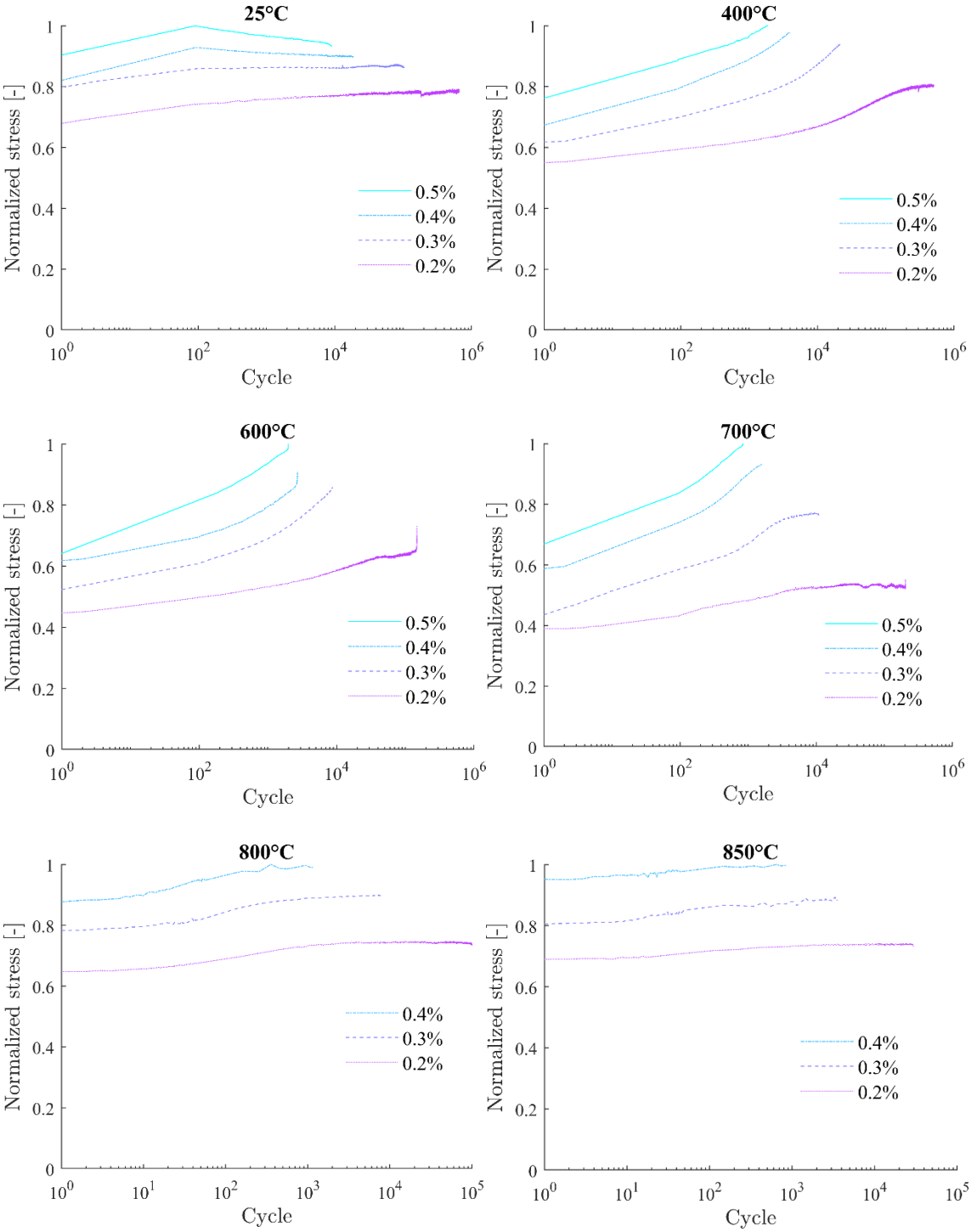

Figure 1.19 – Stress amplitude for various low-cycle fatigue tests at 25°C; 400°C; 500°C; 600°C; 700°C; 750°C; 800°C; 850°C

Figure 1.20 shows the normalized stress-strain hysteresis loops at cycles 2, 100, 5500 and 10000 (near rupture) for a low-cycle fatigue test at 700°C with a 0.3% strain amplitude.

There is a noticeable thinning of the hysteresis loop with increasing cycles, which is evidence of the cyclic hardening. The stress-strain hysteresis loops for cycles 5500 and 10000 overlap almost perfectly, which shows the stabilization of the material behaviour.

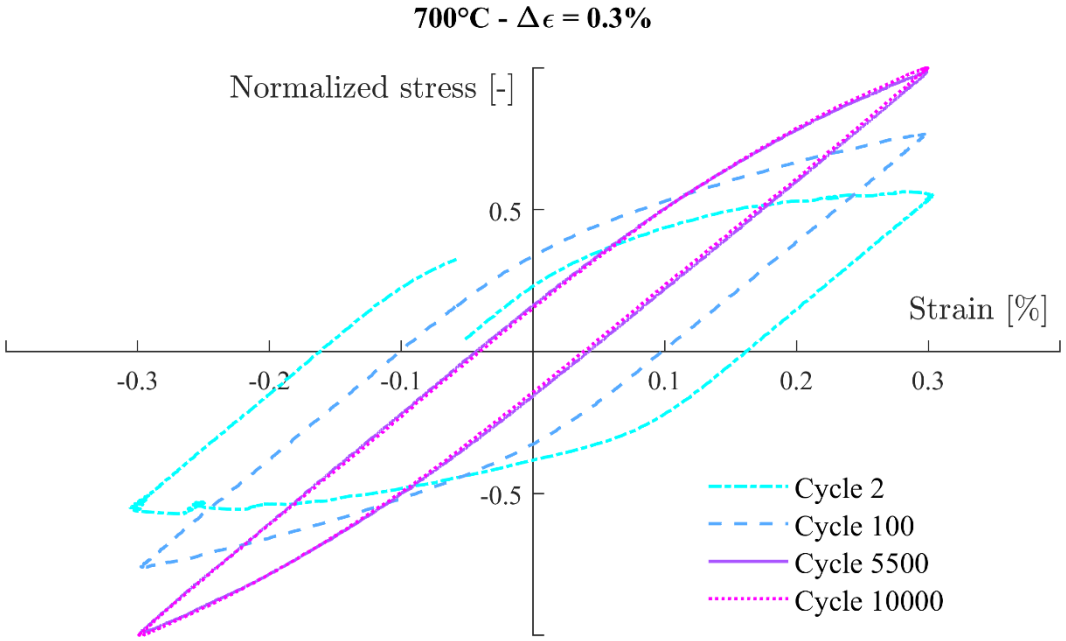

Figure 1.20 – Normalized stress vs. strain hysteresis loops at different cycles for the LCF test at 700°C with a 0.3% strain amplitude

2.5 COMBINED CREEP-FATIGUE

2.5.1 Isothermal creep-fatigue

At high temperature, alloy 230 exhibits viscous behaviour, which can be influenced by the viscosity of the material. In order to test the effect of viscosity on the cyclic behaviour, creep-fatigue tests were performed. These tests are cyclic tests that include one or several hold times in each cycle, as represented in Figure 1.21. The test characteristics are summarized in Table 1.2, where T is the temperature, t_H^- the hold time under compressive strain, t_H^+ the hold time under tensile strain, $\Delta\varepsilon$ the strain amplitude, and $\dot{\varepsilon}$ the strain rate during the ramp loading.

Table 1.2 – Creep-fatigue test characteristics

Test	T	t_H^-	t_H^+	$\Delta\varepsilon$	$\dot{\varepsilon}$
C700	700°C	t_1	0s	0.3%	0.6%/s
TC700			t_1		
C800 1	800°C	t_1	0s	0.25%	0.1%/s
C800 2		$5t_1$			
C800 3		$30t_1$			

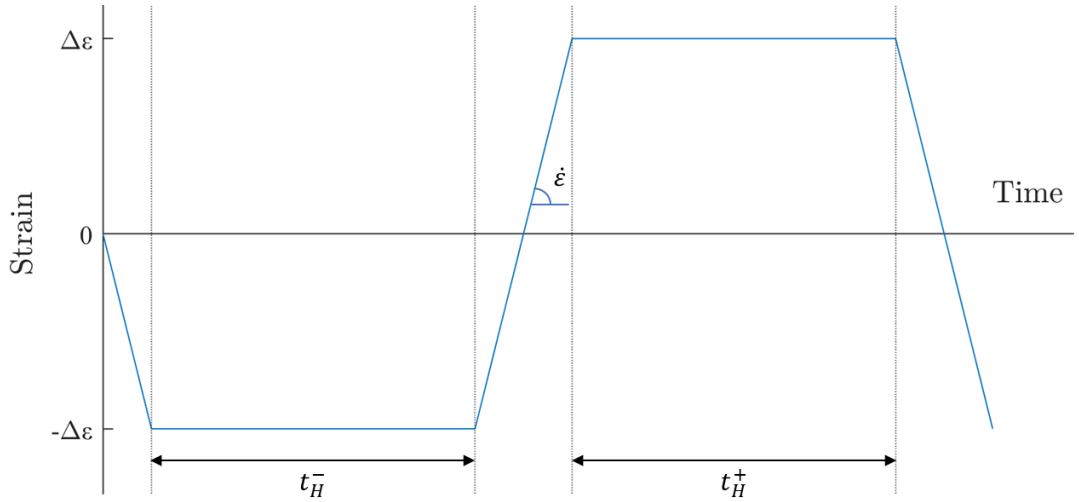

Figure 1.21 – Loading for the isothermal creep-fatigue tests

Figure 1.22 shows the normalized maximum and minimum stresses for the creep-fatigue tests performed at 800°C with a strain amplitude of 0.25% (C800-1, C800-2, and C800-3). The stress amplitude from fatigue tests with 0.2% and 0.3% strain amplitude is also plotted for comparison. The stress amplitude for creep-fatigue tests is more or less the same, regardless of the hold time. Compared to the fatigue tests, there is a clear shift towards tensile stresses with increasing number of cycles. This shift also seems to be more significant for higher hold times. The shift towards tensile stress is due to the asymmetry of the loading: during the compressive strain hold, the stress relaxes towards smaller values of the compressive stress, as can be seen in Figure 1.23 for test C800-3. After 10 cycles, the maximum compressive stress is approximately 80% of the maximum tensile stress.

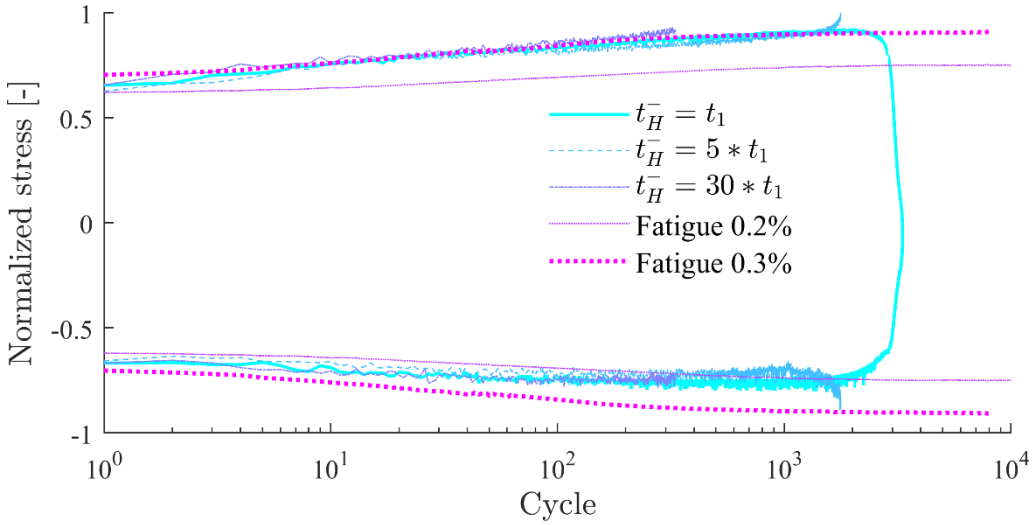

Figure 1.22 – Normalized stress amplitude for the creep-fatigue tests at 800°C

The lifetime in terms of number of cycles is significantly reduced for tests with hold times compared to pure fatigue tests, and the reduction is larger for longer hold times. Since the stress levels are similar for the three 800°C creep-fatigue tests, a likely explanation for

this reduction is the influence of thermal ageing and the larger amount of plastic deformation that occurs during the relaxation phase.

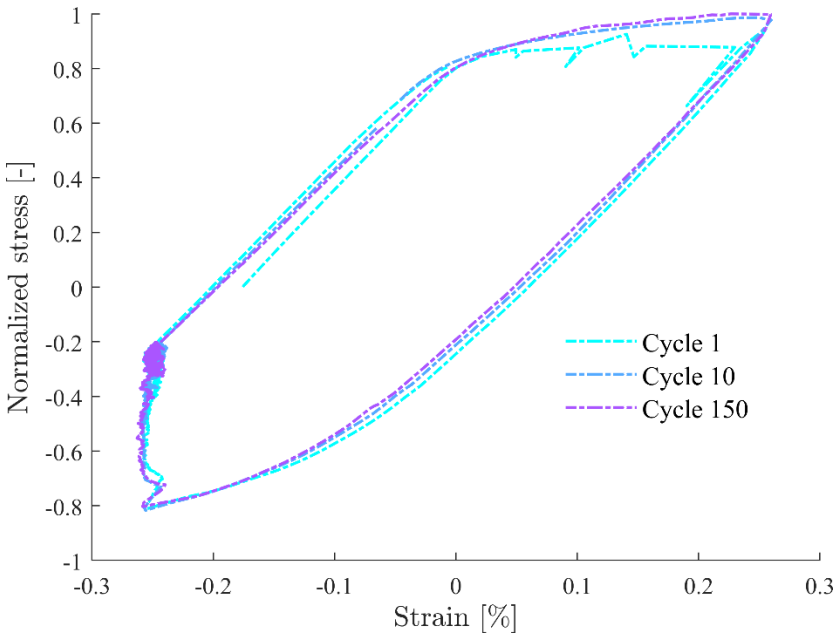

Figure 1.23 – Normalized stress-strain hysteresis loop for the creep-fatigue test C800-3 at 800°C with $30t_1$ hold time in compression

The hysteresis loops shown in Figure 1.23 are similar for all cycles. However, it can be noted that the Young modulus (i.e., the slope of the linear parts of the loop) decreases slightly with increasing number of cycles. This could also be due to thermal ageing or to damage of the material.

2.5.2 Anisothermal creep-fatigue

The behaviour of the material under varying temperature is studied using anisothermal creep-fatigue tests, similar to the isothermal ones described in section 2.5.1 above. The imposed loading is shown in Figure 1.24: a mechanical strain ε^m is imposed to the sample while the temperature is made to vary at the same time. The mechanical strain is defined by Eq. (1.2) where ε is the total strain and ε^{th} is the thermal strain caused by thermal expansion. Practically, a first cycle without mechanical strain, i.e., the temperature is varied at zero applied force, is performed to measure the thermal strain with an extensometer. The total strain to apply as a function of time on one cycle is then calculated as the sum of the targeted mechanical and measured thermal strains.

$$\varepsilon^m = \varepsilon - \varepsilon^{th} \tag{1.2}$$

The sample is held under compressive mechanical strain at high temperature T_{max} and under tensile strain at low temperature T_{min}, as shown in Figure 1.24. Two maximum temperatures were tested. For confidentiality reasons, the values of temperatures T_{min}

and T_{max} are not disclosed here, but the unique T_{min} is in the range of 25°C to 500°C (temperatures at which no creep or relaxation occurs) and the two chosen values of T_{max} were above 600°C (temperatures at which creep and relaxation are present).

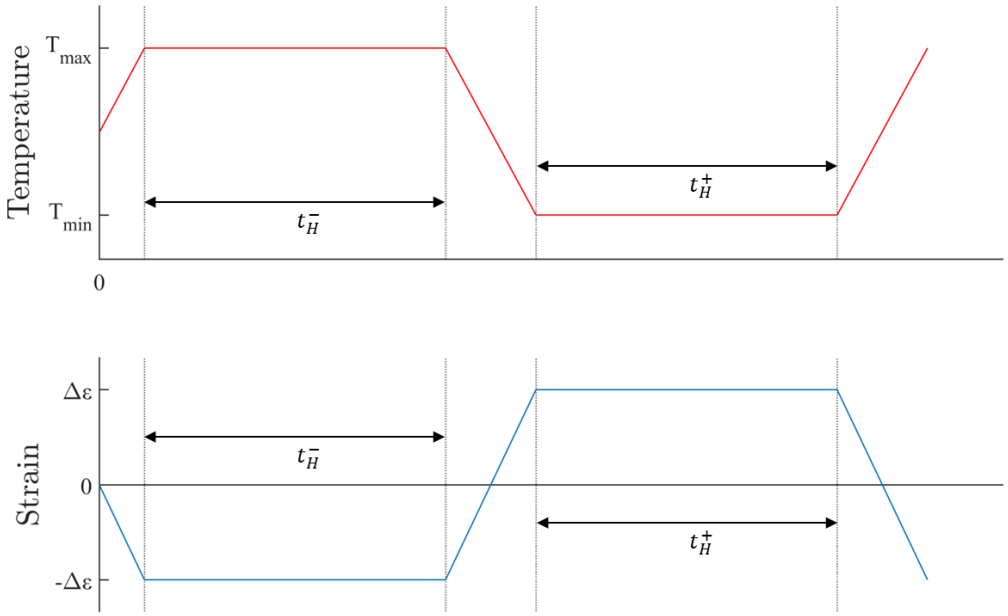

Figure 1.24 – Loading of the anisothermal creep-fatigue tests: imposed temperature (top) and imposed mechanical strain (bottom)

Figure 1.25 shows the hysteresis loops at different cycles for one of the anisothermal creep-fatigue tests. When the mechanical strain increases from -0.25% to +0.25%, the behaviour is similar to the behaviour under isothermal loading, i.e., the stress increases with increasing strains. It can be observed that despite the hold time, no stress relaxation occurs at +0.25%, which is expected since this value of the strain corresponds to temperature T_{min} where the material shows no creep or relaxation. When the strain is lowered to negative values, the absolute value of the stress increases at first, and then decreases. This is due to the temperature changes: as the compressive strain is increased, so is the temperature. Increasing the temperature leads to a softening of the material, as shown in sections 2.1 and 2.4. Once the peak compressive strain is reached, the stress relaxes (i.e., decreases in absolute value) during the hold time t_H^-.

By comparing the curves at different cycles, it can be observed that the Young modulus decreases significantly with increasing number of cycles, similarly to what was observed for the isothermal test (Figure 1.23). It is likely that the effect of thermal ageing is more visible at lower temperatures, therefore, the decrease of the Young modulus seems more significant here than in the isothermal test which is kept at T_{max}.

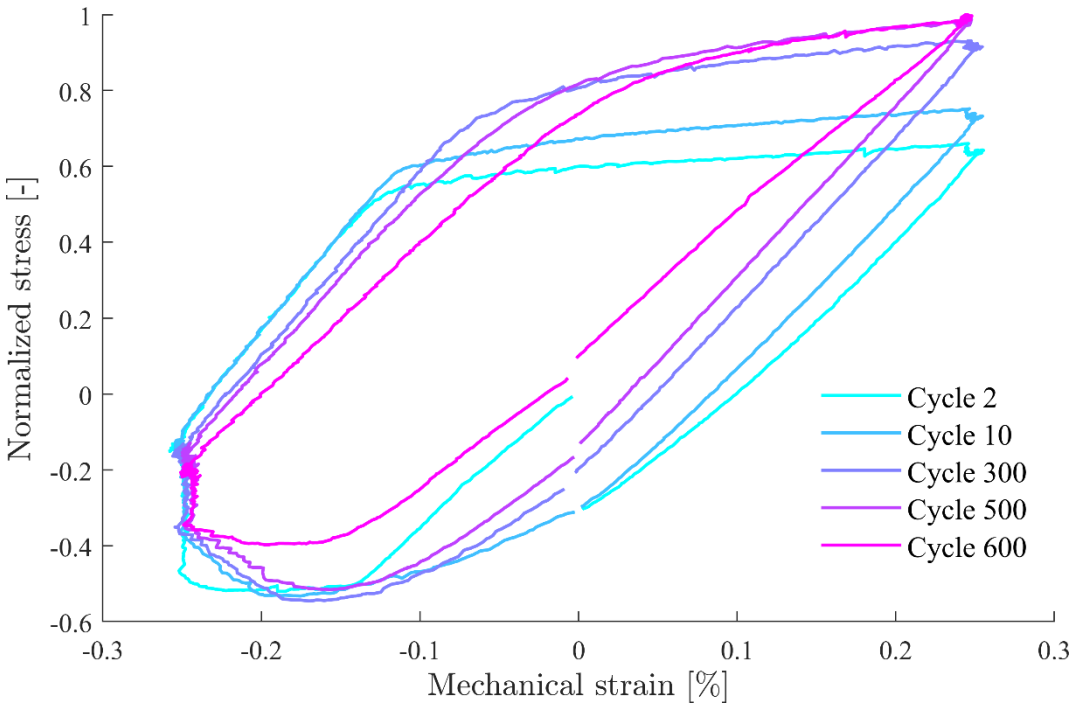

Figure 1.25 – Hysteresis loops for an anisothermal creep-fatigue test at cycles 2, 10, 300, 500, and 600

Figure 1.26 shows the normalized maximum and minimum stresses per cycle for an anisothermal test and the equivalent isothermal test at T_{max} (same $\Delta\varepsilon$ and same t_H^-). The compressive stresses are more or less the same, however, the tensile stresses are much higher for the anisothermal tests. This is due to the fact that the tensile stresses develop at lower temperatures, where hardening of the material is more significant. The lifetime in terms of number of cycles is significantly reduced with the anisothermal loading compared to the isothermal loading.

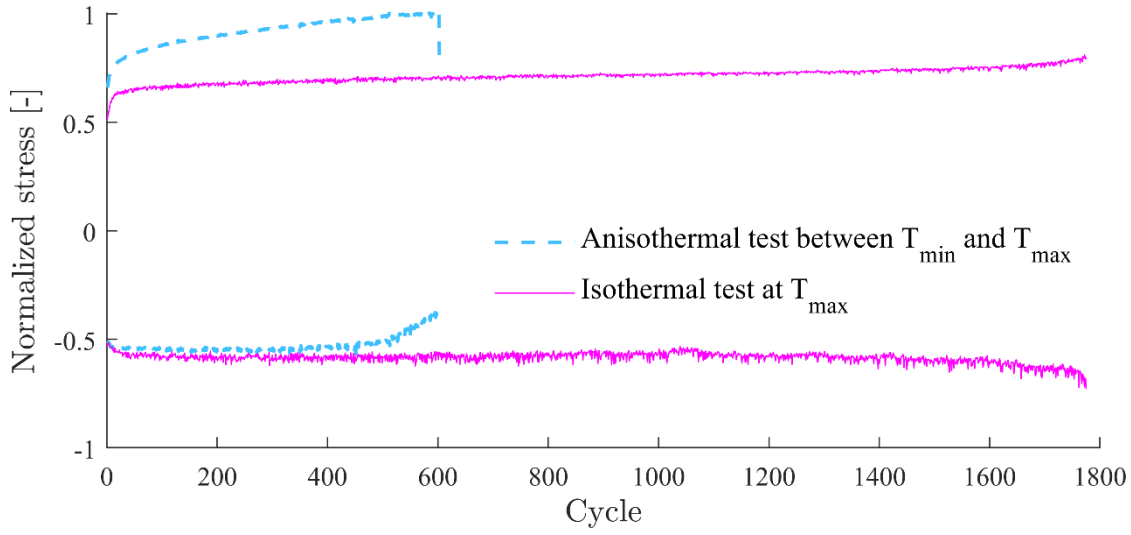

Figure 1.26 – Normalized stress amplitude for an anisothermal creep-fatigue test between T_{min} and T_{max} and a corresponding isothermal creep-fatigue test at T_{max}

3 CONCLUSION

In this chapter, the mechanical behaviour of alloy 230 was studied at different temperatures and under varying temperatures.

In the first part, an analysis of the microstructure allowed to get a better understanding of the rupture mechanisms of alloy 230 under creep-fatigue loadings. This analysis was based on observations made by the Metallurgy and Materials Science lab at the University of Liège and works from the literature. The results show that the addition of compressive hold times in a cyclic loading do not affect the cracking mode, which remains transgranular. However, it leads to much shorter lifetimes which could be explained by the increased importance of thermal ageing and corrosion.

In the second part, the results from the experimental campaign are shown and analysed. The tensile and fatigue behaviour of alloy 230 is rather stable at temperatures ranging from 200°C to 700°C. Alloy 230 exhibits significant cyclic hardening at all temperatures. Viscoplastic effects are visible from 600°C but become really significant at temperatures above 700°C. The resistance to fatigue and creep are reduced with increasing temperatures. For tests with asymmetrical loadings, such as creep-fatigue tests with hold times only in tension or only in compression, a significant evolution of the mean stress is observed. At high temperature, the Young modulus tends to decrease with increasing number of cycles in creep-fatigue tests, due to thermal ageing or damage.

4 REFERENCES

[1] D. L. Klarstrom, H. M. Tawancy, D. E. Fluck, and M. F. Rothman, “New Gas Turbine Combustor Alloy.,” Am. Soc. Mech. Eng., no. 4, 1984, doi: 10.1115/84-gt-70.

[2] “INCONEL ALLOY N06230,” Alloy Dig., vol. 58, no. 3, pp. 1–8, Mar. 2009, doi: 10.31399/asm.ad.ni0667.

[3] Haynes International, “HAYNES® 230® alloy.” 2017.

[4] Haynes, “Haynes 230 alloy,” High-temperature Tech Brief. 2009.

[5] H. M. Tawancy, D. L. Klarstrom, and M. F. Rothman, “Development of a New Nickel-Base Superalloy,” J. Met., vol. 36, no. 9, pp. 58–62, Sep. 1984, doi: 10.1007/BF03338564.

[6] S. Chatterjee and A. K. Roy, “Mechanism of creep deformation of Alloy 230 based on microstructural analyses,” Mater. Sci. Eng. A, vol. 527, no. 29–30, pp. 7893–7900, 2010, doi: 10.1016/j.msea.2010.08.069.

[7] H. M. Tawancy, “High temperature creep behaviour of an Ni-Cr-W-B alloy,” J. Mater. Sci., vol. 27, no. 23, pp. 6481–6489, 1992, doi: 10.1007/BF00576301.

[8] J. Veverkova, A. Strang, G. R. Marchant, G. M. McColvin, and H. V. Atkinson, “High temperature microstructural degradation of Haynes Alloy 230,” in Proceedings of the 11th International Symposium on Superalloys, 2008, pp. 479–488, doi: 10.7449/2008/superalloys_2008_479_488.

[9] X. Chen, Z. Yang, M. A. Sokolov, D. L. Erdman, K. Mo, and J. F. Stubbins, “Low cycle fatigue

and creep-fatigue behavior of Ni-based alloy 230 at 850°C," Mater. Sci. Eng. A, vol. 563, pp. 152–162, 2013, doi: 10.1016/j.msea.2012.11.063.

[10] A. K. Roy, S. Chatterjee, M. H. Hasan, J. Pal, and L. Ma, "Crack-growth behavior of alloy 230 under creep-fatigue conditions," Mater. Sci. Eng. A, vol. 527, no. 18–19, pp. 4830–4836, 2010, doi: 10.1016/j.msea.2010.04.005.

[11] D. Ewest, P. Almroth, B. Sjödin, D. Leidermark, and K. Simonsson, "Isothermal and thermomechanical fatigue crack propagation in both virgin and thermally aged Haynes 230," Int. J. Fatigue, vol. 120, no. June 2018, pp. 96–106, 2019, doi: 10.1016/j.ijfatigue.2018.11.004.

[12] R. Ahmed, "Constitutive Modeling for Very High Temperature Thermo- Mechanical Fatigue Responses," North Carolina State University, 2013.

Chapter 2: Modelling of the thermo-mechanical behaviour of alloy 230

TABLE OF CONTENTS

1 MODEL

The constitutive model that was chosen to represent the thermo-mechanical behaviour of alloy 230 was originally developed by Ahmed and Hassan [1]. It is based on a previous isothermal version of the model [2] which derives from the Chaboche viscoplastic constitutive model framework [3].

1.1 BASIC CHABOCHE MODEL

Chaboche developed a general model for the description of the mechanical plastic and viscoplastic behaviour of materials. In this model, the state of the material at a given time depends on the current values of observable variables – such as temperature and total strain – and on a set of internal variables [4].

The main features of the Chaboche model are summarized hereafter.

1.1.1 Notation

In a 3-dimensional case, stresses and strains are represented by 3-by-3 second-order tensors (bold $\boldsymbol{\sigma}$ or $\boldsymbol{\varepsilon}$). Owing to their symmetry, these tensors can be rewritten as 6-by-1 vectors using the Voigt notation (underlined $\underline{\sigma}$). Eq. (2.1) shows the stress tensor in its original form, and the equivalent Voigt notation ($\underline{\sigma}$).

$$\boldsymbol{\sigma} = \begin{bmatrix} \sigma_{xx} & \sigma_{xy} & \sigma_{xz} \\ \sigma_{yx} & \sigma_{yy} & \sigma_{yz} \\ \sigma_{zx} & \sigma_{zy} & \sigma_{zz} \end{bmatrix} \Leftrightarrow \underline{\sigma} = \begin{Bmatrix} \sigma_1 \\ \sigma_2 \\ \sigma_3 \\ \sigma_4 \\ \sigma_5 \\ \sigma_6 \end{Bmatrix} = \begin{Bmatrix} \sigma_{xx} \\ \sigma_{yy} \\ \sigma_{zz} \\ \sigma_{xy} \\ \sigma_{xz} \\ \sigma_{yz} \end{Bmatrix} \tag{2.1}$$

Using the notation $\underline{\sigma}$ defined in Eq. (2.1), the double contracted product of two 2nd order tensors $\underline{\sigma}^A$ and $\underline{\sigma}^B$ is given by Eq. (2.2), using Einstein's summation convention:

$$\begin{gathered} \boldsymbol{\sigma}^A : \boldsymbol{\sigma}^B = \sigma_{ij}^A \sigma_{ij}^B \\ \Leftrightarrow \underline{\sigma}^A : \underline{\sigma}^B = \sigma_1^A \sigma_1^B + \sigma_2^A \sigma_2^B + \sigma_3^A \sigma_3^B + 2(\sigma_4^A \sigma_4^B + \sigma_5^A \sigma_5^B + \sigma_6^A \sigma_6^B) \end{gathered} \tag{2.2}$$

Similarly, the 4th order elasticity tensor can be simplified and rewritten as a 6-by-6 array, as shown in Eq. (2.3), where E is the Young modulus and ν is the Poisson's ratio:

$$\underline{\underline{E}} = \frac{E}{1+\nu}\begin{bmatrix} \frac{1-\nu}{1-2\nu} & \frac{\nu}{1-2\nu} & \frac{\nu}{1-2\nu} & 0 & 0 & 0 \\ \frac{\nu}{1-2\nu} & \frac{1-\nu}{1-2\nu} & \frac{\nu}{1-2\nu} & 0 & 0 & 0 \\ \frac{\nu}{1-2\nu} & \frac{\nu}{1-2\nu} & \frac{1-\nu}{1-2\nu} & 0 & 0 & 0 \\ 0 & 0 & 0 & 1/2 & 0 & 0 \\ 0 & 0 & 0 & 0 & 1/2 & 0 \\ 0 & 0 & 0 & 0 & 0 & 1/2 \end{bmatrix} \tag{2.3}$$

The double contracted product (tensor $\boldsymbol{c}$) of a 4th order tensor $\boldsymbol{C}$ and a 2nd order tensor $\boldsymbol{a}$ is defined by Eq. (2.4):

$$\begin{aligned} &\boldsymbol{c} = \boldsymbol{C}:\boldsymbol{a} \\ &c_{ij} = C_{ijkl}a_{kl} \end{aligned} \tag{2.4}$$

This product can be rewritten using Voigt notation, as shown in Eq. (2.5):

$$\begin{aligned} &\underline{c} = \underline{\underline{C}}:\underline{a} \\ &c_i = C_{i1}a_1 + C_{i2}a_2 + C_{i3}a_3 + 2(C_{i4}a_4 + C_{i5}a_5 + C_{i6}a_6) \;\; with\; i = 1{:}6 \end{aligned} \tag{2.5}$$

The Voigt notation is particularly useful for the implementation of the model in a computer code, as it reduces the necessary memory storage and simplifies mathematical operations on tensors.

1.1.2 Elastic domain

The total strain can be decomposed into thermal $\underline{\varepsilon}^{th}$, elastic $\underline{\varepsilon}^{e}$, and plastic (or inelastic) $\underline{\varepsilon}^{p}$ strains, as expressed in Eq. (2.6):

$$\underline{\varepsilon} = \underline{\varepsilon}^{th} + \underline{\varepsilon}^{e} + \underline{\varepsilon}^{p} \tag{2.6}$$

The stress and elastic strain are related through Hooke's law:

$$\underline{\sigma} = \underline{\underline{E}}:\underline{\varepsilon}^{e} \tag{2.7}$$

The yield locus is defined using the von Mises criterion given by Eq. (2.8), where $\underline{X}$ is the back-stress representing kinematic hardening, R is the isotropic hardening parameter, and σ_y is the yield stress. In the principal stress space, the von Mises criterion describes a sphere of radius $R + \sigma_y$ with its centre translated by a vector $\underline{X}$ from the origin, as shown in Figure 2.1. Initially, while no hardening has occurred, the yield surface is centred at the origin and has a radius σ_y. As hardening occurs, the yield surface can grow in size (isotropic hardening) and/or be translated (kinematic hardening).

$$f = J(\underline{\sigma} - \underline{X}) - R - \sigma_y \leq 0 \tag{2.8}$$

The von Mises stress $J(\underline{\sigma})$ is defined by Eq. (2.9), where $\underline{\hat{\sigma}}$ is the deviatoric stress:

$$J(\underline{\sigma}) = \sqrt{\frac{3}{2}\underline{\hat{\sigma}}:\underline{\hat{\sigma}}} \tag{2.9}$$

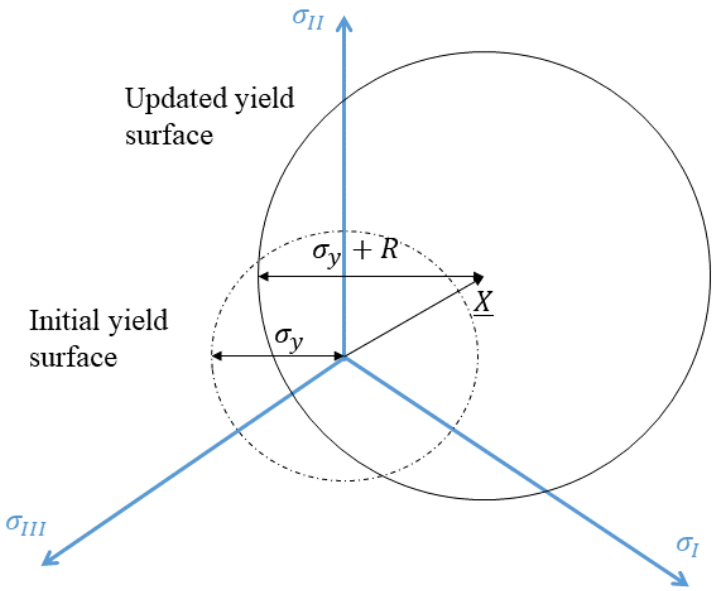

Figure 2.1 - Schematics of the von Mises criterion with isotropic and kinematic hardening

Plastic flow occurs when $f = 0$ and $\frac{\partial f}{\partial \underline{\sigma}}:\underline{\dot{\sigma}} > 0$, i.e., when the yield surface has been reached and loading is applied. The normal plastic flow rule is written as Eq. (2.10), where p is the plastic multiplier (also known as cumulative plastic strain) defined by Eq. (2.11):

$$\underline{\dot{\varepsilon}}^p = \dot{p}\frac{\partial f}{\partial \underline{\sigma}} \tag{2.10}$$

$$\dot{p} = \sqrt{\frac{2}{3}\underline{\dot{\varepsilon}}^p:\underline{\dot{\varepsilon}}^p} \tag{2.11}$$

To solve Eq. (2.10) the different hardening rules must first be defined.

1.1.3 Isotropic hardening

Isotropic hardening corresponds to the evolution of the size of the yield surface with the increase of the cumulated plastic strain p. In the Chaboche model, isotropic hardening is represented by a scalar variable R, also known as drag stress. The evolution of the drag stress R can be defined by a simple differential equation (2.12), which leads to a stable asymptotic behaviour. b and Q are material parameters that depend on temperature. As

can be deduced from the integrated form of the isotropic hardening equation (2.13), Q is the asymptotic value of the drag stress and b is related to the rate of evolution of R.

$$\dot{R} = b(Q - R)\dot{p} \tag{2.12}$$

$$R = Q(1 - e^{-bp}) \tag{2.13}$$

Since the drag stress is a function of the cumulated plastic strain, isotropic hardening can be used to describe cyclic hardening. Figure 2.2 shows the evolution of the stress-strain hysteresis loop for a virtual material subjected to a uniaxial cyclic loading. At cycle 1, where no hardening has occurred, the size of the yield surface corresponds to the yield stress σ_y (120 MPa). After a large number of cycles, isotropic hardening has saturated, and the size of the yield surface is equal to $\sigma_y + Q$ (270 MPa).

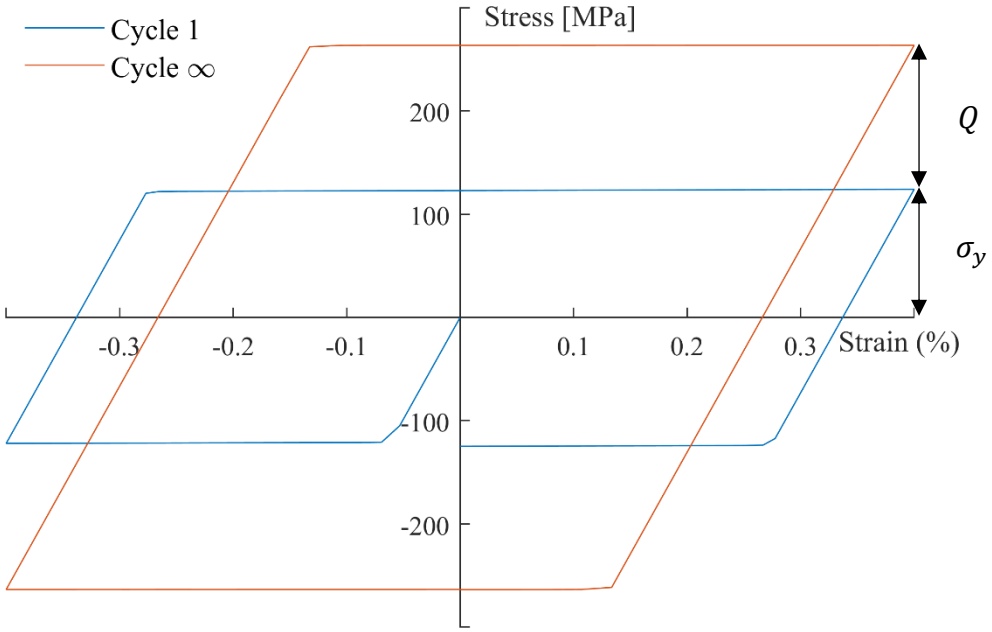

Figure 2.2 - Isotropic hardening for a virtual material under strain-controlled uniaxial cyclic loading

1.1.4 Kinematic hardening

Kinematic hardening can be understood as the translation of the elastic domain in the stress space.

Kinematic hardening can be represented numerically using the Armstrong-Frederick nonlinear flow rule [5], [6]:

$$\dot{\underline{X}} = \frac{2}{3} C \dot{\underline{\varepsilon}}^p - \gamma \underline{X} \dot{p} \tag{2.14}$$

The first term of Eq. (2.14) corresponds to the linear rule proposed by Edelman and Drucker [7] based on the works of Prager [8]. With the linear rule, an increment of the

plastic strain $\delta\underline{\varepsilon}^p$ leads to an increase of the resistance in the direction of the plastic strain increment, i.e., the yield surface is translated following the direction of $\delta\underline{\varepsilon}^p$.

The recall term $-\gamma\underline{X}\dot{p}$ added by Armstrong and Frederick diminishes the effect of the initial conditions after the increment of plastic strain has occurred. The idea is that the material behaviour at a given point depends on the most recent plastic strain increments and not on the whole plastic strain path. The recall term therefore creates an evanescent strain memory effect.

Figure 2.3 shows the stress-strain hysteresis loop for a virtual material subjected to a strain-controlled uniaxial loading with and without kinematic hardening, modelled using the Armstrong-Frederick flow rule. For the material with no hardening, the stress evolves linearly with the strain until it reaches the yield limit σ_y. For the case with kinematic hardening, the stress increases further once the yield limit is reached. However, upon reversal of the loading, the size of the yield surface (part where the stress is a linear function of the strain) remains unchanged and equal to $2\sigma_y$.

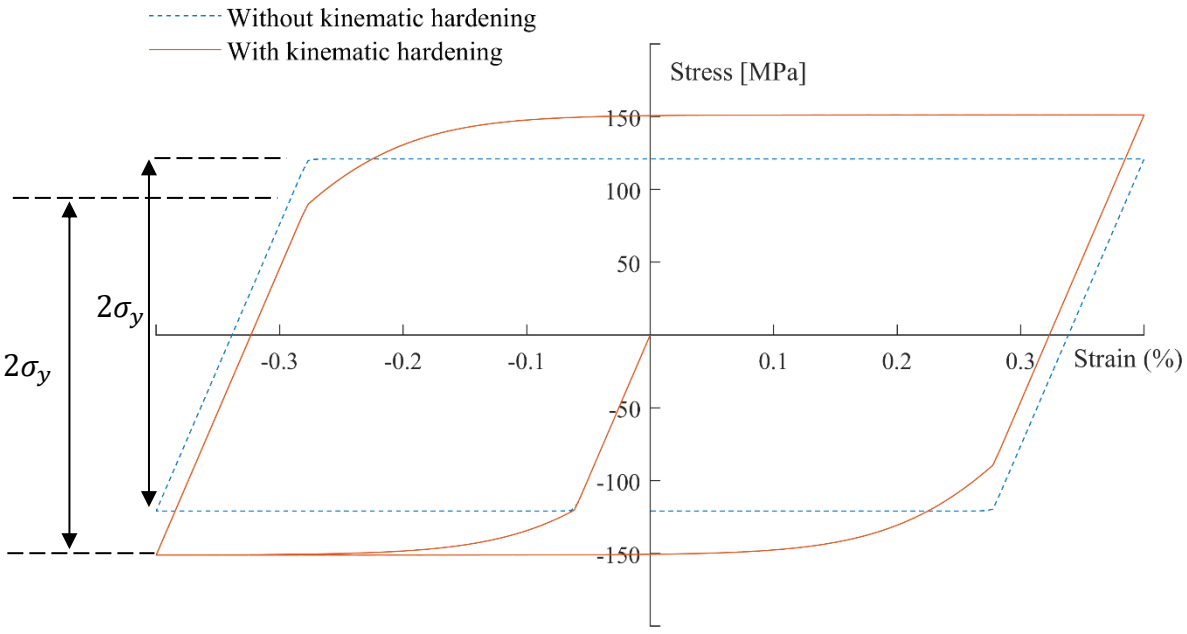

Figure 2.3 - Visualisation of kinematic hardening for a virtual material without any isotropic hardening subjected to uniaxial strain-controlled loading

The Armstrong-Frederick flow rule also allows to represent the Bauschinger effect, as can be seen in Figure 2.3 for the hysteresis loop with kinematic hardening: following the initial compressive load, the tensile yield limit is lower than its initial value σ_y.

One drawback of the Armstrong-Frederick formulation is the limited validity of the model: if the kinematic hardening is identified for small values of the plastic strain, it will quickly reach a saturated value and produce no hardening for higher values of the plastic

strain. Similarly, if the parameters are adapted to higher plastic strains, the behaviour of the material will not be reproduced properly in the range of small plastic strains. To remedy that problem, Chaboche [9] proposed to simply add multiple back-stresses:

$$\underline{X} = \sum_i \underline{X_i} \tag{2.15}$$

$$\underline{\dot{X}_i} = \frac{2}{3} C_i \underline{\dot{\varepsilon}^p} - \gamma_i \underline{X_i} \dot{p} \tag{2.16}$$

Having several back-stresses gives the model more flexibility and increases its validity domain.

1.1.5 Viscoplasticity

At high temperatures, metallic materials exhibit a viscoplastic behaviour, meaning time and strain rate influence the inelastic behaviour. The elastic domain can still be defined using Eq. (2.8) and the hardening equations presented above are still valid for the viscoplastic model, however, the stress state can be such that $f > 0$. The viscous overstress σ_v is defined by Eq. (2.17):

$$\sigma_v = J(\underline{\sigma} - \underline{X}) - R - \sigma_y > 0 \tag{2.17}$$

A viscoplastic potential was defined by Malinin and Khajinsky [10], with two material parameters K and n:

$$\Omega = \frac{K}{n+1} \left\langle \frac{J(\underline{\sigma} - \underline{X}) - R - \sigma_y}{K} \right\rangle^{n+1} \tag{2.18}$$

Where $\langle x \rangle$ denotes the Macaulay brackets defined by Eq. (2.19):

$$\langle x \rangle = \begin{cases} x \text{ if } x \geq 0 \\ 0 \text{ if } x < 0 \end{cases} \tag{2.19}$$

The normal flow rule defined by Eq. (2.10) for rate-independent plasticity becomes:

$$\underline{\dot{\varepsilon}^p} = \dot{p} \frac{\partial \Omega}{\partial \underline{\sigma}} = \frac{3}{2} \dot{p} \frac{\underline{\hat{\sigma}} - \underline{X}}{J(\underline{\sigma} - \underline{X})} \tag{2.20}$$

$$\dot{p} = \left\langle \frac{J(\underline{\sigma} - \underline{X}) - R - \sigma_y}{K} \right\rangle^n \tag{2.21}$$

This finally gives Eq. (2.22), which is similar to the Norton-Hoff equation:

$$\sigma_v = K \dot{p}^{\frac{1}{n}} \tag{2.22}$$

Viscous effects can also be modelled by introducing a recovery term in the kinematic hardening flow rule. Indeed, at high temperatures metals are subjected to thermal recovery, during which grains reduce their stored energy by removing or rearranging defects such as dislocations. This results in a decrease of hardening. A mathematical model of this phenomenon was initially proposed by Orowan [11] and later generalized by Chaboche and Rousselier [4] as Eq. (2.23), introducing material parameters b_i and r_i:

$$\underline{\dot{X}}_i = \frac{2}{3} C_i \underline{\dot{\varepsilon}}^p - \gamma_i \underline{X}_i \dot{p} - b_i J\left(\underline{X}_i\right)^{r_i - 1} \underline{X}_i \tag{2.23}$$

For high values of the strain rate, the two first terms of Eq. (2.23) are dominant and kinematic hardening evolves as displayed in 1.1.4. However, for low values of the strain rate, hardening is lowered and can be completely recovered if the material is maintained at a zero strain rate for a long enough time.

1.1.6 Thermal variation

The behaviour of a given material changes with the temperature T. To take this into account, the material parameters of the Chaboche model can be considered temperature dependent. To also take into account the rate of temperature variation $\dot{T}$, an additional term is necessary in the hardening equations, as shown in equations (2.24) and (2.25) where $\left[\underline{\dot{X}}_i\right]_{\dot{T}=0}$ and $\left[\dot{R}\right]_{\dot{T}=0}$ denote the expressions of $\underline{\dot{X}}_i$ and $\dot{R}$ without thermal variation (equations (2.23) and (2.12)):

$$\underline{\dot{X}}_i = \left[\underline{\dot{X}}_i\right]_{\dot{T}=0} + \frac{1}{C_i}\frac{dC_i}{dT}\dot{T}\underline{X}_i \tag{2.24}$$

$$\dot{R} = \left[\dot{R}\right]_{\dot{T}=0} + \left(\frac{1}{b}\frac{\partial b}{\partial T} + \frac{1}{Q}\frac{\partial Q}{\partial T}\right) R\dot{T} \tag{2.25}$$

1.2 Advanced features of the Chaboche model

1.2.1 Cyclic hardening and strain memory surface

As mentioned in Section 1.1.3, isotropic hardening can be used to model cyclic hardening. However, cyclic hardening does not necessarily manifest as an increase of the size of the yield surface. This is the case for alloy 230, which displays significant cyclic hardening without any change in the size of the yield surface, as demonstrated by Ahmed et al. [2]. In this case, kinematic hardening can be used to model cyclic hardening by making the hardening modulus γ_i dependent on the plastic strain multiplier p, as proposed by Marquis [12]. The parameter γ_i evolves from its initial value γ_i^{init} to a saturated value γ_i^f at a rate D_{γ_i} as shown in Eq. (2.26). It changes the amplitude of variation of the back-stress $\underline{X}_i$.

$$\dot{\gamma}_i = D_{\gamma_i}\left(\gamma_i^f - \gamma_i\right)\dot{p} \tag{2.26}$$

Experiments show that the amount of cyclic hardening is dependent on the strain amplitude. In order to model this, the asymptotic value of the hardening modulus γ_i^f can be calculated as a function of the strain memory surface, which is used to model the strain-range dependence of the material [13]. The strain memory surface g_M is defined by Eq. (2.27) to (2.29), where H is the Heaviside step function, $\langle x \rangle$ are the Macaulay brackets, and η a material parameter representing the rate of evolution to a steady memory surface. The value of η is set to 0.5 for an instantaneous memorization. The vectors $\underline{n}$ and $\underline{n}^*$ defined by Eq. (2.30) and (2.31) correspond to the normal to the yield surface f and to the memory surface g_M, respectively. The plastic strain memory surface defines a sphere of centre ζ and radius q in the plastic strain space.

$$g_M\left(\underline{\varepsilon}^p - \underline{\zeta}\right) = \frac{2}{3}J\left(\underline{\varepsilon}^p - \underline{\zeta}\right) - q \tag{2.27}$$

$$\dot{q} = \sqrt{\frac{2}{3}}\eta H(g_M)\langle \underline{n} : \underline{n}^* \rangle \dot{p} \tag{2.28}$$

$$\underline{\dot{\zeta}} = (1-\eta)H(g_M)\langle \underline{n} : \underline{n}^* \rangle \underline{n}^* \dot{p} \tag{2.29}$$

With:

$$\underline{n} = \frac{3}{2}\frac{\hat{\underline{\sigma}} - \underline{X}}{J(\underline{\sigma} - \underline{X})} \tag{2.30}$$

$$\underline{n}^* = \frac{3}{2}\frac{\underline{\varepsilon}^p - \underline{\zeta}}{J\left(\underline{\varepsilon}^p - \underline{\zeta}\right)} \tag{2.31}$$

The saturated value of the hardening modulus γ_i^f can be calculated as a function of the plastic strain memory surface radius and 3 material parameters a_{γ_i}, b_{γ_i}, c_{γ_i}:

$$\gamma_i^f = a_{\gamma_i} + b_{\gamma_i}\exp\left(-c_{\gamma_i}q\right) \tag{2.32}$$

1.2.2 Mean stress evolution

Ahmed and Hassan [1] showed that asymmetrical cyclic loading of alloy 230 (such as creep-fatigue with hold times only in tension or only in compression) resulted in a significant evolution of the mean stress: in the case of cyclic loading with compressive dwell times, the hysteresis loops tend to shift towards tensile stresses. In order to model this effect, Yaguchi et al. [14] proposed a modification of the kinematic hardening rule. More specifically, the second term (recall term) of Eq. (2.23) is modified by the addition of a tensor $\underline{Y_i}$, as initially proposed by Chaboche and Nouailhas [15]:

$$\dot{\underline{X}}_i = \frac{2}{3} C_i \dot{\underline{\varepsilon}}^p - \gamma_i \left(\underline{X}_i - \underline{Y}_i\right)\dot{p} - b_i J(\underline{X}_i)^{r_i - 1}\dot{\underline{X}}_i \tag{2.33}$$

Tensor $\underline{Y_i}$ evolves according to Eq. (2.34), where $\alpha_{b,i}$ is the rate of evolution of $\underline{Y_i}$ and $Y_{st,i}$ controls the saturated value of $\underline{Y_i}$:

$$\dot{\underline{Y}}_i = -\alpha_{b,i}\left(\frac{3}{2} Y_{st,i} \frac{\underline{X}_i}{J(\underline{X}_i)} + \underline{Y}_i\right) J(\underline{X}_i)^{r_i} \tag{2.34}$$

1.2.3 Temperature history

In the case of thermo-mechanical loading, the material is exposed alternatively to high temperatures and low temperatures. It is well known that for most metallic materials, exposure to high temperatures leads to changes in the microstructure. These changes are often irreversible and influence the subsequent material behaviour even if lower temperatures are reached.

To take into account the influence of the maximum temperature in the loading history T_{max}, Ahmed and Hassan [1] proposed to make some of the model parameters dependent on T_{max}. This dependence is controlled by the equivalent plastic strain p, which can be seen as a measure of microstructural changes. Moreover, in the case of cyclic loading, p increases with the number of cycles, i.e., with the amount of time the material is exposed to T_{max}.

The parameter D_{γ_i}, which controls the rate of cyclic hardening (see Eq. (2.26) in section 1.2.1) is made dependent on the maximum temperature through Eq. (2.35), where $D_{\gamma_i}^{T_{max}}$ is the saturation value of parameter D_{γ_i} at temperature T_{max} and b_{D_γ} is a rate parameter:

$$\dot{D}_{\gamma_i} = b_{D_\gamma}\left(D_{\gamma_i}^{T_{max}} - D_{\gamma_i}\right)\dot{p} \tag{2.35}$$

The Young modulus E is also made dependent on the maximum temperature, using a weighted average as shown in Eq. (2.36), where t is the time since the beginning of loading, and T_{max} the maximum temperature encountered so far in the loading. $E(T, 0)$ denotes the value of the Young modulus of the virgin material at temperature T.

$$E(T, t) = f_E E(T, 0) + (1 - f_E) E(T_{max}, 0) \tag{2.36}$$

The value of the weighing factor f_E evolves as a function of the cumulative plastic strain towards its saturation value f_E^S at a rate b_E:

$$\dot{f}_E = b_E (f_E^S - f_E)\dot{p} \tag{2.37}$$

1.3 NUMERICAL IMPLEMENTATION

The Chaboche model described above was implemented in the Lagamine finite-element code developed at the University of Liège [16] as a material subroutine. Table 2.1 summarizes the different features of the model and their corresponding equations. The mention optional means that the feature will be ignored if it is not activated by the user through the choice of model parameters.

Table 2.1 - Summary of the features available for the advanced Chaboche model

Features	Equations
Strain partition	$\underline{\varepsilon} = \underline{\varepsilon}^{th} + \underline{\varepsilon}^{e} + \underline{\varepsilon}^{p}$
Hooke's law	$\underline{\sigma} = \underline{\underline{E}} : \underline{\varepsilon}^{e}$
Yield surface (von Mises)	$f = J(\underline{\sigma} - \underline{X}) - R - \sigma_y \leq 0$
Viscoplasticity	$\dot{p} = \left\langle \frac{J(\underline{\sigma} - \underline{X}) - R - \sigma_y}{K} \right\rangle^{n}$ for $f = J(\underline{\sigma} - \underline{X}) - R - \sigma_y > 0$
Isotropic hardening	$\dot{R} = b(Q - R)\dot{p}$
Kinematic hardening Optional: • Static recovery • Thermal variation • Mean stress evolution	$\dot{\underline{X}}_i = \frac{2}{3} C_i \dot{\underline{\varepsilon}}^{p} - \gamma_i (\underline{X}_i - \underline{Y}_i)\dot{p} - b_i J(\underline{X}_i)^{r_i - 1}\dot{\underline{X}}_i + \frac{1}{C_i}\frac{dC_i}{dT}\dot{T}\underline{X}_i$ With: $\dot{\underline{Y}}_i = -\alpha_{b,i}\left(\frac{3}{2} Y_{st,i} \frac{\underline{X}_i}{J(\underline{X}_i)} + \underline{Y}_i\right) J(\underline{X}_i)^{r_i}$
Cyclic hardening (optional)	$\dot{\gamma}_i = D_{\gamma_i}(\gamma_i^{f} - \gamma_i)\dot{p}$ With: $\gamma_i^{f} = a_{\gamma_i} + b_{\gamma_i} \exp(-c_{\gamma_i} q)$
Effect of temperature history (optional)	On cyclic hardening: $\dot{D}_{\gamma_i} = b_{D_\gamma}(D_{\gamma_i}^{T_{max}} - D_{\gamma_i})\dot{p}$ On the Young modulus: $E(T,t) = f_E E(T,0) + (1 - f_E)E(T_{max},0)$ With $\dot{f}_E = b_E(f_E^{S} - f_E)\dot{p}$

1.3.1 Model features

The optional features listed in Table 2.1 were implemented in the numerical model along with the base model. This means these features can be activated or deactivated depending on the material and range of temperature studied.

The number of back-stresses n_{AF} for the description of kinematic hardening is a material parameter. For alloy 230, it was chosen to use $n_{AF} = 3$ to have a high flexibility without excessively increasing the number of material parameters.

Among the total n_{AF} back-stresses, the number of back-stresses that are used to describe cyclic hardening is $n_{AF,cyc}$. It can be equal to 0 if no cyclic hardening occurs or if cyclic hardening is modelled entirely through isotropic hardening. For alloy 230, the value is $n_{AF,cyc} = 2$.

Similarly, for the description of the mean stress evolution, only $n_{AF,Y}$ back-stresses are used. For alloy 230, $n_{AF,Y} = 2$.

To sum things up, the two first back-stresses follow Eq. (2.33) with a varying γ_i parameter as described in Section 1.2.1, while the third back-stress follows Eq. (2.23) with a constant γ_3.

The dependence to the maximum temperature, which only has an influence for anisothermal loadings, can be activated or deactivated using parameter $i_{anisoth}$.

1.3.2 Description of the algorithm

In a finite-element analysis, the goal of the material law is to determine, for each element, the consistent tangent matrix $\underline{\underline{C}}$ and the stress increment $\Delta\underline{\sigma}$ obtained for a given strain increment $\Delta\underline{\varepsilon}$. The elementary consistent tangent matrices are then assembled within the FE code to build the global tangent matrix, which is used for the resolution of the global equilibrium of the structure.

The implementation of the Chaboche model as a material law was done following the work of Ahmed [17]. The details of the discretization of the equations can be found in his thesis and in Appendix 1. A summary of the algorithm implemented in Lagamine is provided in this section.

The constitutive model consists in a set of differential equations detailed in Table 2.1 above. At each time step (i.e., for each strain increment $\Delta\underline{\varepsilon}$ corresponding to a time increment Δt), these equations are linearized using the implicit Euler method. This numerical method is used to solve differential equations such as Eq. (2.38) using values of y and t at the end of the time step, as shown in Eq. (2.39), where subscripts k and $k+1$ stand for the beginning and the end of the time step, respectively: $\Delta t = t_{k+1} - t_k$. Because the value of the unknown y_{k+1} appears on both sides of Eq. (2.39), an iterative process such as the Newton-Raphson method is required to numerically solve it.

$$\frac{dy}{dt} = f(t, y) \tag{2.38}$$

$$y_{k+1} = y_k + \Delta t * f(t_{k+1}, y_{k+1}) \tag{2.39}$$

The radial return mapping algorithm, first introduced by Wilkins [18], is used to solve the viscoplasticity equations. This algorithm consists in the two following steps:

- First, a predictor elastic step is computed. For this step, the increment of plastic strain Δp is considered equal to zero. Applying Hooke's law gives a direct evaluation of the trial stress increment $\Delta\underline{\sigma}^{tr}$.
- Secondly, the von Mises criterion is checked using the trial stress obtained from the first step, that is $f^{tr} = J(\underline{\sigma}_k + \Delta\underline{\sigma}^{tr} - \underline{X}) - R - \sigma_y$:
  - If $f^{tr} \leq 0$, the stress state becomes $\underline{\sigma}_{k+1} = \underline{\sigma}_k + \Delta\underline{\sigma}^{tr}$ and the code can move on to the next time step;
  - If $f^{tr} > 0$, a plastic corrector $\Delta p > 0$ is applied iteratively until $f_{k+1} \leq 0$, or, in the case of viscoplasticity (see section 1.1.5), until $f_{k+1} = K\left(\frac{\Delta p}{\Delta t}\right)^{\frac{1}{n}}$.

The two steps of the radial return mapping algorithm are illustrated in Figure 2.4 for a uniaxial loading.

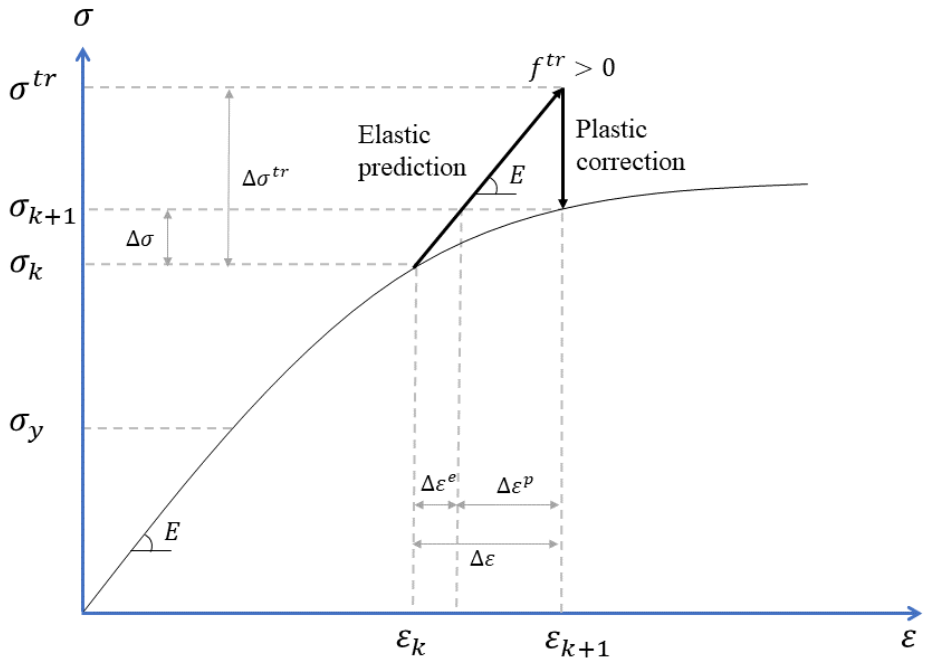

Figure 2.4 - Radial return mapping for a uniaxial loading case

1.3.2.1 Elastic predictor

For the computation of the elastic predictor, the increment of plastic strain is zero. Therefore, the total strain increment can be rewritten as Eq. (2.40):

$$\Delta\underline{\varepsilon} = \Delta\underline{\varepsilon}^{e} + \Delta\underline{\varepsilon}^{th} \tag{2.40}$$

The increment of thermal strain $\Delta\underline{\varepsilon}^{th}$ is computed using Eq. (2.41), where α is the thermal expansion coefficient and $\underline{I}$ the identity matrix in the Voigt notation. The increment of temperature ΔT is computed using a thermal law in Lagamine. Mechanical loading is considered to have no influence on heat transfer, which is a valid hypothesis for the solar receivers where there is no fast deformation.

$$\Delta\underline{\varepsilon}^{th} = \frac{\alpha(T_k) + \alpha(T_{k+1})}{2}\Delta T\underline{I} \tag{2.41}$$

The value of the elastic predictor $\Delta\underline{\sigma}^{tr}$ is determined using the discretized expression of Hooke's law:

$$\Delta\underline{\sigma}^{\mathrm{tr}} = \Delta\left(\underline{\underline{E}}:\underline{\varepsilon}^{e}\right) = \Delta\underline{\underline{E}}:\underline{\varepsilon}^{e}_{k+1} + \underline{\underline{E}}_{k+1}:(\Delta\underline{\varepsilon} - \Delta\underline{\varepsilon}^{th}) \tag{2.42}$$

Although the elasticity tensor $\underline{\underline{E}}$ is not time-dependent, it is temperature dependent. Therefore, in the case of thermal loading with a variation of temperature $\Delta T = T_{k+1} - T_k$, the value of $\underline{\underline{E}}$ is not constant over the time step:

$$\Delta\underline{\underline{E}} = \underline{\underline{E}}(T_{k+1}) - \underline{\underline{E}}(T_k) \tag{2.43}$$

Ahmed and Hassan [1] showed that if the variation of the elasticity tensor is not taken into account, the stress-plastic strain hysteresis loops shift towards higher absolute values of the plastic strain, i.e., there is a wrong numerical accumulation of plastic strain. As a result, the radius and centre of the plastic strain memory surface are also modified. This has an impact on the computation of cyclic hardening parameters and therefore results in inaccurate representation of the material behaviour.

Another problem occurs with the discretization shown in Eq. (2.42). Consider an out-of-phase thermo-mechanical loading such as the one described in Section 2.5.2 of Chapter 1 and represented in Figure 2.5 (a), that is, a creep-fatigue loading with varying temperatures where the maximal strain corresponds to the minimal temperature. The mechanical strain is defined as:

$$\underline{\varepsilon}^{m} = \underline{\varepsilon} - \underline{\varepsilon}^{th} \tag{2.44}$$

By using the end-of-step values, the Young modulus is slightly underestimated during the loading phases (increase of the temperature and increase of the deformation in absolute value) and it is slightly overestimated during unloading (decrease of temperature and decrease of the deformation in absolute value). This causes a shift in the plastic and elastic

strain, as shown in Figure 2.5 (b). To avoid this issue, Eq. (2.42) is rewritten using the values at mid-step instead of the values at the end of the step for the elasticity tensor and the elastic strain:

$$\Delta\underline{\sigma}^{\mathrm{tr}} = \Delta\underline{\underline{E}}:\frac{1}{2}\left(\underline{\varepsilon}_k^e + \underline{\varepsilon}_{k+1}^e\right) + \frac{1}{2}\left(\underline{\underline{E}}_{k+1} + \underline{\underline{E}}_k\right):\left(\Delta\underline{\varepsilon} - \Delta\underline{\varepsilon}^{th}\right) \tag{2.45}$$

Using Eq. (2.45), the model gives the hysteresis loops shown in Figure 2.5 (c). The stress-elastic strain curve is close to a straight line, corresponding to Hooke's law (note: in this case, the effect of the temperature history is not taken into account).

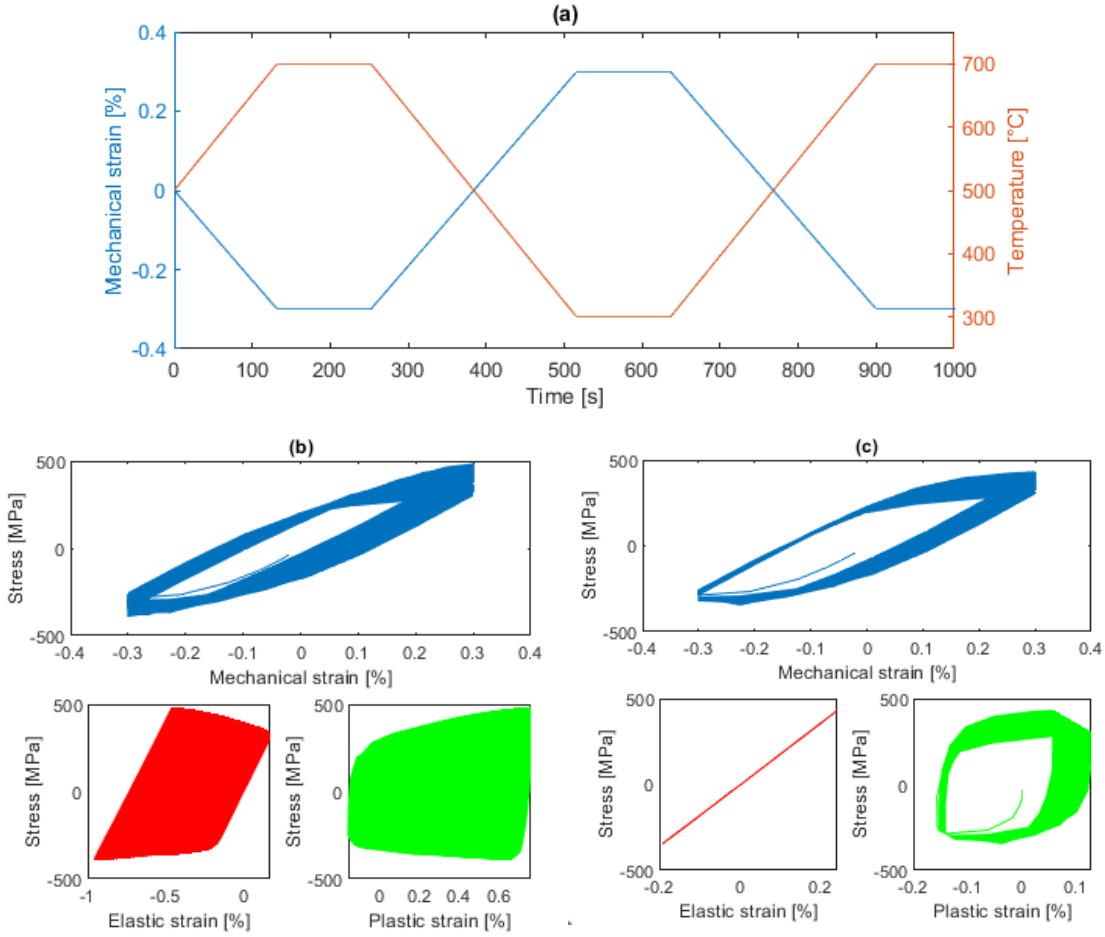

Figure 2.5 – Out-of-phase thermo-mechanical test: (a) Loading; (b) Stress-strain hysteresis loops computed using values of $\underline{\underline{E}}$ and $\underline{\varepsilon}^e$ at the end of the time step and (c) in the middle of the time step

Once the trial stress is computed, the back-stress also needs to be updated. Indeed, in the absence of plastic deformation, the equation for the evolution of the back-stress becomes:

$$\dot{\underline{X}}_i^{tr} = -b_i J\left(\underline{X}_i^{tr}\right)^{r_i-1}\dot{\underline{X}}_i^{tr} + \frac{1}{C_i}\frac{dC_i}{dT}\dot{T}\underline{X}_i^{tr} \tag{2.46}$$

This equation is discretized using the implicit backward Euler scheme and solved using the Newton-Raphson method. Details can be found in the thesis of Ahmed [17].

As the model was developed for alloy 230 which shows negligible amounts of isotropic hardening, the temperature dependence of the drag stress proposed in Eq. (2.25) was not implemented in the model. Therefore, the parameters for isotropic hardening are considered constant with temperature.

With the updated value of the back-stress, the von Mises criterion is checked:

$$f^{tr} = J(\underline{\sigma}^{tr} - \underline{X}^{tr}) - R - \sigma_y \tag{2.47}$$

If $f^{tr} \leq 0$, the von Mises criterion is verified. In this case, the tensors $\underline{Y_i}$ ($i = [1, nAFY]$) can be updated using Eq. (2.48) based on Eq. (2.34) and the computation of the step is terminated. Otherwise, the algorithm proceeds with the plastic corrector.

$$\frac{\underline{Y}_{i,k+1} - \underline{Y}_{i,k}}{\Delta t} = -\alpha_{b,i}\left(\frac{3}{2}Y_{st,i}\frac{\underline{X}_{i,k+1}}{J(\underline{X}_{i,k+1})} + \underline{Y}_{i,k+1}\right)J(\underline{X}_{i,k+1})^{r_i} \tag{2.48}$$

1.3.2.2 Plastic corrector

For the computation of the plastic corrector, the viscoplastic framework described in section 1.1.5 is considered. This framework can also be used to model rate-independent plasticity by choosing appropriate values for the viscosity parameters K and n as shown by Chaboche [9]. Indeed, for $K \approx 0$, equations (2.17) and (2.22) lead to the expression of the von Mises yield surface for the rate-independent case:

$$f = \sigma_v = K\dot{p}^{\frac{1}{n}} \approx 0 \tag{2.49}$$

If the von Mises criterion is not verified in the elastic predictor step, a plastic strain increment $\Delta\underline{\varepsilon}^p$ defined by Eq. (2.51), where $\underline{n}$ is the normal to the yield surface defined by Eq. (2.30), is added to the total strain increment:

$$\Delta\underline{\varepsilon} = \Delta\underline{\varepsilon}^e + \Delta\underline{\varepsilon}^p + \Delta\underline{\varepsilon}^{th} \tag{2.50}$$

$$\Delta\underline{\varepsilon}^p = \sqrt{\frac{3}{2}}\Delta p\underline{n} \tag{2.51}$$

The discretization of Hooke's law leads to:

$$\underline{\sigma}_{k+1} = \underline{\sigma}_k + \Delta\underline{\sigma} = \underline{\sigma}_k + \Delta\underline{\underline{E}}:\left(\underline{\varepsilon}_{k+1} - \underline{\varepsilon}^p_{k+1} - \underline{\varepsilon}^{th}_{k+1}\right) + \underline{\underline{E}}_{k+1}:\left(\Delta\underline{\varepsilon} - \Delta\underline{\varepsilon}^p - \Delta\underline{\varepsilon}^{th}\right) \tag{2.52}$$

With the assumption of plastic strain incompressibility, Eq. (2.52) can be rewritten as Eq. (2.53) by using Eq. (2.42) defining $\Delta\underline{\sigma}^{tr}$. G is the shear modulus defined by Eq. (2.54):

$$\underline{\sigma}_{k+1} = \underline{\sigma}_k + \Delta\underline{\sigma}^{tr} - 2(G_k + \Delta G)\Delta\underline{\varepsilon}^p \tag{2.53}$$

$$G = \frac{1}{2}\frac{E}{1+\nu} \tag{2.54}$$

The equations to solve are equations (2.51), (2.53), (2.48), and equations (2.21), (2.24), (2.13) written in their incremental form as equations (2.55), (2.56), (2.57). By combining these equations together, Ahmed [17] reduced the problem to one equation for the unknown Δp and nAF equations for the unknowns $J\left(\underline{X}_{i,k+1}\right)$ (with $i \in [\![1, nAF]\!]$). The rest of the variables can be computed from these $1 + nAF$ variables. The details of the mathematical developments and the final equations are presented in Appendix 1.

$$\frac{\Delta p}{\Delta t} = \left\langle \frac{J\left(\underline{\sigma}_{k+1} - \underline{X}_{k+1}\right) - R_{k+1} - \sigma_y}{K} \right\rangle^n \tag{2.55}$$

$$\begin{aligned} \frac{\underline{X}_{i,k+1} - \underline{X}_{i,k}}{\Delta t} = \frac{2}{3} C_i \frac{\Delta \underline{\varepsilon}^p}{\Delta t} - \gamma_i \left(\underline{X}_{i,k+1} - \underline{Y}_{i,k+1}\right) \frac{\Delta p}{\Delta t} - b_i J\left(\underline{X}_{i,k+1}\right)^{r_i - 1} \underline{X}_{i,k+1} \\ + \frac{1}{C_i} \frac{dC_i}{dT} \frac{\Delta \mathrm{T}}{\Delta t} \underline{X}_{i,k+1}, \text{for } i \in [\![1, nAF]\!] \end{aligned} \tag{2.56}$$

$$R = Q\left(1 - e^{-b(p_k + \Delta p)}\right) \tag{2.57}$$

The final system of equations is solved in a 2-step scheme: first the equation for Δp is solved using Newton-Raphson method with an initial value $\Delta p = \dot{p}_k * \Delta t$ and considering $\underline{X}_{i,k+1} = \underline{X}_i^{tr}$. If the Newton-Raphson method converges towards a negative value of Δp, which does not make sense physically, the current value of the increment of cumulative plastic strain is set to: $\Delta p^{curr} = \frac{\Delta p^{init}}{10}$, where Δp^{init} is the value at the beginning of the Newton-Raphson iterative process. Then, using Δp^{curr}, the nAF remaining equations are solved (using Newton-Raphson method) to find $J\left(\underline{X}_i\right)^{curr}$.

These two steps are repeated, using updated values $J\left(\underline{X}_i\right)^{curr}$ and Δp^{curr}, until convergence is achieved successively in both steps. This separation was proposed by Ahmed [17] to avoid the full computation of the Jacobian matrix at every Newton-Raphson iteration, and to prevent issues that might arise due to the difference of order of magnitude between Δp and $J\left(\underline{X}_i\right)$.

Finally, a closed-form expression of the consistent tangent modulus $\underline{\underline{C}}$ defined by Eq. (2.58) can be derived from the equations. Details are presented in Appendix 1. In the elastic case, the tangent modulus is equal to the elasticity tensor $\underline{\underline{E}}$.

$$\underline{\underline{C}} = \frac{d\underline{\sigma}}{d\underline{\varepsilon}} \tag{2.58}$$

Having a closed-form expression of the tangent modulus helps with solving the global equilibrium in the finite-element code. It is usually more efficient and saves computation time compared to numerical approximations of the tangent modulus.

1.3.2.3 Flow chart

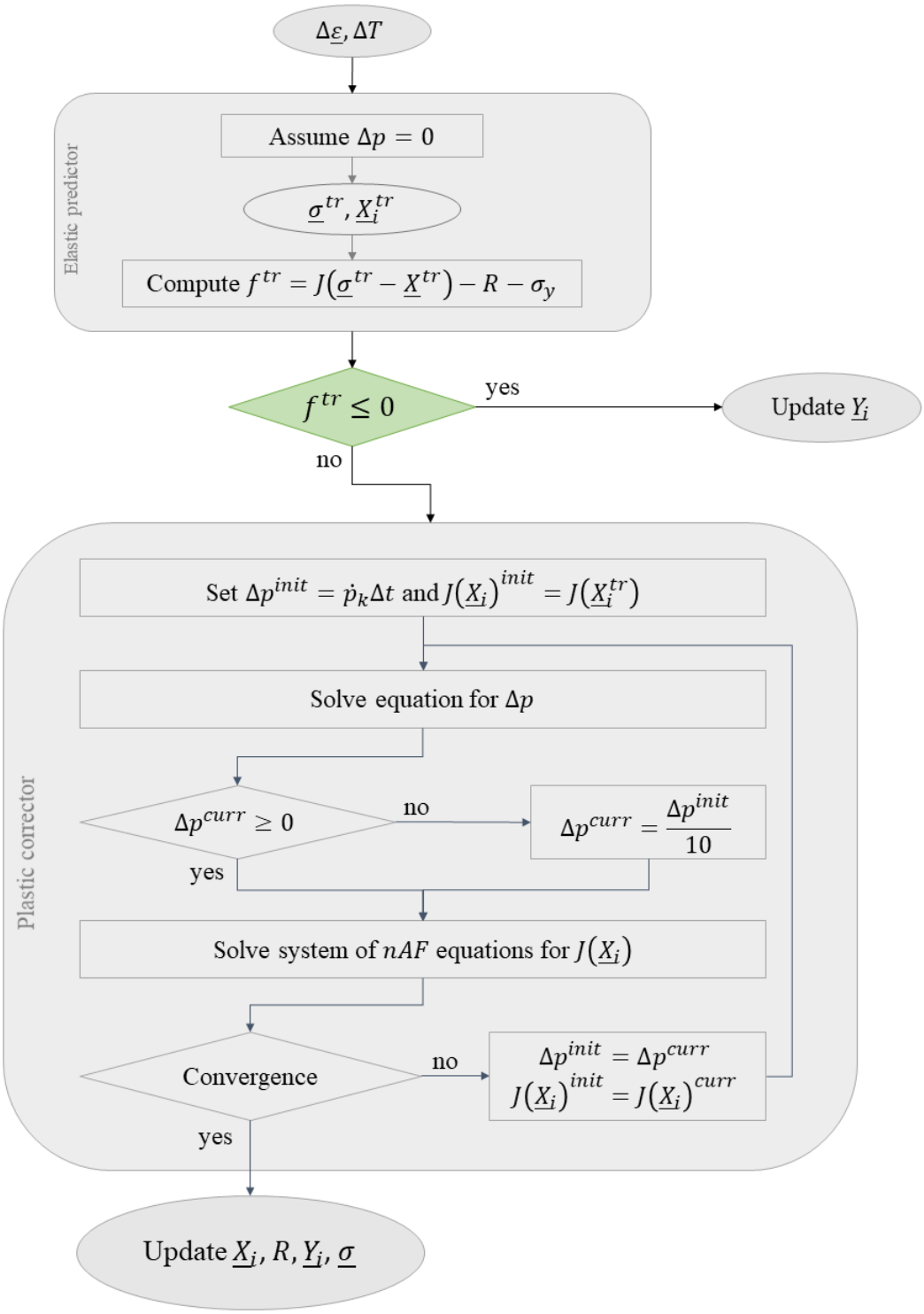

2 PARAMETER IDENTIFICATION

The Chaboche-type model implemented contains multiple features and can model complex material behaviours. However, due to this complexity, a large number of material parameters is required. For a complete model (all features included) the following parameters must be identified:

- 3 elasticity parameters: the Young modulus E, the Poisson's ratio ν, and the yield stress σ_y;
- 2 viscosity parameters K and n;
- 2 isotropic hardening parameters b and Q;
- $2* n_{AF}$ kinematic hardening parameters C_i and γ_i and $2 * n_{AF}$ static recovery parameters b_i and r_i;
- $4* n_{AF,cyc}$ parameters for cyclic hardening $a_{\gamma_i}, b_{\gamma_i}, c_{\gamma_i}$, and D_{γ_i};
- $2* n_{AF,Y}$ parameters for the mean stress evolution $\alpha_{b,i}$ and $Y_{st,i}$;
- 3 parameters for the influence of the maximum temperature b_{D_γ}, b_E, f_E^S. Contrarily to the rest of the parameters, these 3 parameters are not temperature-dependent.

Some of these parameters, such as the Young modulus and the Poisson's ratio, are well-known and can be found in the literature or identified from simple tests (typically tensile tests). However, it can be more difficult to understand the precise effect of other parameters and their influence on the results of the constitutive model. To get a better understanding of the role of each parameter, a sensitivity analysis was performed (section 2.1). Using the results of the sensitivity analysis and information found in the literature, a procedure for the identification of parameters was then established.

The results of the sensitivity analysis were presented at the XIV International Conference on Computational Plasticity (COMPLAS 2017) [19].

2.1 SENSITIVITY ANALYSIS

2.1.1 Method

The sensitivity analysis is based purely on numerical tests. The sensitivity of the model to a particular parameter P is evaluated by performing a specific numerical test with a set of parameters, and then repeating the same test while changing the value of P and observing the changes in the obtained results.

2.1.1.1 Numerical tests

The temperature-dependent parameters listed above were tested on two isothermal uniaxial cyclic tests represented in Figure 2.6 (a). The different characteristics of the two

tests (strain amplitude, strain rate, hold time, frequency) are given in Table 2.2. The two tests differ regarding the strain rate and the hold time applied. This is done so the effect of time-dependent features (static recovery, stress relaxation) can be better observed. The parameters related to the influence of the maximum temperature were tested on anisothermal cyclic test, similar to the isothermal tests but with the addition of temperature variations represented in Figure 2.6 (b).

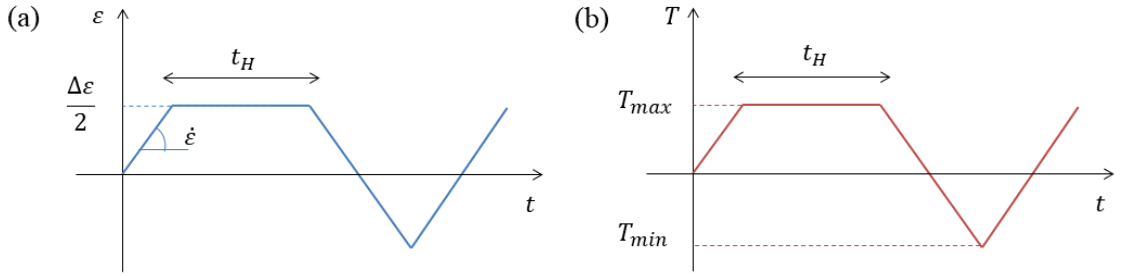

Figure 2.6 – Loading of the numerical tests: (a) imposed strain and (b) imposed temperature for the anisothermal tests

Table 2.2 – Isothermal test characteristics: strain amplitude, strain rate, hold time, and frequency

Test 1 (high rate)	Test 2 (low rate)	Test 3 (anisothermal)
$\Delta\varepsilon = 2\%$ $\dot{\varepsilon} = 0.2\%/s$ $t_H = 20s$ $f = 0.025\ Hz$	$\Delta\varepsilon = 2\%$ $\dot{\varepsilon} = 0.002\%/s$ $t_H = 1000s$ $f = 3.33 * 10^{-4}\ Hz$	$\Delta\varepsilon = 2\%$ $\dot{\varepsilon} = 0.2\%/s$ $t_H = 20s$ $f = 0.025\ Hz$ $T \in [450 - 850]°C$

2.1.1.2 Sensitivity measure

In order to evaluate the sensitivity in a simple and objective way, 4 scalar criteria were defined based on the test results:

- F_1 is the tensile stress obtained during the 1st cycle right before the hold time. This is equivalent to a tensile test (see Figure 2.7).
- F_2 is the amount of relaxation computed on the 1st cycle during the hold time, illustrated in Figure 2.8.
- F_3 is the stress amplitude at the 50th cycle, where the hysteresis loop is stabilized. F_3 is equal to $\frac{\sigma_{max}-\sigma_{min}}{2}$ as illustrated in Figure 2.9.
- $F_4$is the mean stress at the 50th cycle, equal to $\frac{\sigma_{max}+\sigma_{min}}{2}$ as illustrated in Figure 2.9.

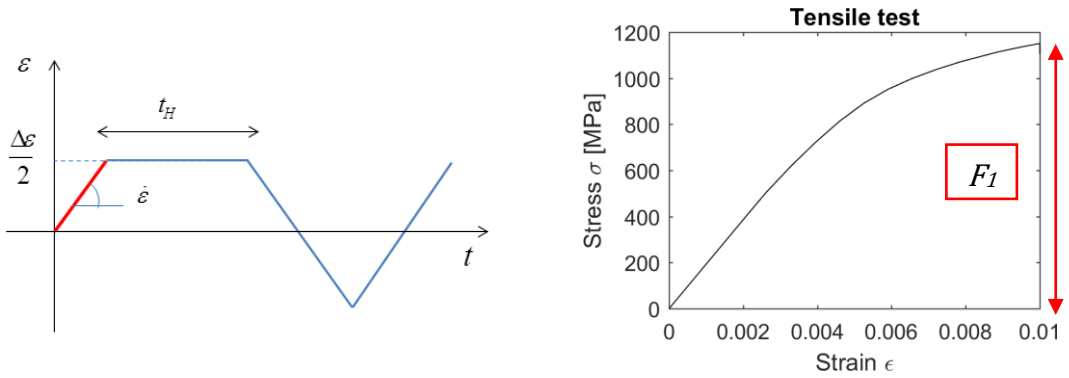

Figure 2.7 – Criterion F_1 (tensile stress) for the measure of parameter sensitivity

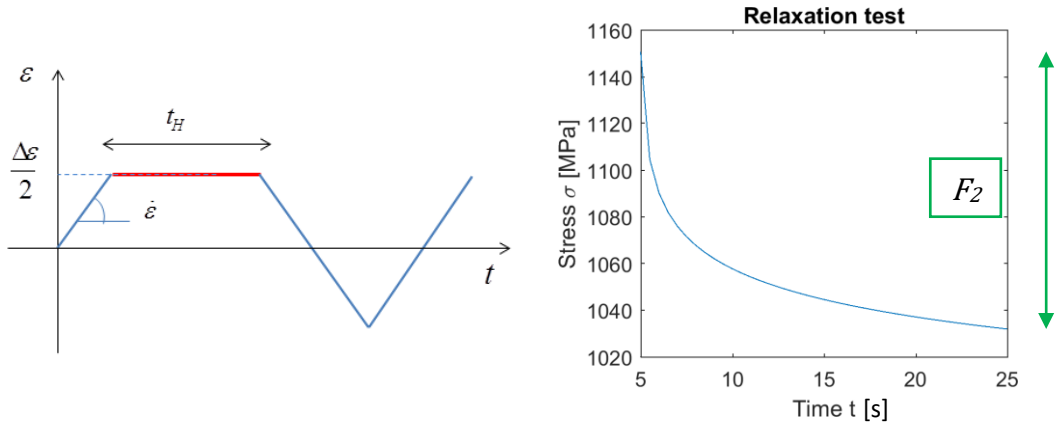

Figure 2.8 – Criterion F_2 (relaxation) for the measure of parameter sensitivity

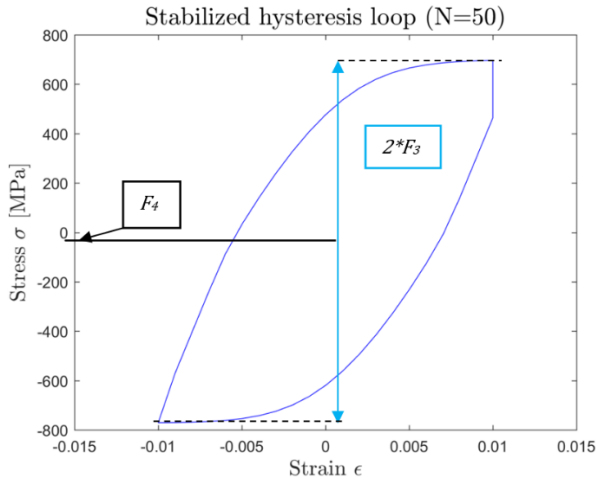

Figure 2.9 – Criteria F_3 (cyclic hardening) and F_4 (mean stress)

2.1.1.3 Reference parameters

The sensitivity analysis requires coherent sets of parameters to obtain consistent results from the numerical tests. Reference parameters corresponding to other nickel alloys were taken from the literature. The lists of studied parameters with the corresponding reference set are detailed in Table 2.3. The first column indicates the parameters for which the sensitivity analysis is performed; the second column indicates the reference article from which parameters are taken and the list of parameters used in their model. The values of the parameters can be found in the given references.

Table 2.3 – Reference parameters used for the sensitivity analysis

Studied parameters	Reference set of parameters	Material
$K, n, b, Q, C_1, C_2, \gamma_1, \gamma_2$	Zhan and Tong [20] $E, \sigma_y, K, n, b, Q, C_1, \gamma_1, C_2, \gamma_2, \alpha_{b,1}, Y_{st,1}, r_1$	RR1000
$b_1, r_1, \alpha_{b,1}, Y_{st,1}, D_{\gamma_1}, a_{\gamma_1}, b_{\gamma_1}, c_{\gamma_1}, \eta$	Yaguchi et al. [14] $E, (\sigma_y = 0), K, n, C_1, \gamma_1 b_1, r_1, \alpha_{b,1}, Y_{st,1}$	IN738LC
b_E, f_E^s	Yaguchi et al. [21] $E, (\sigma_y = 0), K, n, C_1, \gamma_1 b_1, r_1, \alpha_{b,1}, Y_{st,1}$	IN738LC

Some of the model parameters could not be found in the literature. Instead, a reference value was set for those parameters by considering the indications given in the thesis of Ahmed [17]. The values of these parameters are given in Table 2.4 below.

Table 2.4 - Reference values for parameters not found in the literature

D_{γ_1}	a_{γ_1}	b_{γ_1}	c_{γ_1}	η	b_E	f_E^s
10	300	100	10	0.2	1000	0.2

2.1.2 Results

The following sections detail the results of the sensitivity analysis for the studied parameters. The influence of a given parameter P is computed for each criterion F_i defined in section 2.1.1.2 as $\frac{\partial F_i}{\partial P}$:

- If $\frac{\partial F_i}{\partial P} > 0$, the value of F_i increases with increasing P;
- If $\frac{\partial F_i}{\partial P} \approx 0$, P has little to no influence on F_i;
- If $\frac{\partial F_i}{\partial P} < 0$, the value of F_i decreases with increasing P;

$$\dot{p} = \left\langle \frac{J(\sigma - X) - R - \sigma_y}{K} \right\rangle^n$$

2.1.2.1 Viscosity

The influence of the viscosity parameters K and n is shown in Figure 2.10. As can be observed from the values of $\frac{\partial F_i}{\partial K}$ and $\frac{\partial F_i}{\partial n}$, these two parameters influence mostly the stress levels (F_1 on the 1st cycle, F_3 on the stabilized cycle). The parameters also have a small influence on relaxation (F_2): increasing K increases the amount of stress relaxation, however, the effect of the exponent n is less clear. The hysteresis loops shown in Figure 2.10 (d) for different values of n indicate that above a certain value, the behaviour is not affected by changes of n.

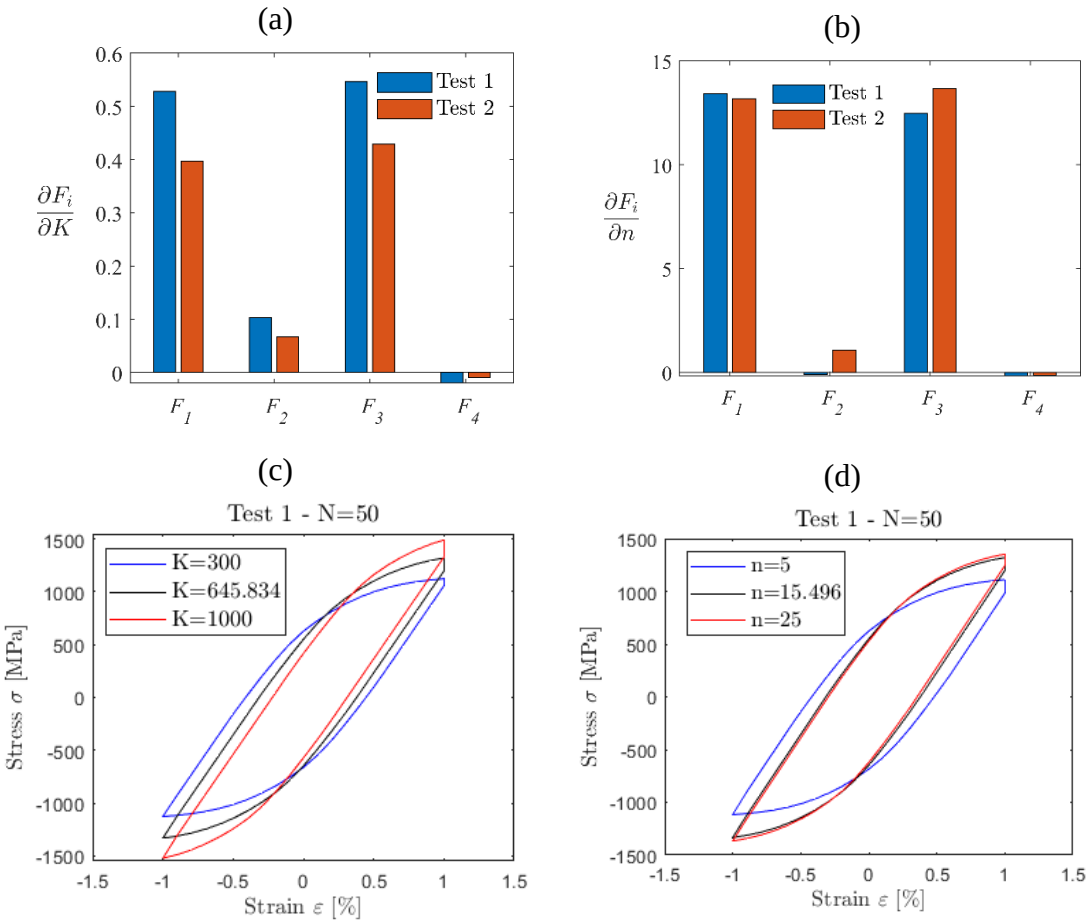

Figure 2.10 – Influence of viscosity parameters (a) effect of K on F_i; (b) effect of n on F_i; (c) effect of K on the stabilized hysteresis loop; (d) effect of n on the stabilized hysteresis loop

2.1.2.2 Isotropic hardening

$$R = Q(1 - e^{-bp})$$

The physical meaning of the isotropic hardening parameters and their effect on the yield surface has already been discussed in section 1.1.3. Q is the asymptotic value of the drag stress R as illustrated in Figure 2.2 of Section 1.1.3. Figure 2.11 illustrates the effect of the rate parameter b on the evolution of the stress amplitude. As expected, for high values of b, the stress amplitude converges faster towards its asymptotic value.

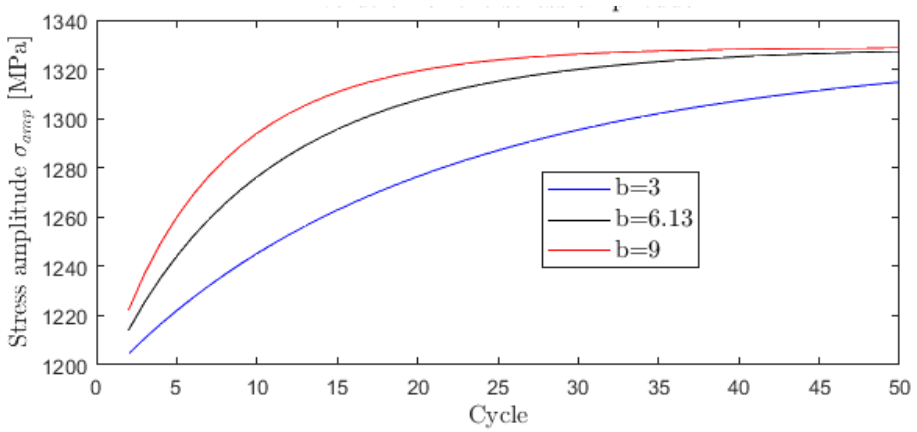

Figure 2.11 – Stress amplitude on test 1 with different values of the isotropic hardening rate b

2.1.2.3 Kinematic hardening

$$\dot{\underline{X}}_i = \frac{2}{3} C_i \dot{\underline{\varepsilon}}^p - \gamma_i \left(\underline{X}_i - \underline{Y}_i\right)\dot{p} - b_i J(\underline{X}_i)^{r_i - 1}\dot{\underline{X}}_i$$

Figure 2.12 shows the effect of a variation in parameters C_i and γ_i. These parameters mostly influence the stress levels (F_1 at cycle 1 and F_3 at cycle 50). It can be observed that they have inverse effects: increasing C_i leads to an increase in stress levels, whereas an increase of γ_i leads to a decrease in the stress levels. In the absence of other effects such as static recovery or mean stress evolution, the Armstrong-Frederick flow rule defined by Eq. (2.16) can be integrated as Eq. (2.59). The value of the back-stress is proportional to $\frac{C_i}{\gamma_i}$, which explains the results observed in Figure 2.12.

$$\underline{X}_i = \frac{2}{3}\frac{C_i}{\gamma_i}\left(1 - e^{-\gamma_i p}\right)\underline{n} \tag{2.59}$$

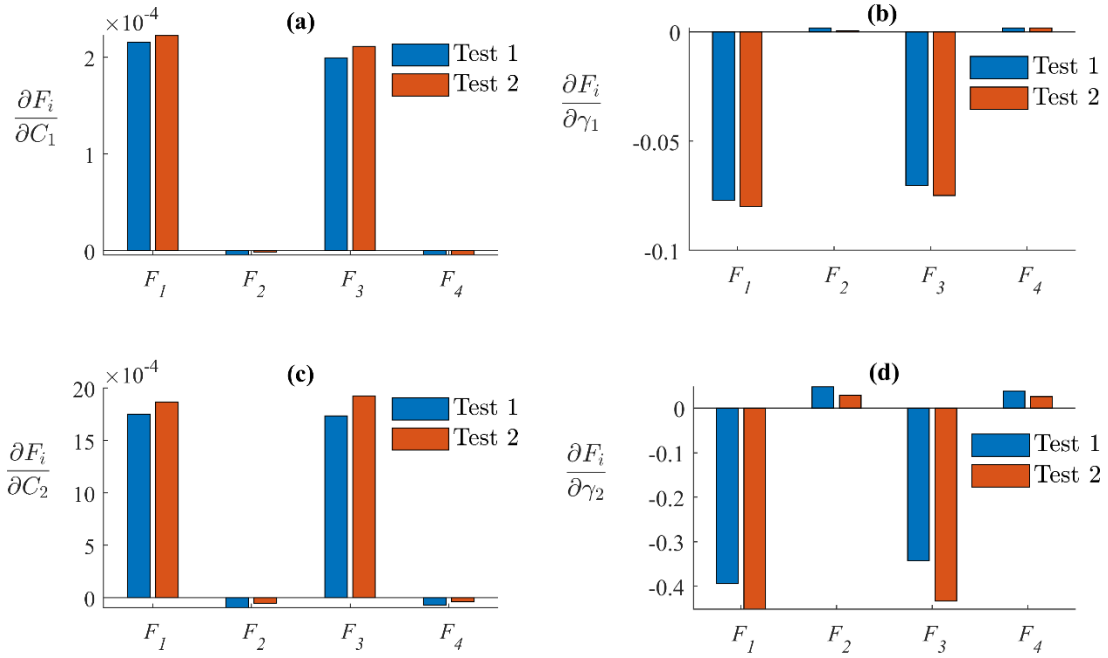

Figure 2.12 – Sensitivity to parameters (a) C_1; (b) γ_1; (c) C_2; and (d) γ_2

The value of $\frac{\partial F_j}{\partial C_i}$ and $\frac{\partial F_j}{\partial \gamma_i}$ is around 10 times smaller for $i = 1$ than for $i = 2$. This can be explained by the respective order of magnitude of the reference values of the parameters. Parameters C_1 and γ_1 are about 10 times bigger than C_2 and γ_2. Because the impact of these parameters is proportional to the ratio $\frac{C_i}{\gamma_i}$, multiplying C_1 by two will have more or less the same impact on F_1 and F_3 as multiplying C_2 by two (same ΔF_j). This can be seen in Figure 2.13 (a): the blue solid line represents a decrease of 50% for C_1 and the blue dashed line a decrease of 33% for C_2; the two curves are very close, especially when considering the extrema. However, when computing $\frac{\partial F_j}{\partial C_i}$ by finite differences, the value of the denominator ΔC_i is 10 times larger for C_1. This explains the difference of order of magnitude observed between Figure 2.12 (a) and (c).

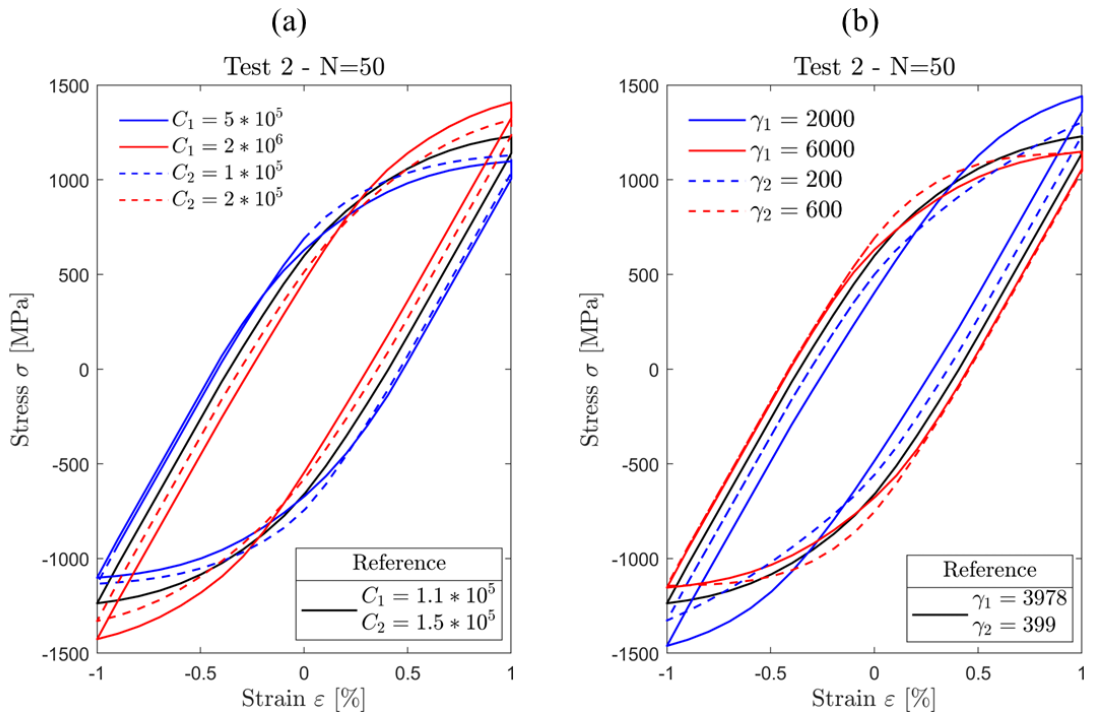

Figure 2.13 – Effect of the variation of parameters C_i and γ_i on the shape of the hysteresis loop (a) parameters C_1 and C_2; (b) parameters γ_1 and γ_2

2.1.2.4 Static recovery

$$\dot{\underline{X}}_i = \frac{2}{3} C_i \dot{\underline{\varepsilon}}^p - \gamma_i \left(\underline{X}_i - \underline{Y}_i\right)\dot{p} - b_i J(\underline{X}_i)^{r_i - 1}\dot{\underline{X}}_i$$

Static recovery is controlled by parameters b_i and r_i in the equation for kinematic hardening. It is a time-dependent effect. Therefore, the influence of these parameters is more visible for test 2 which is slower and has longer hold times. This is clearly visible in Figure 2.14. Since r_i is also used in the calculation of tensor Y_i representing the mean stress evolution, the tests for the sensitivity to r_i as a static recovery parameter were performed by setting parameters $\alpha_{b,1}$ and $Y_{st,1}$ to 0.

Figure 2.14 shows the influence of parameters b_1 and r_1. As expected, the influence is most significant on the criterion F_2, which corresponds to stress relaxation. An increase in either of these parameters leads to an increase of the stress relaxation.

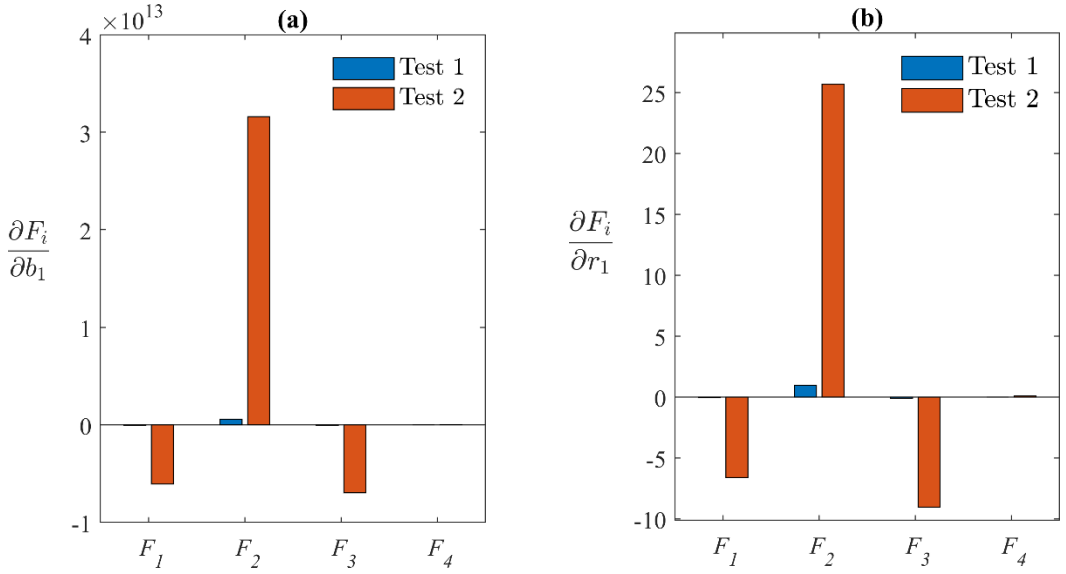

Figure 2.14 – Sensitivity to (a) parameter b_1; (b) parameter r_1

The two parameters also have a small influence on the stress level. Indeed, the static recovery term $b_i J(\underline{X}_i)^{r_i-1}\dot{\underline{X}}_i$ in Eq. (2.23) lowers the absolute value of the back stress, therefore lowering the stress level. This effect is time-dependent and therefore not significant in Test 1 which has high strain rates and short hold times.

2.1.2.5 Mean stress evolution

$$\dot{\underline{Y}}_i = -\alpha_{b,i}\left(\frac{3}{2}Y_{st,i}\frac{\underline{X}_i}{J(\underline{X}_i)} + \underline{Y}_i\right)J(\underline{X}_i)^{r_i}$$

The evolution of the mean stress is controlled by parameters $\alpha_{b,i}, Y_{st,i}$ and r_i. Figure 2.15 shows that as expected, the three parameters mostly influence the value of criterion F_4, the mean stress after 50 cycles.

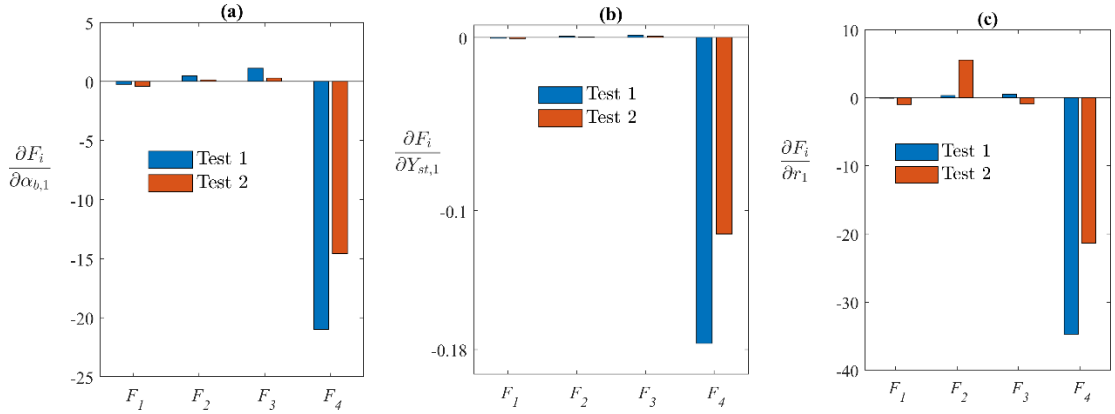

Figure 2.15 – Sensitivity to mean stress evolution parameters (a) $\alpha_{b,1}$; (b) $Y_{st,1}$; (c) r_1

As mentioned in section 1.2.2, $\alpha_{b,i}$ controls the rate of evolution of the mean stress and $Y_{st,i}$ its asymptotic value, as can be seen in Figure 2.16 (a) and (b), respectively. Looking at Eq. (2.34) reminded above, it is also expected that r_i has an influence on the rate of the mean stress evolution towards its asymptotic value. This is confirmed by the results shown in Figure 2.16 (c).

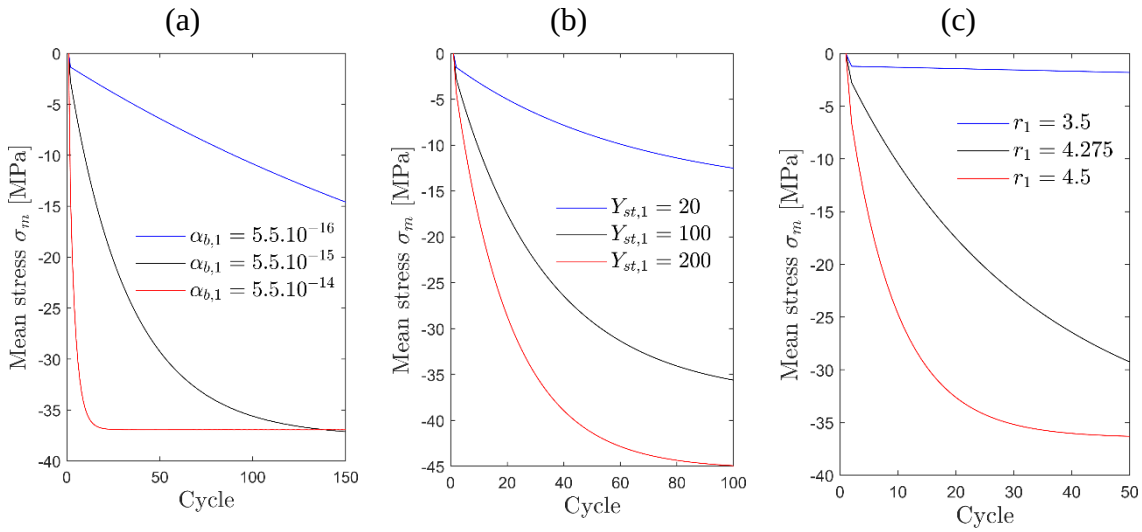

Figure 2.16 – Evolution of the mean stress in Test 1 for different values of (a) $\alpha_{b,1}$, (b) $Y_{st,1}$ and (c) r_1

2.1.2.6 Cyclic hardening

$$\dot{\gamma}_i = D_{\gamma_i}(\gamma_i^f - \gamma_i)\dot{p} \quad \& \quad \gamma_i^f = a_{\gamma_i} + b_{\gamma_i}\exp(-c_{\gamma_i}q)$$

Cyclic hardening is modelled mathematically by making parameter γ_i depend on the plastic strain multiplier p. Four parameters are required: $a_{\gamma_i}, b_{\gamma_i}, c_{\gamma_i}$ for the asymptotic value of γ_i and D_{γ_i} for the rate of evolution. The influence of $a_{\gamma_1}, b_{\gamma_1}, c_{\gamma_1}$ is shown in Figure 2.17. These parameters mainly influence criterion F_3, the stress amplitude after 50 cycles. The 3 parameters also have an influence on the mean stress (F_4). This is because the back stress is used to define the evolution of tensor $\underline{Y_i}$: a change in the amplitude of $\underline{X_1}$ has an impact on the amplitude of $\underline{Y_1}$.

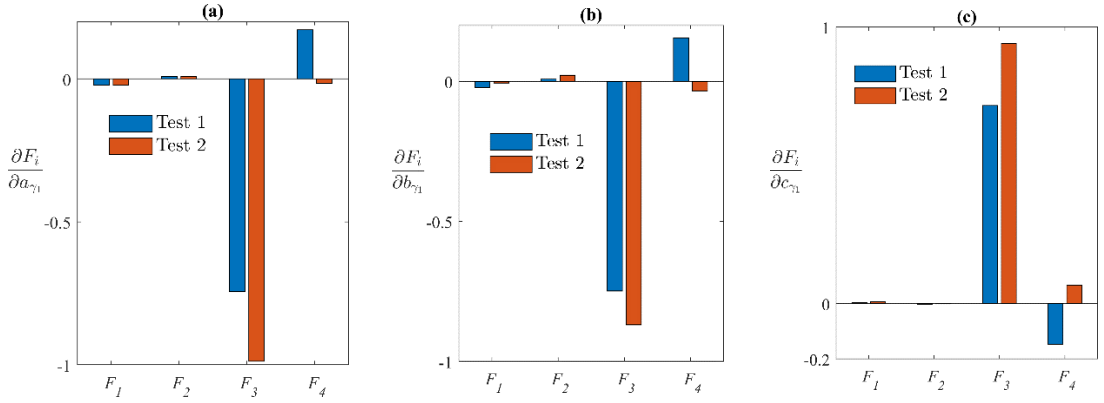

Figure 2.17 – Sensitivity to cyclic hardening parameters (a) a_{γ_1}, (b) b_{γ_1}, and (c) c_{γ_1}

Considering that D_{γ_1} is a rate parameter, its influence is shown more effectively as a function of cycles rather than on a single moment in time. Figure 2.18 (a) shows the sensitivity of the 4 criteria to D_{γ_1}. From these results, it seems that the influence of D_{γ_1} is most significant on F_1, the stress level after the 1st cycle. This is because with the values of D_{γ_1} used for tests, the back-stress reached a stable value before the 50th cycle, as can be seen in Figure 2.18 (b). Therefore, the impact on criterion F_3 appears negligible. Nevertheless, the role of D_{γ_1} in cyclic hardening is clearly shown in Figure 2.18 (b). It can also be noted that, similarly to a_{γ_1}, b_{γ_1} and c_{γ_1}, parameter D_{γ_1} has an influence on the mean stress and on the amount of stress relaxation due to its direct influence on the value of the back-stress.

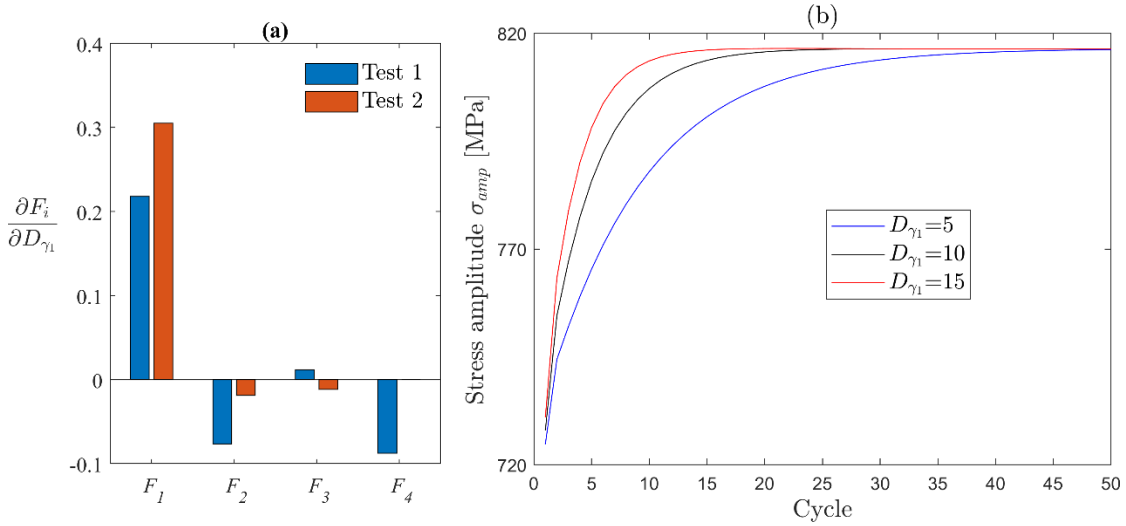

Figure 2.18 – Influence of parameter D_{γ_1} (a) on the 4 criteria and (b) on the evolution of stress amplitude

2.1.2.7 Influence of the maximum temperature

$$E(T,t) = f_E E(T,0) + (1 - f_E)E(T_{max},0)$$
$$\dot{f}_E = b_E(f_E^S - f_E)\dot{p}$$

a. Young modulus

The influence of the maximum temperature on the Young modulus is modelled using 2 parameters b_E and f_E^S. The effect of these parameters can be seen in Figure 2.19. Parameter b_E controls the rate of f_E towards a saturated value f_E^S. As can be seen in Figure 2.19 (a), for a high value of b_E (1000 or 10000), the Young modulus changes during the 1st cycle of loading; for a lower value ($b_E = 10$), the change is more progressive. Parameter f_E^S controls the final proportion of $E(T_{max},0)$ in the value of the Young modulus E for any temperature. Figure 2.19 (b) shows the hysteresis loop at cycle 50 for 3 values of f_E^S. A small value means the Young modulus at all temperature will be close to $E(T_{max},0)$ (blue curve); a larger value means the maximum temperature has less influence.

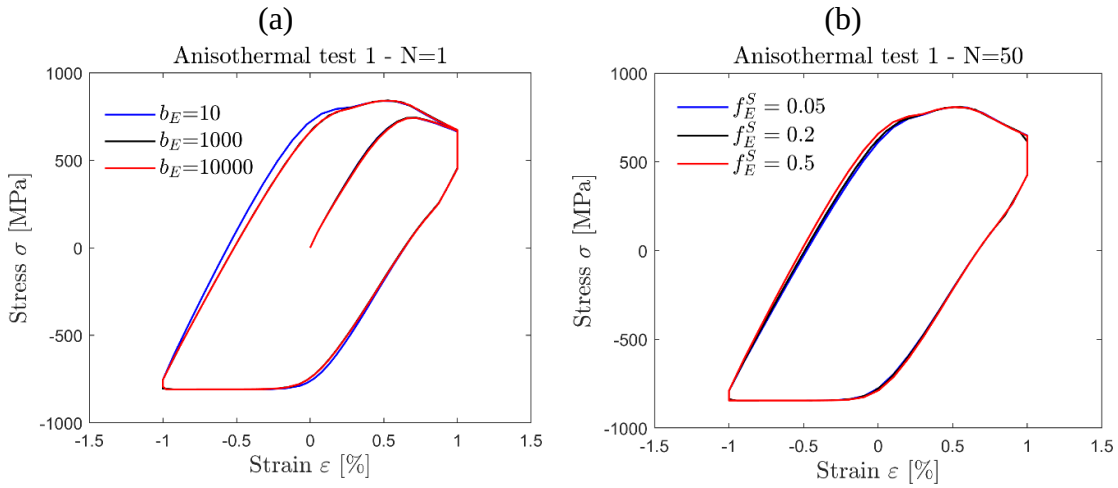

Figure 2.19 – Effect of parameters (a) b_E and (b) f_E^S on the shape of the hysteresis loop of an anisothermal cyclic test

b. Cyclic hardening

$$\dot{D}_{\gamma_i} = b_{D_\gamma}\left(D_{\gamma_i}^{T_{max}} - D_{\gamma_i}\right)\dot{p}$$

Parameter b_{D_γ} was not tested in this sensitivity analysis, as it would have required values of the cyclic hardening parameters at different temperatures. However, from the equation of evolution of D_{γ_i}, it is clear that b_{D_γ} controls the rate of D_{γ_i} towards $D_{\gamma_i}^{T_{max}}$. Ahmed and Hassan [1] showed that adding this feature in their model improves the fitting between the model and the experimental results on the evolution of the mean stress and the stress amplitude for anisothermal tests.

2.2 METHOD FOR THE IDENTIFICATION OF PARAMETERS

Using the results of the sensitivity analysis and results from the literature, a method is proposed for the parameter identification of the advanced Chaboche model implemented. Part of the identification method was presented at the 2018 NUMISHEET conference and published in the proceedings [22].

2.2.1 Direct identification

Some parameters can be identified directly from simple tests, using linear interpolation or other simple methods.

2.2.1.1 Model parameters

The first step is to fix values for $n_{AF}, n_{AF,cyc}$ and $n_{AF,Y}$, the number of equations for kinematic hardening, cyclic hardening, and mean stress evolution, respectively. In the absence of cyclic hardening, 2 back-stresses ($n_{AF} = 2$) are sufficient to model the hardening behaviour of most materials, as shown by Tong et al. [23]. However, when cyclic hardening is represented through the equation of kinematic hardening, the evolution of the stress amplitude and of the mean stress during cyclic tests must be taken into consideration for the choice of n_{AF}. Particularly, it is necessary to have $n_{AF} \geq n_{AF,cyc}$

and $n_{AF} \geq n_{AF,Y}$. For alloy 230, cyclic hardening usually occurs in two phases: a rapid hardening that develops during the first 100 cycles, followed by a slow hardening or softening depending on the strain amplitude and the temperature (see Section 2.4 of Chapter 1). Similar observations can be made for the mean stress. Considering this, a value $n_{AF,cyc} = n_{AF,Y} = 2$ seems appropriate for cyclic hardening and evolution of the mean stress. The total number of back-stresses was set to 3 in order to gain more flexibility and have a third back-stress dedicated to fitting the shape of the hysteresis loop, and more particularly the slope of the stress-strain curves for relatively high values of the plastic strain.

2.2.1.2 Elasticity parameters

Direct identification can be used for elasticity parameters. The Poisson's ration can be found in the literature for most materials; the Poisson's ratio for alloy 230 is given in [24] at several temperatures. The Young modulus corresponds to the slope of the linear part of a tensile or cyclic test, as illustrated in Figure 2.20. Similarly, the yield stress σ_y can be considered as the stress at the end of the linear part in a tensile test, or as twice the size of the linear part in a cyclic test.

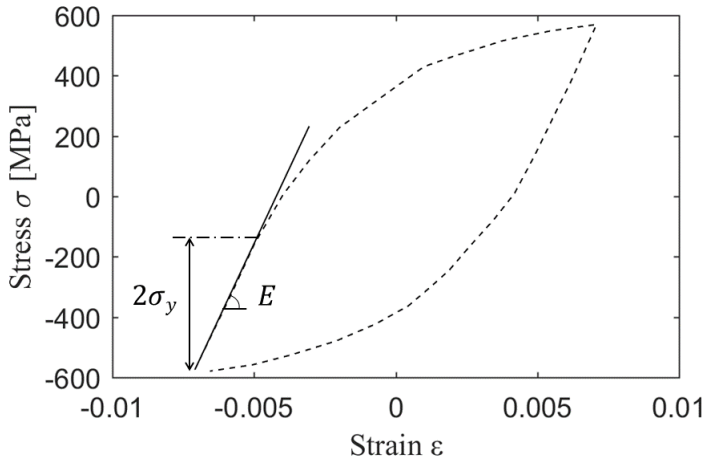

Figure 2.20 – Identification of the Young modulus E and the yield stress σ_y on a cyclic test taken from [17]

2.2.1.3 Isotropic hardening

The asymptotic value of isotropic hardening Q can be determined from a uniaxial cyclic test by measuring the increase of the size of the yield surface (linear part of the hysteresis loop), as shown in Figure 2.2 of section 1.1.3. Similarly, the value of $R(p) = Q(1 - e^{-bp})$ can be measured at different cycles to identify parameter b: the plastic strain multiplier can be expressed as Eq. (2.60), where N is the number of cycles and $\Delta\varepsilon^p$ the amplitude of the plastic strain. Parameter b can then be identified as the slope in the linear regression of $-\ln\left(1 - \frac{R(N)}{Q}\right)$ versus $p(N)$.

$$p(N) = 2N\Delta\varepsilon^p \tag{2.60}$$

An example of this method can be found in [23]. The method was however not used for alloy 230. Indeed, Ahmed et al. [2] showed that the size of the yield surface of alloy 230 does not change during cyclic tests, therefore no isotropic hardening is considered for this material.

2.2.1.4 Kinematic hardening

In the case of uniaxial loading, the back-stress can be expressed as a scalar $X = J(\underline{X})$. For a cyclic loading with no hold time (no time-dependent effects), the value of this total back-stress can be identified similarly to Q, as shown in Figure 2.21. Its value must be identified on the 1st cycle to avoid taking into account cyclic hardening. However, this only gives the value of the total back-stress and not of the parameters C_i and γ_i. Still, this value brings some information for the identification of kinematic hardening parameters:

$$X_\infty = \sum_i \frac{C_i}{\gamma_i} \tag{2.61}$$

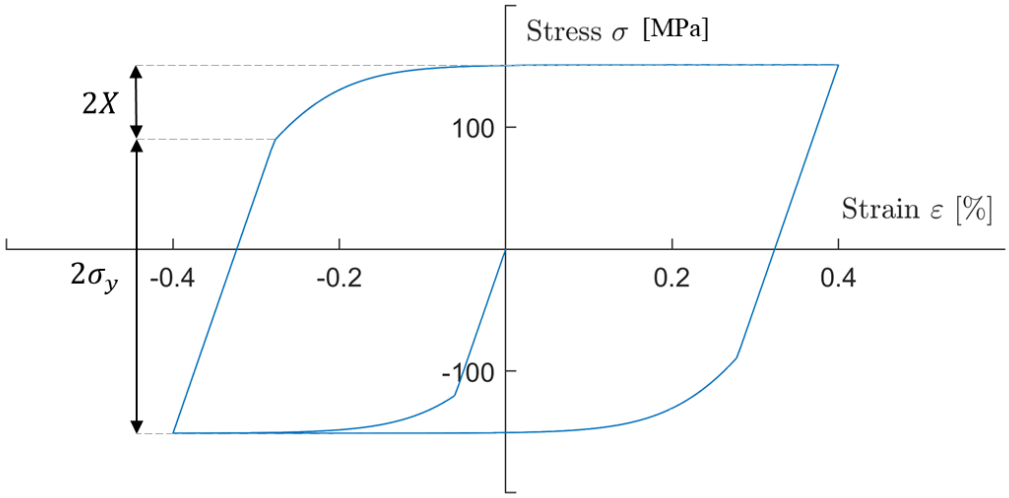

Figure 2.21 – Identification of the total back-stress X for a uniaxial cyclic test

2.2.1.5 Viscosity

The viscosity parameters K and n can be identified directly from relaxation and creep tests performed after saturation of the hardening variables R and X, as proposed by Otin [25]. Indeed, Eq. (2.21) can be rewritten as Eq. (2.62). When the hardening variables have reached their saturated values R_∞ and X_∞, the middle term of Eq. (2.62) can be calculated.

$$\log(\sigma_v) = \log\left(J\left(\underline{\sigma} - \underline{X}\right) - \sigma_y - R\right) = \frac{1}{n}\log(\dot{p}) + \log(K) \tag{2.62}$$

The plastic strain rate can easily be evaluated for an isothermal creep test or an isothermal relaxation test as Eq. (2.63) (the strain and stress are written as scalars as this applies to uniaxial tests):

$$\dot{p} = \dot{\varepsilon} - \dot{\varepsilon}^e = \dot{\varepsilon} - \frac{\dot{\sigma}}{E} \tag{2.63}$$

Parameters K and n can then be identified through linear regression by plotting $\log(\sigma_v)$ versus $\log(\dot{p})$.

The viscosity parameters were not used for alloy 230. Indeed, the model implemented includes two ways of representing time-dependent and rate-dependent effects: viscosity and static recovery. The use of static recovery gives a better representation of relaxation for different loading cases, as there are as many static recovery terms as there are back-stresses. This provides a way to finely tune the parameters. Both viscosity and static recovery can be used simultaneously, however, to simplify the identification process, viscosity parameters were discarded for alloy 230.

2.2.2 Identification through trial and error

Once the parameters that can be identified through direct methods are set, the following 27 parameters must be identified:

- $2* n_{AF}$ kinematic hardening parameters C_i and γ_i and $2 * n_{AF}$ static recovery parameters b_i and r_i (with $n_{AF} = 3$);
- 4* $n_{AF,cyc}$ parameters for cyclic hardening $a_{\gamma_i}, b_{\gamma_i}, c_{\gamma_i}$, and D_{γ_i} (with $n_{AF,cyc} = 2$);
- 2* $n_{AF,Y}$ parameters for the mean stress evolution $\alpha_{b,i}$ and $Y_{st,i}$ (with $n_{AF,Y} = 2$);
- 3 parameters for the influence of the maximum temperature b_{D_γ}, b_E, f_E^S.

Considering the multitude of parameters and their interdependence, the identification must be done through trial and error. This can be done manually or by using an optimizing algorithm with reasonable initial values.

The parameters can be split into different categories that can be identified on specific tests. For instance, the kinematic hardening parameters C_i and γ_i can be identified using the first cycles of a cyclic test with high strain rates. Having high strain rates ensures that static recovery will not take place, and therefore parameters b_i and r_i will have no influence, as shown in the sensitivity analysis (Section 2.1.2.4). The static recovery parameters can then be identified using relaxation tests. For the identification of cyclic hardening, multiple low-cycle fatigue tests can be used. Finally, for the evolution of the mean stress, it is necessary to use tests with asymmetrical loading – otherwise the mean stress remains equal to 0.

For the optimisation process to reach a good solution, it is essential to have initial values that are based on physical considerations and are likely to be close to an optimal solution. For each group of parameters, a first initial estimate is identified using simple forms of the equations of the model and/or by performing a few numerical tests manually.

The group of parameters is then optimised using an optimisation algorithm. For this study, the Fortran program OPTIM [26] developed at the University of Liège was used. OPTIM is based on the Levenberg-Marquardt algorithm.

Sections 2.2.2.1 to 2.2.2.5 give detailed explanations on how to obtain reliable estimates for the parameters. After the initial estimate, a fine tuning is then performed for each group of parameters using OPTIM. Section 2.2.2.6 gives detailed explanations on the functioning of OPTIM.

2.2.2.1 Kinematic hardening

Tong et al. [23] proposed a method to find an estimate of C_i and γ_i for $n_{AF} = 2$ based on the first cycle of a uniaxial test. This method is based on the assumption that the first back-stress controls the evolution of hardening for low values of the plastic strain and the second the evolution for higher values of the plastic strain. With this hypothesis, one can assume that the first back-stress quickly reaches a stationary value and the slope of the hysteresis curve at high levels of plastic deformation is controlled by the second back-stress. For the model with 3 back-stresses, the same method is used. In the case of $n_{AF} = 3$ however, it is the third back-stress $\underline{X}_3$ that controls the behaviour at higher values. The two other back-stresses $\underline{X}_1$ and $\underline{X}_2$ – which are also used for the modeling of cyclic hardening and mean stress evolution – are assumed to be equal for the initial estimate, as it is impossible to distinguish a separate contribution of these two back-stresses on the 1st cycle, i.e., $C_1 = C_2$ and $\gamma_1 = \gamma_2$.

2.2.2.2 Static recovery

As shown in the sensitivity analysis, the effect of static recovery is mostly visible on relaxation tests. The assumption of $\underline{X}_1 = \underline{X}_2$ made for kinematic hardening can also be made for static recovery for the initial estimate. This reduces the number of parameters to estimate from 6 to 4.

2.2.2.3 Cyclic hardening

For cyclic hardening, the saturated value γ_i^f can be identified for cyclic tests with different strain amplitudes. For a given test, the cycle number n corresponding to the peak of stress amplitude curve (see Figure 2.22) and the cycle number r corresponding to the rupture of the sample must first be identified.

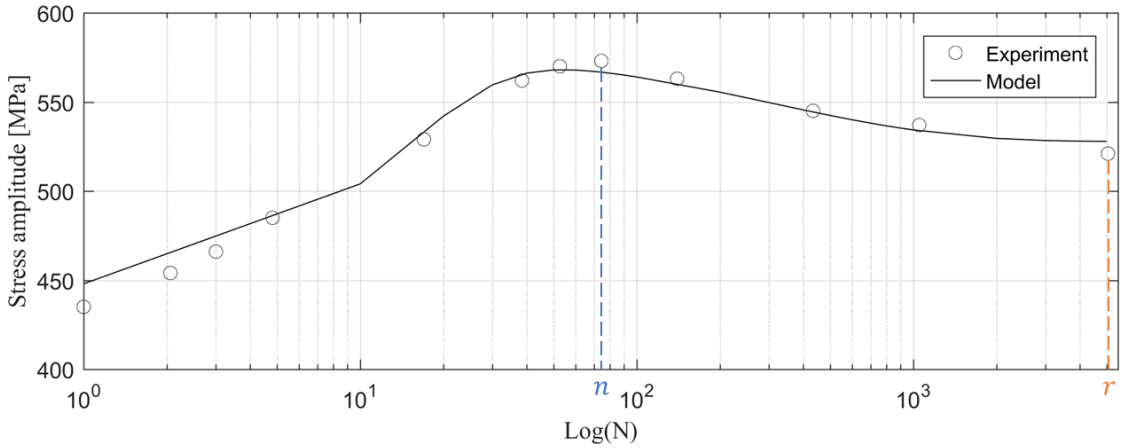

Figure 2.22 – Identification of cycles n (maximum stress) and r (rupture) on the stress amplitude curve of a fatigue test at room temperature (experimental result taken from [17])

Parameters γ_1^f and γ_2^f can be identified using the values of the stress amplitude respectively at cycle n and r to solve Eq. (2.64), where N is the cycle number and $p(N)$ can be approximated using Eq. (2.60). Considering γ_2 represents the long-term cyclic hardening, at cycle n (which is below 100, i.e., short-term), the value of γ_2 is assumed to be equal to $\gamma_2(N=1)$.

$$\sigma_{amp} = \sigma_y + \sum_{i=1}^{n_{AF}} \frac{C_i}{\gamma_i(N)} \left(1 - e^{-\gamma_i(N)p(N)}\right) \tag{2.64}$$

Using values of γ_i^f obtained for different strain amplitudes, the parameters a_{γ_i}, b_{γ_i}, and c_{γ_i} can be identified using Eq. (2.32). For a uniaxial test, the radius of the plastic strain memory surface q can be approximated as the maximum plastic strain in absolute value during the loading history.

The rates of cyclic hardening D_{γ_1} and D_{γ_2} can be identified manually by trial and error from the stress amplitude curve, using Eq. (2.64) and Eq. (2.26).

2.2.2.4 Mean stress evolution

Due to the complexity of the equations for mean stress evolution, the simplest approach for a first estimate of the parameters is to start from values found in the literature. Then, more adequate values can be obtained manually by trial and error using the mean stress evolution of a cyclic test with asymmetrical loading (e.g., hold time only in compression).

2.2.2.5 Maximum temperature influence

The 3 parameters controlling the influence of maximum temperature can finally be identified using anisothermal cyclic tests. The initial values of parameters f_E^S and b_E were taken from the work of Ahmed and Hassan [1], who also worked on alloy 230.

The rate of evolution of cyclic hardening parameters D_{γ_i} towards their value at maximum temperature is controlled by the rate parameter b_{D_γ} in Eq. (2.35). It is difficult to estimate the value of this parameter by looking at experimental results only. The most efficient approach in this case is to use the optimization code directly, with a reasonable initial value. For instance, choosing an initial value of b_{D_γ} of the same order of magnitude as D_{γ_1} or D_{γ_2} gives good results.

2.2.2.6 OPTIM code

OPTIM is an optimisation algorithm based on the Levenberg-Marquardt method [27]. The objective of the algorithm is to minimise an objective function representing the difference between one or several reference curve(s) – usually experimental curves – and one or several numerical curves obtained using the FE Lagamine code. Figure 2.23 illustrates the calculation of the difference between two curves. The values u_i^{REF} and u_i^{FE} of the curves are interpolated at each x_i to compute the difference S using Eq. (2.65):

$$S = \sqrt{\sum_i (u_i^{FE} - u_i^{REF})^2} \tag{2.65}$$

The variable u can be any variable computed by the FE model and available from experimental tests: a stress, a strain, a nodal displacement, etc.

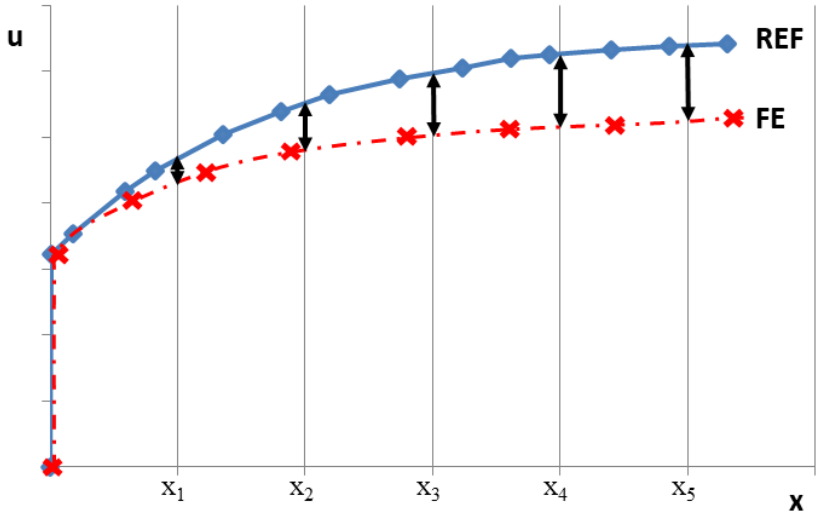

Figure 2.23 – Estimation of the difference between a reference curve (REF) and a finite-element curve (FE)

Optimisation is an iterative process. Figure 2.24 illustrates the different steps that make up one iteration for the optimization of n_P parameters:

1. An initial set of parameters to optimize P_j $(j = 1{:}\,n_P)$ is given as an input to the program.

2. The FE code computes the wanted FE curve with parameters P_j. At the same time, the code also computes two additional curves for each P_j: one with a positive perturbation of the parameter and another with a negative perturbation. This way, it is possible to determine the effect of each parameter on the FE curve at each time step.
3. The objective function S is computed in OPTIM.
4. The derivatives of S with respect to each P_j is computed in OPTIM using the perturbed FE curves computed in step 2. The details of the equations can be found on the Dokuwiki website for OPTIM [26].
5. A new set of parameters P_j is determined by OPTIM from the derivatives of S and the values of S using a Levenberg-Marquardt algorithm. The process is then restarted from step 1 using the new values of P_j until a stop criterion is met (either stabilization of the objective function, or until the maximum number of iterations is reached).

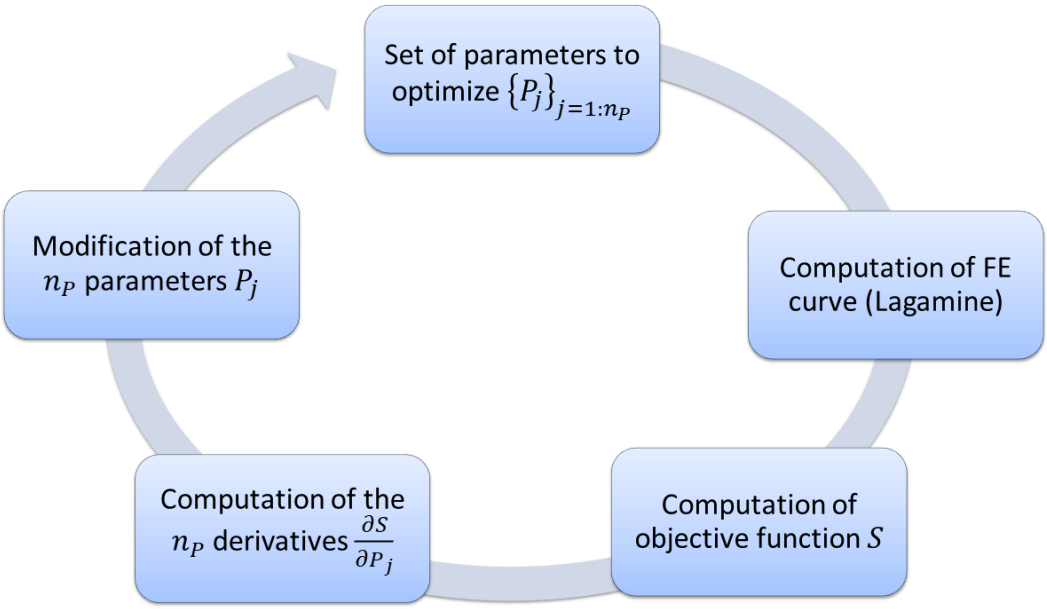

Figure 2.24 – Flowchart of the OPTIM algorithm

3 TEMPERATURE-DEPENDENCE OF THE MATERIAL PARAMETERS

Using the method described in section 2.2, the parameters were identified for alloy 230 at the temperatures for which sufficient experimental data were available. For intermediate temperatures, parameters can then be interpolated between identified values. This can be done using different methods of interpolation, such as linear [28]–[30],

polynomial [21], or exponential [31], [32] functions. However, another way to tackle the issue of temperature-dependence is to define the parameters as mathematical functions of the temperature prior to the identification step, and then directly identify the coefficients of these functions [33]. This section details the different approaches which were implemented in the FE code. The content presented in this section is a summary of the study published in the European Journal of Mechanics/A Solids in 2021 [34].

3.1 MATHEMATICAL FORMULATION OF TEMPERATURE DEPENDENCE

3.1.1 Linear interpolation of parameters

As a first approach, the parameters were identified for several temperatures separately (see Section 2.2). The choice of the interpolation function between two testing temperatures then depends on the shape of the curve defined by the identified parameters. For instance, parameters C_2 and γ_2 identified at five temperatures are shown in Figure 2.25. Piecewise linear interpolation is the simplest and most efficient interpolation method, as it does not require additional parameters and it is adapted to non-monotonous evolutions, as illustrated for C_2 in Figure 2.25 (a).

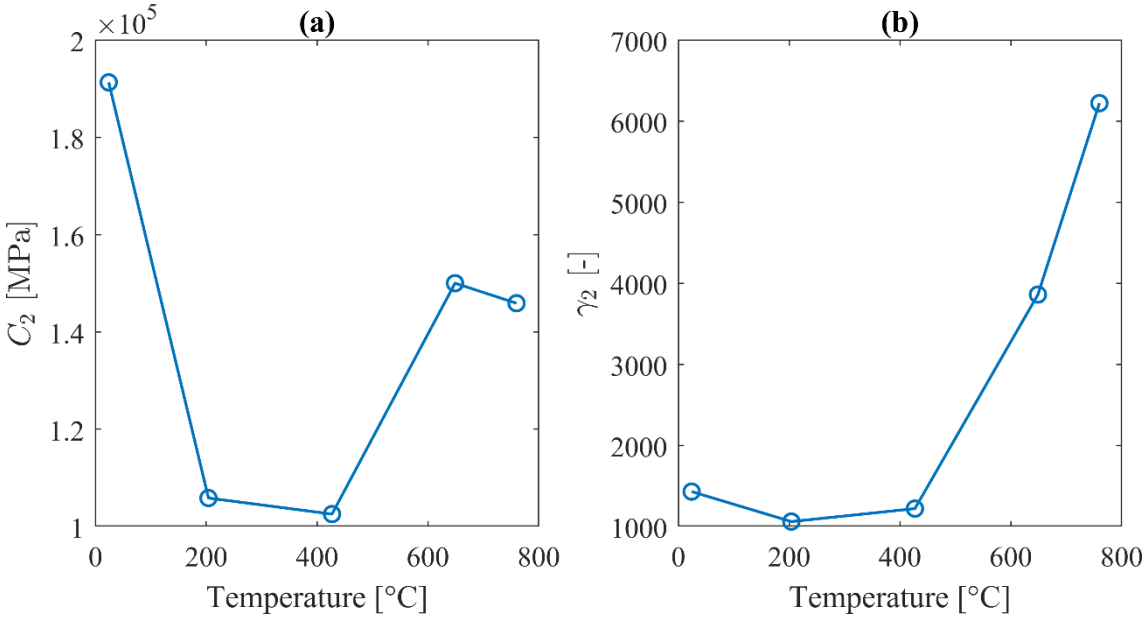

Figure 2.25 – Linear interpolation of parameters (a) C_2 and (b) γ_2 identified at five different temperatures independently

Due to the complexity of the model, the solution to the identification problem at a given temperature is not unique. Therefore, there is no guarantee that sets of parameters identified independently for each test temperature are coherent with one another. This makes the validity of the model uncertain for temperatures in-between the identification temperatures when using linear interpolation.

3.1.2 Exponential function

To ensure the consistency of parameters across temperatures, Hosseini et al. [33] proposed a new formulation of the parameters as exponential functions of the temperature and showed that it gave good results for the representation of mid-life cycle of fatigue and creep-fatigue tests. This formulation described by Eq. (2.66) defines any P parameter of the Chaboche model as a function of the temperature T in Kelvin, A_P, B_P, C_P being the parameters associated to $P(T)$:

$$P = A_P \left(1 - B_P \exp\left(\frac{T}{C_P}\right)\right) \tag{2.66}$$

Let n_P the number of parameters and n_T the number of test temperatures, this means instead of identifying each parameter for each temperature – therefore a total of $n_T * n_P$ parameters – only 3 temperature-dependence parameters must be identified for each parameter P – a total of $3 * n_P$ parameters. The parameters $B_{Ci}, B_{\gamma i}, B_{bi}$ and $C_{Ci}, C_{\gamma i}, C_{bi}$ related to the various back-stresses X_i are the same for every i. This choice is made for practical reasons, as it is impossible to differentiate the effect of temperature on each back-stress separately. For similar reasons, exponent parameters $b, r_i, c_{\gamma i}$ are kept constant with temperature.

3.1.3 Double exponential

The formulation with a single exponential has one major drawback: the evolution of parameters with temperature – and therefore the behaviour it represents – is necessarily monotonous. It is the case for the majority of parameters: the Young modulus and the yield stress decrease with temperature; time-dependent effects such as static recovery increase with temperature; etc. However, experimental results taken from Barrett et al. [35] show that the cyclic hardening behaviour of alloy 230 is not monotonous with temperature. Long-term cyclic hardening, for instance, can be quantified as the difference between the stress amplitude at the end of the test and the stress amplitude after the saturation of the short-term hardening (around the 100th cycle for alloy 230), as shown in Figure 2.26 for LCF tests with a strain amplitude of 0.8% at different temperatures. It can be observed that alloy 230 shows increasing amounts of cyclic hardening between 24°C and 427°C, but decreasing amounts of cyclic hardening between 649°C and 760°C. The high amount of cyclic hardening around 600°C can be explained by the significant precipitation of fine carbides at this temperature, while the decrease in hardening between 649°C and 760°C is due to the less dense carbide distribution at higher temperatures [36], [37].

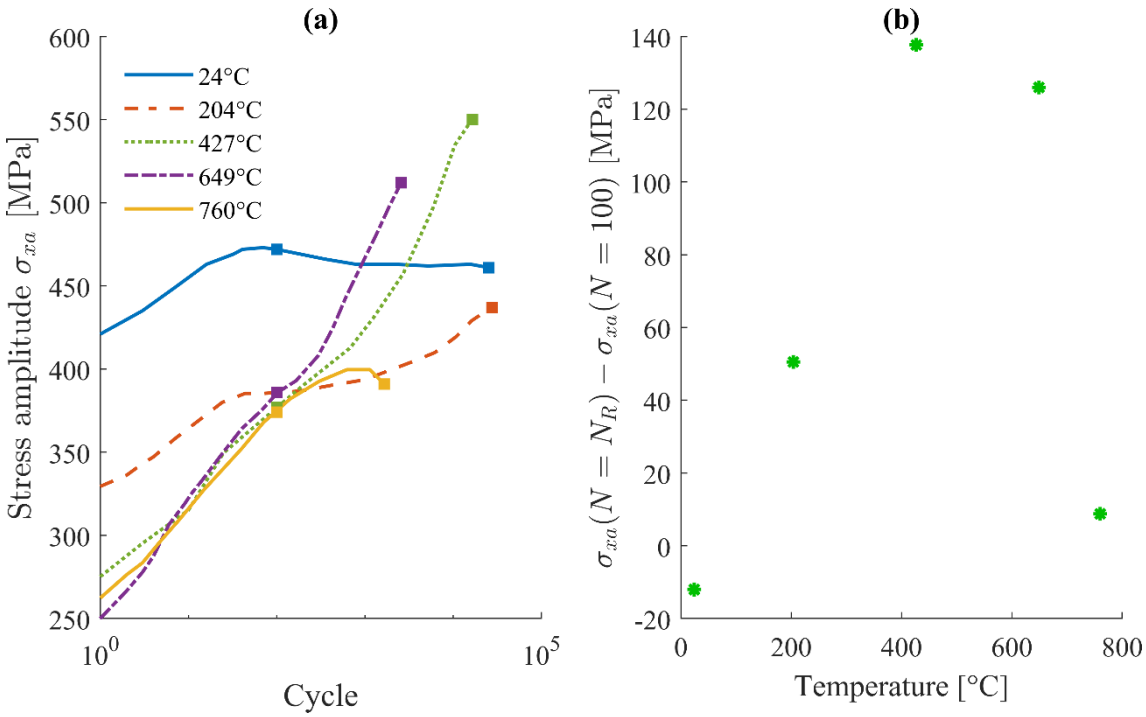

Figure 2.26 – (a) Stress amplitude at different temperatures for a strain-controlled LCF test with 0.8% total strain amplitude from Barrett et al., (2016) with the 100th and the rupture cycles highlighted (b) Evolution of long-term cyclic hardening with temperature

Long-term cyclic hardening is modelled through the variation of parameter γ_2 from its initial value γ_2^{init} towards its saturated value γ_2^f. When static recovery and evolution of mean stress can be neglected – this is the case for LCF tests – kinematic hardening can be integrated yielding to Eq. (2.59) (see 2.1.2.3). At the end of an LCF test, considering that $e^{-\gamma_i p} \ll 1$ and combining Eq. (2.59) with the von Mises criterion in uniaxial form, the stress amplitude can be approximated by Eq. (2.67):

$$\sigma_{amp} \approx \sigma_y + R + \sum_{i=1}^{3} \frac{C_i}{\gamma_i} \tag{2.67}$$

Considering that R is equal to 0 for alloy 230, it can be inferred from Eq. (2.67) that a value of $\gamma_i^f / \gamma_i^{init}$ larger than 1 induces softening, while for smaller values of this ratio, hardening is significant. Considering the experimental data shown in Figure 2.26, the value of $\gamma_2^f / \gamma_2^{init}$ should be above 1 at 24°C, decrease between 24°C and 427°C, and then increase between 649°C and 760°C.

To account for the variation in the cyclic hardening behaviour of alloy 230 with temperature, a new formulation was set for cyclic hardening parameters a_{γ_i}, b_{γ_i} and c_{γ_i} with the sum of two exponential functions and five temperature dependence parameters, as shown in Eq. (2.68):

$$P = A_P\left(1 - B_P \exp\left(\frac{T}{C_P}\right)\right) + A_P\left(1 - D_P \exp\left(\frac{T}{E_P}\right)\right) \tag{2.68}$$

Similarly to what was done in section 3.1.2, the parameters $B_P, C_P, D_P,$ and E_P are considered identical for a_{γ_i} and b_{γ_i} for a given i, that is: $B_{a_{\gamma_i}} = B_{b_{\gamma_i}}$; $C_{a_{\gamma_i}} = C_{b_{\gamma_i}}$; $D_{a_{\gamma_i}} = D_{b_{\gamma_i}}$; $E_{a_{\gamma_i}} = E_{b_{\gamma_i}}$ for $i \in [1,2]$. Using the double exponential formulation in Eq. (2.32) and writing $e^{-c_{\gamma_i} q}$ as K_q, parameter γ_i^f can be expressed as Eq. (2.69):

$$\begin{aligned}\gamma_i^f = &\underbrace{\left(A_{a_{\gamma_i}} + A_{b_{\gamma_i}} K_q\right)\left(1 - B_{a_{\gamma_i}} \exp\left(\frac{T}{C_{a_{\gamma_i}}}\right)\right)}_{P_1} \\ &+ \underbrace{\left(A_{a_{\gamma_i}} + A_{b_{\gamma_i}} K_q\right)\left(1 - D_{a_{\gamma_i}} \exp\left(\frac{T}{E_{a_{\gamma_i}}}\right)\right)}_{P_2}\end{aligned} \tag{2.69}$$

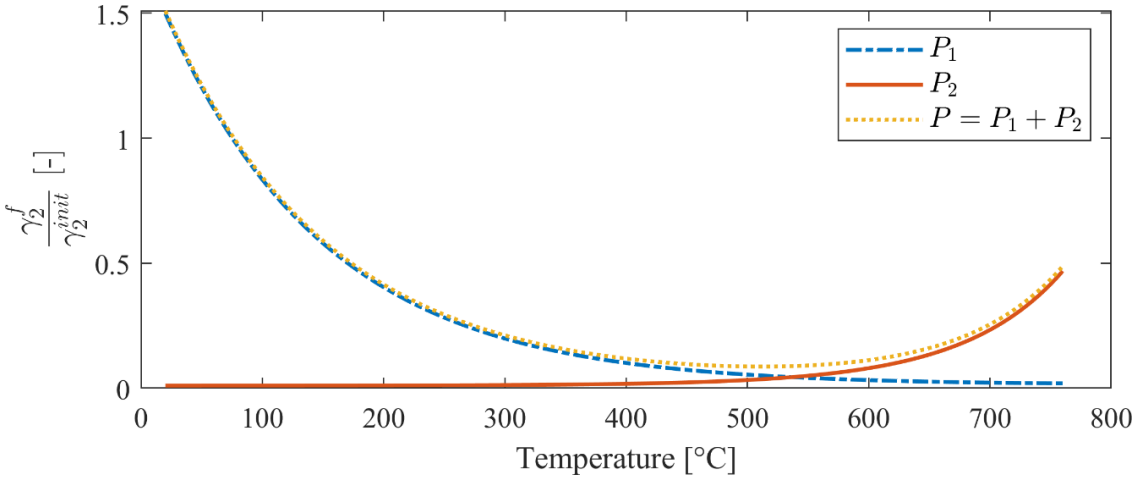

Figure 2.27 – Double-exponential formulation of parameter γ_2^f as a function of temperature, normalized with γ_2^{init} which is almost constant with temperature.

Figure 2.27 shows the evolution of parameter γ_2^f with temperature using the double-exponential formulation. The initial value γ_2^{init} is almost constant with temperature, which makes its influence on the shape of $\gamma_2^f/\gamma_2^{init}$ negligible. The values are consistent with the analysis above: $\gamma_2^f/\gamma_2^{init}$ is above 1 at 24°C, decreases between 24°C and 427°C, and increases between 649°C and 760°C.

3.1.4 Parameter identification

With the exponential and double-exponential formulation, the identification of the parameters can be done using the procedure detailed in section 2.2. All the temperature-dependent parameters follow the single exponential formulation, except for the 3*$n_{AF,cyc}$ cyclic hardening parameters that are used to define γ_i^f. For alloy 230, considering the

choice of parameters $n_{AF} = 3$, $n_{AF,cyc} = 2$, and $n_{AF,Y} = 2$, the total number of parameters to identify with the exponential and double-exponential formulations is:

$$n_{P,exp} = 3 * \left(7 + 4n_{AF} + 2n_{AF,Y} + n_{AF,cyc}\right) + (4 + 3)n_{AF,cyc} = 89 \quad (2.70)$$

To put things in perspective, the number of temperature-dependent parameters with linear interpolation would be expressed as Eq. (2.71), where n_T is the number of temperatures for which parameters are identified:

$$n_{P,lin} = n_T * \left(7 + 4n_{AF} + 2n_{AF,Y} + 4n_{AF,cyc}\right) = 31n_T \quad (2.71)$$

$n_{P,lin}$ is higher than $n_{P,exp}$ if $n_T \geq 3$, therefore it is interesting to use the exponential formulation to limit the total number of parameters.

The direct identification and the initial estimates of parameters is first done separately for several temperatures. The parameters for the exponential and double-exponential formulations can then be computed using the Excel solver. The optimisation process can be performed using the groups of parameters defined in section 2.2.2.

3.2 COMPARISON OF THE DIFFERENT APPROACHES

The temperature-dependent formulation proposed with the (double) exponential function improves the model on two aspects:

- The continuity and consistency of the model across temperatures.
- A better representation of cyclic hardening with the double exponential formulation.

3.2.1 Continuity under anisothermal loading

The use of linear interpolation of parameters can lead to convergence problems when performing anisothermal simulations. Indeed, the discontinuity of the derivative of the parameters with respect to the temperature often induces issues around temperatures presenting strong parameter value peaks. However, this problem can be resolved simply by using a function of class C^1 to describe the parameter evolution with the temperature, which is the case of the exponential formulation.

Figure 2.28 shows the results of a strain-controlled out-of-phase thermo-mechanical test taken from [38] where the imposed mechanical strain decreases with increasing temperatures. The loading is shown in Figure 2.28 (a). The stress-strain curve obtained on the first cycle was computed using either the linear interpolation of parameters or the single-exponential formulation. The double-exponential formulation was not used here because it only applies to cyclic hardening, which has no effect on the first cycle. The parameters for the linear interpolation were identified at 204°C, 427°C, 649°C, 760°C,

and 871°C based on experimental results from [17]. The results of the simulations are shown in Figure 2.28 (b). The curve obtained using linear interpolation is almost identical to the curve obtained with the exponential formulation. However, a strong discontinuity appears in the curve with linear interpolation around 649°C. This phenomenon can be explained by the fact that one or several parameters reach a peak at 649°C, in this case parameter γ_2. The continuity of parameter γ_2 as a function of the temperature can be significantly improved with the exponential formulation.

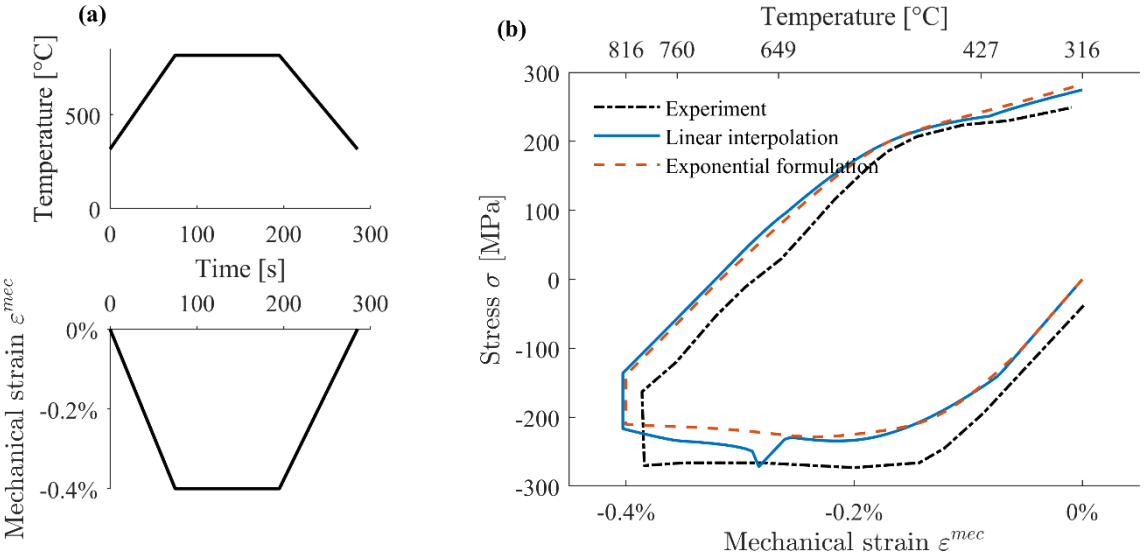

Figure 2.28 – Anisothermal results: (a) thermal and mechanical loading; (b) hysteresis loop for the 1st cycle showing a comparison between experiment and simulations with linear interpolation and exponential formulation.

3.2.2 Cyclic hardening

As shown in section 3.1.3, the cyclic hardening behaviour of alloy 230 is not monotonous with temperature. The stress amplitude of low-cycle-fatigue tests at different temperatures with a strain amplitude $\Delta\varepsilon = 0.8\%$ taken from [35] are compared with the simulations in Figure 2.29. Numerical results were obtained using either the single-exponential or the double-exponential formulation for the cyclic hardening parameters. The rest of the parameters are expressed using the single-exponential formulation.

The single-exponential formulation does not give good results at all temperatures, as can be seen in Figure 2.29. In particular, the long-term cyclic hardening is underestimated at temperatures of 24°C, 427°C, and 649°C, while it is over-estimated at 760°C. This can be a major issue when trying to estimate the lifetime of the material under a specific loading: if the stress is not estimated properly, the lifetime may be over or under-estimated as well. The results obtained with the double-exponential formulation are closer to the experimental curves and bring significant improvement compared to the single-exponential formulation.

Although using double-exponential formulation increases the number of parameters to be identified (5 parameters for double-exponential versus 3 parameters for single-exponential), it significantly improves the accuracy of the model. Moreover, the double-exponential is only necessary for a restrained number of parameters (cyclic hardening parameters $a_{\gamma_i}, b_{\gamma_i}, i = 1{:}\,2$), this only adds 4 parameters.

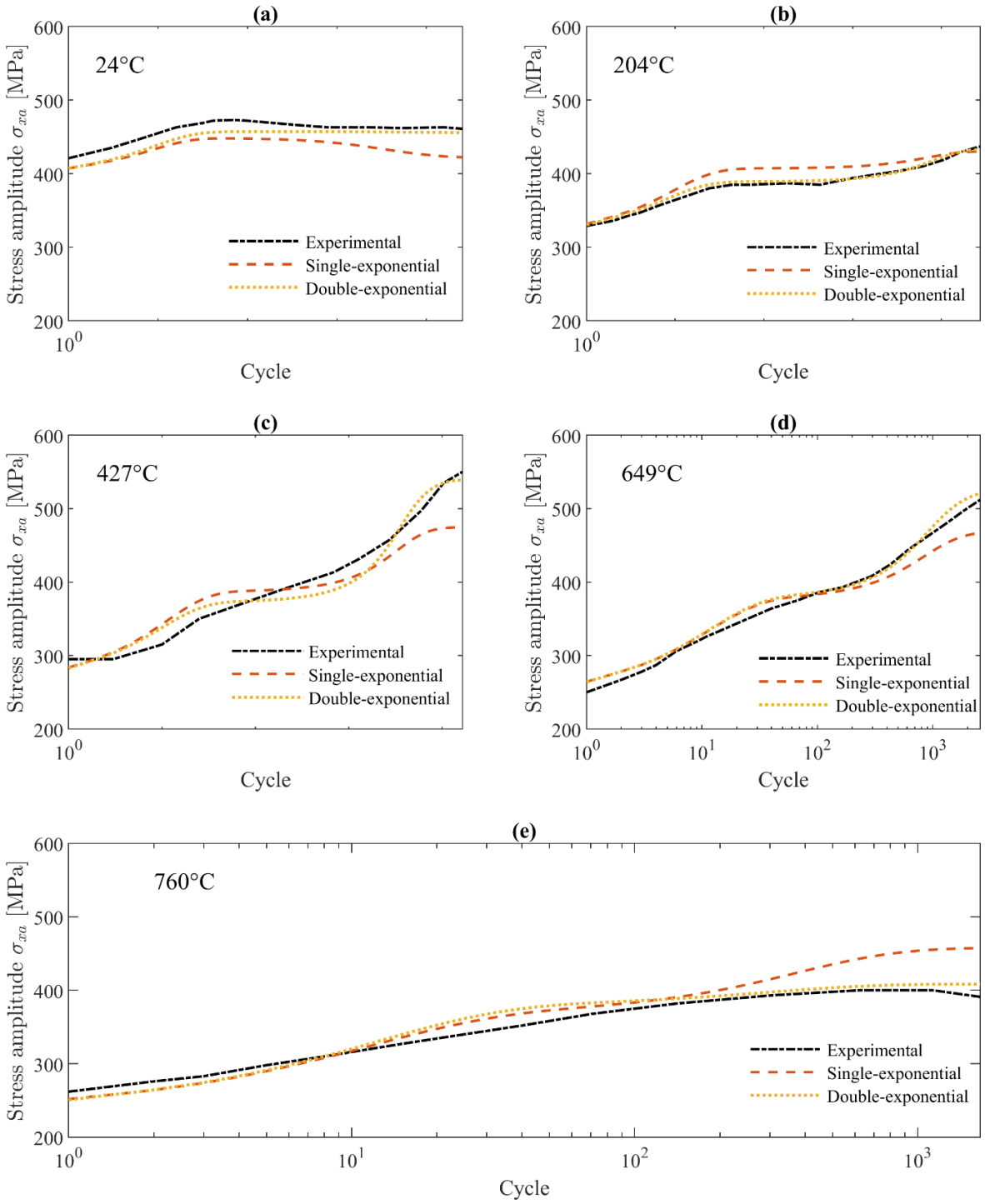

Figure 2.29 – Stress amplitude for strain-controlled LCF tests with $\Delta\varepsilon = 0.8\%$ at:
(a) 24°C; (b) 204°C; (c) 427°C; (d) 649°C; (e) 760°C

4 CONCLUSION

In this chapter, a material model was developed for the simulation of thermo-mechanical behaviour of Haynes 230 at temperatures ranging from room temperature to 850°C. The material model is based on the Chaboche model framework and contains multiple features to describe the macroscopic material behaviour as accurately as possible such as:

- Isotropic hardening
- Kinematic hardening
- The modelling of viscous effect: this can be done using the Norton law or within the kinematic hardening rule by simulating static recovery.
- The modelling of cyclic hardening through the kinematic hardening rule
- The evolution of the mean stress for asymmetrical cyclic loadings
- The influence of the maximum temperature in the loading history.

The material law containing all these features was implemented as part of the Lagamine finite-element code developed at the University of Liège.

Because the model contains numerous features, it also requires a large number of material parameters. A sensitivity analysis was performed to determine the influence of each parameter on the model response and get a better understanding of the impact of each individual feature on the global behaviour. Thanks to this analysis, a step-by-step identification method was designed based on the use of specific mechanical tests. Finally, a specific formulation was developed for the expression of the temperature-dependence of the material parameters. This formulation smoothens the evolution of parameters with temperature and improves the continuity of the model on anisothermal tests.

5 REFERENCES

[1] R. Ahmed and T. Hassan, "Constitutive modeling for thermo-mechanical low-cycle fatigue-creep stress–strain responses of Haynes 230," Int. J. Solids Struct., vol. 126–127, pp. 122–139, 2017, doi: 10.1016/j.ijsolstr.2017.07.031.

[2] R. Ahmed, P. R. Barrett, and T. Hassan, "Unified viscoplasticity modeling for isothermal low-cycle fatigue and fatigue-creep stress-strain responses of Haynes 230," Int. J. Solids Struct., vol. 88–89, pp. 131–145, 2016, doi: 10.1016/j.ijsolstr.2016.03.012.

[3] J. L. Chaboche, "A review of some plasticity and viscoplasticity constitutive theories," Int. J. Plast., vol. 24, no. 10, pp. 1642–1693, 2008, doi: 10.1016/j.ijplas.2008.03.009.

[4] J. L. Chaboche and G. Rousselier, "On the plastic and viscoplastic constitutive equations-part I: Rules developed with internal variable concept," J. Press. Vessel Technol. Trans. ASME, vol. 105, no. 2, pp. 153–158, 1983, doi: 10.1115/1.3264257.

[5] P. J. Armstrong and C. O. Frederick, "A mathematical representation of the multiaxial Bauschinger effect," 1966.

[6] C. O. Frederick and P. J. Armstrong, "A mathematical representation of the multiaxial Bauschinger effect," Mater. High Temp., vol. 24, no. 1, pp. 1–26, 2007, doi: 10.3184/096034007X207589.

[7] F. Edelman and D. C. Drucker, "Some extensions of elementary plasticity theory," J. Franklin Inst., vol. 251, no. 6, pp. 581–605, 1951, doi: 10.1016/0016-0032(51)90406-1.

[8] W. Prager, "Recent developments in the mathematical theory of plasticity," J. Appl. Phys., vol. 20, no. 3, pp. 235–241, 1949, doi: 10.1063/1.1698348.

[9] J. L. Chaboche, "Constitutive equations for cyclic plasticity and cyclic viscoplasticity," Int. J. Plast., vol. 5, no. 3, pp. 247–302, 1989, doi: 10.1016/0749-6419(89)90015-6.

[10] N. N. Malinin and G. M. Khadjinsky, "Theory of creep with anisotropic hardening," Int. J. Mech. Sci., vol. 14, no. 4, pp. 235–246, 1972, doi: 10.1016/0020-7403(72)90065-3.

[11] E. Orowan, "The Creep of Metals," J. West Scotl. Iron Steel Inst., vol. 54, pp. 45–53, 1946.

[12] D. Marquis, "Etude théorique et vérification expérimentale d'un modèle de plasticité cyclique," Paris VI, 1979.

[13] J. L. Chaboche, K. D. Van, and G. Cordier, "Modelization of the Strain Memory Effect on the Cyclic Hardening of 316 Stainless Steel.," Transactions of the International Conference on Structural Mechanics in Reactor Technology, vol. L. 1979.

[14] M. Yaguchi, M. Yamamoto, and T. Ogata, "A viscoplastic constitutive model for nickel-base superalloy, part 1: Kinematic hardening rule of anisotropic dynamic recovery," Int. J. Plast., vol. 18, no. 8, pp. 1083–1109, 2002, doi: 10.1016/S0749-6419(01)00029-8.

[15] J. L. Chaboche and D. Nouailhas, "Constitutive modeling of ratchetting effects-part II: Possibilities of some additional kinematic rules," J. Eng. Mater. Technol. Trans. ASME, vol. 111, no. 4, pp. 409–416, 1989, doi: 10.1115/1.3226488.

[16] University of Liege, "Lagamine FE code." http://www.lagamine.uliege.be/dokuwiki/doku.php/.

[17] R. Ahmed, "Constitutive Modeling for Very High Temperature Thermo- Mechanical Fatigue Responses," North Carolina State University, 2013.

[18] M. L. Wilkins, "Calculations of elastic-plastic flow," Methods Comput. Phys., pp. 211–263, 1964.

[19] H. Morch, L. Duchêne, and A. M. Habraken, "Visco-plastic chaboche model for nickel-based alloys under anisothermal cyclic loading," Proc. 14th Int. Conf. Comput. Plast. - Fundam. Appl. COMPLAS 2017, vol. 2017-Janua, pp. 447–457, 2017.

[20] Z. L. Zhan and J. Tong, "A study of cyclic plasticity and viscoplasticity in a new nickel-based superalloy using unified constitutive equations. Part II: Simulation of cyclic stress relaxation," Mech. Mater., vol. 39, no. 1, pp. 73–80, 2007, doi: 10.1016/j.mechmat.2006.01.006.

[21] M. Yaguchi, M. Yamamoto, and T. Ogata, "A viscoplastic constitutive model for nickel-base superalloy, part 2: Modeling under anisothermal conditions," Int. J. Plast., vol. 18, no. 8, pp. 1111–1131, 2002, doi: 10.1016/S0749-6419(01)00030-4.

[22] H. Morch, L. Duchêne, and A. M. Habraken, "Identification method of an advanced constitutive law for nickel-based alloy Haynes 230 used in solar receivers," J. Phys. Conf. Ser., vol. 1063, no. 1, Jul. 2018, doi: 10.1088/1742-6596/1063/1/012149.

[23] J. Tong, Z. L. Zhan, and B. Vermeulen, "Modelling of cyclic plasticity and viscoplasticity of a nickel-based alloy using Chaboche constitutive equations," Int. J. Fatigue, vol. 26, no. 8, pp. 829–837, 2004, doi: 10.1016/j.ijfatigue.2004.01.002.

[24] D. L. Klarstrom, "Haynes 230," Aerosp. High Perform. Alloy. Database, pp. 1–8, 2009.

[25] S. Otin, "Lois d 'endommagement incrémentales isotrope/ anisotropes pour applications thermomécaniques complexes," ENS Cachan, 2008.

[26] ULiège, "OPTIM code." http://www.lagamine.uliege.be/dokuwiki/doku.php/optim/start.

[27] K. Levenberg and F. Arsenal, "A Method for the Solution of Certain Non-Linear Problems in Least Squares," Q. Appl. Math., vol. 1, no. 278, pp. 536–538, 1943.

[28] G. Maier et al., "Cyclic deformation and lifetime of Alloy 617B during thermo-mechanical fatigue," Mater. High Temp., vol. 30, no. 1, pp. 27–35, 2013, doi: 10.3184/096034013X13636905345685.

[29] C. Zhou, Z. Chen, J. W. Lee, M. G. Lee, and R. H. Wagoner, "Implementation and application of a temperature-dependent Chaboche model," Int. J. Plast., vol. 75, pp. 121–140, 2015, doi: 10.1016/j.ijplas.2015.03.002.

[30] C. Wang, D. Shi, X. Yang, S. Li, and C. Dong, "An improved viscoplastic constitutive model and its application to creep behavior of turbine blade," Mater. Sci. Eng. A, vol. 707, no. April, pp. 344–355, 2017, doi: 10.1016/j.msea.2017.09.067.

[31] R. Desmorat and S. Otin, "Cross-identification isotropic/anisotropic damage and application to anisothermal structural failure," Eng. Fract. Mech., vol. 75, no. 11, pp. 3446–3463, 2008, doi: 10.1016/j.engfracmech.2007.05.011.

[32] N. Ohno, Y. Takahashi, and K. Kuwabara, "Constitutive modeling of anisothermal cyclic plasticity of 304 stainless steel," J. Eng. Mater. Technol. Trans. ASME, vol. 111, no. 1, pp. 106–114, 1989, doi: 10.1115/1.3226424.

[33] E. Hosseini, S. R. Holdsworth, I. Kühn, and E. Mazza, "Temperature dependent representation for Chaboche kinematic hardening model," Mater. High Temp., vol. 32, no. 4, pp. 404–411, 2015, doi: 10.1179/1878641314Y.0000000036.

[34] H. Morch, L. Duchêne, R. Harzallah, V. Tuninetti, and A. M. Habraken, "Efficient temperature dependence of parameters for thermo-mechanical finite element modeling of alloy 230," Eur. J. Mech. A/Solids, vol. 85, no. September 2020, 2021, doi: 10.1016/j.euromechsol.2020.104116.

[35] P. R. Barrett, R. Ahmed, M. Menon, and T. Hassan, "Isothermal low-cycle fatigue and fatigue-creep of Haynes 230," Int. J. Solids Struct., vol. 88–89, pp. 146–164, 2016, doi: 10.1016/j.ijsolstr.2016.03.011.

[36] M. Hasselqvist, "Viscoplastic modelling for Industrial Gas Turbine (IGT) application with emphasis on the sheet material Haynes 230," Am. Soc. Mech. Eng. Int. Gas Turbine Institute, Turbo Expo IGTI, vol. 3 B, no. May, pp. 1229–1233, 2002, doi: 10.1115/GT2002-30659.

[37] J. Veverkova, A. Strang, G. R. Marchant, G. M. McColvin, and H. V. Atkinson, "High temperature microstructural degradation of Haynes Alloy 230," in Proceedings of the 11th International Symposium on Superalloys, 2008, pp. 479–488, doi: 10.7449/2008/superalloys_2008_479_488.

[38] R. Ahmed, P. R. Barrett, M. Menon, and T. Hassan, "Thermo-mechanical low-cycle fatigue-creep of Haynes 230," Int. J. Solids Struct., vol. 126–127, pp. 90–104, 2017, doi: 10.1016/j.ijsolstr.2017.07.033.

Chapter 3: Damage model for thermo-mechanical creep-fatigue

TABLE OF CONTENTS

1 DAMAGE MODELLING

One of the objectives of the Solar Perform project was to predict the lifetime of solar receivers made of alloy 230. The loading of the receivers is complex, as it includes daily cycling, large temperature variations and gradients, and long hold times at high temperatures. As a consequence, the material undergoes creep, fatigue, and possibly thermal ageing. All these effects can interact and accelerate the degradation of the material. Due to this complexity, it is impossible to determine the lifetime by simple extrapolation of experimental results.

A mathematical model that takes into account both creep and fatigue, as well as their interaction, is necessary to accurately predict the failure of the solar receivers. In this section, a brief review of existing mathematical models for damage is given, followed by a detailed presentation of the Lemaitre damage model.

1.1 PREDICTING FAILURE

1.1.1 Linear summation of damage

The linear summation of damage for fatigue was developed by Miner in 1945 [1]. It is a very simple rule that can be applied to cyclic loadings of known stress level. The damage produced by a number of cycles N_i at a stress level σ_i is defined as $\frac{N_i}{N_{R,i}}$, where $N_{R,i}$ is the number of cycles to rupture for that stress level. The Miner rule, written as Eq. (3.1), supposes that damages at different stress levels can be added and rupture occurs when the sum of these damages is equal to 1:

$$\sum_i \frac{N_i}{N_{R,i}} = 1 \tag{3.1}$$

Similarly, Robinson [2] proposed a summation rule for creep shown in Eq. (3.2), where t_i is the time spent at a given stress level and temperature, and $t_{R,i}$ the rupture time for that stress level and temperature.

$$\sum_i \frac{t_i}{t_{R,i}} = 1 \tag{3.2}$$

The two rules can be combined as Eq. (3.3) in the case of creep-fatigue:

$$\sum_i \frac{N_i}{N_{R,i}} + \sum_j \frac{t_j}{t_{R,j}} = 1 \tag{3.3}$$

This rule can be practical for a rapid preliminary assessment of lifetime, however, it has been shown to be conservative and not well adapted to the creep-fatigue of alloy 230 [3], as shown in Figure 3.1 where the fatigue damage D_f corresponds to the first sum in Eq. (3.3) and the creep damage D_c corresponds to the second sum. The two damages were calculated for different creep fatigue tests with strain amplitudes of 0.5%, 1%, or 1.5% and tensile hold times of 3 min, 10 min, or 30 min. For the five tests, the combined fatigue and creep damage is largely above 1.

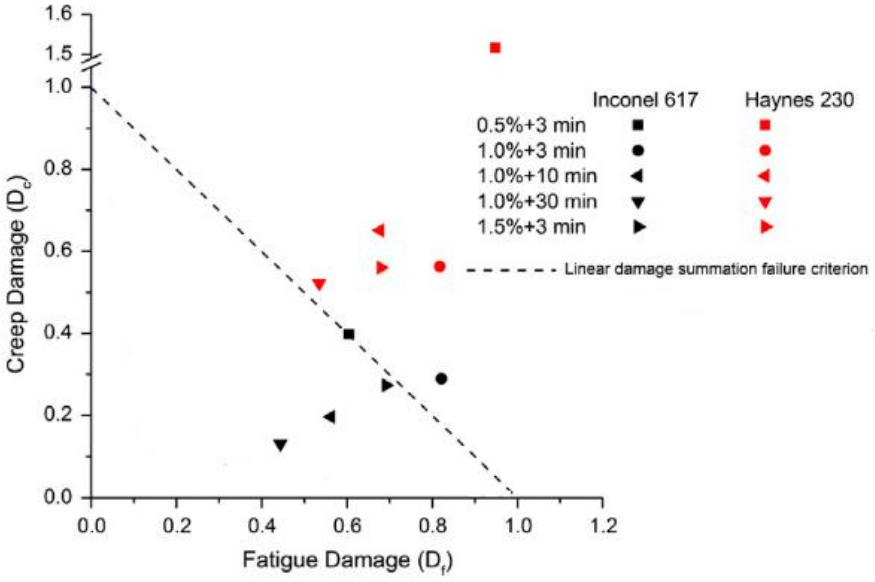

Figure 3.1 – Linear damage summation for creep-fatigue tests on Inconel 617 and Haynes 230 alloys. Results from Chen et al. [3]

1.1.2 Strain range partitioning

The concept of strain range partitioning was introduced in 1971 by Manson and Halford [4]. Their idea was to separate the contributions of creep deformation, which is associated to diffusion mechanisms and grain boundary sliding, and other plastic deformations, caused by sliding within the grains, for the computation of lifetime. They proposed to divide the total inelastic strain range into four components:

- Plastic strain reversed by plasticity $\Delta\varepsilon_{pp}$
- Creep strain reversed by creep $\Delta\varepsilon_{cc}$
- Plastic strain reversed by creep $\Delta\varepsilon_{pc}$
- Creep strain reversed by plasticity $\Delta\varepsilon_{cp}$

In this notation, the first letter refers to the type of strain imposed in the tensile part of the cycle (loading), while the second letter refers to the type of strain imposed during the compressive part of the cycle (reversed loading).

A Manson-Coffin law, relating the inelastic strain amplitude $\Delta\varepsilon_{xy}$ (subscripts x and y refer to either creep or plasticity) to the number of cycles to failure N_{xy}, can be fitted for each of these contributions based on specific tests:

$$\Delta\varepsilon_{xy} = C\left(N_{xy}\right)^{\beta} \tag{3.4}$$

The total number of cycles to failure is then computed by adding the contribution of each strain component as shown in Eq. (3.5) where F_{xy} is the ratio of the strain component $\Delta\varepsilon_{xy}$ on the total strain amplitude:

$$\frac{1}{N} = \frac{F_{pp}}{N_{pp}} + \frac{F_{cc}}{N_{cc}} + \frac{F_{pc}}{N_{pc}} + \frac{F_{cp}}{N_{cp}} \tag{3.5}$$

Although this method was shown to give good results for 2¼ Cr-1Mo steel, it is very difficult to apply in general. Firstly, it requires multiple very specific tests to identify the Manson-Coffin parameters N_{xy} for each component; secondly, it is difficult to partition the strain properly on any loading cycle.

Wu [5] proposed a method inspired by strain range partitioning for the life prediction of gas turbine materials. In this model, the strain is divided in two physics-based components:

- Intragranular deformation ε_g;
- Deformation due to grain boundary sliding ε_{gbs}, which usually develops under creep loading.

The lifetime prediction model of Wu is interesting because it is based on physical considerations, however, it also requires extensive knowledge of the material behaviour at a microscopic scale, which is not easily obtained, especially when considering a wide range of temperatures as is the case for the application in this study.

1.1.3 Continuum damage theory

In 1958, Kachanov introduced the concept of 'continuity' to model the microcracking in materials under creep loading [6]. The idea was to model the continuity of the material by a scalar variable $\psi \in [0,1]$. The absence of damage is characterized by $\psi = 1$, whereas rupture – i.e., the appearance of a mesoscopic crack – corresponds to $\psi = 0$.

Creep normally consists of three stages:

- Primary creep, characterized by a relatively high initial strain rate which decreases with time due to hardening of the material.
- Secondary creep, during which the strain rate is constant and microcracks form gradually.

- Tertiary creep, where the strain rate increases exponentially due to coalescence of voids at grain boundaries which accelerates fracturing.

To model the progressive build-up of microcracks, Kachanov proposed to use a power law to describe the evolution of the continuity variable ψ, where A and n are material parameters:

$$\dot{\psi} = -A\left(\frac{\sigma}{\psi}\right)^n \tag{3.6}$$

The ration σ/ψ can be interpreted as an effective stress.

Rabotnov later modified the law proposed by Kachanov, using a scalar damage variable $\omega = 1 - \psi$ instead of the continuity variable ψ and introducing a new material parameter k [7]:

$$\dot{\omega} = \frac{A}{(1-\omega)^k}\left(\frac{\sigma}{1-\omega}\right)^n \tag{3.7}$$

The concept of a scalar variable to model damage and the use of the effective stress was later expanded by Lemaitre and Chaboche to a more general thermodynamic framework, detailed in Section 1.2 hereafter.

1.2 LEMAITRE UNIFIED DAMAGE MODEL

1.2.1 Concept

The unified damage model proposed by Lemaitre is based on the concepts introduced by Kachanov and Rabotnov. In the Lemaitre model, the state of the material is represented by a scalar variable D, equivalent to the ω variable of Rabotnov. This variable can also be in the form of a tensor to represent anisotropic damage. In this work, however, only the scalar form is used, i.e., damage is considered isotropic. This assumption was made because the only experimental data available (from the experimental campaign and from the literature) consist in uniaxial tests. Therefore, it would be impossible to quantify the effect of damage produced in one direction on the behaviour in other directions.

The damage variable D varies between 0 (no damage) and 1 (rupture). The value of 1 is a theoretical value corresponding to rupture; numerically, the value of D is limited to a critical damage value $D_{crit} < 1$ that would correspond to the appearance of a mesoscopic crack. At a microscopic level, D can be understood as a representation of the concentration of voids in the material. An effective stress $\underline{\tilde{\sigma}}$ can be defined according to Eq. (3.8).

$$\underline{\tilde{\sigma}} = \frac{\underline{\sigma}}{1 - D} \tag{3.8}$$

This effective stress corresponds to the stress that would be required to produce the same strain on the undamaged material, as illustrated in Figure 3.2.

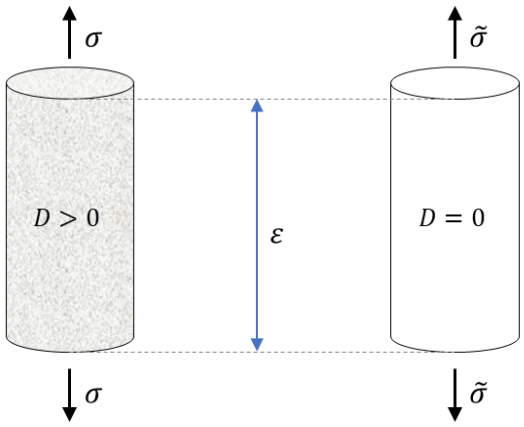

Figure 3.2 – Schematic representation of the concept of effective stress $\tilde{\sigma}$; on the left: damaged material under stress σ; on the right: equivalent undamaged material under stress $\tilde{\sigma}$

In the case of unidimensional elasticity, this is equivalent to considering that the Young modulus is decreased by a factor $1 - D$.

$$\tilde{\sigma} = \frac{\sigma}{1 - D} = E\varepsilon^e \Leftrightarrow \sigma = (1 - D)E\varepsilon^e \tag{3.9}$$

In the 3D case, this leads to the modified Hooke's law written with the effective stress as Eq. (3.10) using the Voigt notation described in Section 1.1.1 of Chapter 2:

$$\underline{\tilde{\sigma}} = \underline{\underline{E}} : \underline{\varepsilon}^e \tag{3.10}$$

Which can be written in index notation as Eq. (3.11), where δ_{ij} is the Kronecker symbol:

$$\tilde{\sigma}_{ij} = \frac{E}{1 + \nu}\left(\varepsilon^e_{ij} + \frac{\nu}{1 - 2\nu}\varepsilon^e_{kk}\delta_{ij}\right) \tag{3.11}$$

The inverse relationship can also be expressed using index notation:

$$\varepsilon^e_{ij} = \frac{1 + \nu}{E}\tilde{\sigma}_{ij} - \frac{\nu}{E}\tilde{\sigma}_{kk}\delta_{ij} \tag{3.12}$$

1.2.2 Mathematical model

To define the evolution of the damage variable D, Lemaitre introduced the thermodynamic variable Y [8] – not to be mistaken with the tensor $\underline{Y_i}$ which represents mean stress evolution in the behaviour model – as shown in Eq. (3.13), where $\dot{p}$ is the

equivalent plastic strain rate defined in Section 1.1.2 of Chapter 2, S and s are material parameters.

$$\dot{D} = \left(\frac{Y}{S}\right)^{s} \dot{p} \tag{3.13}$$

The thermodynamic variable Y is the strain energy density release rate and can be expressed as Eq. (3.14):

$$Y = \frac{1}{2}\underline{\varepsilon}^{e} : \underline{\underline{E}} : \underline{\varepsilon}^{e} \tag{3.14}$$

Considering the modified Hooke's law with the effective stress, the variable Y can be rewritten as a function of the stress $\underline{\sigma}$:

$$Y(\underline{\sigma}) = \frac{1}{2}\underline{\underline{E}}^{-1} : \underline{\tilde{\sigma}} : \underline{\tilde{\sigma}} = \frac{1+\nu}{2E}\frac{\sigma_{ij}\sigma_{ij}}{(1-D)^2} - \frac{\nu}{2E}\left(\frac{\sigma_{kk}}{1-D}\right)^2 \tag{3.15}$$

1.2.2.1 Microdefects closure

Under compressive loading, microdefects tend to close; this means the area which carries the load is larger in compression compared to the area carrying the load in tension. The value of damage is however not modified by microdefects closure as this closure is only momentary and does not correspond to a healing of the material. Experimentally, this can be observed by measuring the Young modulus in tension and compression: the apparent Young modulus in compression is bigger than the apparent Young modulus in tension.

To mathematically express the effect of microdefects closure, a crack closure parameter h is introduced [9]. For a unidimensional stress state, the effective stress is then redefined as Eq. (3.16) in compression, while the regular expression of Eq. (3.8) is used in tension. The parameter h is usually equal to 0.2 for metals [10].

$$\tilde{\sigma} = \frac{\sigma}{1-hD} \tag{3.16}$$

In a 3D stress state, separating compressive and tensile components is not as simple. The model proposed by Lemaitre divides the stress tensor into a positive part $\langle\underline{\sigma}\rangle^{+}$ and a negative part $\langle\underline{\sigma}\rangle^{-}$. The positive/negative part of the tensor can be computed from its positive/negative eigenvalues s_K and the corresponding normalized eigenvectors $\vec{q}^{K}$, as shown in Eq. (3.17), where $\langle . \rangle$ denotes the Macaulay brackets:

$$\langle\sigma\rangle_{ij}^{+} = \sum_{K=1}^{3} \langle s_K \rangle q_i^K \, q_j^K \quad \text{and} \quad \langle\sigma\rangle_{ij}^{-} = \sigma_{ij} - \langle\sigma\rangle_{ij}^{+} \tag{3.17}$$

The definition of the effective stress given by Eq. (3.8) and the modified Hooke's law of Eq. (3.11) are no longer valid under the assumption of microdefects closure. Instead, the effective stress can be written as Eq. (3.18):

$$\tilde{\sigma}_{ij} = \frac{\langle\sigma\rangle_{ij}^{+}}{1-D} + \frac{\langle\sigma\rangle_{ij}^{-}}{1-hD} + \frac{\nu}{1-2\nu}\left[\frac{\delta_{kl}\langle\sigma\rangle_{kl}^{+} - \langle\sigma_{kk}\rangle}{1-D} + \frac{\delta_{kl}\langle\sigma\rangle_{kl}^{-} + \langle-\sigma_{kk}\rangle}{1-hD}\right]\delta_{ij} \tag{3.18}$$

Similarly, the relation between the stress and the elastic strain which was expressed by Eq. (3.12) is now written as Eq. (3.19):

$$\varepsilon_{ij}^{e} = \frac{1+\nu}{E}\left[\frac{\langle\sigma\rangle_{ij}^{+}}{1-D} + \frac{\langle\sigma\rangle_{ij}^{-}}{1-hD}\right] - \frac{\nu}{E}\left[\frac{\langle\sigma_{kk}\rangle}{1-D} - \frac{\langle-\sigma_{kk}\rangle}{1-hD}\right]\delta_{ij} \tag{3.19}$$

The strain energy density release rate Y, previously defined by Eq. (3.15) can then be calculated as a function of the stress tensor $\underline{\sigma}$ using Eq. (3.20):

$$Y(\underline{\sigma}) = \frac{1+\nu}{2E}\left[\frac{\langle\sigma\rangle_{ij}^{+}\langle\sigma\rangle_{ij}^{+}}{(1-D)^2} + h\frac{\langle\sigma\rangle_{ij}^{-}\langle\sigma\rangle_{ij}^{-}}{(1-hD)^2}\right] - \frac{\nu}{2E}\left[\frac{\langle\sigma_{kk}\rangle^2}{(1-D)^2} + h\frac{\langle-\sigma_{kk}\rangle^2}{(1-hD)^2}\right] \tag{3.20}$$

Note that in the case where $h = 1$, Eq. (3.19) is equivalent to the modified Hooke's law of Eq. (3.12) and Eq. (3.20) becomes equivalent to Eq. (3.15). However, from a numerical standpoint, it is much more efficient to use equations (3.10) and (3.15) when $h = 1$ since they do not require the computation of the positive and negative parts of the stress tensor.

1.2.2.2 Damage threshold

Damage only occurs in a material after a certain cumulative plastic strain p_D is reached [8]. The threshold is dependent on the material, on the temperature, as well as on the type of loading. A more objective threshold can be defined using the energy stored by hardening w_s (Eq. (3.21)). Damage occurs once the energy stored over time w_s reaches a threshold w_D, which is a temperature-dependent material parameter.

$$w_s = \int_0^t \left(\frac{A}{m} p^{\frac{1-m}{m}} R(p)\dot{p}\right) dt + \sum_i \frac{3}{2} C_i \underline{X}_i : \underline{X}_i \tag{3.21}$$

In Eq. (3.21), A and m are correction parameters to take into account the saturation of energy stored from isotropic hardening once isotropic hardening is saturated [11]. R and $\underline{X}_i$ are respectively the drag stress and the back-stresses defined in Chapter 2; C_i is a parameter associated to kinematic hardening.

1.2.3 Parameter identification

In the unified Lemaitre damage model, when h is fixed at a constant value of 0.2, there are 5 parameters to identify at each temperature:

- 2 damage parameters s and S;
- 3 parameters for the initialisation of damage A, m, and w_D.

To identify these parameters, Otin proposed a simple method based on creep tests and fatigue tests [12]. The parameters s and S are first identified from creep tests, by considering that the damage threshold is reached when secondary creep starts. For a uniaxial tensile creep test, the effect of microdefects closure is not taken into account since the stress is always positive (i.e., $\langle \underline{\sigma} \rangle^{-} = \underline{0}$). Therefore, the theoretical time to rupture $t_{R,th}$ can be obtained by integrating Eq. (3.13) as Eq. (3.22), where t_D is the time to start of secondary creep, and σ the creep stress. The critical value of damage D_{crit} is set to 0.3, as is usually the case for metallic materials [11].

$$t_{R,th} = t_D + \left(\frac{2ES}{\sigma^2}\right)^s \frac{1}{\dot{p}} \int_0^{D_{crit}} (1-D)^{2s} dD \tag{3.22}$$

For alloy 230 at 760°C, the parameters in case of pure creep are identified through trial and error using Eq. (3.22) and experimental data from Haynes. The resulting points are shown in Figure 3.3 for parameters $s = 3.5$ and $S = 8$ (optimised values).

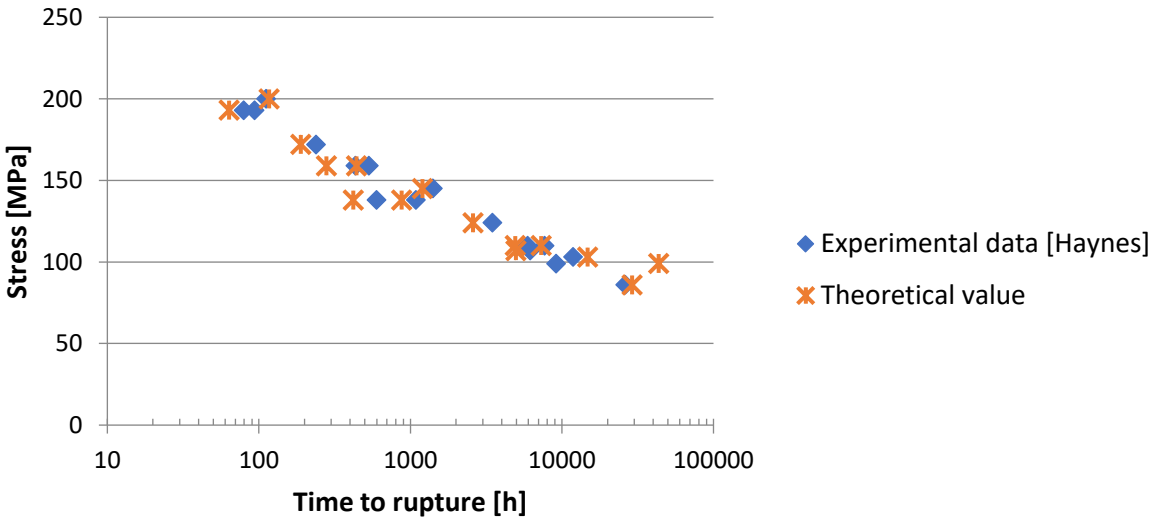

Figure 3.3 – Theoretical and experimental creep times to rupture used for the identification of parameters s and S at 760°C

Using these values, it is now possible to identify the parameters for the damage threshold. For a uniaxial fatigue test, the number of cycles to rupture N_R can be approximated by Eq. (3.23), where N_D is the number of cycles corresponding to the damage threshold, $\Delta\varepsilon_p$ is the plastic strain amplitude on a cycle, and σ is the stress amplitude:

$$N_R = N_D + \frac{D_{crit}}{2\Delta\varepsilon_p}\left(\frac{2ES}{\sigma^2}\right)^s \tag{3.23}$$

From this equation, it is possible to estimate the value of N_D for different fatigue tests by using the experimental values of N_R, $\Delta\varepsilon_p$ and σ. Using results of fatigue tests at 760°C from the literature [13], values of N_D were computed. These values are shown in Table 3.1. The values obtained for N_D are very close to the values of N_R. This result means that with the parameters identified from creep tests, damage due to fatigue evolves extremely rapidly towards a critical value once initiated. In addition, these parameters lead to considering that the material remains undamaged for most of the duration of the test, which seems unlikely at such a high temperature.

Table 3.1 – Number of cycles to rupture and number of cycles for the appearance of damage for 3 fatigue tests at 760°C

$\Delta\varepsilon$	N_R	N_D
0.8%	1657	1622
0.6%	4196	4138
0.4%	85079	84878

Considering these results, the identification of parameters was not conducted further, as it seems the model is not well adapted to alloy 230. In particular, having the same two parameters for both creep and fatigue damage does not seem appropriate for this material.

2 ADVANCED LEMAITRE-TYPE MODEL FOR CREEP-FATIGUE

In this section, a new damage model derived from the Lemaitre unified model is proposed to represent the damage of materials, and more specifically alloy 230, under thermomechanical creep-fatigue.

In this model, the damage caused by fatigue and the damage caused by creep are separated in two components D_f and D_c, such that the total mechanical damage is $D = D_f + D_c$. Indeed, it is known from experimental observations that fatigue and creep cause different effects in alloy 230 [14]–[17].

2.1 FATIGUE DAMAGE

The fatigue damage is modelled using Eq. (3.24), which is the same as Eq. (3.13) with parameters specific to fatigue S_f and s_f. The expression for $Y(\underline{\sigma})$ is given by Eq. (3.15) if no microdefects closure is taken into account, or by Eq. (3.20) in the case with microdefects closure.

$$\dot{D}_f = \left(\frac{Y(\underline{\sigma})}{S_f}\right)^{s_f} \dot{p} \tag{3.24}$$

For simplification, no damage threshold is considered: damage starts with plasticity. Although this assumption is not physically accurate, it is acceptable in the case of the model for solar receivers. Indeed, the solar receivers are exposed to a combination of creep and fatigue; the time to the onset of secondary creep is short for alloy 230 (a few hours or less, depending on the stress and temperature) therefore it is fair to assume that the damage threshold is rapidly achieved for the receiver tubes exposed to daily high-temperature thermomechanical loading with hold times of several hours.

2.2 CREEP DAMAGE

Creep damage is modelled using the Rabotnov-Kachanov equation (Eq. (3.7)) shown in section 1.1.3, with the variable $Y(\underline{\sigma})$ instead of $\underline{\sigma}$, D the total mechanical damage, and s_c, S_c, and k_c the creep damage parameters:

$$\dot{D}_c = \left(\frac{Y(\underline{\sigma})}{S_c}\right)^{s_c} \frac{1}{(1-D)^{k_c}} \tag{3.25}$$

One drawback of this formulation for creep damage is that numerically, creep damage will occur even for short loadings, or for cyclic loadings with high frequencies. In reality, creep is a long-term phenomenon and creep damage takes time to develop. Therefore, a delayed stress concept is introduced to prevent creep damage from occurring for high-frequency loadings. The stress used for the computation of creep damage is a delayed stress $\underline{\sigma}^d$, defined by Eq. (3.26) where τ is the characteristic time for the appearance of creep.

$$\frac{d\underline{\sigma}^d}{dt} = \frac{\underline{\sigma} - \underline{\sigma}^d}{\tau} \tag{3.26}$$

The concept of delayed stress is illustrated in Figure 3.4 for a unidimensional cyclic loading with a frequency $f = 0.25s^{-1}$. The real stress (in blue) and the stress with a value of $\tau = 0.1s$ are almost the same. Indeed, if it is considered that creep damage appears after 0.1s, the original curve of σ with a frequency $0.25s^{-1}$ can be used for the computation of creep. However, if creep damage only appears after 10 or 100 seconds, then creep will not develop under a loading frequency of $0.25s^{-1}$. The delayed stress for these values remains close to 0.

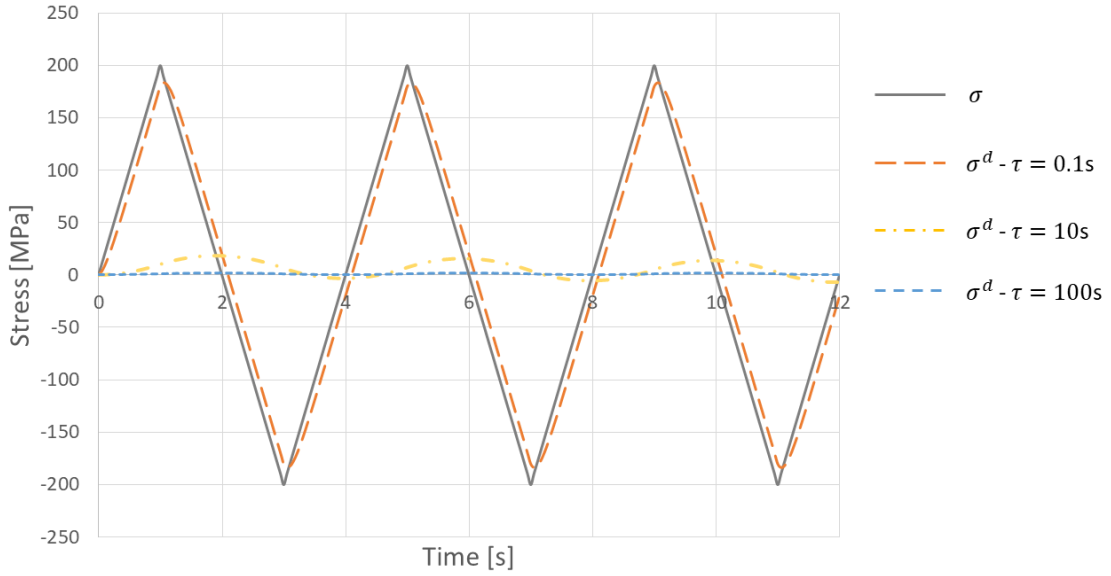

Figure 3.4 – Delayed stress on a cyclic loading of frequency 0.25s^{-1} for different values of the characteristic time τ

2.3 COUPLED FATIGUE-CREEP

As mentioned above, the fatigue and creep damages are summed to form the total mechanical damage $D = D_f + D_c$. However, the two damages are not completely independent of one another as would be the case in the linear summation damage model (see Section 1.1.1).

Experimental observations on alloy 230 show that the two phenomena can interact. This can be deduced from the study of cracks that form in the material during mechanical tests. At 850°C, low-cycle fatigue loadings lead to transgranular cracking [14], whereas creep loading generates cracks at grain boundaries (intergranular cracking) [18]. When creep and fatigue are combined by introducing hold times in the cyclic loading, the fracture mode evolves from transgranular (no hold time) to mixed transgranular/intergranular (short hold times), and even to mainly intergranular cracking (long hold times) [14], [19]. The presence of mixed transgranular/intergranular modes of fracture shows that fatigue and creep damages interact and tend to enhance one another. This is true for combined creep-fatigue when tensile creep is applied. The results of the metallurgical analysis detailed in Section 1.3 of Chapter 1 seem to indicate this is not the case for compressive creep. These results, however, were not yet available at the time of development of the damage model, which was based purely on considerations from the literature.

The coupling between creep and fatigue is done through the use of the effective stress in the computation of Y (Eq. (3.15)). Indeed, the total damage D is used in the expression of variable Y. A high value of either creep or fatigue damage increases the value of Y, which

is proportional to $1/(1-D)^2$ (in the case without microdefects closure). This increase of Y creates in turn an increase of both creep and fatigue damage rates.

2.4 IMPLEMENTATION

The equations for creep and fatigue damage were implemented in the Lagamine code as an additional feature of the behaviour model presented in Chapter 2. In the first version of the model, the behaviour is not coupled to damage. This means the value of damage does not impact the behaviour of the material, i.e., the effective stress is not used in the material law. A second version of the model with coupling, detailed in Section 3 of the present chapter, was later implemented.

In the non-coupled version, the equations for creep and fatigue damage are solved at the end of the time step; the values of the stress $\underline{\sigma}_{k+1}$ and the cumulative plastic strain p_{k+1} at the end of the time step are known. For simplification, the values at the end of the time step are written without indices in the following paragraphs: $\underline{\sigma}_{k+1} \rightarrow \underline{\sigma}$; $D_{k+1} \rightarrow D$; $p_{k+1} \rightarrow p$.

Equations (3.24) and (3.25) expressing the evaluation of D_f and D_c respectively are discretised using an implicit Euler scheme:

$$D_f = D_{f,k} + \left(\frac{Y(\underline{\sigma}, D)}{S_f}\right)^{s_f} (p - p_k) \tag{3.27}$$

$$D_c = D_{c,k} + \left(\frac{Y(\underline{\sigma}^d, D)}{S_c}\right)^{s_c} \frac{1}{(1-D)^{k_c}} \Delta t \tag{3.28}$$

With $D = D_f + D_c$.

Equations (3.27) and (3.28) can be rewritten in a residual form as Equations (3.29) and (3.30). These are nonlinear equations that can be solved using the Newton-Raphson method.

$$F_f = D_f - D_{f,k} - \left(\frac{Y(\underline{\sigma}, D)}{S_f}\right)^{s_f} (p - p_k) = 0 \tag{3.29}$$

$$F_c = D_c - D_{c,k} - \left(\frac{Y(\underline{\sigma}^d, D)}{S_c}\right)^{s_c} \frac{1}{(1-D)^{k_c}} = 0 \tag{3.30}$$

For the solution of these equations, a staggered scheme is used:

A. The Newton-Raphson method (also called Newton method) is applied to equation (3.29) to find the converged value D_f^A and D^A while considering $D_c = D_{c,k}$. Let n

the subscript denoting the n-th iteration of the Newton method. The method consists in computing the consecutive values of D_f^n using Eq. (3.31):

$$D_f^{n+1} = D_f^n - \left(\frac{\partial F_f}{\partial D_f}\left(D_f^n\right)\right)^{-1} F_f(D_f^n) \tag{3.31}$$

At the end of each iteration, the value of D is updated to $D^{n+1} = D_f^{n+1} + D_c$. Convergence for this step is achieved when the difference between two consecutive iterations is smaller than the imposed precision ϵ: $\frac{\left|D_f^{n+1} - D_f^n\right|}{D_f^n} < \epsilon$.

B. Eq. (3.30) is solved to find the converged values D_c^B and D^B using the new value of $D_f = D_f^A$. The consecutive values of D_c^n are computed using Eq. (3.32):

$$D_c^{n+1} = D_c^n - \left(\frac{\partial F_c}{\partial D_c}(D_c^n)\right)^{-1} F_c(D_c^n) \tag{3.32}$$

At the end of each iteration, the value of D is updated to $D^{n+1} = D_f^A + D_c^{n+1}$. Convergence for this step is achieved when the difference between two consecutive iterations is smaller than the imposed precision ϵ: $\frac{\left|D_c^{n+1} - D_c^n\right|}{D_c^n} < \epsilon$.

C. Step A is performed again while considering the updated value of creep damage: $D_c = D_c^B$.

Steps B and C are repeated until both steps converge with $\frac{\left|D^A - D^B\right|}{D_k} < \epsilon$, where ϵ is the precision for the convergence of the Newton-Raphson method.

The expressions for the derivatives of F_f and F_c are given in Appendix 2.

2.5 PARAMETER IDENTIFICATION

There are two types of parameters to identify for the damage model:

- S_f and s_f for fatigue damage.
- S_c, s_c and k_c for creep damage.

2.5.1 Fatigue damage parameters

The expression of the number of cycles to rupture for a uniaxial fatigue test can be derived from the integration of Eq. (3.24), as done in Section 1.2.3. Here, the damage threshold is considered to be close to zero, i.e., $N_D \approx 0$:

$$N_R \approx \frac{D_{crit}}{2\Delta\varepsilon_p}\left(\frac{2ES_f}{\sigma^2}\right)^{s_f} \tag{3.33}$$

Since the stress amplitude σ and the plastic strain amplitude $\Delta\varepsilon_p$ are not constant over the whole duration of the test, the value of N_R is approximated by using the values at mid-life. Using the Excel solver on the set of data obtained from the experimental campaign, a first approximation of parameters s_f and S_f can be found.

Figure 3.5 shows the result of the identification of parameters s_f and S_f, where $N_{R,th}$ are the values of number of cycles to rupture calculated using Eq. (3.33), and $N_{R,exp}$ the experimental number of cycles to rupture.

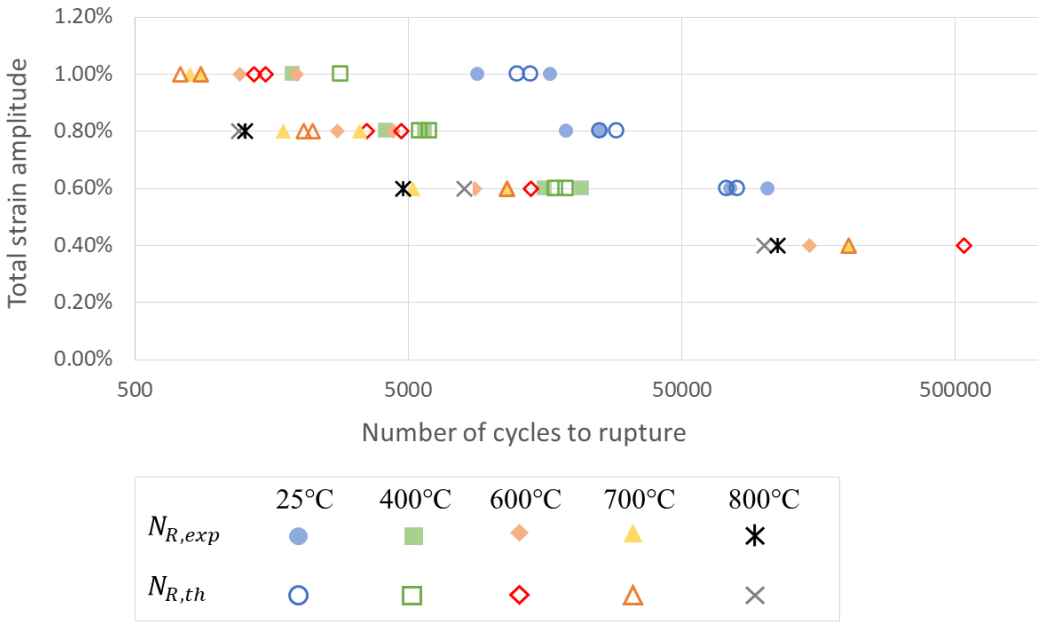

Figure 3.5 – Identification of fatigue damage parameters at different temperatures

This first approximation can then be refined using an optimization code such as OPTIM to obtain parameters based on the full stress and strain histories.

2.5.2 Creep damage parameters

As for the Lemaitre unified model, an analytical expression of the time to rupture t_R in pure creep can be obtained from the integration of Eq. (3.25) (in this case, the total damage is equivalent to the creep damage):

$$t_R = \left(\frac{2ES_c}{\sigma^2}\right)^{s_c} \int_0^{D_{crit}} (1 - D_c)^{k_c + 2s_c} dD \tag{3.34}$$

Using this equation, the 3 parameters can be identified manually through trial and error and optimized by minimizing the relative error between experimental values $t_{R,exp}$ and theoretical values $t_{R,th}$ obtained from Eq. (3.34) using the Excel solver. For simplification, exponent parameters s_c and k_c are kept constant with the temperature. This ensures that the evolution of S_c with temperature is monotonous.

Figure 3.6 shows the result of the identification at 5 different temperatures: the experimental times to rupture from Haynes data and from the creep tests performed by CRM are shown in grey, while the computed theoretical values are shown with transparent shapes outlined in black. No data is available at temperatures below 600°C, as almost no creep occurs below this temperature. The identification was not performed for temperatures above 800°C since it would be beyond the range of temperature that is used for solar receivers.

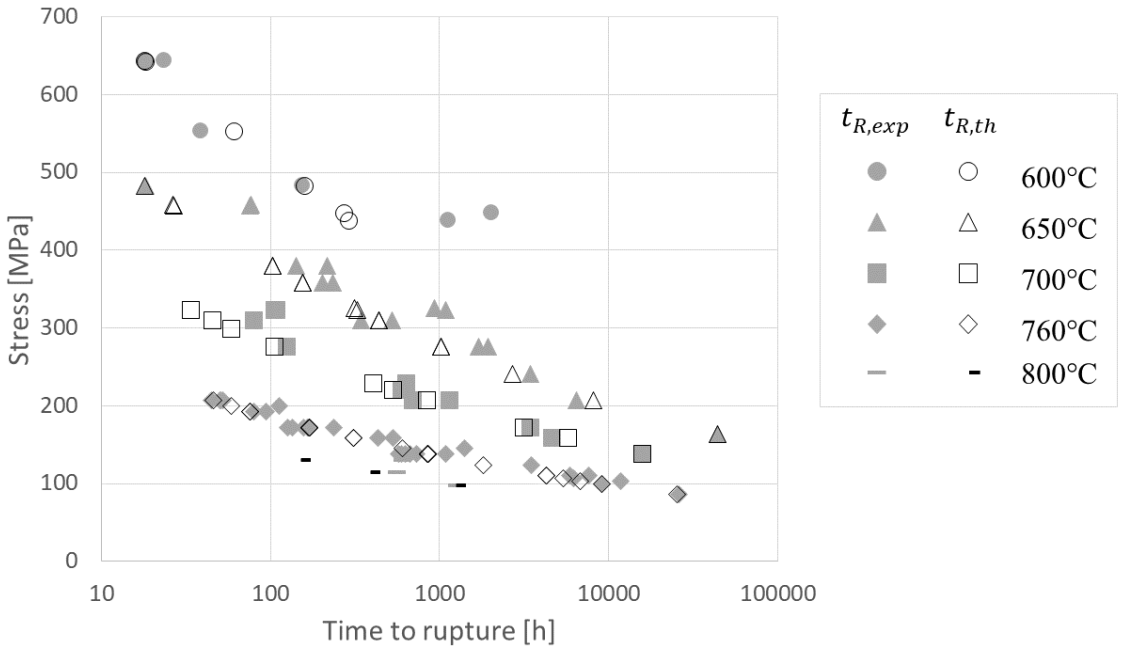

Figure 3.6 – Identification of the creep damage parameters at different temperatures

2.6 INFLUENCE OF THE MATERIAL FORMING

The experimental tests used for the identification of the parameters were performed on samples manufactured from bars of alloy 230. This was done for practical reasons, as tube samples are more sensitive to buckling and would have been more difficult to adapt to the testing machines.

Tubes are manufactured from sheets of alloy 230 which are bent and welded. Sheets and bars do not have the same properties, especially regarding the lifetime under creep and fatigue. In particular, sheets have shorter lifetimes under creep and fatigue. This could be due to the presence of residual stresses from rolling. However, the exact origin of this difference is not known. A comparative analysis of the microstructure of samples of tubes or sheets and samples of bars after creep and fatigue testing would be necessary to find out what causes the reduction in lifetime, however, this was not included in the project.

Figure 3.7 shows the stresses required to reach rupture in creep for different durations of the test. It is clear that for a given stress, the time to reach rupture is smaller for sheets

than for bars and plates. This is true at all temperatures considered. However, when multiplying the rupture stress for sheet by a correction coefficient k, the resulting curve is approximately the same as the rupture curve for bars and plates.

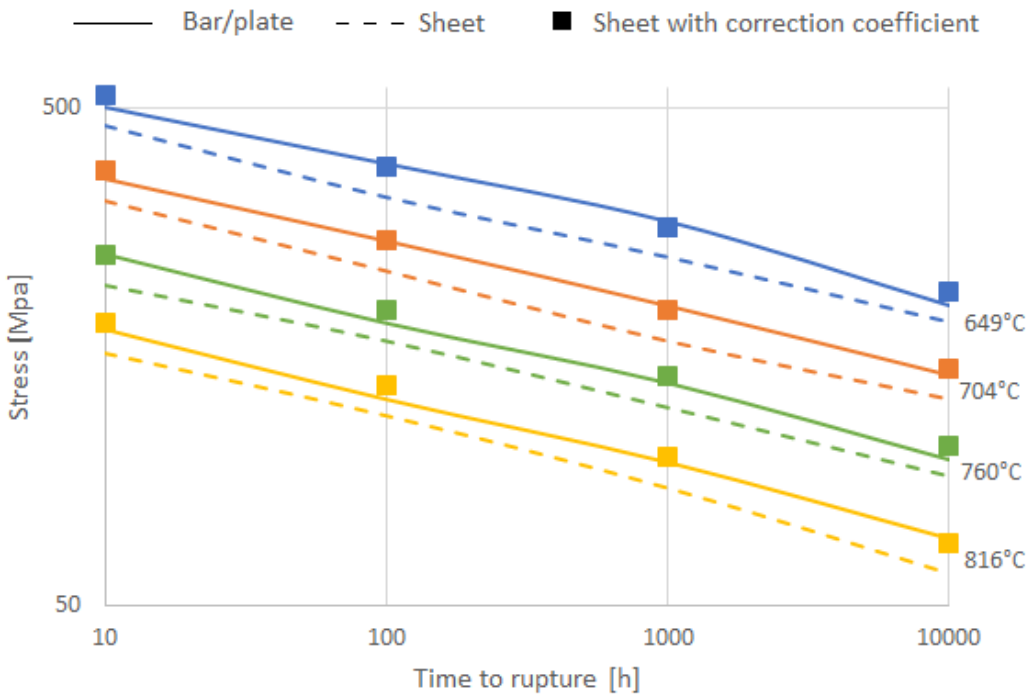

Figure 3.7 – Creep rupture properties of alloy 230 for Bar/Plate and Sheet - data from Haynes [20]. The square points correspond to ruptures for sheet with the stress multiplied by a correction coefficient $K_c \approx 1.13$

Let $\sigma_{b/p}^{T,t_R}$ and σ_{sh}^{T,t_R} the stresses required to reach rupture under t_R hours at a temperature T respectively for a bar or plate and for a sheet. The correction coefficient K_c was determined using the Excel solver to minimize the sum of the squares of the relative differences between $\sigma_{b/p}^{T,t_R}$ and $K_c\sigma_{sh}^{T,t_R}$, as shown in Eq. (3.35). The obtained value is $K_c = 1.125$.

$$S = \sum_{T}\sum_{t_R} \frac{\left(\sigma_{b/p}^{T,t_R} - K_c\sigma_{sh}^{T,t_R}\right)}{\sigma_{b/p}^{T,t_R}} \tag{3.35}$$

This correction coefficient can then be applied in the model by multiplying by k the stress used to compute the creep damage.

For fatigue, a difference between bars/plates and sheets/tubes can also be observed, although data is scarcer due to the difficulty of performing fatigue tests on sheets. Data found for welded tubes at 595°C [21] and for sheets at 816°C [17] are shown in Figure 3.8. Considering the equation for fatigue damage, it would seem best to apply a correction coefficient either on the stress level or on the plastic strain. However, neither of these

values are available for the data comparing plates/bars to sheets/tubes for the fatigue of Haynes 230. Therefore, a general coefficient on the lifetime is applied instead. For each set of points in Figure 3.8 (a) and (b), a power law is fitted so the number of cycles to rupture N_R can be expressed as a function of the total strain amplitude $\Delta\varepsilon$ as shown in Eq. (3.36), where a and b are parameters of the power law.

$$\Delta\varepsilon = a(N_R)^b \Leftrightarrow N_R = \left(\frac{\Delta\varepsilon}{a}\right)^{\frac{1}{b}} \tag{3.36}$$

A coefficient K_f is then determined so as to minimize the sum S written in Eq. (3.37). The value obtained with the Excel solver is $K_f = 3.144$.

$$S = \sum_{T}\sum_{\Delta\varepsilon} \frac{\left((N_R)_{sheet}^{T,\Delta\varepsilon} - \frac{1}{K_f}(N_R)_{bar}^{T,\Delta\varepsilon} \right)}{(N_R)_{sheet}^{T,\Delta\varepsilon}} \tag{3.37}$$

The resulting corrected curves are shown in grey in Figure 3.8. The corrected curve is very conservative for the results at 816°C, but give a good approximation at 595°C.

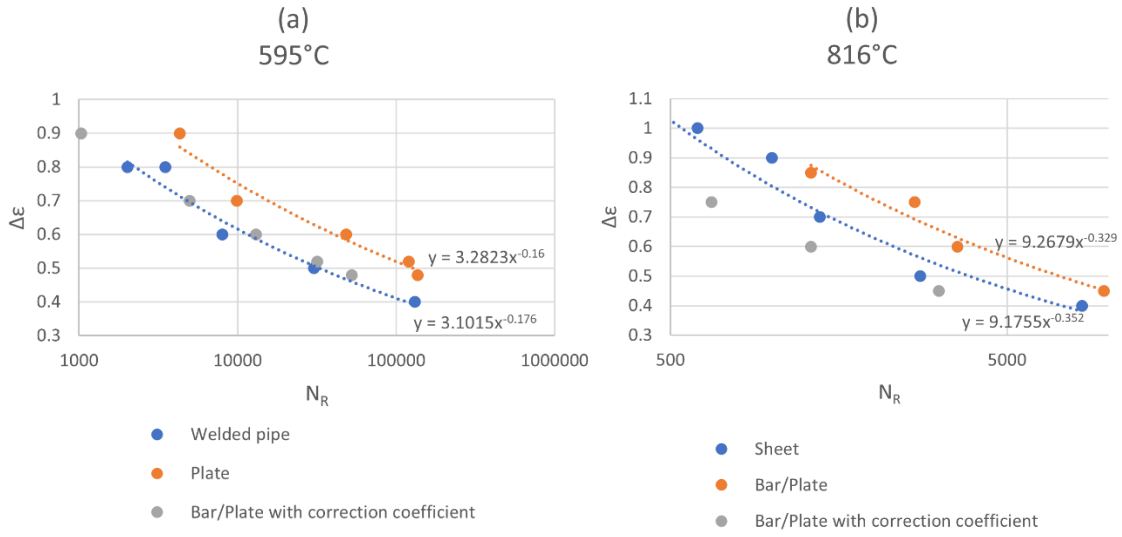

Figure 3.8 – Fatigue life comparison between bar/plate and tube/sheet at (a) 595°C and (b) 816°C

In the finite-element model, the equations for damage are modified to include 4 correction coefficients K_1, K_2, K_3 and K_4, as shown in Eq. (3.38) and (3.39). Coefficient K_1 is equivalent to K_f and K_4 is equivalent to K_c. Coefficients K_2 and K_3 are not used in the model for alloy 230 but were implemented so they could be used for other materials, depending on the available data.

$$\dot{D}_f = K_1 \left(\frac{Y\left(K_2 * \underline{\sigma}\right)}{S_f} \right)^{s_f} \frac{dp}{dt} \tag{3.38}$$

$$\dot{D}_c = K_3 \left(\frac{Y\left(K_4 * \underline{\sigma}^d\right)}{S_c} \right)^{s_c} \frac{1}{(1-D)^{k_c}} \tag{3.39}$$

3 COUPLED BEHAVIOUR-DAMAGE MODEL

Damage impacts the behaviour of the material. This can be seen experimentally from a softening of the material or a decrease of the Young modulus. In the Chaboche-Lemaitre model, damage can be coupled to the behaviour through the effective stress.

3.1 INTEGRATION OF DAMAGE IN THE BEHAVIOUR MODEL

The coupling of damage with the Chaboche model described in Chapter 2 can be done by using the effective stress $\underline{\tilde{\sigma}}$ in the elasticity law:

$$\underline{\varepsilon}^e = \underline{\underline{E}}^{-1} : \underline{\tilde{\sigma}} \tag{3.40}$$

The effective stress $\underline{\tilde{\sigma}}$ is defined by Eq. (3.8) in the case with no microdefects closure and by Eq. (3.18) in the case with microdefects closure. In the yield criterion, however, the value of the stress is replaced by $\frac{\underline{\sigma}}{1-D}$ in both cases. Indeed, the yield criterion is written for the viscoplastic case in Eq. (3.41). For the plastic case, the same equation can be used by setting $\sigma_v = 0$.

$$f - \sigma_v = J\left(\frac{\underline{\sigma}}{1-D} - \underline{X}\right) - R - \sigma_y - \sigma_v = 0 \tag{3.41}$$

Plasticity is controlled by slips and produced by shear stresses, and the sign has no influence [8]. Therefore the decomposition in positive and negative parts is not necessary. The normal to the yield surface $\underline{n}$ can then be defined as Eq. (3.42), where $\underline{\hat{\sigma}}$ is the deviatoric stress:

$$\underline{n} = \frac{\partial f}{\partial \underline{\sigma}} = \frac{1}{1-D} \frac{3}{2} \frac{\frac{\underline{\hat{\sigma}}}{1-D} - \underline{X}}{J\left(\frac{\underline{\sigma}}{1-D} - \underline{X}\right)} \tag{3.42}$$

In the framework of damage coupling, the plastic multiplier p from the non-coupled framework (see Chapter 2, Section 1.1.2, Eq. (2.11)) is replaced by the variable r defined by Eq. (3.43):

$$\dot{r} = (1-D)\dot{p} \tag{3.43}$$

The plastic strain rate can then be expressed as Eq. (3.44):

$$\underline{\dot{\varepsilon}}^p = \dot{r}\underline{n} \tag{3.44}$$

The hardening equations remain the same as those defined in Chapter 2, but the new plastic multiplier r is used instead of p. The isotropic hardening is therefore defined by Eq. (3.45), while the kinematic hardening is defined by Eq. (3.46) hereafter:

$$\dot{R} = b(Q - R)\dot{r} \tag{3.45}$$

$$\underline{\dot{X}_i} = \frac{2}{3}C_i(1-D)\underline{\dot{\varepsilon}}^p - \gamma_i\left(\underline{X_i} - \underline{Y_i}\right)\dot{r} - b_i J\left(\underline{X_i}\right)^{r_i - 1}\underline{X_i} + \frac{1}{C_i}\frac{dC_i}{dT}\dot{T}\underline{X_i} \tag{3.46}$$

The value of the drag stress R can be expressed directly as a function of r, similarly to the case without damage (see Chapter 2 – Section 1.1.3):

$$R = Q(1 - e^{-br}) \tag{3.47}$$

The evolution of damage is described by Eq. (3.24) for fatigue damage and Eq. (3.25) for creep damage, defined respectively in sections 2.1 and 2.2 of this chapter.

The material model coupled with damage can be described by combining the equations detailed above into a system of nonlinear equations. This system is shown in Eq. (3.48):

$$\begin{cases} \underline{\dot{\varepsilon}} - \underline{\dot{\varepsilon}}^{th} - \underline{\dot{\varepsilon}}^{e} - \dot{r}\underline{n} = 0 \\ J\left(\dfrac{\underline{\sigma}}{1-D} - \underline{X}\right) - R - \sigma_y - \sigma_v = 0 \\ \underline{\dot{X}_i} - \dfrac{2}{3}C_i(1-D)\underline{\dot{\varepsilon}}^p + \gamma_i\left(\underline{X_i} - \underline{Y_i}\right)\dot{r} + b_i J\left(\underline{X_i}\right)^{r_i-1}\underline{X_i} - \dfrac{1}{C_i}\dfrac{dC_i}{dT}\dot{T}\underline{X_i} = 0 \ (i = 1{:}\, n_{AF}) \\ \underline{\varepsilon^e} - \underline{\underline{E}}^{-1}{:}\,\underline{\tilde{\sigma}} = 0 \\ \begin{cases} \dot{D}_f - \left(\dfrac{Y(\underline{\sigma}, D)}{S_f}\right)^{s_f}\dot{p} = 0 \\ \dot{D}_c - \left(\dfrac{Y(\underline{\sigma}^d, D)}{S_c}\right)^{s_c}\dfrac{1}{(1-D)^{k_c}} = 0 \end{cases} \end{cases} \tag{3.48}$$

Note: the second equation, related to the von Mises criterion, is different in the case of a viscoplastic material for which the Norton law is applied. In this case, Eq. (3.49) is used.

$$\mathcal{R}_r = \Delta r - (1-D)\Delta t\left\langle \frac{J\left(\dfrac{\underline{\sigma}}{1-D} - \underline{X}\right) - R(r) - \sigma_y}{K} \right\rangle^n \tag{3.49}$$

To compute the values of the stresses, strains, and other internal variables, these equations must be discretized to be solved numerically at each time step in the finite element code.

3.2 IMPLEMENTATION

3.2.1 Strong vs. weak coupling

The system of equations given in Eq. (3.48) consists of 5+n_{AF} equations that need to be solved at every time step. With the exception of the yield surface and the damage equations which are scalar, these equations are in tensorial form (or vectorial, considering the Voigt notation is used). This means that the system actually consists of 15+6*n_{AF} nonlinear scalar equations.

To solve this type of system of equations, a numerical method such as the Newton method, already mentioned in Section 2.4, can be used. This method requires the computation of the Jacobian matrix. Let $\underline{\mathcal{R}}(\underline{\mathcal{W}})$ a system of equations of dimension n, where $\underline{\mathcal{W}}$ is the vector of variables to find:

$$\underline{\mathcal{R}}(\underline{\mathcal{W}}) = \begin{Bmatrix} \mathcal{R}_1(\mathcal{W}_1, \dots, \mathcal{W}_n) \\ \dots \\ \mathcal{R}_n(\mathcal{W}_1, \dots, \mathcal{W}_n \end{Bmatrix} \tag{3.50}$$

The Jacobian matrix $\underline{\underline{\mathcal{J}}}$ is the n-by-n matrix defined by Eq. (3.51):

$$\underline{\underline{\mathcal{J}}} = \begin{bmatrix} \frac{\partial \mathcal{R}_1}{\partial \mathcal{W}_1} & \dots & \frac{\partial \mathcal{R}_1}{\partial \mathcal{W}_n} \\ \vdots & \ddots & \vdots \\ \frac{\partial \mathcal{R}_n}{\partial \mathcal{W}_1} & \dots & \frac{\partial \mathcal{R}_n}{\partial \mathcal{W}_n} \end{bmatrix} \tag{3.51}$$

In the Newton method, the Jacobian matrix is inverted to compute successive guesses $\underline{\mathcal{W}}^k$ of the $\underline{\mathcal{W}}$ vector following Eq. (3.52):

$$\underline{\mathcal{W}}^{k+1} = \underline{\mathcal{W}}^k - \left[\underline{\underline{\mathcal{J}}}(\underline{\mathcal{W}}^k)\right]^{-1} \underline{\mathcal{R}}(\underline{\mathcal{W}}^k) \tag{3.52}$$

Numerically, the Jacobian is not directly inverted (this would require a large number of calculations and be very inefficient from a computational point of view), but the term $\underline{\mathcal{X}} = \left[\underline{\underline{\mathcal{J}}}(\underline{\mathcal{W}}^k)\right]^{-1} \underline{\mathcal{R}}(\underline{\mathcal{W}}^k)$ is calculated by solving Eq. (3.53) for $\underline{\mathcal{X}}$ through an LU (Lower-Upper) decomposition of $\underline{\underline{\mathcal{J}}}(\underline{\mathcal{W}}^k)$.

$$\underline{\mathcal{R}}(\underline{\mathcal{W}}^k) = \underline{\underline{\mathcal{J}}}(\underline{\mathcal{W}}^k)\underline{\mathcal{X}} \tag{3.53}$$

A larger Jacobian matrix results in slower computations of the successive iterations of the Newton method, since the CPU time for solving Eq. (3.53) is dependent on the size of the Jacobian.

In order to limit the size of the Jacobian, and therefore limit computational times, the system of equations (3.48) can be solved in two steps, by separating the damage from the behaviour equations. The behaviour is still coupled to damage, but the values of damage D_f and D_c used for the computation of the behaviour (stress, strains, hardening, etc.) are the values of the previous time step. Once the stresses and strains have been computed, their updated values are used to compute the damages as was done for the non-coupled model (see details in Section 2.4). This is referred to as "weak coupling". Not only this method is advantageous regarding the computational time, but this also allows to re-use the implementation of the non-coupled damage model for the solution of the damage equations. Moreover, the derivatives of the behaviour equations with respect to the damage variables do not need to be analytically computed.

The system to solve for the behaviour model with weak coupling is therefore a system of 13+6*n_{AF} equations:

$$\begin{cases} \underline{\dot{\varepsilon}} - \underline{\dot{\varepsilon}}^{th} - \underline{\dot{\varepsilon}}^{e} - \dot{r}\underline{n} = 0 \\ J\left(\dfrac{\underline{\sigma}}{1-D} - \underline{X}\right) - R - \sigma_y - \sigma_v = 0 \\ \underline{\dot{X}}_i - \dfrac{2}{3}C_i(1-D)\underline{\dot{\varepsilon}}^p + \gamma_i\left(\underline{X}_i - \underline{Y}_i\right)\dot{r} + b_i J\left(\underline{X}_i\right)^{r_i-1}\underline{X}_i - \dfrac{1}{C_i}\dfrac{dC_i}{dT}\dot{T}\underline{X}_i = 0 \ (i = 1{:}\, n_{AF}) \\ \underline{\varepsilon}^{\,e} - \underline{\underline{E}}^{-1}{:}\,\underline{\tilde{\sigma}} = 0 \end{cases} \tag{3.54}$$

Once Eq. (3.54) has been solved, Eq. (3.55) is solved using the method detailed in Section 2.4.

$$\begin{cases} \dot{D}_f - \left(\dfrac{Y\left(\underline{\sigma}, D\right)}{S_f}\right)^{s_f}\dot{p} = 0 \\ \dot{D}_c - \left(\dfrac{Y\left(\underline{\sigma}^d, D\right)}{S_c}\right)^{s_c}\dfrac{1}{(1-D)^{k_c}} = 0 \end{cases} \tag{3.55}$$

3.2.2 Discretization of the behaviour equations

To solve numerically Eq. (3.54), the equations must be discretized with respect to the time step Δt. Similarly to what was done in Section 1.3 of Chapter 2, Eq. (3.54) is linearized using the implicit Euler method. For simplicity, the values at the end of the time step (e.g.: $\underline{\sigma}_{k+1}$) are written without a subscript ($\underline{\sigma}$). Each equation becomes a local residual $\mathcal{R}$ which is a function of the unknown increments of variables $\Delta\underline{\varepsilon}^e$, Δr, $\Delta\underline{X}_i$, and $\Delta\underline{\sigma}$.

The local residual associated to the elastic strain $\underline{\mathcal{R}}_{\underline{\varepsilon}^e}$ are written as Eq. (3.56):

$$\underline{\mathcal{R}}_{\underline{\varepsilon}^e} = \Delta\underline{\varepsilon}^e + \Delta\underline{\varepsilon}^{th} - \Delta\underline{\varepsilon} + \Delta r\underline{n} \tag{3.56}$$

The local residual associated to the plastic strain multiplier $\mathcal{R}_r$ is expressed as Eq. (3.57) for a plastic material and as Eq. (3.58) for a viscoplastic material:

$$\mathcal{R}_r = J\left(\frac{\underline{\sigma}}{1-D} - \underline{X}\right) - R(r) - \sigma_y \tag{3.57}$$

$$\mathcal{R}_r = \Delta r - (1-D)\Delta t \left\langle \frac{J\left(\frac{\underline{\sigma}}{1-D} - \underline{X}\right) - R(r) - \sigma_y}{K} \right\rangle^n \tag{3.58}$$

The local residual(s) corresponding to kinematic hardening is written as Eq. (3.59):

For $i \in [1, n_{AF}]$:

$$\begin{aligned} \underline{\mathcal{R}}_{\underline{X}_i} = \Delta\underline{X}_i - \frac{2}{3}C_i(1-D)\Delta r\underline{n} + \gamma_i\left(\underline{X}_i - \underline{Y}_i\right)\Delta r + b_i J\left(\underline{X}_i\right)^{r_i - 1}\underline{X}_i\,\Delta t \\ - \frac{1}{C_i}\frac{dC_i}{dT}\Delta T\underline{X}_i \end{aligned} \tag{3.59}$$

Finally, the local residual associated to the stress is written as Eq. (3.60):

$$\underline{\mathcal{R}}_{\underline{\sigma}} = \underline{\varepsilon}^e - \underline{\underline{E}}^{-1} : \underline{\tilde{\sigma}} \tag{3.60}$$

The complete system of equations can finally be written as Eq. (3.61):

$$\underline{\mathcal{R}}\left(\Delta\underline{\mathcal{W}}\right) = \begin{Bmatrix} \underline{\mathcal{R}}_{\underline{\varepsilon}^e}\left(\Delta\underline{\varepsilon}^e, \Delta r, \Delta\underline{X}_i, \Delta\underline{\sigma}\right) \\ \mathcal{R}_r\left(\Delta\underline{\varepsilon}^e, \Delta r, \Delta\underline{X}_i, \Delta\underline{\sigma}\right) \\ \underline{\mathcal{R}}_{\underline{X}_i}\left(\Delta\underline{\varepsilon}^e, \Delta r, \Delta\underline{X}_i, \Delta\underline{\sigma}\right) \\ \underline{\mathcal{R}}_{\underline{\sigma}}\left(\Delta\underline{\varepsilon}^e, \Delta r, \Delta\underline{X}_i, \Delta\underline{\sigma}\right) \end{Bmatrix} = \{0\} \tag{3.61}$$

3.2.3 Solution of the behaviour equations

3.2.3.1 Elastic predictor

Similarly to what was done for the behaviour model without damage, an initial elastic predictor is estimated by assuming $\Delta r = 0$. This means the system of equations (3.61) is first solved assuming $\Delta r = 0$, which simplifies the equations a lot. For instance, the increment of elastic strain can be immediately computed as Eq. (3.62), where the total strain $\Delta\underline{\varepsilon}$ is given to the constitutive model by the finite-element code, and $\Delta\underline{\varepsilon}^{th}$ is computed from the temperature variation computed by the thermal law.

$$\Delta\underline{\varepsilon}^e = \Delta\underline{\varepsilon} - \Delta\underline{\varepsilon}^{th} \tag{3.62}$$

In the case without microdefects closure, solving for the elastic predictor is done in the same way as in the case with no damage (see Chapter 2 – Section 1.3.2.1). The only difference is that the stress $\underline{\sigma}$ is replaced by the effective stress $\underline{\tilde{\sigma}}$ and r is used instead of

the plastic multiplier p. In the case with microdefects closure, however, $\underline{\mathcal{R}}_{\underline{\sigma}}$ is not linear and the Newton method must be used to find the updated value of $\underline{\sigma}$. The use of the Newton method is further detailed in the next paragraphs.

Once the elastic predictor has been estimated, the von Mises yield criterion f is checked (see Eq. (3.41)). If $f \leq 0$, the initial hypothesis of $\Delta r = 0$ is validated and the calculation is complete for this time step and element. If not, the nonlinear system of equations (3.61) must be solved considering $\Delta r > 0$.

For the coupled model, although an elastic predictor is computed, the radial return mapping method is not used. This means instead of computing an elastic estimate of $\underline{\sigma}$ and then trying to find an additional term to the stress to verify the von Mises criterion ($-2(G + \Delta G)\Delta\underline{\varepsilon}^p$ in the non-coupled model), the full system of equations (3.61) is solved in the plastic step. The interests of using an elastic predictor anyway are:

1. The computation is much simpler and time-efficient; computing the solution of the full equations in the case where the material is in the elastic domain would unnecessarily increase computation times.
2. The elastic predictor can be used as an initial guess for the Newton method when solving for the plastic case.

3.2.3.2 Solution for the plastic case: $\boldsymbol{\Delta r > 0}$

First, an initial estimate of $\Delta\underline{\mathcal{W}} = \left\{\Delta\underline{\varepsilon}^e, \Delta r, \Delta\underline{X}_j, \Delta\underline{\sigma}\right\}^T$ is evaluated, using the values obtained in the elastic predictor step. Let $\Delta\underline{\mathcal{W}}^0$ be the initial estimate, and $\Delta\underline{\mathcal{W}}^k$ the value of $\Delta\underline{\mathcal{W}}$ at the k-th iteration of the Newton method. The Newton method consists in computing the successive values $\Delta\underline{\mathcal{W}}^k$ given by Eq. (3.63) and solved as explained in Section 3.2.1:

$$\Delta\underline{\mathcal{W}}^{k+1} = \Delta\underline{\mathcal{W}}^k - \left[\underline{\underline{\mathcal{J}}}\left(\Delta\underline{\mathcal{W}}^k\right)\right]^{-1} \underline{\mathcal{R}}\left(\Delta\underline{\mathcal{W}}^k\right) \tag{3.63}$$

The iterations are computed until the convergence criterion written as Eq. (3.64) is achieved. ϵ_{NR} is the user-defined precision for the convergence of the Newton-Raphson method, and $\|x\|$ denotes the Euclidian norm.

$$\left\|\underline{\mathcal{R}}\left(\Delta\underline{\mathcal{W}}^k\right)\right\| < \epsilon_{NR} \tag{3.64}$$

To compute the successive iterations $\Delta\underline{\mathcal{W}}^k$, the expression of the Jacobian matrix of the system must be analytically derived from Eqs. (3.56) to (3.60).

3.2.3.3 Jacobian matrix

The Jacobian matrix of $\underline{\mathcal{R}}$ is a square matrix of dimension 13+6*n_{AF}:

$$\underline{\underline{J}} = \begin{bmatrix} \frac{\partial \underline{\mathcal{R}}_{\underline{\varepsilon}^e}}{\partial \Delta \underline{\varepsilon}^e} & \frac{\partial \underline{\mathcal{R}}_{\underline{\varepsilon}^e}}{\partial \Delta r} & \frac{\partial \underline{\mathcal{R}}_{\underline{\varepsilon}^e}}{\partial \Delta \underline{X}_j} & \frac{\partial \underline{\mathcal{R}}_{\underline{\varepsilon}^e}}{\partial \Delta \underline{\sigma}} \\ \frac{\partial \mathcal{R}_r}{\partial \Delta \underline{\varepsilon}^e} & \frac{\partial \mathcal{R}_r}{\partial \Delta r} & \frac{\partial \mathcal{R}_r}{\partial \Delta \underline{X}_j} & \frac{\partial \mathcal{R}_r}{\partial \Delta \underline{\sigma}} \\ \frac{\partial \underline{\mathcal{R}}_{\underline{X}_i}}{\partial \Delta \underline{\varepsilon}^e} & \frac{\partial \underline{\mathcal{R}}_{\underline{X}_i}}{\partial \Delta r} & \frac{\partial \underline{\mathcal{R}}_{\underline{X}_i}}{\partial \Delta \underline{X}_j} & \frac{\partial \underline{\mathcal{R}}_{\underline{X}_i}}{\partial \Delta \underline{\sigma}} \\ \frac{\partial \underline{\mathcal{R}}_{\underline{\sigma}}}{\partial \Delta \underline{\varepsilon}^e} & \frac{\partial \underline{\mathcal{R}}_{\underline{\sigma}}}{\partial \Delta r} & \frac{\partial \underline{\mathcal{R}}_{\underline{\sigma}}}{\partial \Delta \underline{X}_j} & \frac{\partial \underline{\mathcal{R}}_{\underline{\sigma}}}{\partial \Delta \underline{\sigma}} \end{bmatrix} \tag{3.65}$$

Using the Voigt notation, the derivative of a 6-by-1 vector such as $\underline{\mathcal{R}}_{\underline{\varepsilon}^e}$ (which is a 3-by-3 matrix in tensorial notation) with respect to a 6-by-1 vector such as $\Delta\underline{\varepsilon}^e$ (also a 3-by-3 matrix in tensorial notation) is a 6-by-6 matrix:

$$\frac{\partial \underline{\mathcal{R}}_{\underline{\varepsilon}^e}}{\partial \Delta \underline{\varepsilon}^e} = \begin{bmatrix} \frac{\partial \left(\mathcal{R}_{\underline{\varepsilon}^e}\right)_1}{\partial \Delta \varepsilon_1^e} & \cdots & \frac{\partial \left(\mathcal{R}_{\underline{\varepsilon}^e}\right)_1}{\partial \Delta \varepsilon_6^e} \\ \vdots & \ddots & \vdots \\ \frac{\partial \left(\mathcal{R}_{\underline{\varepsilon}^e}\right)_6}{\partial \Delta \varepsilon_1^e} & \cdots & \frac{\partial \left(\mathcal{R}_{\underline{\varepsilon}^e}\right)_6}{\partial \Delta \varepsilon_6^e} \end{bmatrix} = \begin{bmatrix} 1 & & & & & \\ & 1 & & & & \\ & & 1 & & & \\ & & & 1 & & \\ & & & & 1 & \\ & & & & & 1 \end{bmatrix} \tag{3.66}$$

The different components of the Jacobian matrix are given in Appendix 3.

3.2.3.4 Consistent tangent modulus

The consistent tangent modulus $\underline{\underline{C}}$, necessary for solving the global equilibrium in a finite-element model, is defined by Eq. (3.67) and can be derived from the Jacobian.

$$\underline{\underline{C}} = \frac{d\underline{\sigma}}{d\underline{\varepsilon}} \tag{3.67}$$

As proposed by Lemaitre and Desmorat [8], the local residual $\underline{\mathcal{R}}$ can be split into two parts for the calculation of the tangent matrix: $\underline{\mathcal{R}}_i$, the contribution from the internal variables; and $\underline{\mathcal{R}}_e$, the contribution from the external loading:

$$\underline{\mathcal{R}} = \underline{\mathcal{R}}_i - \underline{\mathcal{R}}_e \text{ with } \underline{\mathcal{R}}_e = \begin{Bmatrix} \Delta\underline{\varepsilon} \\ 0 \\ \vdots \\ 0 \end{Bmatrix} \tag{3.68}$$

By performing a small perturbation on Eq. (3.68) after convergence, this gives:

$$\delta\underline{\mathcal{R}} = \delta\underline{\mathcal{R}}_i - \delta\underline{\mathcal{R}}_e = \underline{0} \Leftrightarrow \delta\underline{\mathcal{R}}_i = \delta\underline{\mathcal{R}}_e \tag{3.69}$$

By definition of the Jacobian matrix, the following relation can be written as Eq. (3.70) (brackets have been added to make it more understandable):

$$\{\delta\underline{\mathcal{R}}_i\} = \left[\underline{\underline{\mathcal{J}}}\right]\{\delta\Delta\underline{\mathcal{W}}\} \tag{3.70}$$

Therefore, the relation between $\delta\Delta\underline{\sigma}$ and $\delta\Delta\underline{\varepsilon}$ can be found:

$$\begin{Bmatrix} \delta\Delta\underline{\varepsilon}^e \\ \delta\Delta r \\ \delta\Delta\underline{X}_i \\ \delta\Delta\underline{\sigma} \end{Bmatrix} = \left[\underline{\underline{\mathcal{J}}}\right]^{-1} \begin{Bmatrix} \delta\Delta\underline{\varepsilon} \\ 0 \\ 0 \\ 0 \end{Bmatrix} \tag{3.71}$$

Finally, the consistent tangent modulus can be approximated as:

$$\underline{\underline{C}} \approx \frac{\delta\Delta\underline{\sigma}}{\delta\Delta\underline{\varepsilon}} = \left[\underline{\underline{\mathcal{J}}}\right]^{-1}_{\{\underline{\sigma},\underline{\varepsilon}^e\}} \tag{3.72}$$

$\left[\underline{\underline{\mathcal{J}}}\right]^{-1}_{\{\underline{\sigma},\underline{\varepsilon}^e\}}$ corresponds to the part of the inverse of the Jacobian situated from line $8 + 6n_{AF}$ to line $13 + 6n_{AF}$ and columns 1 to 6.

3.3 IMPROVEMENT OF THE ROBUSTNESS OF THE MODEL

As established in the previous sections, the coupled model with microdefects closure consists of a large number of nonlinear equations. To solve this type of system of equations, the Newton method is most commonly used [22]. However, this method is not always successful. This proved to be the case for the coupled model with microdefects closure, in which there is no analytical expression of the Jacobian matrix and therefore an approximation is used (see Appendix 3). When the Newton method cannot reach a solution in the material law for an element, the time increment is reduced for the finite-element computation. If this occurs frequently, the total number of time steps to complete the calculation is significantly increased, and therefore the computation time as well. Thus, finding a method that is more robust to solve the nonlinear system of equations of the coupled model is of critical importance to have reasonable computation times.

To find a more robust algorithm, the performances of 14 Newton-like methods were studied and compared with the classical Newton algorithm. More precisely, the robustness and efficiency of each method were evaluated on 10 systems of equations taken from the literature. For each algorithm, the effect of numerical damping was also studied. Figure 3.9 shows the number of iterations and CPU time obtained with the 15 algorithms used on the 10 systems of equations. The points at $N_{iter} = 250$ correspond to a failure of the method to converge within the required precision and maximum number of iterations. The size of the points corresponds to the maximum value of the condition

number of the Jacobian, which can be understood as a measure of how difficult the system is to solve. It can be deduced from Figure 3.9 that the classic Newton algorithm is generally the best regarding of computational time.

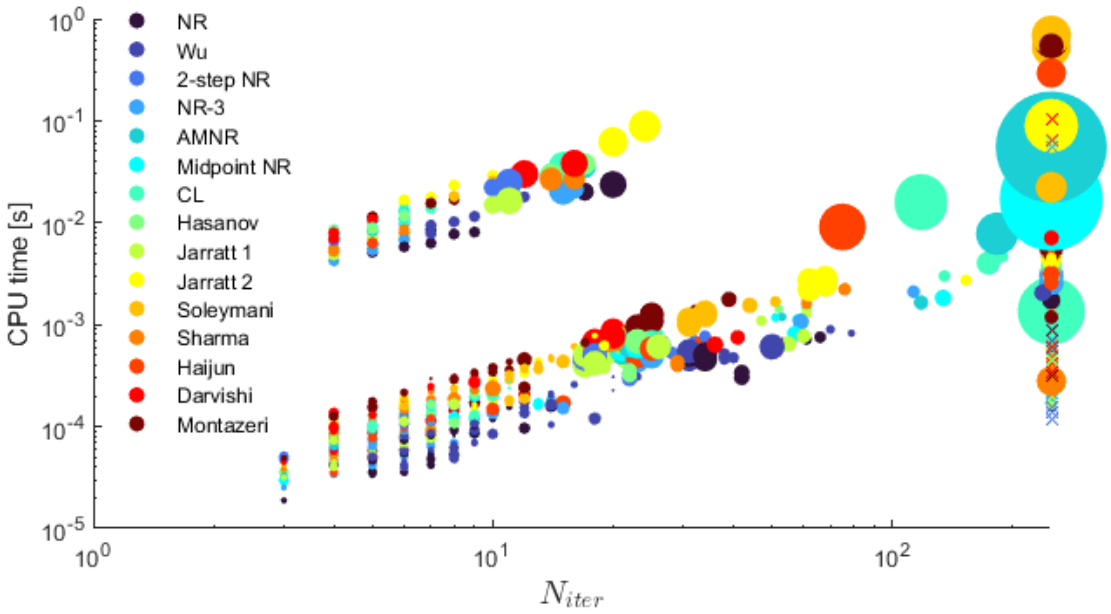

Figure 3.9 – CPU time vs. number of iterations for solving the 10 systems of equations, using 9 different starting points for each system.

The algorithms with and without damping were then tested on the material law with coupled damage. The conclusion of the study was that in general, the Newton method is the fastest method. For robustness in the material law, the best option turned out to be the use of numerical damping on the Newton algorithm.

An article was published in the journal Finite Elements in Analysis and Design in 2022 about this study [23]. The preprint version of this article is included in the thesis as Appendix 4.

3.4 VALIDATION OF THE DAMAGE MODEL

The parameters of the damage model were identified based on fatigue tests and creep tests. To verify that the model is valid for the application to the receiver tubes, it is necessary to check the results the model gives on combined creep-fatigue tests. Indeed, the receiver tubes are subjected to thermo-mechanical cyclic loadings with hold times at high temperature, i.e., anisothermal creep-fatigue loadings.

Due to a lack of comparative data on the influence of tensile hold times versus compressive hold times, the effect of microdefects closure was not considered here (i.e., parameter h is set to 1).

The results given by the model are first compared to the isothermal creep-fatigue results of the tests detailed in Chapter 1. Figure 3.10 shows the number of cycles to rupture obtained with the model and the experimental number of cycles to rupture of isothermal creep-fatigue tests at 800°C for different hold times in compression with a strain amplitude of 0.25%. The experimental value corresponding to a 0s hold time (i.e., a fatigue test) was extrapolated from the fatigue data at 800°C as it was not tested experimentally. The hold times are expressed as multiples of the base hold time t_1 for confidentiality purposes. The base hold time t_1 is in the order of a few minutes. It can be observed that the lifetime predicted by the model are in good agreement with the experimental results, except for the test with $5t_1$ hold time which is much smaller than the experimental value. When looking at the results from the model, it seems that the number of cycles to rupture converges towards an asymptotic value for increasing hold times. This can be explained by the phenomenon of relaxation: during the hold time, the stress relaxes towards smaller absolute values, at which creep damage becomes smaller. The longer the time hold, the more the stress relaxes, and the less significant the additional damage becomes. For instance, for the test with $30t_1$ hold times, the stress relaxes below 100 MPa in absolute value after $5t_1$. The creep lifetime at 100 MPa is around 1200 h, making the creep damage increment small for a hold time less than a few hours.

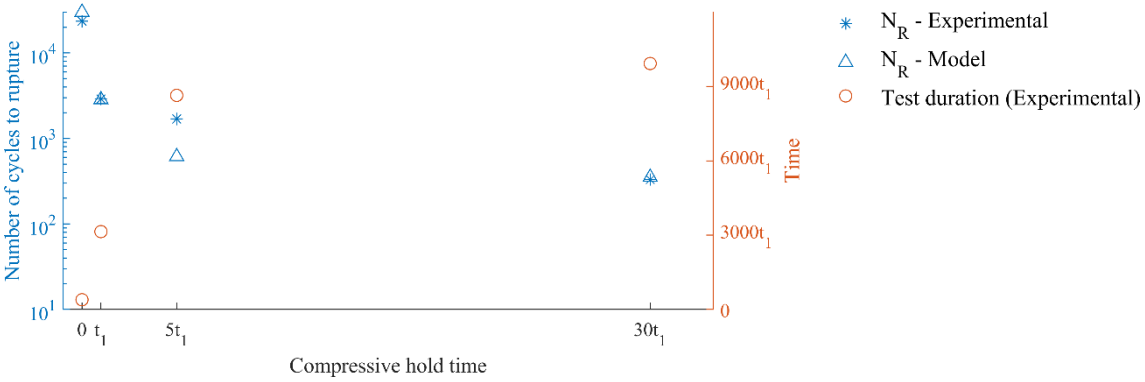

Figure 3.10 – Number of cycles to rupture (left axis) and duration (right axis) of the creep-fatigue tests at 800°C with $\Delta\varepsilon = \pm 0.25\%$ as a function of the compressive hold time

However, this damage behaviour does not seem to be completely confirmed experimentally. Indeed, in Figure 3.10, it is clear that the number of cycles to rupture diminishes continuously with increasing hold times, contrarily to the numerical results which seem to tend to an asymptote. When looking at the duration of the tests, it can be observed that the $5t_1$ and the $30t_1$ tests last about the same amount of time.

The anisothermal test performed between 300°C and 800°C with hold times of $5t_1$ in compression (at 800°C) and in tension (at 300°C) was also modelled. The obtained numerical lifetime is $N_R = 291$ cycles, which is much lower than the experimental result

of 603 cycles. However, this result is consistent with the isothermal results, since the model also gave an underestimated lifetime for the $5t_1$ isothermal test.

As observed in the metallographic analysis (see Chapter 1, Section 1.3.2), the addition of compressive hold times at high temperature does not change the cracking mode, which tends to indicate that creep does not play a significant role in the decrease of lifetime with compressive hold times. Instead, the decrease in number of cycles to rupture could be explained by thermal ageing, which is known to decrease the fatigue lifetime of alloy 230, as explained in Section 1.3.2.3 of Chapter 1. From a modelling point of view, it would therefore be more accurate to activate the microdefects closure effect (no creep damage in compression) and to change the fatigue damage parameters depending on the temperature history (thermal ageing). Unfortunately, the metallurgical analysis and the creep-fatigue tests with different hold times were done in the last year of the project, which did not leave time to develop a new model.

A damage model that includes thermal ageing, for instance by expressing the fatigue damage parameters as a function of the time spent at high temperature in the loading history, would probably give better results on the creep-fatigue tests with compressive hold times and would be an interesting perspective for future improvements of the existing model. A damage model with thermal ageing would also require extensive experimental research to accurately quantify the effects of different hold times in compression and tension.

4 CONCLUSION

In this chapter, a Lemaitre-type damage model was developed for the modelling of creep and fatigue damage of Haynes 230 under thermo-mechanical loading. This model is based on two damage variables – one for fatigue and one for creep – that represent the volume fraction of voids in the material due to fatigue and creep, respectively. The evolution of fatigue damage is based on the Lemaitre damage formulation and depends on the rate of the cumulative plastic strain. The creep damage, on the other hand, is based on the equation of Kachanov and depends only on the stress level and temperature. The parameters related to fatigue and creep damage were identified using fatigue tests and creep tests, respectively.

The model can also take into account the effect of microdefects closure that takes place under compressive stress through the decomposition of the stress tensor into a positive part (tensile) and a negative part (compressive).

The effect of damage can be coupled with the material behaviour by using the concept of effective stress. The model was implemented in the Lagamine finite-element code and

coupled with the behaviour law presented in Chapter 2. A non-coupled version was also implemented.

The model performs well for fatigue tests and creep tests, however, it does not give optimal results for combined creep and fatigue. In particular, the model does not simulate properly the influence of thermal ageing on the fatigue lifetime. Further improvements to the model could be developed by including the modelling of thermal ageing.

5 REFERENCES

[1] M. A. Miner, "Cumulative Damage in Fatigue," J. Appl. Mech., vol. 12, no. 3, pp. A159–A164, Sep. 1945, doi: 10.1115/1.4009458.

[2] E. L. Robinson, "Effect of Temperature Variation on the Long-Time Rupture Strength of Steels," Trans. ASME, vol. 74, pp. 777–780, 1952.

[3] X. Chen et al., "Experimental and modeling results of creep-fatigue life of Inconel 617 and Haynes 230 at 850 °c," J. Nucl. Mater., vol. 432, no. 1–3, pp. 94–101, 2013, doi: 10.1016/j.jnucmat.2012.08.040.

[4] S. S. Manson, G. R. Halford, and M. H. Hirschberg, "Creep-fatigue analysis by strain-range partitioning," 1971.

[5] X. Wu, "Life Prediction of Gas Turbine Materials," Gas Turbines, 2010, doi: 10.5772/10213.

[6] L. M. Kachanov, "Rupture time under creep conditions," Int. J. Fract., vol. 97, pp. 11–18, 1999, doi: 10.1023/A:1018671022008.

[7] Y. N. Rabotnov, "A mechanism of the long term fracture," AN SSSR. 1959.

[8] J. Lemaitre and R. Desmorat, Engineering Damage Mechanics. Berlin/Heidelberg: Springer-Verlag, 2005.

[9] P. Ladeveze and J. Lemaitre, "Damage effective stress in quasi-unilateral conditions," 1984.

[10] J. Lemaitre and J. P. Sermage, "One damage law for different mechanisms," Comput. Mech., vol. 20, no. 1–2, pp. 84–88, 1997, doi: 10.1007/s004660050221.

[11] J. Lemaitre, J. Chaboche, A. Benallal, and R. Desmorat, Mécanique des Matériaux Solides, Dunod. Paris, 2009.

[12] S. Otin, "Lois d 'endommagement incrémentales isotrope/ anisotropes pour applications thermomécaniques complexes," ENS Cachan, 2008.

[13] R. Ahmed, "Constitutive Modeling for Very High Temperature Thermo- Mechanical Fatigue Responses," North Carolina State University, 2013.

[14] X. Chen, Z. Yang, M. A. Sokolov, D. L. Erdman, K. Mo, and J. F. Stubbins, "Low cycle fatigue and creep-fatigue behavior of Ni-based alloy 230 at 850°C," Mater. Sci. Eng. A, vol. 563, pp. 152–162, 2013, doi: 10.1016/j.msea.2012.11.063.

[15] G. J. Pataky, H. Sehitoglu, and H. J. Maier, "Creep deformation and mechanisms in Haynes 230 at 800°C and 900°C," J. Nucl. Mater., vol. 443, no. 1–3, pp. 484–490, 2013, doi: 10.1016/j.jnucmat.2013.08.009.

[16] G. J. Pataky, H. Sehitoglu, and H. J. Maier, "High temperature fatigue crack growth of Haynes 230," Mater. Charact., vol. 75, pp. 69–78, 2013, doi: 10.1016/j.matchar.2012.09.012.

[17] Y. L. Lu et al., "Hold time effects on low cycle fatigue behavior of HAYNES 230® superalloy at high temperatures," Mater. Sci. Eng. A, vol. 409, no. 1–2, pp. 282–291, 2005, doi:

10.1016/j.msea.2005.05.120.

[18] S. Chatterjee and A. K. Roy, “Mechanism of creep deformation of Alloy 230 based on microstructural analyses,” Mater. Sci. Eng. A, vol. 527, no. 29–30, pp. 7893–7900, 2010, doi: 10.1016/j.msea.2010.08.069.

[19] A. K. Roy, S. Chatterjee, M. H. Hasan, J. Pal, and L. Ma, “Crack-growth behavior of alloy 230 under creep-fatigue conditions,” Mater. Sci. Eng. A, vol. 527, no. 18–19, pp. 4830–4836, 2010, doi: 10.1016/j.msea.2010.04.005.

[20] Haynes International, “HAYNES® 230® alloy.” 2017.

[21] J. Keiser, “Corrosion Fatigue Studies of High Nickel Tubular samples Containing molten salt,” 2013.

[22] M. T. Heath, Scientific Computing. Philadelphia, PA: Society for Industrial and Applied Mathematics, 2018.

[23] H. Morch, S. Yuan, L. Duchêne, R. Harzallah, and A. M. Habraken, “A review of higher order Newton type methods and the effect of numerical damping for the solution of an advanced coupled Lemaitre damage model,” Finite Elem. Anal. Des., vol. 209, no. June, p. 103801, 2022, doi: 10.1016/j.finel.2022.103801.

Chapter 4: Corrosion modelling

TABLE OF CONTENTS

1 SCOPE

Nickel alloys are known for their good resistance to corrosion. However, the use of highly corrosive molten salts at high temperature in solar receivers could have a significant impact on the long-term integrity of the tubes. Moreover, the potential material loss that can result from corrosion can modify the geometry of the tubes and influence the thermo-mechanical behaviour. Therefore, it is essential to include corrosion in the modelling of the receiver tubes for an accurate lifetime prediction.

1.1 CORROSION IN NICKEL ALLOYS

Corrosion is a complex phenomenon that can take different forms:

- Uniform corrosion, where oxides are formed as a uniform layer on the surface of the material.
- Localized corrosion, which can lead to pitting or the formation of crevices. This type of corrosion is often due to initial defaults in the surface.
- Stress corrosion cracking, where corrosion and mechanical loading interact.

In the literature, some information can be found on the corrosion behaviour of nickel alloys, as summarised hereafter.

1.1.1 Air oxidation

Although the solar receivers are not directly concerned by oxidation in air (a coating is applied on the external surface of the tubes), it can be interesting to study it as the chemical reactions involved are globally the same. Both in the case of air oxidation and corrosion by solar salts, oxygen diffuses to form oxides with metallic elements in the material. Moreover, experimental tests involving oxidation in air are easier to perform than experiments involving corrosion in salts. The literature is therefore more extensive on the combination between oxidation and mechanical behaviour.

Calvarin-Amiri et al. [1] studied the effect of a tensile creep stress on the formation of oxides in a Ni-Cr20 alloy at 600°C and 900°C. They observed that the addition of the stress does not affect the type of oxides being formed. However, the rate of corrosion is increased. They determined that above a critical strain, the diffusion of O_2 is increased, leading to thicker layers of corroded material.

Fournier et al. [2] studied the influence of a cyclic loading with either compressive or tensile hold times at 550°C on a 9Cr-Mo steel. They observed that the lifetime was shorter with compressive hold times than with tensile hold times, which can seem counter-intuitive at first since tensile stresses tend to generate higher amounts of damage in the material (see Chapter 3). The shorter lifetime observed with compressive hold times could

be due to the repeated cracking of the oxide layer, as explained by Aoto et al. [3]. First, the oxide layer forms during the compressive hold time. While the original material is under a compressive strain, the newly formed oxide is at a near zero-strain state. When the loading is reversed, the oxide is subjected to a larger tensile strain than the base material, considering their respective initial states. As a result, the oxide is more likely to crack and allow oxidation to progress further.

Several studies on stainless steels or nickel-base alloys report shorter lifetimes with compressive hold times [2], [4], or lifetimes equivalent to cases with tensile hold times [5].

1.1.2 Corrosion by solar salts

Solar salt, which is in use for the 2nd generation of concentrated solar power (CSP) plants, is composed of 60% $NaNO_3$ and 40% KNO_3. The effect of exposure to this salt has been tested on various stainless steels and nickel-based alloys at different temperatures. Most of the available results are from static corrosion tests: the material is immersed in the salt at high temperature for a long duration (a few hundred to a few thousand hours). Afterwards, the oxide is removed, and the weight loss is measured. Alternatively, microscopic analyses can be done on the oxide layer (before removal) to determine its composition.

Generally, the corrosion of nickel alloys by solar salts is characterized by:

- The formation of a protective NiO layer on the surface of the material [6], [7];
- The outwards migration of Cr and its dissolution in the salt [6], [8].

For alloy 230, a layer of chromium oxide Cr_2O_3 can be observed under the protective nickel oxide layer, as shown in Figure 4.1. The dissolution of tungsten (W) in the salt is also observed [7]. At 600°C after 3000 h of exposure to solar salt, the corrosion rate of alloy 230 was estimated to be around 24 µm/year. This corrosion rate is estimated from the descaled mass loss and takes into account both the reduction of material from dissolution in the salt and the amount of material turned into oxide. The actual mass loss before removing the oxide is in fact around 1.1 mg/cm², corresponding to a corrosion rate of 3.26 µm/year. Another study [9] found that the actual weight loss (not counting the oxide layer) at 600°C after 3000h was about 1.05 mg/cm², which corresponds to a corrosion rate of 3.12 µm/year, which is consistent with the results from the aforementioned study.

Sandia laboratories also performed dynamic corrosion tests on several materials, among which alloy 230 [10]. The test consists in pumping molten salt at 600°C from a tank to make it flow through a heated section of a pipe made of alloy 230, representing a solar receiver tube. The temperature of the inner wall of the pipe is maintained at 670°C using

inductive heating. After passing through this pipe section, the salt flows to another test section where coupons of materials are placed. These coupons remain at the same temperature as the salt (around 600°C). Finally, the salt is sent back into the initial tank where it can be pumped and sent again through the test piping. The resulting corrosion rates were 8 to 20 times higher than those obtained from static tests. Specifically, for the coupons of alloy 230, the corrosion rate was estimated at 403 ± 71 µm/year. The oxides were found to be the same as in static tests, but local pitting was observed on the surface. However, the results were different for the pipe. In particular, the analysis of the pipe revealed a depletion of Ni in the corrosion layer and a higher concentration of Cr. A possible explanation is that with the increased corrosion rate due to both high temperature (670°C) and flowing medium (salt), the rapid dissolution of Cr and W leads to a weaker oxidation layer. This type of oxide layer would result in a progressive uniform removal of pipe material.

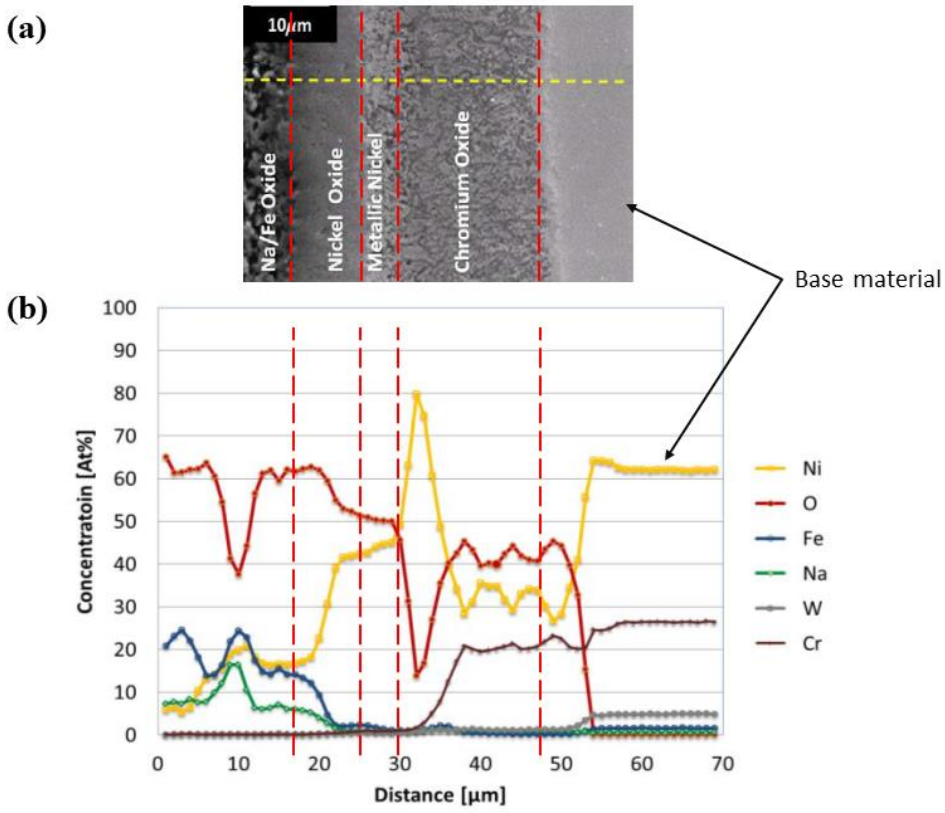

Figure 4.1 – Corrosion of alloy 230 by solar salt at 680°C after 1025 hours
(a) Scanning Electron Microscopy; (b) Wavelength Dispersive Spectroscopy Line scan [7]

1.1.3 Corrosion by molten chloride salts

Chloride salts are particularly interesting for the 3rd generation of Concentrated Solar Power plants thanks to their good stability at high temperatures. Solar salts used in 2nd generation plants start degrading at temperatures above 565°C, whereas chloride salts

remain stable at up to 800°C. The major problem with these salts is the corrosion caused by impurities such as H_2O, O_2, or OH^-.

A study from the Sandia Laboratories [11] concluded that the presence of cobalt or refractory metals such as tungsten, molybdenum, or tantalum could increase the corrosion resistance because these elements form stable spinel that block the diffusion of chromium. Alloy 230 contains significant amounts of tungsten, cobalt, and molybdenum, making it a good candidate for the 3rd generation solar receivers.

However, a study conducted on several Ni-based alloys in a ternary NaCl-KCl-$MgCl_2$ salt at 700°C showed that alloy 230 corroded more than other alloys containing higher contents of molybdenum [12]. The corrosion phenomenon for alloy 230 included pitting and significant intergranular corrosion, along with a depletion of chromium in the material.

Other studies with $MgCl_2$-KCl showed that corrosion rates are multiplied by a factor 4 to 5 with fluid flow [13], [14]. The corrosion mechanism was identified to be caused by selective oxidation of chromium occurring mainly at grain boundaries. However, with the addition of Mg as an inhibitor in the salt, the corrosion rate was close to 0 for alloy 230 [13]. For chloride salts, the best solution may be to find chemical inhibitors or to apply a protective coating on the inside of the tubes.

1.2 MODEL REQUIREMENTS

To model the behaviour of the tubes from the solar receiver, a Chaboche-type model was implemented (see Chapter 2). Along with the behaviour model, a mechanical damage model was implemented to predict the lifetime of the tubes (Chapter 3). These two models are coupled, so that mechanical damage influences the behaviour of the material and vice-versa.

Ideally, the modelling of corrosion should be integrated with the thermo-mechanical and damage model. Indeed, it is expected that potential material loss occurring from corrosion could affect the overall thermo-mechanical behaviour of the tubes. The design chosen by John Cockerill with a safety margin allows for a reduction of the thickness of about one third during the lifetime of the tube. Such a reduction could have a significant impact on the stress distribution in the tube.

In addition, the model must be relatively generic to be adaptable to different combinations of materials and corrosive environments (solar salt/chloride salts), as well as efficient in terms of computation times, even for a large structure such as the tubes of the receivers, which are about 20 meters long with a diameter of a few centimetres.

On the other hand, corrosion is a complex phenomenon, particularly in the case of thermal cycling. The following aspects remain unknown due to lack of experimental results:

- The effects of the flowing salt: erosion, renewal of corrosive elements.
- The effect of temperature variation; although it is evident that this has a deleterious impact compared to static tests, it is difficult to quantify the impact of the temperature variation.
- The interaction between creep and corrosion or fatigue and corrosion.

Strong simplifying hypotheses must be made for the modelling of corrosion.

2 CORROSION MODELLING

Various models for corrosion can be found in the literature. Three main types of models can be distinguished:

- Crack-growth models, in which the propagation of cracks at the microstructural level is studied.
- Diffusion model, which aim at representing the progression of corrosion in a structure through the diffusion of corrosive elements.
- Models based on a corrosion damage variable, in which the effect of corrosion is represented by a damage variable similar to the one from Lemaitre damage model.

2.1 CRACK-GROWTH MODELS

Crack-growth models are among the most common for the simulation of corrosion. A crack-growth model can simply constitute of an equation to determine the moment of crack initiation and an equation describing the crack growth [15]. Much more complex models have also been developed, such as the model of Sedlak et al. [16] or the model of Bolotin and Shipkov [17], who developed a more comprehensive model of the crack which includes equations for the diffusion of corrosive elements within the crack, the computation of the stress at the crack tip, and the change of geometry of the crack depending on the loading.

Crack-growth models can also be implemented within a finite-element framework. Wenman et al. [18] proposed a 2D model to simulate the corrosion cracking in the section of a pipe. The pitting phenomenon is represented by the deactivation of elements. To take into account the initial defects on the material surface, each element on the surface is initially assigned a random number: if that number is above a certain value and the plastic strain in that element reaches a predefined threshold, the element is deactivated. This corresponds to the crack initiation, illustrated in Figure 4.2 (a). Once a crack is initiated, it can propagate to any neighbouring element (i.e., the neighbouring elements become

candidates for deactivation) if the equivalent stress in this element is above a predefined threshold.

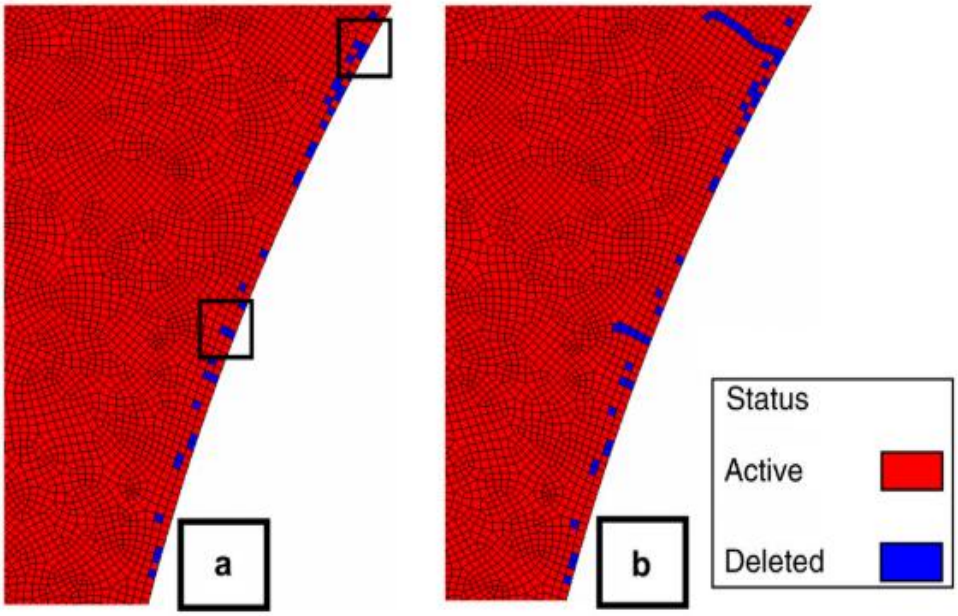

Figure 4.2 – Finite-element cracking model (a) Initiation of cracking by deactivation of elements in the two layers closest to the surface; (b) Crack propagation – Wenman et al. [18]

This model is compatible with the previously developed model; however, it requires extremely fine meshes, which would make it impossible to model a whole tube of the receiver. Moreover, the sudden deactivation of elements creates discontinuities which are likely to cause convergence problems in a finite element code.

2.2 DIFFUSION-BASED MODELS

Several models of corrosion are based on the diffusion of the corrosive chemical elements or of the elements in the material which are likely to form oxides or dissolve in the corrosive environment. Those diffusion models can be separated in two categories depending on the scale at which they are applied: microscopic models and macroscopic models.

Microscopic models can be of interest to get a better understanding of the corrosion phenomenon and its interaction with the mechanical behaviour. Zhao et al. [19] developed a model for the outwards diffusion of aluminium in nickel alloy RR1000 exposed to air oxidation. The diffusion model is coupled with a crystal plasticity model to consider the changes in behaviour depending on the Al concentration. A similar model was developed by Karabela et al. [20] for the diffusion of oxygen in the same alloy. In their models, the diffusion of oxygen is determined using a modified version of Fick's second law of diffusion, where C_O is the concentration of oxygen, t is the time, ∇ is the gradient operator, D_O the oxygen diffusivity, P the mean pressure, and M a pressure factor:

$$\frac{\partial C_O}{\partial t} = \nabla(D_O \nabla C_O - D_O C_O M \nabla P) \tag{4.1}$$

The second term on the right-hand side of Eq. (4.1) models the influence of mechanical loading on the diffusion process. This equation of diffusion was also coupled with a Chaboche-like model to model the crack-growth behaviour in nickel alloy RR1000 [21].

In the finite-element framework, the concentration of any diffusing element is defined as an additional degree of freedom, similarly to the temperature (the equation of diffusion is analogous to the heat equation). This approach requires the development of specific elements with additional degrees of freedom for the concentration of the diffusing chemical elements.

For a macroscopic approach, the same concept can be used with a mobile boundary defining the frontier between the base material and the corrosive environment [22], [23]. The velocity of the boundary is determined from the diffusion of the corroded chemical elements modelled using Fick's second law. This type of model is particularly well adapted for the simulation of gradual material loss due to corrosion. For instance, such models were developed for the corrosion of bioabsorbable metal stents [22], [23], using the Arbitrary Lagrangian-Eulerian (ALE) adaptive remeshing method within the Abaqus software. The ALE technique allows for large variations in the geometry even with an initially coarse mesh [24]. Figure 4.3 shows the evolution of the geometry of a bar of Mg-1Ca in a corrosive environment [23]. The thickness of the bar reduces significantly.

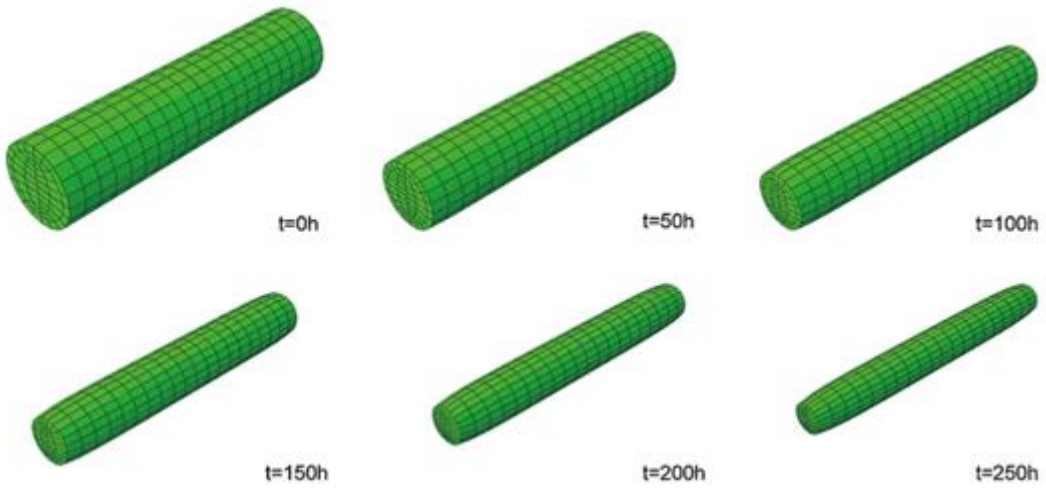

Figure 4.3 – Change of geometry due to corrosion modelled by a mobile boundary [23]

2.3 CORROSION DAMAGE VARIABLE

Corrosion can also be modelled using the concept of damage variable initially developed for mechanical damage (see Chapter 3). The advantage of this type of modelling is that it

is readily integrable in the existing model developed for the thermo-mechanical behaviour and damage of alloy 230. To take corrosion into account, a corrosion damage variable D_{corr} can be added to the existing mechanical damage variable:

$$D = D_{mech} + D_{corr} = D_f + D_c + D_{corr} \tag{4.2}$$

This concept of damage variable was used by Neu and Sehitoglu [25] in a linear summation damage model, where the damage variable corresponds to $D = N/N_R$, with N the current number of cycles and N_R the number of cycles to rupture (unlike the Lemaitre damage variable, which represents the proportion of voids in the material). The total damage is considered as the sum of 3 contributions: fatigue damage D_f, creep damage D_c, and oxidation damage D_{ox} (analogous to D_{corr} in Eq. (4.2)). The oxidation damage is based on the growth rate of the oxide layer. It is computed using a power function of time, to represent the repeated cracking of the oxide layer. A phase factor is also included in their formulation to consider the influence of the temperature/deformation phasing: when tensile strain is present at high temperature, creep is estimated to be the principal cause for damage; however, when compressive strain is maintained at high temperature, the oxide layer formed is more likely to rupture when the strain is reversed, as explained in section 1.1.1 of this chapter. The creep damage is also dependent on this phasing factor.

More recently, models based on the concept of damage variable as defined by Lemaitre [26] were developed for corrosion. Notably, da Costa-Mattos et al. [27] proposed to add a stress corrosion cracking variable D_{SC} defined by Eq. (4.3) to the classic unified damage model of Lemaitre. S and R are parameters dependent on the material and the corrosive environment, and D is the total damage. This equation is almost equivalent to the Kachanov model for creep damage (see Section 1.1.3 of Chapter 3).

$$\dot{D}_{SC} = \left(\frac{S\sigma}{1-D}\right)^R \tag{4.3}$$

Gastaldi et al. used this stress corrosion cracking damage [28] with an added uniform corrosion damage D_u for the simulation of the degradation of bioresorbable stents. The uniform corrosion is modelled by a simple linear corrosion law, where k_u is a parameter related to the corrosion kinetics, δ_u is a characteristic dimension of the uniform corrosion (such as the critical thickness), and L_e is a characteristic length of the finite element:

$$\dot{D}_u = \frac{\delta_u}{L_e} k_u \tag{4.4}$$

For a brick element, the characteristic length L_e is defined by Eq. (4.5), where V_e is the volume of the element:

$$L_e = \sqrt[3]{V_e} \tag{4.5}$$

Once the damage is above a critical value D_{crit}, the finite element is deactivated to represent the material loss due to corrosion.

Figure 4.4 shows the modelling of a bioabsorbable stent using the stress corrosion model, the uniform corrosion model, or both. In cases where uniform corrosion is taken into account, the stent is noticeably thinner due to the deactivation of finite elements that reached the damage threshold.

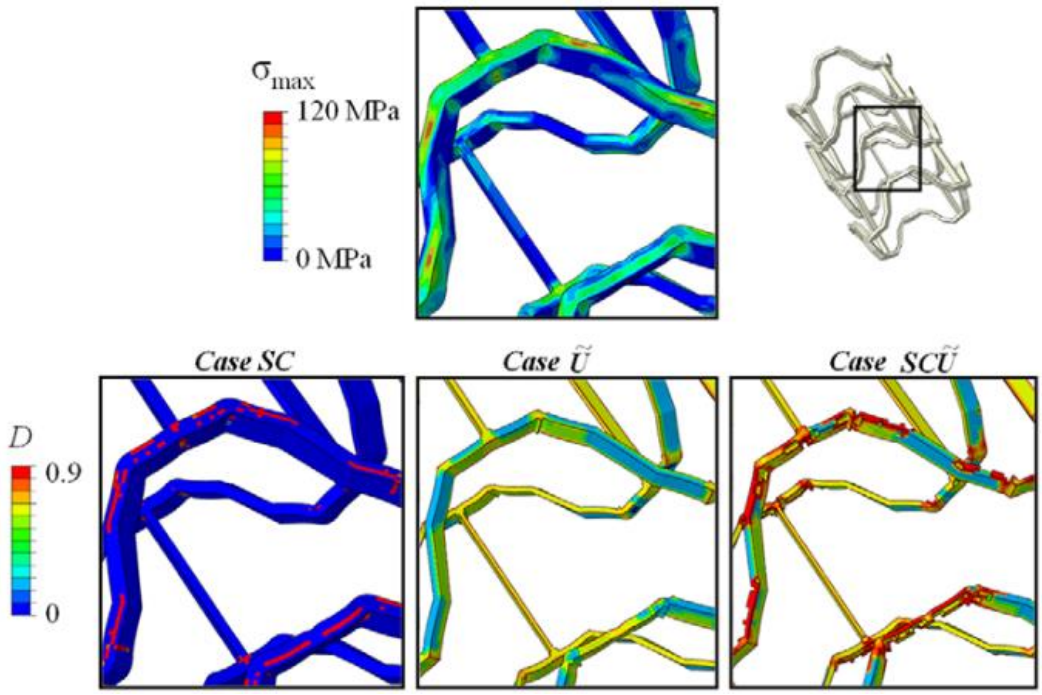

Figure 4.4 – Stress distribution and damage in a bioabsorbable stent – (SC) Stress corrosion model; (U) Uniform corrosion model; (SCU) Combined stress corrosion and uniform corrosion [28]

Galvin at al. [29] added two parameters to Eq. (4.4):

$$\dot{D}_u = \frac{\delta_u}{L_e} k_u \phi_e \kappa_e \tag{4.6}$$

Parameter ϕ_e is dependent on the plastic strain amplitude in the element and on the corrosion time. Parameter κ_e relates to the number of faces of the element exposed to corrosion: an element exposed to the corrosive environment on all its faces will corrode much faster than an element exposed on only one face.

Amerinatanzi et al. [30] added a factor λ_e in Eq. (4.4) to model the susceptibility to pitting corrosion of surface elements. A random value of this parameter is attributed to each element at the beginning of the simulation to represent the initial surface defects. This is similar to the Wenman model described in section 2.1.

3 CORROSION MODEL FOR THE RECEIVER TUBES

3.1 CONCEPT

Based on the models found in the literature and the requirements exposed in section 1.2, the chosen model is a model based on a corrosion damage variable. More specifically, uniform corrosion is modelled through a variable D_u which can be added to the mechanical damages D_f (fatigue) and D_c (creep) to form the total damage:

$$D = D_f + D_c + D_u \tag{4.7}$$

The stress corrosion damage model described in section 2.3 is not taken into account due to lack of experimental results: indeed, the equation for stress corrosion is similar to the equation of creep damage and it is difficult to distinguish these two phenomena from experimental results. Both creep and oxidation/corrosion occur at high temperature and over long periods of time. The measure of pure creep damage could only be done from creep tests performed in vacuum or in protective atmosphere to avoid oxidation from air.

The deactivation of elements is not used either in the model. Indeed, the deactivation of elements is only of interest if the corrosion is made to progress through the structure: once a surface element is deactivated, the code searches for neighbouring elements that have become exposed to the corrosive environment and activates corrosion damage in these elements. This approach requires complex developments in the finite element code and is not necessary for the application to the tubes. Indeed, the tubes are very thin (less than 2 mm thick for a diameter of around 5 cm), and the allowable material loss due to corrosion corresponds to one third of the thickness. Therefore, a mesh with three elements along the thickness, as shown in Figure 4.5, with corrosion damage only in the inner layer of the tube is sufficient to model corrosion in the tubes (N.B. due to the symmetry, only half of the tube needs to be modelled). When the total damage in the elements with corrosion reaches a value close to 1, this means a third of the thickness of the tube has been consumed, which can be considered as a failure criterion. Note: the critical damage allowed for other elements is $D_{crit} = 0.3$, but in the case of corrosion the critical damage can be set to a value close to 1 since destruction of the element is allowed.

Although the corroded elements are not deactivated, the coupling between damage and behaviour allows the simulation of loss of resistance through the use of the effective stress (see Section 1.2.1 of Chapter 3). Indeed, the increased damage in the corroded elements results in a loss of stiffness and, as a result, in a redistribution of the stresses towards the less damaged elements.

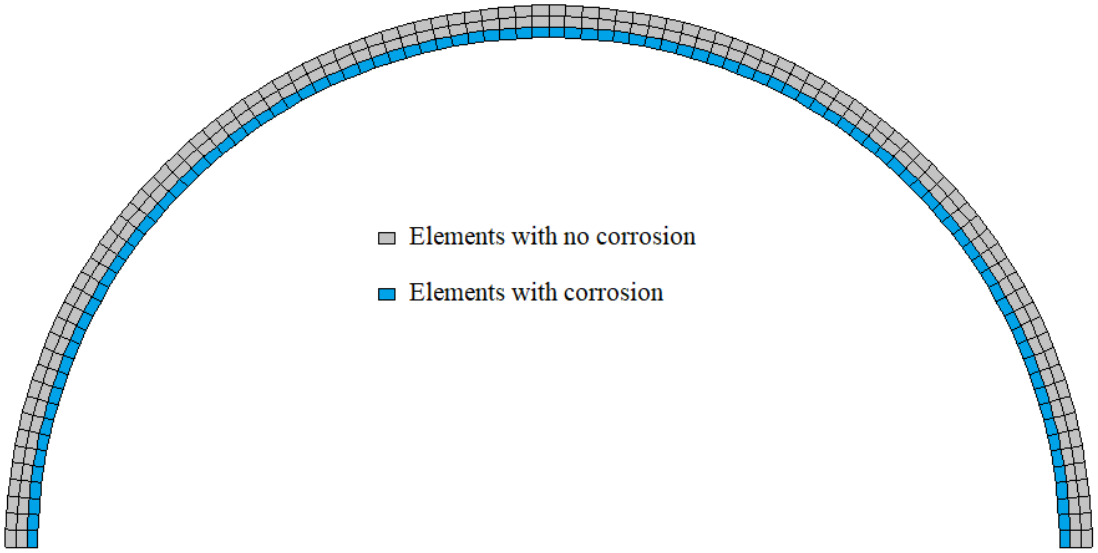

Figure 4.5 – Distinction between elements with corrosion damage and elements without corrosion damage in the mesh of the tube

3.2 EQUATIONS AND IMPLEMENTATION

The uniform corrosion is considered to be independent of the stress state. The numerical integration of uniform damage equation is therefore done independently of the rest of the computation. In the material law, the uniform corrosion damage is simply added to the other damages at the end of the time step, as written in Eq. (4.7).

Following the works presented in section 2.3, a simple linear damage law is implemented using Eq. (4.8), where K_u is a parameter related to the kinetics of corrosion, and L_e the characteristic length of the element:

$$\dot{D}_u = \frac{K_u}{L_e} \tag{4.8}$$

This equation is equivalent to Eq. (4.4) above, with parameters δ_u and k_u being assembled into a unique parameter K_u, which is the linear corrosion rate expressed as a corroded length per unit time, e.g., in µm/year. The uniform corrosion damage D_u can be understood as the proportion of the element that has been corroded.

Eq. (4.8) can easily be discretized using the finite difference method:

$$D_u^{n+1} = D_u^n + \frac{K_u}{L_e}\Delta t \tag{4.9}$$

By default, the characteristic length of the element L_e is defined as the cubic root of the volume of the element (Eq. (4.5)) for a 3D element, or as the square root of the area of the element in 2D. However, in the tubes, elements are only exposed to the corrosive environment on one side and corrosion progresses in the radial direction. Therefore, it makes more sense to consider L_e as the initial size of the element in the radial direction. In the code, L_e can be defined as a parameter or be computed automatically if no value is given by the user.

Linear corrosion works well with materials such as Mg alloys which degrade over time, however, for materials that form a protective oxide layer like alloy 230, corrosion usually follows a parabolic law [31]. Let h be the thickness of the oxide layer and K_p the parabolic rate of corrosion, the evolution of h with time follows Eq. (4.10):

$$\frac{dh}{dt} = \frac{K_p}{h} \tag{4.10}$$

Considering D_u as the proportion of element that is corroded gives Eq. (4.11):

$$D_u = \frac{h}{L_e} \tag{4.11}$$

From Eq. (4.10) and Eq. (4.11), the parabolic law of corrosion can be derived:

$$\frac{dD_u}{dt} = \frac{K_p}{L_e^2 D_u} \tag{4.12}$$

This equation can be integrated as Eq. (4.13):

$$D_u = \frac{1}{L_e}\sqrt{2K_p t} \tag{4.13}$$

The uniform corrosion damage D_u is proportional to the square root of time, meaning the rate of corrosion decreases with time. In the numerical model, Eq. (4.12) is discretized using an explicit Euler scheme:

$$D_u^{n+1} = \begin{cases} \frac{1}{L_e}\sqrt{2K_p\Delta t} & for\ n = 0 \\ D_u^n + \frac{K_p}{L_e^2 D_u^n}\Delta t & for\ n > 0 \end{cases} \tag{4.14}$$

3.3 PARAMETER IDENTIFICATION

The parameters for the corrosion of alloy 230 in solar salts can be identified based on data from the literature, mainly data from Sandia Laboratories [6], [7]. As mentioned in section 1.1.2, the studies give values of the mass loss with and without counting the oxide. The weight difference between the initial sample and the sample with oxide does not give a precise information on the volume or thickness of material that got depleted. Indeed, while some elements of the alloy are migrating outwards and being dissolved in the salt, oxygen is diffusing inwards to form oxides, which do not have the same density as the base material. For some materials, such as 347 stainless steel at 500°C, the weight after corrosion is actually higher than the weight before corrosion. Therefore, the oxidation rate parameters (K_u for linear rate and K_p for parabolic rate) are based on the thickness of the oxide and not on the actual weight loss. Figure 4.6 shows the descaled weight loss – that is, the difference of weight between the sample after the test and the sample after removal of the oxide – of samples of alloy 230 immersed in molten solar salt at 400°C, 500°C, and 600°C for different durations. The evolution of the weight loss indicates a parabolic rate of corrosion; therefore, the parabolic law is chosen for alloy 230 in molten solar salt.

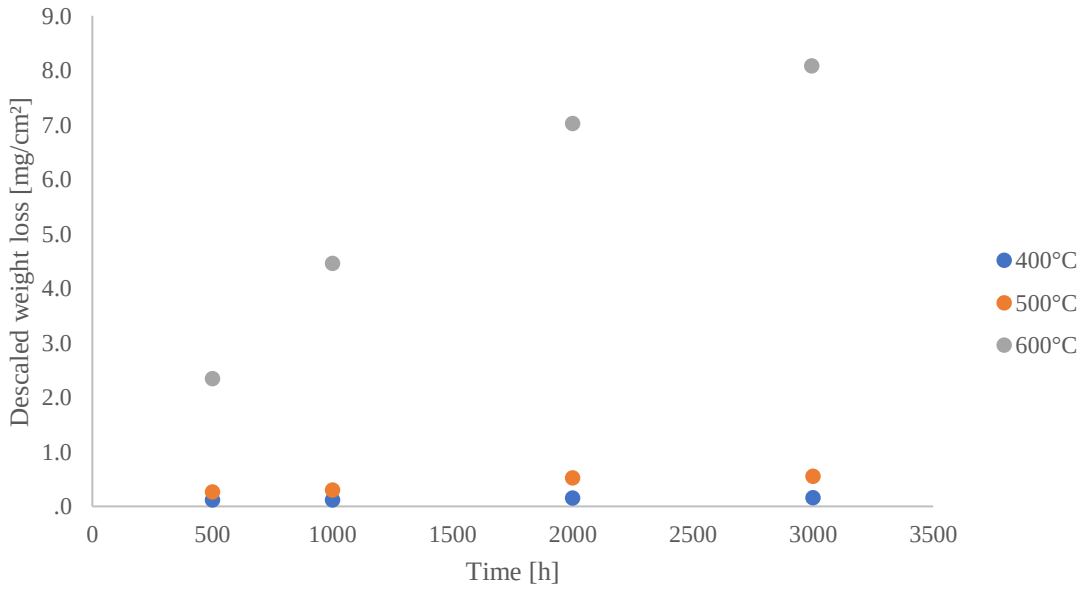

Figure 4.6 – Descaled weight loss of alloy 230 in solar salt at different temperatures [6], [7]

Let w_l the descaled weight loss. From this value, the oxide thickness h can be computed using Eq. (4.15), where ρ is the density of alloy 230:

$$h(t,T) = \frac{w_l(t,T)}{\rho} \tag{4.15}$$

Using Eq. (4.11) above, the corresponding corrosion damage can be calculated for a virtual element with an arbitrary characteristic length L_e. Note that L_e should be larger than the maximum value of h, otherwise D_u becomes larger than 1, which physically does not make sense. Combining Eq. (4.11) with Eq. (4.13), the following equation is obtained:

$$D_u = \frac{h}{L_e} = \frac{1}{L_e}\sqrt{2K_p t} \Longrightarrow h(t,T) = \sqrt{2K_p(T)t} \tag{4.16}$$

For each temperature, the value of $K_p(T)$ can be estimated as the slope of $h^2(t)/2$ by performing a linear regression. Figure 4.7 shows the evolution with time of the oxide layer thickness at different temperatures obtained with the model and from experimental data. The results obtained with the model – i.e., Eq. (4.16) – fit the experimental data well.

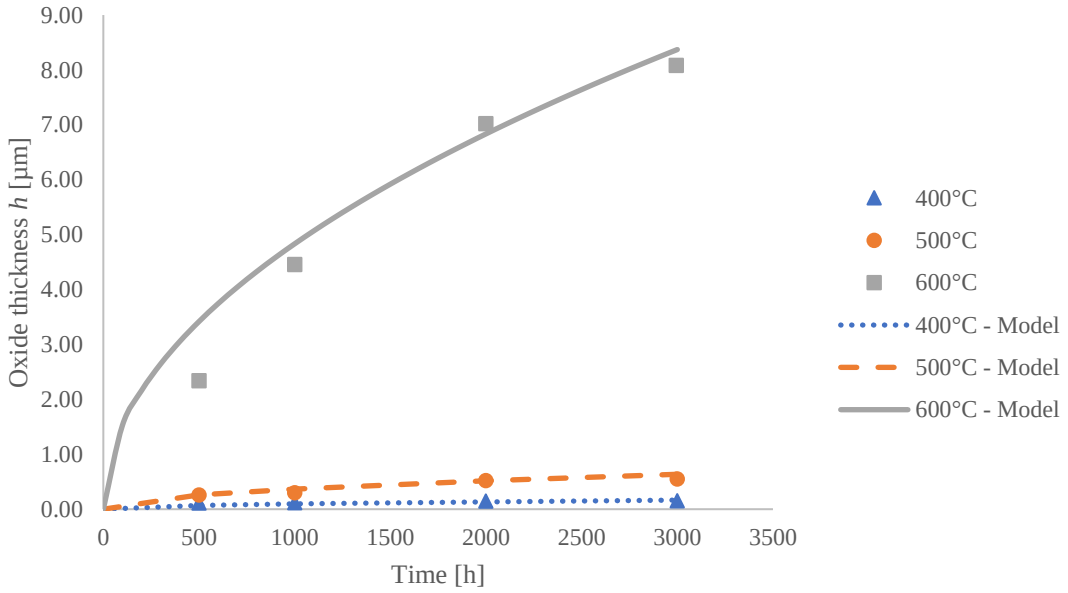

Figure 4.7 – Oxide thickness h at different temperatures; experimental data from [6], [7]

3.4 VERIFICATION OF THE MODEL

To verify the implemented model, a simple case study was designed. A beam, shown in Figure 4.8, is subjected to a uniformly distributed stress evolving from 0 to 20 MPa along the x direction. The nodes on the left side of the beam are fixed in the x direction, the nodes on the bottom side are fixed in the y direction, and the nodes on the back are fixed in the z direction to avoid rigid body motion as well as bending of the beam. The upper surface of the beam is exposed to corrosion and only the elements in blue in the figure have corrosion damage activated. The model is tested with the linear law and a fictitious value of K_u chosen to reach high values of D_u under a small time.

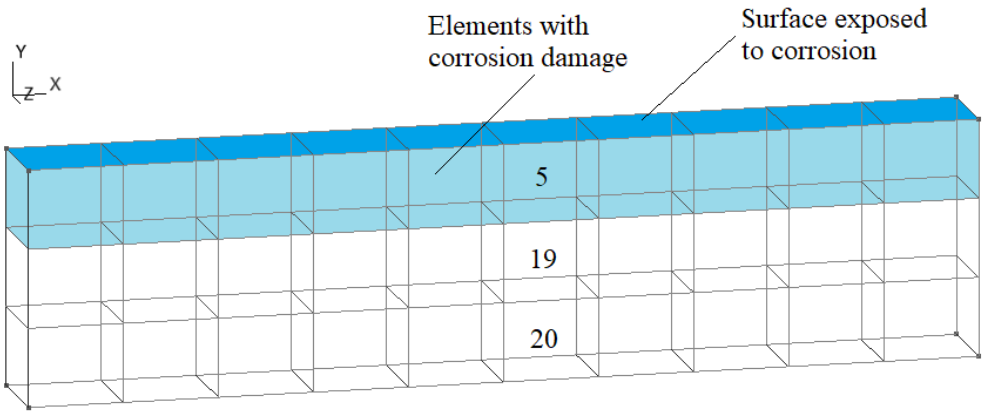

Figure 4.8 – Mesh of the beam with elements 5, 19, 20 indicated

The evolution of damage in elements 5, 19, and 20 is plotted in Figure 4.9 (a). Elements 19 and 20 are not exposed to corrosion, therefore, their corrosion damage remains equal to 0. In element 5 however, the damage evolves linearly up to a value of about 0.65. The stress-strain curves are plotted in Figure 4.9 (b). For elements 19 and 20, the curve is linear, since the material remains in the elastic domain, and the maximum stress is around 26 MPa. For element 5 however, the stress is much smaller and is not linear with the strain. Indeed, with the coupled damage model, the relation between the unidirectional stress σ^5 in element 5 and the elastic strain ε^e becomes:

$$\sigma^5 = (1 - D)E\varepsilon^e \tag{4.17}$$

It is clear that the model takes into account the reduction of the stress due to the corrosion damage. As a result, the imposed load is redistributed to the other elements. Instead of ending the test with a stress of 20 MPa in each element (as would be the case in the absence of corrosion), the stress in the elements of the surface is smaller and the elements underneath compensate with a larger stress. Let σ^{top} be the stress in the top elements of the beam, σ^{bot} the stress in the bottom elements (elements 19 and 20 in Figure 4.9), and S^{el} the surface of the elements perpendicularly to the applied load. The total can be rewritten as:

$$3S^{el}\sigma = \sigma^{top}S^{el} + 2\sigma^{bot}S^{el} \tag{4.18}$$

Considering a total imposed load σ = 20 MPa and a corrosion damage $D = 0.65$, the values of σ^{top} and σ^{bot} can be derived from the combination of Eq. (4.17) and (4.18):

$$\sigma^{top} = (1 - D)\frac{\sigma}{1 - \frac{D}{3}} = 8.93\ MPa \tag{4.19}$$

$$\sigma^{bot} = \frac{\sigma}{1 - \frac{D}{3}} = 25.53\ MPa \tag{4.20}$$

These correspond to the values for element 5 (σ^{top}), 19 and 20 (σ^{bot}) shown in Figure 4.9.

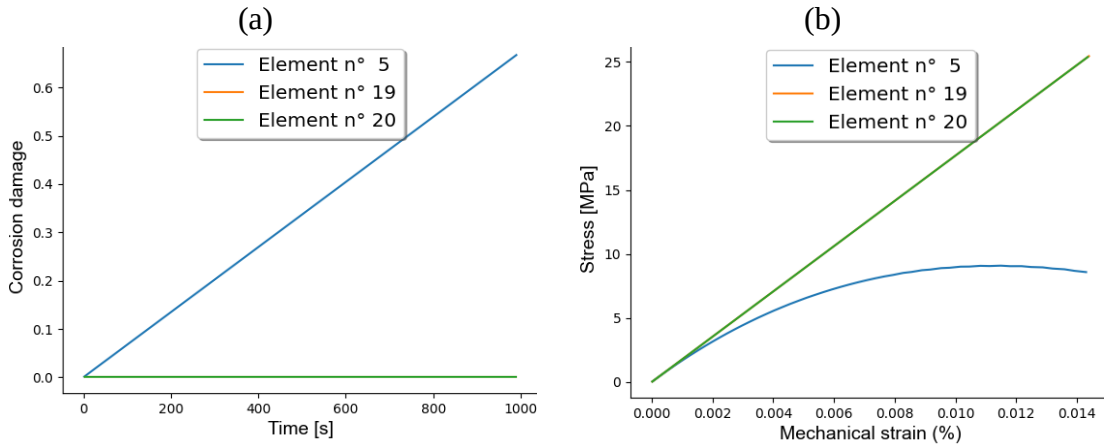

Figure 4.9 – Evolution of (a) corrosion damage and (b) stress for elements 5, 19, and 20 of the beam

This simple case study shows that the corrosion model behaves as expected with the behaviour model. More advanced test cases are studied in Chapter 6.

4 CONCLUSION

Corrosion in nickel-based alloys, and in alloy 230 in particular, is a complex phenomenon. Depending on the environment (air, solar salt, chloride salt), the temperature, and the loading conditions, the rate of corrosion and the type of oxide that form can change. Modelling corrosion in a physically accurate manner would require extensive experimental data and analysis to identify the underlying chemical mechanisms responsible for corrosion.

A simplified model was developed for the modelling of uniform corrosion of alloy 230 in solar salt or chloride salts.

Based on the results of static corrosion tests, the corrosion law was identified to be parabolic. The parameters for corrosion of alloy 230 in solar salt were identified at different temperatures based on static corrosion tests from the literature.

John Cockerill and the CRM are currently carrying further experimental tests activating the effects of corrosion, including fatigue tests in molten salts and dynamic tests, where the molten salt flows inside tubes of alloy 230. The results of these tests will probably

bring information on how to improve the modelling of corrosion damage, particularly regarding stress corrosion cracking and the influence of salt flow.

5 REFERENCES

[1] G. Calvarin-Amiri, A. M. Huntz, and R. Molins, "Effect of an applied stress on the growth kinetics of oxide scales formed on Ni-20Cr alloys," Mater. High Temp., vol. 18, no. 2, pp. 91–99, 2001, doi: 10.1179/mht.2001.010.

[2] B. Fournier et al., "Creep-fatigue-oxidation interactions in a 9Cr-1Mo martensitic steel. Part II: Effect of compressive holding period on fatigue lifetime," Int. J. Fatigue, vol. 30, no. 4, pp. 663–676, 2008, doi: 10.1016/j.ijfatigue.2007.05.008.

[3] K. Aoto, R. Komine, F. Ueno, H. Kawasaki, and Y. Wada, "Creep-fatigue evaluation of normalized and tempered modified 9Cr1Mo," Nucl. Eng. Des., vol. 153, no. 1, pp. 97–110, 1994, doi: 10.1016/0029-5493(94)90024-8.

[4] R. L. Hecht and J. R. Weertman, "Periodic oxide cracking on fe2.25Cr1 Mo produced by high-temperature fatigue tests with a compression hold," Metall. Trans. A, vol. 24, no. 2, pp. 327–333, 1993, doi: 10.1007/BF02657319.

[5] R.-Z. Wang, S.-P. Zhu, J. Wang, X.-C. Zhang, S.-T. Tu, and C.-C. Zhang, "High temperature fatigue and creep-fatigue behaviors in a Ni-based superalloy: Damage mechanisms and life assessment," Int. J. Fatigue, vol. 118, no. December 2017, pp. 8–21, 2019, doi: 10.1016/j.ijfatigue.2018.05.008.

[6] A. M. Kruizenga, D. D. Gill, and M. Laford, "Materials Corrosion of High Temperature Alloys Immersed in 600°C Binary Nitrate Salt," 2013.

[7] A. M. Kruizenga, D. D. Gill, M. Laford, and G. Mcconohy, "Corrosion of High Temperature Alloys in Solar Salt at 400, 500, and 680°C," 2013.

[8] K. L. Summers and D. Chidambaram, "Corrosion Behavior of Structural Materials for Potential Use in Nitrate Salts Based Solar Thermal Power Plants," J. Electrochem. Soc., vol. 164, no. 8, pp. H5357–H5363, 2017, doi: 10.1149/2.0501708jes.

[9] S. McCoy, J. DeBarbadillo, B. Baker, and M. Anderson, "High Temperature Corrosion Resistance of Alloy N07740 in Solar and Low Emission-Supercritical Power Generation," 2020.

[10] A. M. Kruizenga et al., "Loop for the Observation of Film Temperature Effects on Decomposition (LOFTED)," 2014.

[11] A. M. Kruizenga, "Corrosion mechanisms in chloride and carbonate salts," 2012.

[12] H. Sun, J. Wang, Z. Li, P. Zhang, and X. Su, "Corrosion behavior of 316SS and Ni-based alloys in a ternary NaCl-KCl-MgCl2 molten salt," Sol. Energy, vol. 171, no. July 2018, pp. 320–329, 2018, doi: 10.1016/j.solener.2018.06.094.

[13] B. Garcia-Diaz, L. Olson, M. Martinez-Rodriguez, R. Fuentes, H. Colon-Mercado, and J. Gray, "High Temperature Electrochemical Engineering and Clean Energy Systems," J. South Carolina Acad. Sci., vol. 14, no. 1, p. 4, 2016.

[14] H. S. Cho et al., "Dimensionless analysis for predicting Fe-Ni-Cr alloy corrosion in molten salt systems for concentrated solar power systems," Corrosion, vol. 72, no. 6, pp. 742–760, 2016, doi: 10.5006/1865.

[15] B. Fournier et al., "Creep-fatigue-oxidation interactions in a 9Cr-1Mo martensitic steel. Part III: Lifetime prediction," Int. J. Fatigue, vol. 30, no. 10–11, pp. 1797–1812, 2008, doi: 10.1016/j.ijfatigue.2008.02.006.

[16] M. Sedlak, B. Alfredsson, and P. Efsing, "A coupled diffusion and cohesive zone model for intergranular stress corrosion cracking in 316L stainless steel exposed to cold work in primary

water conditions," Eng. Fract. Mech., vol. 217, no. October 2018, p. 106543, 2019, doi: 10.1016/j.engfracmech.2019.106543.

[17] V. V. Bolotin and A. A. Shipkov, "Mechanical aspects of corrosion fatigue and stress corrosion cracking," Int. J. Solids Struct., vol. 38, no. 40–41, pp. 7297–7318, 2001, doi: 10.1016/S0020-7683(01)00002-6.

[18] M. R. Wenman, K. R. Trethewey, S. E. Jarman, and P. R. Chard-Tuckey, "A finite-element computational model of chloride-induced transgranular stress-corrosion cracking of austenitic stainless steel," Acta Mater., vol. 56, no. 16, pp. 4125–4136, 2008, doi: 10.1016/j.actamat.2008.04.068.

[19] L. G. Zhao, N. P. O'Dowd, and E. P. Busso, "A coupled kinetic-constitutive approach to the study of high temperature crack initiation in single crystal nickel-base superalloys," J. Mech. Phys. Solids, vol. 54, no. 2, pp. 288–309, 2006, doi: 10.1016/j.jmps.2005.09.001.

[20] A. Karabela, L. G. Zhao, B. Lin, J. Tong, and M. C. Hardy, "Oxygen diffusion and crack growth for a nickel-based superalloy under fatigue-oxidation conditions," Mater. Sci. Eng. A, vol. 567, pp. 46–57, 2013, doi: 10.1016/j.msea.2012.12.088.

[21] L. G. Zhao, J. Tong, and M. C. Hardy, "Prediction of crack growth in a nickel-based superalloy under fatigue-oxidation conditions," Eng. Fract. Mech., vol. 77, no. 6, pp. 925–938, 2010, doi: 10.1016/j.engfracmech.2010.02.005.

[22] J. A. Grogan, S. B. Leen, and P. E. McHugh, "A physical corrosion model for bioabsorbable metal stents," Acta Biomater., vol. 10, no. 5, pp. 2313–2322, 2014, doi: 10.1016/j.actbio.2013.12.059.

[23] Z. Shen et al., "Predicting the degradation behavior of magnesium alloys with a diffusion-based theoretical model and in vitro corrosion testing," J. Mater. Sci. Technol., vol. 35, no. 7, pp. 1393–1402, 2019, doi: 10.1016/j.jmst.2019.02.004.

[24] J. Donea, A. Huerta, J.-P. Ponthot, and A. Rodriguez-Ferran, "Arbitrary Lagrangian-Eulerian Methods," in Encyclopedia of Computational Mechanics, Chichester, UK: John Wiley & Sons, Ltd, 2004, pp. 1–25.

[25] R. W. Neu and H. Sehitoglu, "Thermomechanical Fatigue, Oxidation, and Creep: Part II. Life Prediction," Metall. Trans. A, vol. 20A, no. September, pp. 1769–1783, 1989.

[26] J. Lemaitre and R. Desmorat, Engineering Damage Mechanics. Berlin/Heidelberg: Springer-Verlag, 2005.

[27] H. S. da Costa-Mattos, I. N. Bastos, and J. A. C. P. Gomes, "A simple model for slow strain rate and constant load corrosion tests of austenitic stainless steel in acid aqueous solution containing sodium chloride," Corros. Sci., vol. 50, no. 10, pp. 2858–2866, 2008, doi: 10.1016/j.corsci.2008.07.020.

[28] D. Gastaldi, V. Sassi, L. Petrini, M. Vedani, S. P. Trasatti, and F. Migliavacca, "Continuum Damage Model for Biodegradable Magnesium Alloy Stent," Adv. Mater. Res., vol. 138, pp. 85–91, Oct. 2010, doi: 10.4028/www.scientific.net/AMR.138.85.

[29] E. Galvin, D. O'Brien, C. Cummins, B. J. Mac Donald, and C. Lally, "A strain-mediated corrosion model for bioabsorbable metallic stents," Acta Biomater., vol. 55, pp. 505–517, 2017, doi: 10.1016/j.actbio.2017.04.020.

[30] A. Amerinatanzi, R. Mehrabi, H. Ibrahim, A. Dehghan, N. S. Moghaddam, and M. Elahinia, "Predicting the biodegradation of magnesium alloy implants: Modeling, parameter identification, and validation," Bioengineering, vol. 5, no. 4, 2018, doi: 10.3390/BIOENGINEERING5040105.

[31] A. S. Khanna, "High Temperature Oxidation," in Handbook of Environmental Degradation of Materials, Second Edi., Elsevier, 2012, pp. 127–194.

Chapter 5: Methods for accelerated calculations

TABLE OF CONTENTS

INTRODUCTION

The behaviour and damage models detailed in Chapter 2 and 3 are used to simulate the behaviour of solar receivers over long time-periods (around 30 years, i.e., more than 10000 cycles). In a finite-element (FE) code, the computational time (CPU time) for the simulation of one cycle varies depending on the refinement of the mesh. Using the Lagamine FE code, simulations were run with a mesh of 1000 elements. The simulation of one cycle (i.e., one day) takes about 10 minutes in Lagamine. The simulation of the whole lifetime of the receiver would therefore take about 3 months. Evidently, this kind of computational times is not acceptable and would make it impossible to design the solar receiver.

Different methods have therefore been put in place to allow computation of the lifetime of the receiver without having to run the full FE code for every cycle.

1 POST-PROCESSOR FOR RAPID LIFETIME ASSESSMENT

The first method consists in a post-processor code applied on a non-coupled simulation that computes the evolution of the damage variables until they reach their critical value.

1.1 CONCEPT

The idea of the post-processor stems from the fact that the behaviour of the material seems to stabilize after a few hundred cycles. Indeed, the change in stress amplitude tends to get slower with increasing number of cycles (note that this is not necessarily obvious when looking at the figures in Chapter 1 since the x axis (number of cycles) is represented using a logarithmic scale). The stabilization of the stress amplitude is particularly visible for cyclic tests with small amplitudes of deformation, as can be seen in Figure 5.1. For the solar receivers, preliminary design studies have shown that the strain amplitude was in the range of 0.1% to 0.4%.

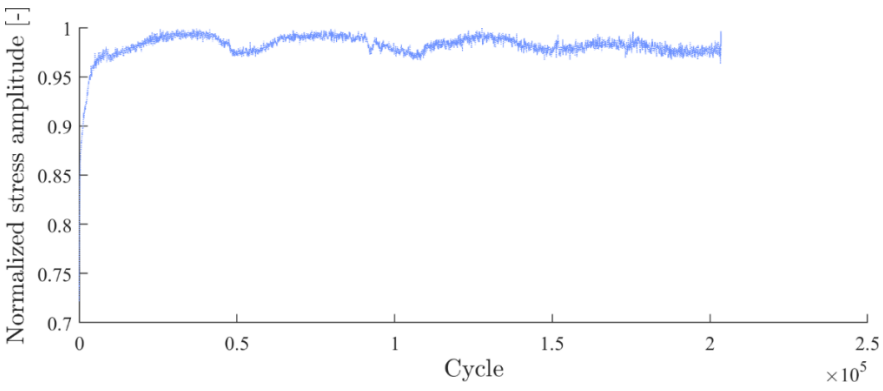

Figure 5.1 – Normalized stress amplitude of a fatigue test at 700°C with a total strain amplitude of 0.4%

Moreover, it can be observed on the creep-fatigue anisothermal tests that the stress tends to shift towards positive stresses (see Chapter 1, Section 2.5.2). Since most of the damage is expected to happen at high temperature, when the front of the tube is under compressive stress, using an early value of the stress amplitude is actually conservative (higher compressive stress at the beginning of the simulation).

Therefore, it is reasonable to make the calculation of the evolution of damage with the hypothesis that the stress amplitude remains constant after a few hundred cycles. In the damage post-processor, the material behaviour is therefore considered constant over the cycles, while the damage variables are updated using the model developed in Chapter 3, Section 2.

The post-processor is however not adapted for the coupled model or for uniform corrosion damage, as corrosion is expected to have a more significant impact on the mid-term behaviour of the structure. These observations explain why the damage post-processor is only implemented for fatigue and creep damage without coupling to the mechanical behaviour model described in Chapter 2.

1.2 PRINCIPLE OF THE COMPUTATION

The damage post-processor was implemented as a Python script that takes several input files and parameters. To use the damage postprocessor, a finite-element simulation must first be run until the behaviour (i.e., the stresses) are more or less stabilized. Then, the damage postprocessor is launched, starting from the last cycle computed in the FE code to calculate the values of D_f and D_c at every following cycle, until the critical damage D_{crit} is reached.

To compute the increment of damages D_f and D_c on a cycle, the evolution of the following variables is required:

- The temperature T;
- The rate of the plastic multiplier $\dot{p}$;
- The stress tensor $\underline{\sigma}$;
- The delayed stress $\underline{\sigma}^d$.

A file containing the values of these variables at the different time steps of the last computed cycle defines the input file of the postprocessor. The last values of the plastic multiplier and of the damage variables are also required since they are used as the starting point for the postprocessor.

Some parameters of the damage model are also necessary. These include the fatigue damage parameters S_f and s_f, the creep damage parameters S_c, s_c, and k_c, the correction

coefficients k_1 to k_4, the microdefects closure parameter h and the critical damage D_{crit}, as well as the elasticity parameters E and ν.

With all these data, the postprocessor can compute the evolution of D_f and D_c using the method described in Section 2.4 of Chapter 3.

1.3 RESULTS

To test the accuracy of the post-processor, a simple test case was considered. The test consists of one cubic element being subjected to a uniaxial isothermal creep-fatigue loading with hold times both in tension and compression. The resulting stress amplitude computed by the FE code is shown in Figure 5.2. It can be observed that the stress amplitude is somewhat stable after 500 cycles.

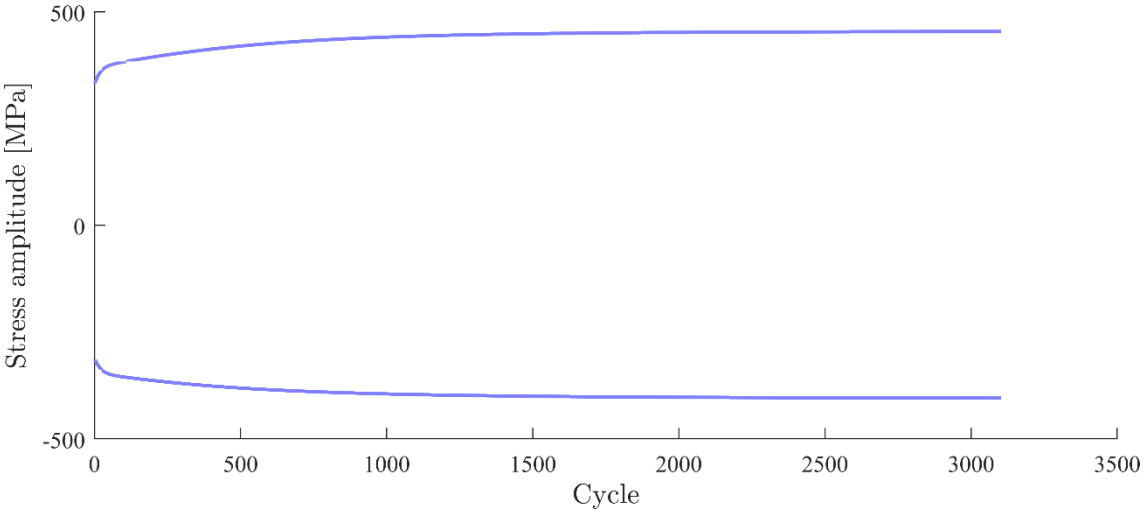

Figure 5.2 – Stress amplitude computed by the FE code for a creep-fatigue test at 700°C

The fatigue and creep damages were also computed with a full simulation by the FE code for validation of the postprocessor. To test the accuracy of the postprocessor, three different starting points are tried: 100 cycles; 500 cycles; 1000 cycles. The results are shown in Figure 5.3 for fatigue damage (a) and creep damage (b). It can be seen that with the 1000 cycles starting point, the results given by the postprocessor match that of the FE simulation. However, for earlier starting points (100 cycles and 500 cycles), the predicted lifetime is longer (lower damage) and therefore not conservative. This is due to the fact that the stress amplitude is smaller at 100 and 500 cycles than the stabilized amplitude. The error on the lifetime (number of cycles where $D_c + D_f = D_{crit}$) is of 109% for the start at 100 cycles, 22.5% for the start at 500 cycles, and 0.3% for the start at 1000 cycles.

The postprocessor only gives good results once the behaviour is really stabilized, and therefore is not ideal for use in simulations where there is no certainty as to when this

stabilization occurs. It can be a good tool to get a rapid assessment of the order of magnitude of the lifetime but is not very accurate as a design tool.

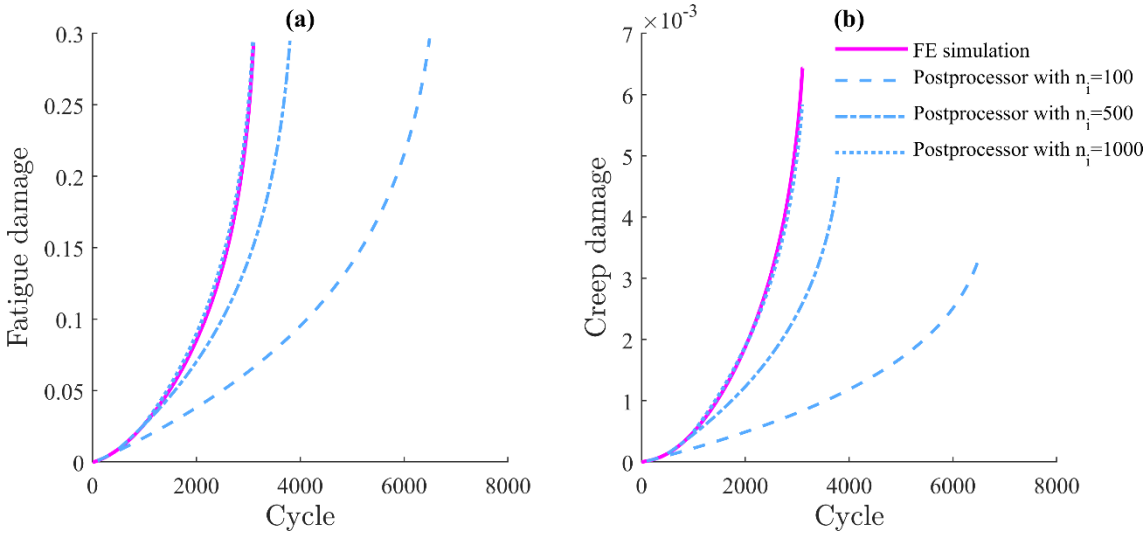

Figure 5.3 – Evolution of (a) fatigue damage and (b) creep damage as computed by the non-coupled FE code and the postprocessor, using different starting points n_i

2 CYCLE-JUMP PROCEDURE

In order to get a more accurate prediction of the lifetime than with the postprocessor and to be able to compute the long-term evolution of damage on large meshes with the coupled model (and with corrosion modelling), it is necessary to have at least a partial FE computation of the behaviour (stresses, hardening, strains, …) over the whole lifetime of the structure.

One commonly used procedure in the case of cyclic loadings is the cycle-jump procedure [1]–[4]. This consists in computing a number of cycles N_i in the FE code, and then extrapolating the results from these N_i cycles over a number of cycles N_j. The FE code is then restarted from cycle $N_i + N_j$ and the process is repeated. Figure 5.4 illustrates the method.

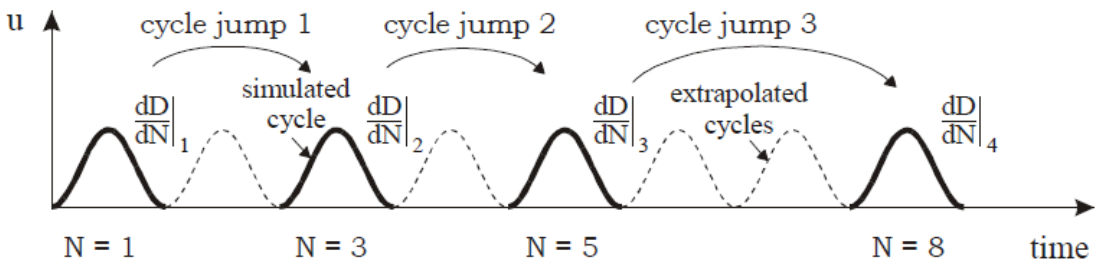

Figure 5.4 – Illustration of the cycle-jump procedure (from [2])

By simulating fewer cycles in the FE code, a significant decrease of the total computational time can be obtained. Moreover, by regularly running the FE code, the stresses and strains are updated and the modelling of damage is made more accurate.

2.1 General description

The cycle-jump procedure was implemented for the Lagamine FE code. It consists of two programs:

- A Fortran extrapolator, which reads the result files from Lagamine, computes the extrapolated variables, and writes them in an input file for Lagamine;
- A Python script, that is used to modify the Lagamine execution files to specify the cycles that need to be computed, launch the FE simulations, and the extrapolator.

Figure 5.5 presents the flowchart of the cycle-jump procedure. The green boxes correspond to functions done by the Python script, while the blue boxes correspond to functions done by the Fortran extrapolator. The use of the Fortran language for the extrapolator was made necessary by the format of the Lagamine input and output files. Indeed, these files are written using the binary 'unformatted' Fortran, which are not easily readable by Python.

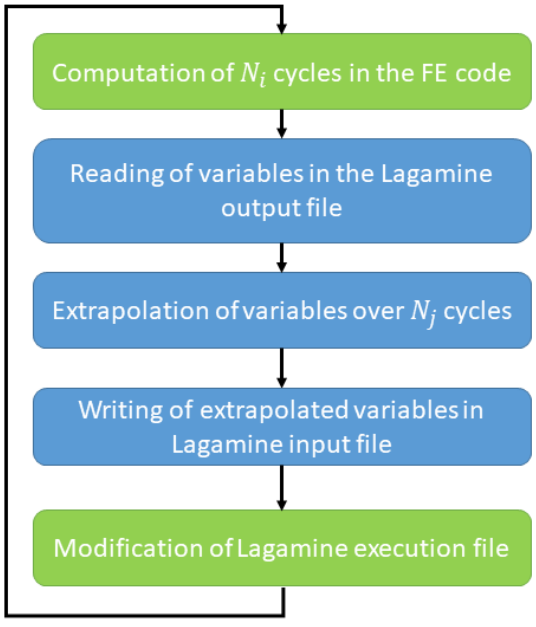

Figure 5.5 – Flowchart of the cycle-jump procedure

Both the Python and Fortran codes use an input file specific to the cycle-jump procedure. In this file, described in the Lagamine Dokuwiki [5], all the information necessary for the cycle-jump is given. The first section of the file contains generic information such as the simulation file names, options for saving the results, the period of the cyclic loading, and

the final value of time for the simulation. The second section defines the choice of number of cycles to compute N_i and number of cycles to jump N_j. Several options are available for the definition of these parameters, which will be described in Section 2.3 hereafter. Finally, the third section defines the extrapolation method and the variables that need to be extrapolated. Indeed, extrapolating all the variables of the FE code is usually not necessary. For instance, in the case of the solar receivers, the applied thermal loading is the same at every cycle. Since the thermal properties of the material do not change over time, the thermal variables (thermal strain, temperature field, …) are the same for every cycle. It is therefore unnecessary to extrapolate these variables.

2.2 EXTRAPOLATION METHOD

The 'jump' consists in extrapolating the values of the variables at the last time step of the cycle over N_j cycles.

The simplest way to perform an extrapolation of variables is to use a linear extrapolation from the results of the last two computed cycles. Let X be a variable and n the last cycle at which it was computed. $X(n)$ represents the value of X at the final time step of cycle n. To compute the increment of X over a cycle $\frac{\Delta X}{\Delta N}$, Eq. (5.1) can be used:

$$\frac{\Delta X}{\Delta N} = X(n) - X(n-1) \tag{5.1}$$

Using a linear extrapolation, the value of X at cycle $n + N_j$ is then calculated using Eq. (5.2):

$$X\left(n + N_j\right) = X(n) + \frac{\Delta X}{\Delta N} * N_j \tag{5.2}$$

The FE simulation can then be restarted from the newly computed values at $n + N_j$.

Figure 5.6 shows the results of a simulation with cycle jumps compared to a full coupled FE simulation for a creep-fatigue test at 700°C. For the full FE simulation, only the maximum and minimum stress curves are plotted. Note that here, contrarily to the example shown in Section 1.3 above, the behaviour is coupled with damage and therefore the stress amplitude decreases over time. For the simulation with jumps, the number of cycles to compute N_i was set to 25 in the first 50 cycles (where the behaviour is not stabilized) and 5 cycles afterwards. Similarly, the number of cycles to jump N_j was set to 10 for the 50 first cycles and to 50 afterwards. It can be noted that the stresses and damage variables are almost equal for both simulations. The cycle-jump procedure gives very accurate results, even when only 5 out of 55 cycles are actually computed in the FE code.

By considering a critical damage D_{crit} of 0.3, the error made on the lifetime using the cycle-jump is equal to 1.4%.

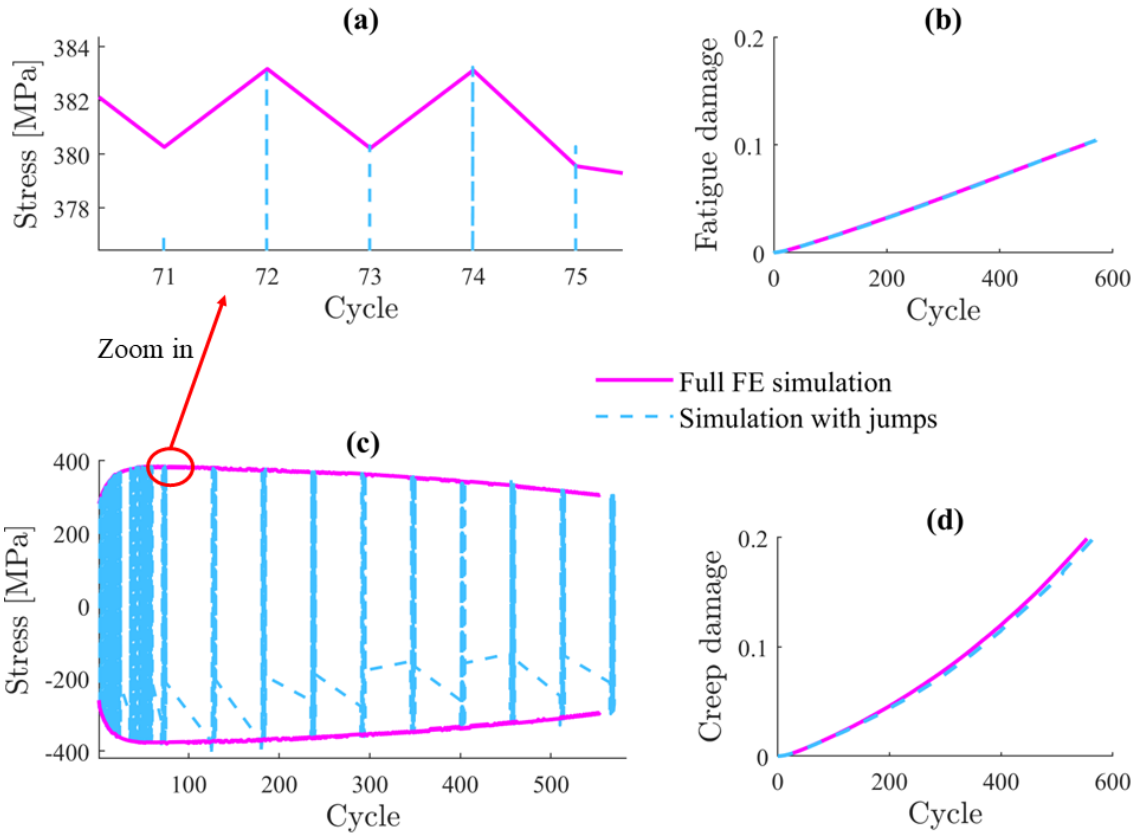

Figure 5.6 – Comparison between a full FE simulation and the cycle-jump using linear extrapolation for a creep-fatigue test at 700°C - (a) and (c) stress amplitude (Full FE) and stress (with jumps), (b) fatigue damage, (d) creep damage

In Figure 5.6 (c), it can be observed that the stresses computed using the cycle-jump procedure are not as regular as those from the full computation. Small peaks can be seen at the beginning of a group of N_i cycles, for instance at cycle 180 and at cycle 510. These peaks are due to small numerical errors between two consecutive cycles that are used for the extrapolation. Figure 5.6 (a) shows a close-up view of the tensile stresses of cycles 71 to 75. Between these cycles, it can be noted that the maximum stress oscillates slightly from one cycle to another. This is due to the numerical precision set in the FE code and has little to no impact on the overall stress evolution in the full computation. However, in the case of the cycle-jump, only the variation on the last two cycles (74 and 75) is taken into account. As a result, the extrapolation enhances the numerical error and creates a shift towards compressive stresses at the beginning of the next simulated cycles.

This does not seem to be a major problem overall since after one cycle computed by the FE code, the stress values fit the full computation values again, but this could cause convergence issues on larger scale simulations (particularly on larger meshes). To prevent this phenomenon, one could simply increase the precision in the FE simulation, however,

this would mean reducing the time steps and therefore increasing the computation times. An alternative is to extrapolate the values on a larger number of cycles. Let m be the number of cycles used for the extrapolation (with $2 < m < 10$). To compute the variation $\frac{\Delta X}{\Delta N}$ from the values on m cycles, the method of least squares can be used. Let $\overline{X}$ the mean value of X at the end of cycles $n - m + 1$ to n and $\overline{N}$ the mean value of the cycles:

$$\overline{X} = \frac{1}{m} \sum_{i=n-m+1}^{n} X(i) \tag{5.3}$$

$$\overline{N} = \frac{1}{m} \sum_{i=n-m+1}^{n} i \tag{5.4}$$

The value of $\frac{\Delta X}{\Delta N}$ can then be calculated using Eq. (5.5):

$$\frac{\Delta X}{\Delta N} = \frac{\sum_{i=n-m+1}^{n} (i - \overline{N})(X(i) - \overline{X})}{\sum_{i=n-m+1}^{n} (i - \overline{N})^2} \tag{5.5}$$

Figure 5.7 shows the comparison between the full simulation and the simulation with cycle-jump, where the extrapolation is done using values from the last 5 computed cycles.

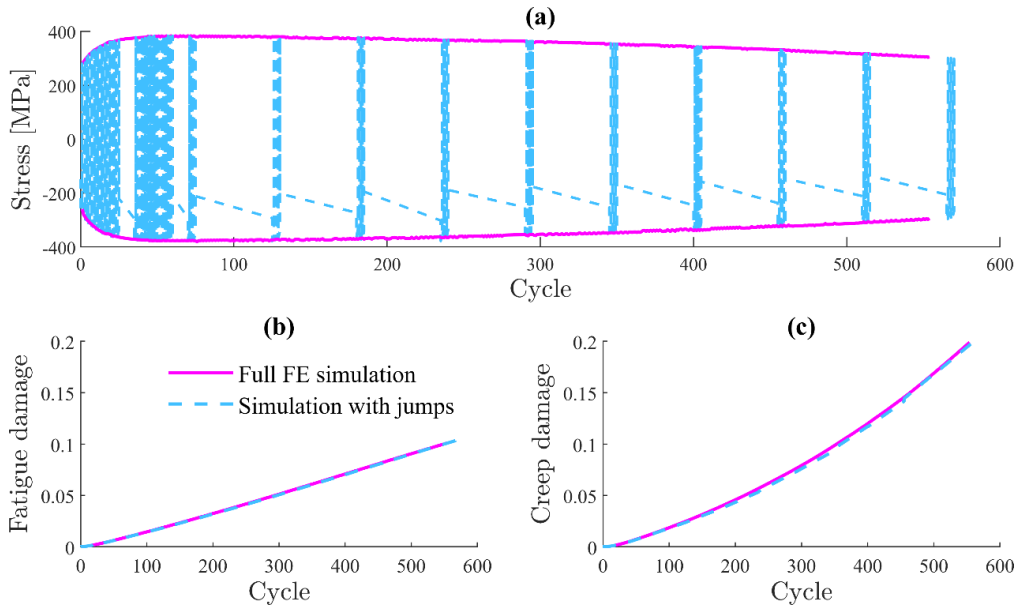

Figure 5.7 – Comparison between a full coupled FE simulation and the cycle-jump using least squares extrapolation on 5 cycles for a creep-fatigue test at 700°C (a) stress amplitude, (b) fatigue damage, (c) creep damage

The small peaks that were visible on the stress curve on Figure 5.6 (a) have disappeared. In addition, the creep damage curve seems slightly improved compared to the cycle-jump with linear extrapolation. The error on the lifetime compared to the full simulation is 0.5%, which is negligible. The use of the least square extrapolation method can therefore be useful in cases where increasing the precision of the FE simulation would result in

prohibitive computational times and linear extrapolation leads to large errors. In this case, visible discrepancies appear in the results, as was the case in Figure 5.6 (c); in other cases, the simple linear interpolation gives good results despite small numerical perturbations.

2.3 CHOOSING N_I AND N_J

The choice of N_i (computed cycles) and N_j (jumped cycles) values is crucial for the accuracy of the simulations with jumps. Indeed, if the number of cycles that are jumped N_j is too large, the linear extrapolation may not be valid anymore (most of the variables do not evolve linearly with cycles). On the other hand, if N_j is too small, the computational time will not be reduced much, which defeats the point of using the cycle-jump method. Similarly, N_i should be large enough to avoid the impact of small numerical perturbations such as the ones seen above, but small enough to limit computational times as much as possible.

2.3.1 Choice of the number of jumped cycles N_j

In the cycle-jump code, several options were implemented for the definition of N_j:

- N_j is kept constant for the whole simulation and must be given by the user.
- N_j is predefined for blocks of cycles.
- N_j is computed automatically depending on a chosen variable in the model.

The first option is the simplest but does not allow a good compromise between accuracy and computation time. Indeed, the material behaviour tends to evolve rapidly in the first 100 to 200 cycles and then stabilizes or evolves more slowly. Ideally, the values of N_j should then be small at the beginning of the simulation and larger for cycle numbers above 100 or 200. The second option allows this flexibility in the choice of N_j. As seen in the previous section (see Figure 5.6 and Figure 5.7), a small value of N_j can be defined for the beginning of the simulation and a larger value for the rest of the simulation. However, it is not always easy to predict which values of N_j are acceptable, and at which cycle number this value can be modified.

The third option allows to compute automatically an optimal value of N_j depending on the evolution of one or several state variables from the model. Several authors use the variation of the damage variable D as a criterion for calculating N_j [2]–[4]. Indeed, the damage variable is a good measure of the global variation of behaviour: the evolution of the mechanical damage variables D_f and D_c are dependent on the stress and on the plastic strain multiplier, and the value of total damage directly impacts the behaviour through the use of the effective stress in the coupled model. Another advantage is that damage is a scalar variable, which makes it easy to use as a mathematical criterion.

To compute the value of N_j, a limit is fixed on the increase of the total damage during a jump. The number of jumped cycles N_j is calculated so as to limit the increase of total damage to a user-defined value $(\Delta D)_{max}$ on all the elements:

$$N_j = \min_{elements} \left(\frac{(\Delta D)_{max}}{\frac{\Delta D}{\Delta N}} \right) \tag{5.6}$$

Figure 5.8 shows the results of the simulation of the creep-fatigue test already used in section 2.2 above with an automatic calculation of N_j and linear extrapolation. The criterion for the maximum damage increment was set to 0.01. By comparing Figure 5.8 to Figure 5.6 where N_j was predefined, it is visible that the jumps are shorter in the case of the automatic calculation, and they get shorter as the evolution of damage tends to accelerate. As a consequence, the results of the two simulations (full computation and simulation with jumps) are closer – the error on the lifetime is 0.5% – but the gain in computation time is less significant (150 cycles computed with the automatic N_j vs. 100 with the predefined N_j).

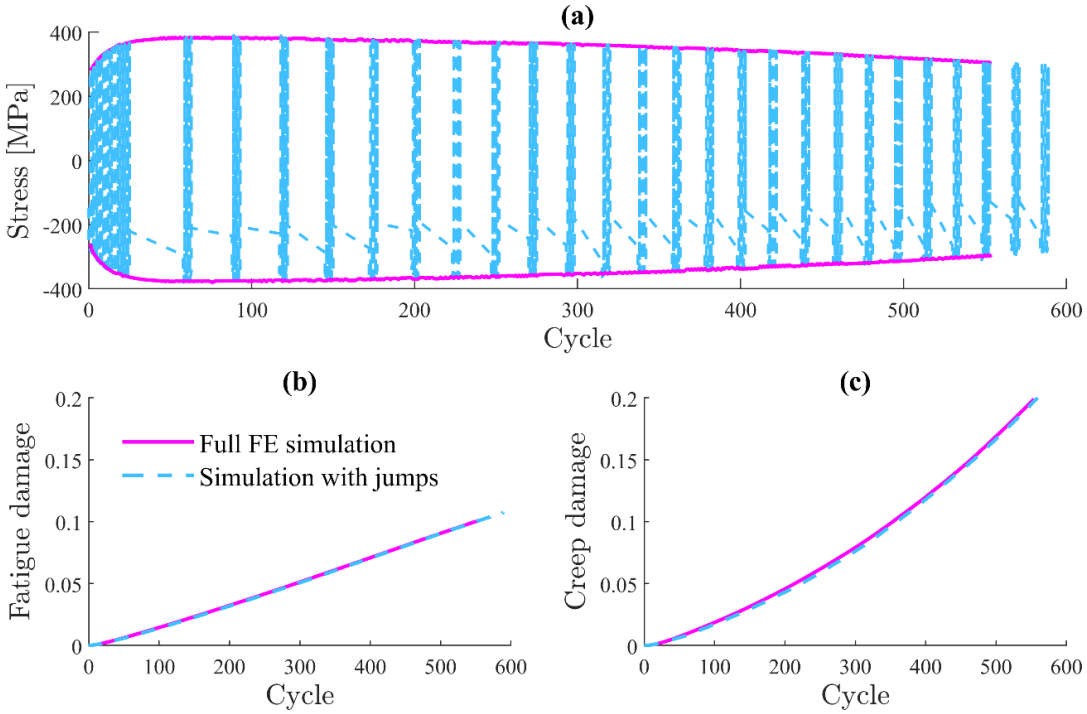

Figure 5.8 – Comparison between a full coupled FE simulation and the cycle-jump using linear extrapolation and with automatic calculation of N_j for a creep-fatigue test at 700°C (a) stress amplitude, (b) fatigue damage, (c) creep damage

On this example, the interest of the automatic calculation of N_j is limited. This result is mainly due to the fact that the simulation is overall rather short (less than 600 cycles), and the damage evolves rapidly. Additional examples with a more complex structure will be shown in Chapter 6.

2.3.2 Choice of the number of computed cycles N_i

The number of cycles computed in the FE code between two jumps should be as small as possible to limit computational times (the computational time for extrapolation is negligible compared to the computational time required for the simulation of a cycle in the FE code). However, N_i should also be large enough to guarantee the validity of the extrapolated results. As seen in Section 2.2, the first cycle after the extrapolation can be affected by small numerical mistakes.

Several values of N_i were tested on the previous creep-fatigue test. Figure 5.9 shows the comparison of the evolution of the total damage $D_f + D_c$ for different values of N_i, using the linear interpolation and automatic computation of N_j. For $N_i = 2$, the results diverge at around cycle 150. This is caused by the problem of propagation of small numerical errors identified in Section 2.2. Indeed, the first cycle after the jump may be affected by the numerical error made in the extrapolation, while the following cycles re-equilibrate. Therefore, the difference between the two first cycles computed by the FE code can be large and lead to even larger errors during the next extrapolation. For values of N_i above 3, the results are equivalent (the difference on total damage between simulations with different values of $N_i > 2$ at cycle 600 is below 1%).

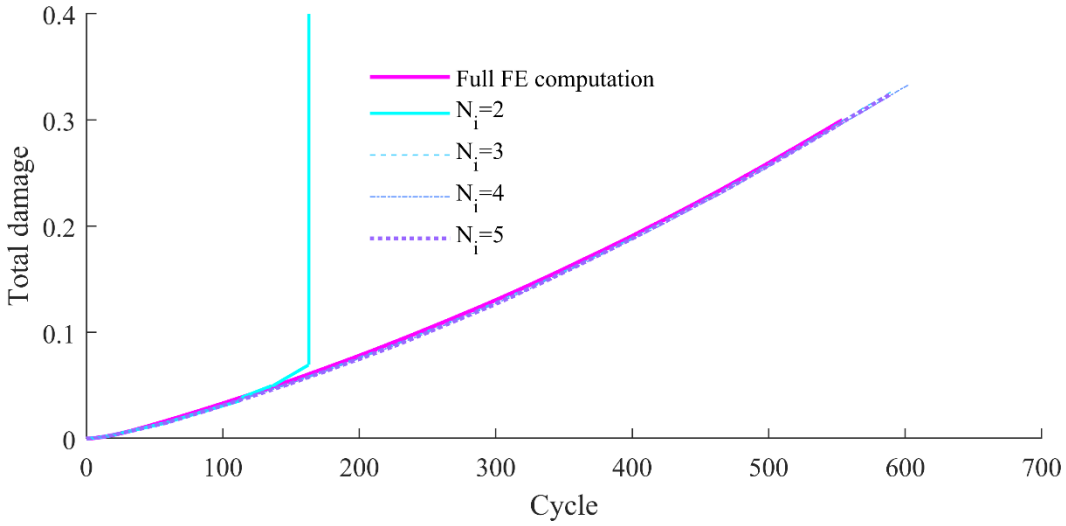

Figure 5.9 – Total damage computed for a creep-fatigue test using different values of N_i

3 CONCLUSION

In this chapter, two methods for a faster calculation of the lifetime were developed. The first method consists in a postprocessing tool that computes the damage variables with the hypothesis that the material behaviour remains constant after a certain number of cycles. This method only works if the damage is not coupled to the behaviour and gives

good results if the hypothesis of quasi-constant behaviour is valid. It is a good tool to get an estimate of the lifetime but does not always give accurate results.

The second method is a cycle-jump procedure, in which part of the FE calculation is replaced by simple linear extrapolations throughout the simulation. This method gives very accurate results but is likely to lead to convergence problems or propagation of numerical errors if the parameters of the jump are not chosen properly.

Both methods were tested and will be compared on a larger scale model in the next chapter.

4 REFERENCES

[1] J. Lemaitre and R. Desmorat, Engineering Damage Mechanics. Berlin/Heidelberg: Springer-Verlag, 2005.

[2] W. Van Paepegem, J. Degrieck, and P. De Baets, “Finite element approach for modelling fatigue damage in fibre-reinforced composite materials,” Compos. Part B Eng., vol. 32, no. 7, pp. 575–588, 2001, doi: 10.1016/S1359-8368(01)00038-5.

[3] K. Nesnas and K. Saanouni, “A cycle jumping scheme for numerical integration of coupled damage and viscoplastic models for cyclic loading paths,” Rev. Eur. des Elem., vol. 9, no. 8, pp. 865–891, 2000, doi: 10.1080/12506559.2000.10511493.

[4] F. Bogard, P. Lestriez, and Y. Q. Guo, “Numerical modeling of fatigue damage and fissure propagation under cyclic loadings,” Int. J. Damage Mech., vol. 17, no. 2, pp. 173–187, 2008, doi: 10.1177/1056789508088961.

[5] H. Morch, “Lagamine documentation - cycle jump procedure.” http://www.lagamine.uliege.be/dokuwiki/doku.php/appendices/a20.

Chapter 6: Modelling of the tube

TABLE OF CONTENTS

1 FINITE-ELEMENT MODEL

1.1 SCOPE AND HYPOTHESES

The objective of the work done as part of this thesis is the modelling of the tubes of the solar receivers. As mentioned in the introduction, the solar receiver consists in a large cylinder made of several panels of tubes. A panel of tubes is about 20 meters tall and consists of around 70 tubes. At the top and at the bottom of the panel, the tubes are connected to a large header that collects and distributes the molten salt, as can be seen in Figure 6.1. The design of the connection between the header and the tubes would require specific calculation. in this chapter. Therefore, this chapter only focuses on the part of the panel inside the red rectangle in Figure 6.1 (b).

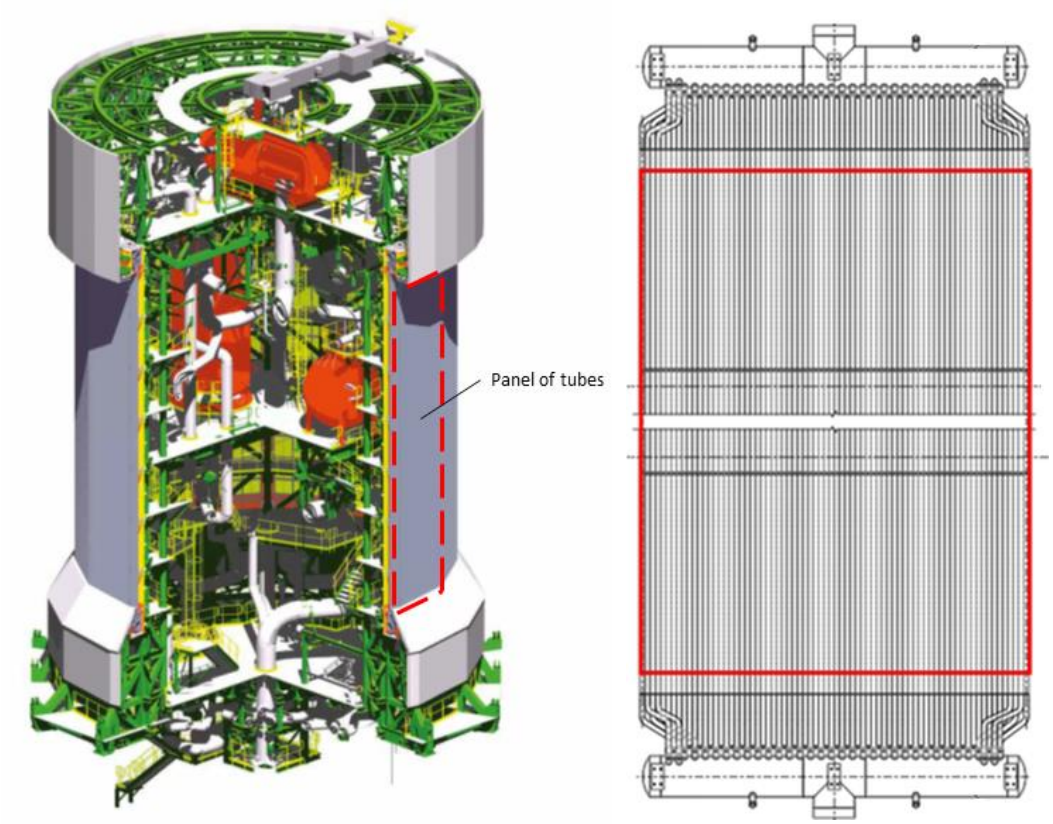

Figure 6.1 – (a) Panel of tubes in a solar receiver; (b) schematics of the panel with the header at the top and bottom.

In addition to being attached at the top and at the bottom, the tubes are fixed in the horizontal direction at regular intervals (around 3 meters) on their height to avoid bending due to the differential heating. Indeed, the front of the tubes, exposed to the concentrated solar flux, reaches higher temperatures than the back of the tube. As a result, the thermal strain is larger at the front than at the back of the tube (more dilatation with higher temperatures). Since the tubes are fixed horizontally at regular intervals, they cannot bend freely as shown in Figure 6.2 and therefore a mechanical strain ε^m appears to compensate

the thermal strain ε^{th}. This generates a compressive stress on the front of the tube and a tensile stress at the back of the tube.

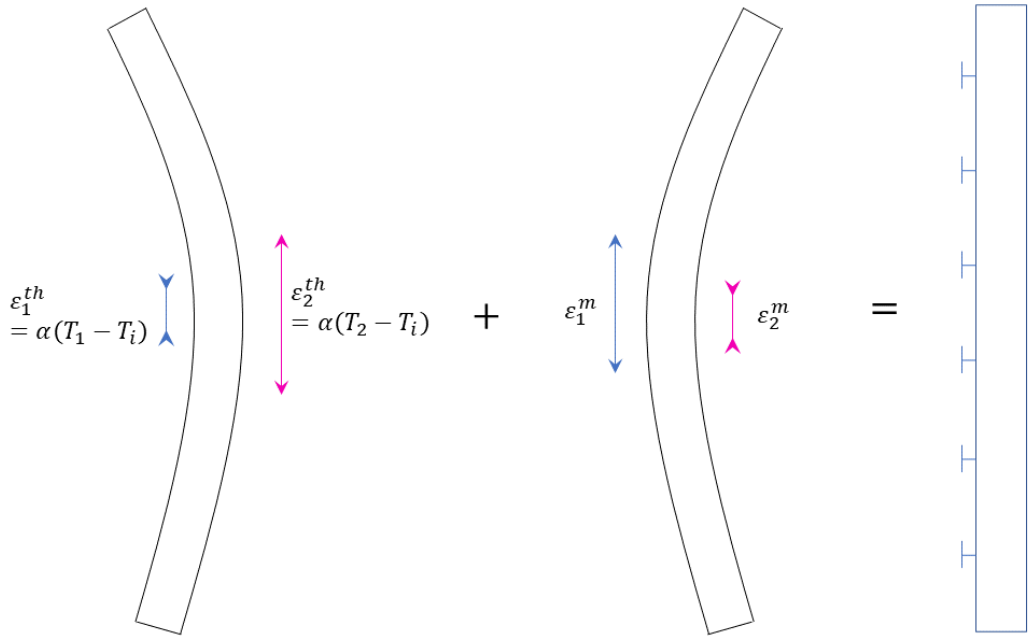

Figure 6.2 – Schematics of the tube deformation under solar flux

Instead of modelling the whole panel of tubes, it is assumed that all the tubes within a panel are exposed to the same sun radiation at a given height, and that the salt temperature inside is the same for every tube. Therefore, only one tube needs to be modelled for a given panel.

1.2 LOADING

The loading of the tube is mainly thermal. As explained in section 1.1 above, the stresses and strains in the tube are caused by thermal dilatation and by the difference of temperature between the back and the front of the tube. The loading is conditioned by two factors: the temperature of the salt inside the tube T_{salt} and the solar flux $\phi_{q,sol}$. Indeed, the temperature at the front of the tube is conditioned by the solar flux and the temperature of the salt, while the temperature at the back of the tube is equal to T_{salt}. The solar flux on a panel, which can be adjusted by changing the focus of the heliostats (mirrors) on the ground, is defined to optimize the efficiency of the solar plant. The temperature of the salt varies from panel to panel, as the salt is gradually heated as it passes inside the tubes of different panels.

A specific loading case defined by John Cockerill Energy [1] is used in the following sections of this chapter. It corresponds to the outlet panel, where the salt temperature and surface temperature of the tube are maximal. The characteristics of this loading case are summarized in Table 6.1.

Table 6.1 – Characteristics of the thermal loading case used in this study

Salt temperature [°C]	565
Internal heat transfer coefficient [W/m²K]	11500
Absorbed solar flux [kW/m²]	890

The absorbed solar flux is applied only to the part of the tube which is exposed to the sun radiation. Moreover, the absorbed flux depends on the angle θ between the flux and the normal to the tube at a given point, as illustrated in Figure 6.3. The absorbed flux ϕ_q at angular coordinate θ (with $\theta \in \left[-\frac{\pi}{2};\frac{\pi}{2}\right]$) is defined using a sinusoidal function:

$$\phi_q = \phi_{q,sol}\cos(\theta) \tag{6.1}$$

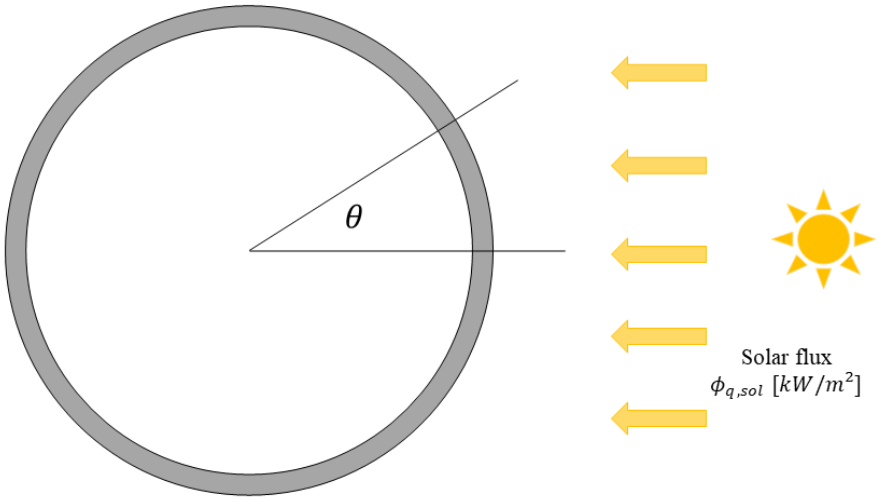

Figure 6.3 – Solar flux on the tube

The thermal loading is applied during daytime. In reality, the solar flux can vary during the day depending on the weather (clouds, changing seasons). At night-time, no loading is applied, and the temperature is uniform in the tube. A simplified loading (with no seasonal or local variations) is applied to the tube, as shown in Figure 6.4. The solar flux (as well as the salt temperature) is gradually increased during the first hour of the cycle – this corresponds to sunrise. Then, it is maintained constant for 11 hours. After that, the solar flux is gradually decreased towards zero to simulate nightfall and stays at zero during the night-time (11 hours).

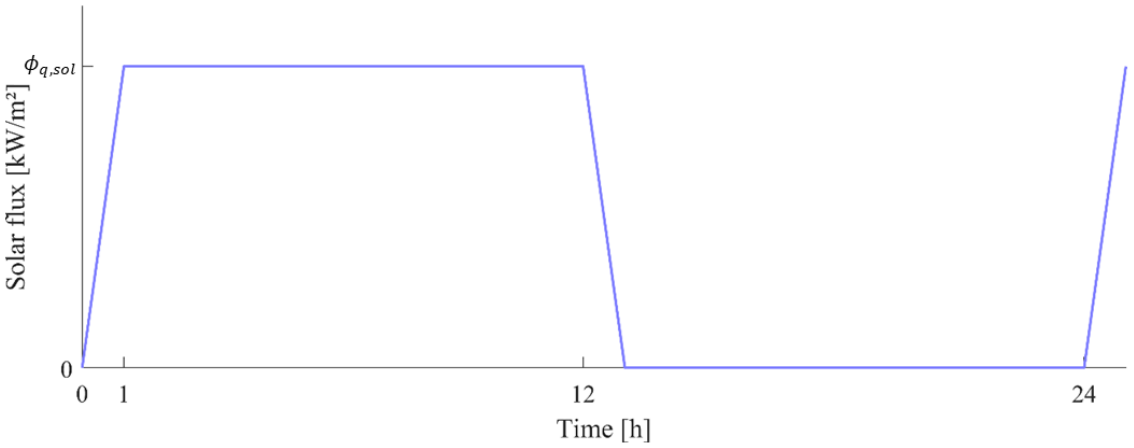

Figure 6.4 – Time variation of the solar flux applied to the tube

1.3 GEOMETRY AND MESHING

The receiver tubes are very slender: to maximize the heat transfer from the tube surface to the salt, its specific surface area (ratio between the volume in the tube and the area through which heat is transmitted) must be maximal and its thickness minimal. The specific surface area of a tube of radius r is equal to 2/r (or 1/r considering that only half of the tube is exposed to the solar flux). Therefore, tubes should have the smallest radius possible to maximize efficiency. In the design chosen by John Cockerill, the diameter of the tube is around 5 cm, its thickness about 1.5 mm, while its height is about 20 m. In a finite-element model, meshing a whole tube would require a large number of elements due to the difference in order of magnitude of the various dimensions. Models with a large number of elements require higher computational times. To avoid this problem, the model is limited here to a small slice of tube, situated at the height where the solar flux is maximal. Moreover, due to the geometry of the tube, only half of it needs to be modelled, as shown in Figure 6.5. The nodes at the bottom (nodes corresponding to the middle of the tube) are fixed in the y direction. The node at the back is fixed in the x direction to simulate the tube supports (see Figure 6.2) and, from a numerical point of view, to block the rigid modes in the x direction. In the z direction, the lower section of the tube is fixed while the upper section is made to remain parallel to the lower section. This is done to model the fact that the tube remains straight.

The slice of tube is meshed using one element along the height (z direction), three elements along the thickness, and 100 elements along the half circumference, as shown in Figure 6.5. The thickness is divided into three layers of elements for the modelling of corrosion. Indeed, as explained in Section 3.1 of Chapter 4, the preliminary design of the tube receiver allows for a third of the thickness to be corroded. Therefore, the inner layer of elements can be modelled with corrosion damage, while the rest of the tube is considered unreachable by corrosion.

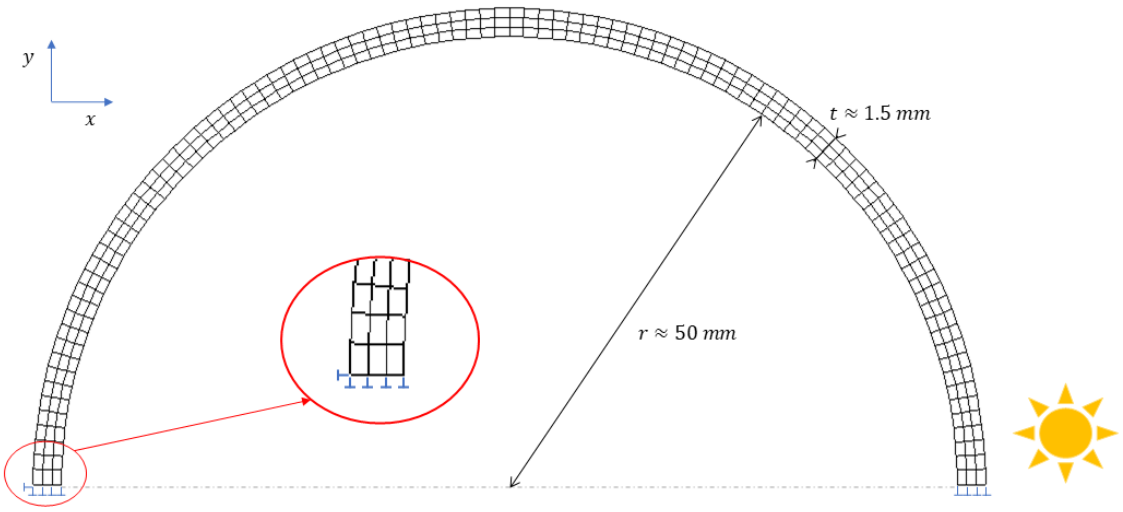

Figure 6.5 – Meshing of the half tube

2 RESULTS

In this section, the tube is modelled using the 300-element mesh described in Section 1.3 and the loading from Section 1.2. The general mechanical behaviour of the tube can be analysed using the constitutive law presented in Chapter 2. The temperature field in the tube is computed using Fourier's law of conductivity. Figure 6.6 shows the temperature field during daytime computed by the finite-element model. The temperature at the very front of the tube reaches 700°C, while the temperature at the back of the tube is equal to the temperature of the salt, 565°C.

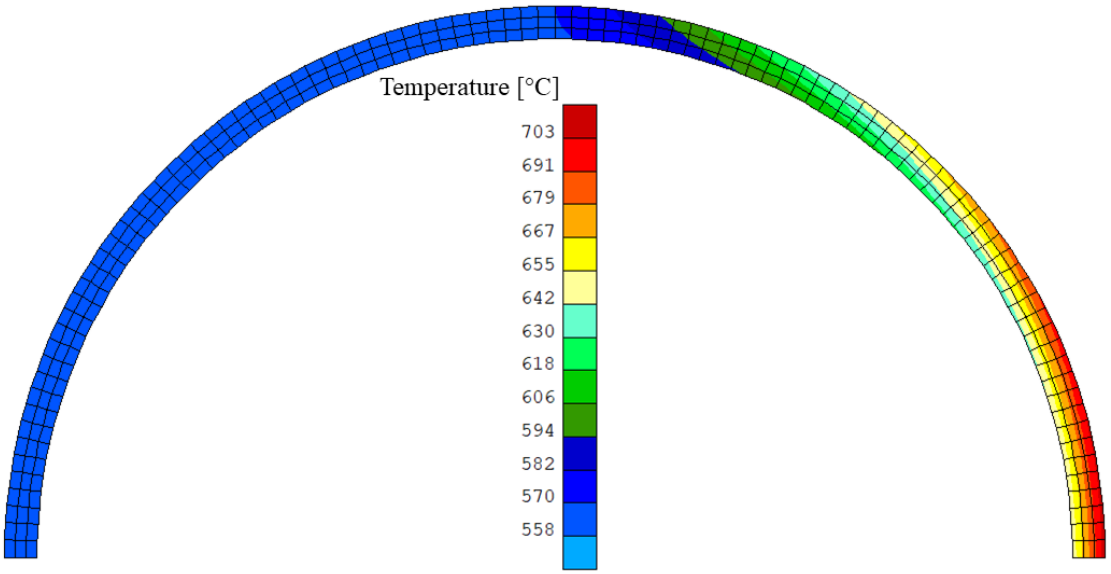

Figure 6.6 - Temperature field in the half tube

The target lifetime for the receiver is 10,000 cycles (days), which corresponds approximately to 25 years or a total of 100,000 hours of electricity production. Several

methods are used and compared to estimate the lifetime of the tube under thermomechanical loading. In the case of the tube, the lifetime is defined as the time at which the damage reaches its critical value D_{crit} somewhere in the tube.

First, the lifetime is computed using the postprocessor described in Section 1 of Chapter 5. Then, the same calculation is made by using the cycle-jump procedure detailed in Section 2 of Chapter 5. Finally, the influence of corrosion is tested by adding corrosion damage to the inner layer of elements.

2.1 BEHAVIOUR

Before estimating the lifetime, it is important to verify the behaviour of the tube and to confirm that the results given by the model are consistent with the applied loading. Figure 6.7 and Figure 6.8 show the axial stress distribution at cycle 100. It is consistent with the considerations detailed in Section 1.1: during the day (Figure 6.7) the tube is prevented from bending and therefore a mechanical strain appears in the z direction to compensate the differential thermal dilatation. The front of the tube is under compression while the back of the tube is under tensile stress, as represented in Figure 6.2.

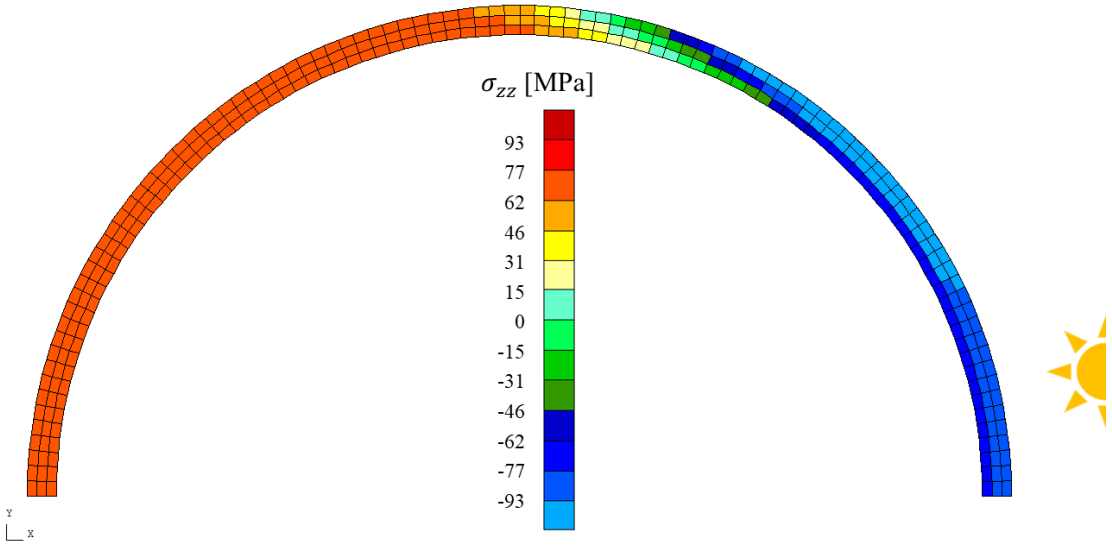

Figure 6.7 – Axial stress distribution at cycle 100 (daytime)

During the day, the mechanical strain is maintained at high temperature. This loading leads to a relaxation of the stresses in the tube. The relaxation phenomenon is more significant at higher temperatures, which explains why the compressive stress is maximal at an angle θ around 30° and 60° (with θ as in Figure 6.3) and not for $\theta = 0°$ where the temperature is maximal. The relaxation that occurs at high temperature during the day causes a shift of the stress curve towards tensile stresses for the front of the tube, which in turn leads to a positive stress upon reversal of the thermal strain at night. As shown in

Figure 6.8, the axial stress is positive (tensile) at the front of the tube during the night, while it is negative and small in absolute value in the rest of the tube.

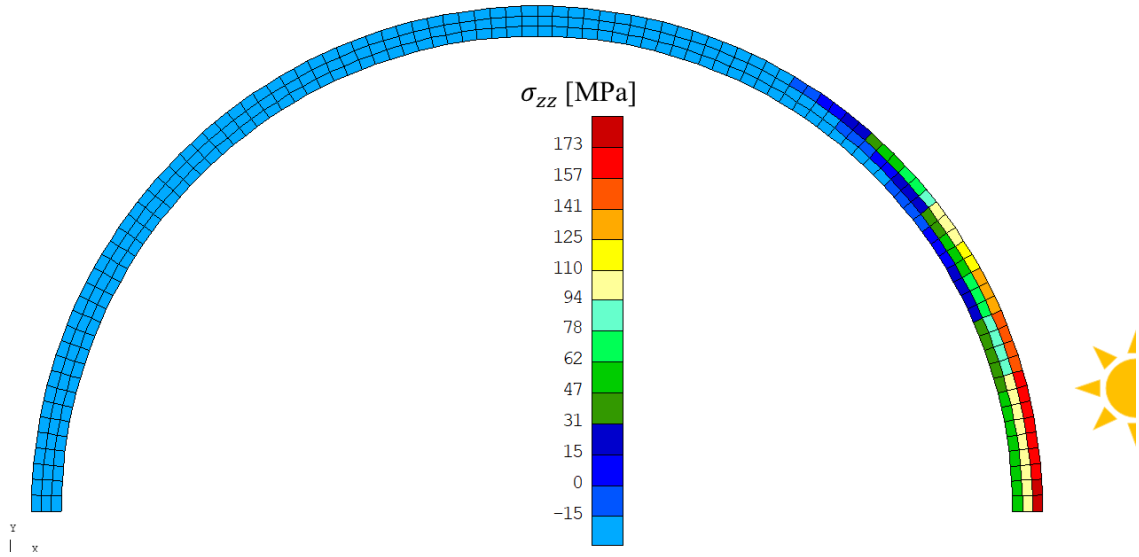

Figure 6.8 – Axial stress distribution at cycle 100 (night-time)

Figure 6.9 shows the evolution of the 6 components of the stress tensor of the element with maximum solar radiation (at the very front of the tube) over the first 100 cycles. The most significant component is σ_{zz}, the axial stress. In the y direction, a small stress also appears due to the fixation in this direction corresponding to the other half of the tube (see Figure 6.5). The rest of the stress components are close to zero. It is clear from the σ_{zz} curve that significant stress relaxation occurs towards tensile stresses during the first few days. After that, the cyclic evolution of the stresses is minimal.

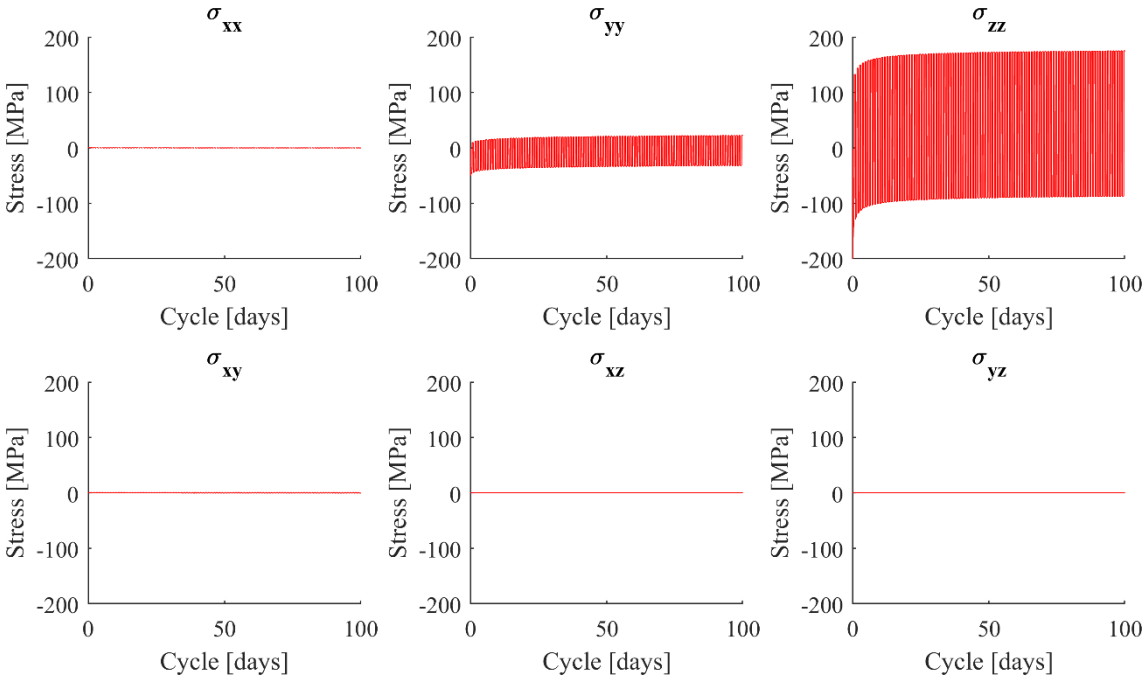

Figure 6.9 – Evolution of the components of the stress tensor for the critical element during the first 100 cycles

2.2 DAMAGE POST-PROCESSOR

The first estimation of the lifetime is done using the damage postprocessor described in Chapter 5. To use the damage postprocessor, it is first necessary to run the finite-element simulation for a certain number of cycles. Then, the stresses, cumulative plastic strain, and damage variables of the last computed cycle are extracted from the result files to serve for the postprocessor calculation.

The postprocessor performs the calculation of damage for only one element at a time. Therefore, the critical element(s) in the tube must first be identified. With the hypothesis of a stabilized behaviour after a certain number of cycles N_{start} from which the postprocessor is started, this element is taken as the element with the maximal value of damage at cycle N_{start}.

Figure 6.10 and Figure 6.11 show the fatigue and creep damage variables in the tube after 100 cycles. For both types of damage, the maximum value is found in the foremost element of the tube, where the solar flux is highest.

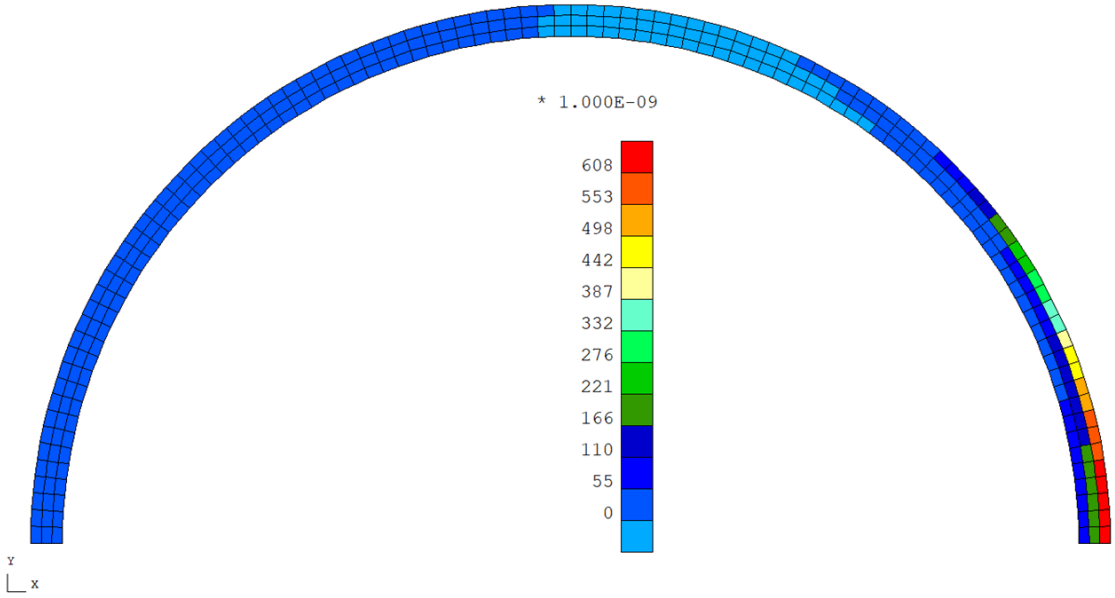

Figure 6.10 – Fatigue damage in the tube at cycle 100

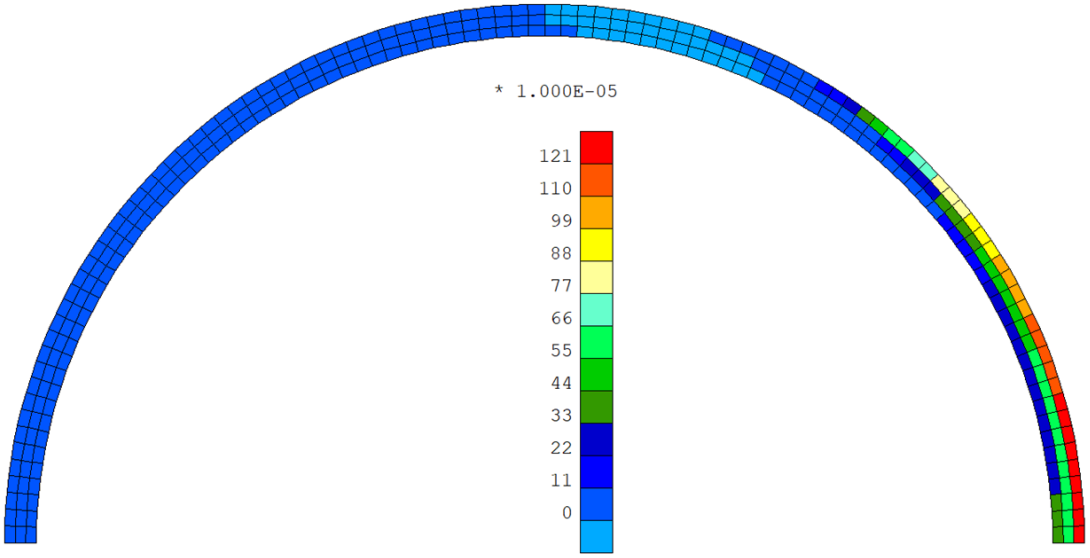

Figure 6.11 – Creep damage in the tube at cycle 100

It can be noted that the creep damage is much higher than the fatigue damage in this loading case. Indeed, the total mechanical deformation remains rather small due to the limited temperature gradient between the back and the front of the tube – the front of the tube is at 700°C while the back of the tube is at salt temperature, i.e., 565°C. Therefore, the plastic strain remains low, which leads to small fatigue damage. On the other hand, the temperature at the front of the tube is high enough to cause creep, which can occur below the elasticity limit.

As was shown in Chapter 5, the validity of the postprocessor approach depends largely on the number of cycles computed and the stabilization of the stress curves. In order to verify if the behaviour is approximately stabilized after 100 cycles, the evolution of the von Mises equivalent stress in the critical element is plotted in Figure 6.12 for the 500 first cycles. The red and blue curves represent the peak daytime von Mises stress and the peak night-time von Mises stress, respectively. It can be seen that most of the variations occur during the first 100 cycles. The peak stresses are however not perfectly constant after 100 cycles, and some minor changes can be observed over the following 400 cycles. In particular, the daytime peak stress continues to decrease due to stress relaxation at high temperature, while the peak night-time stress increases slightly due to cyclic hardening.

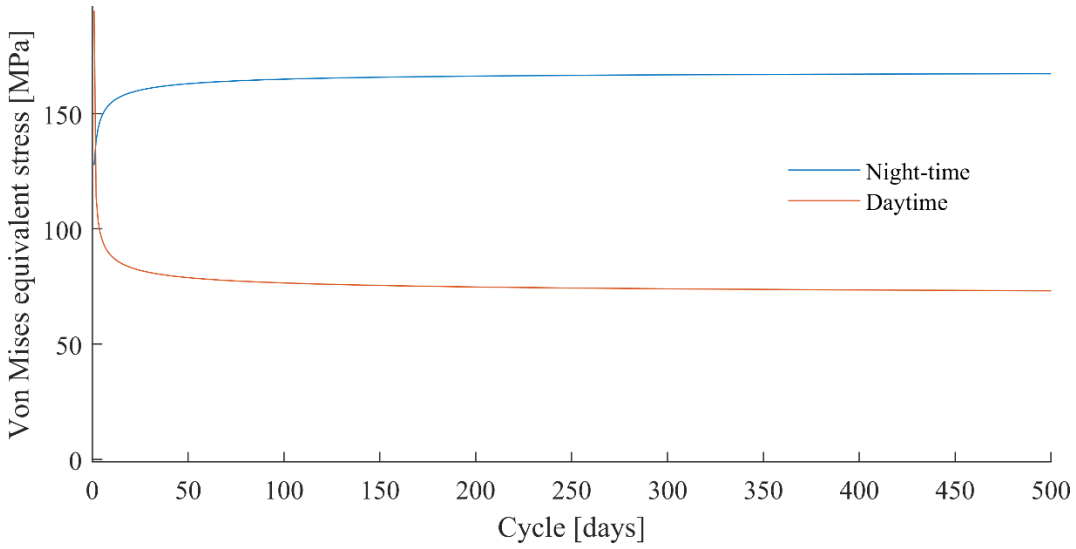

Figure 6.12 – Peak von Mises stresses for daytime and night-time over 500 cycles

To see the impact of the small variations after 100 cycles, the postprocessor was started from cycle 100, 200, and 500. Figure 6.13 shows the evolution of the total damage computed by the postprocessor. It can be noted that smaller values of N_{start} lead to shorter lifetime, which is conservative. For $N_{start} = 100$, the critical value is reached at cycle 8743, which is below the 10,000 cycles target value for the receiver. However, for $N_{start} = 200$ and $N_{start} = 500$, the lifetime is 10,487 and 12,822, respectively. Considering the estimated lifetime increases for increasing values of N_{start}, it is expected that the lifetime that would be obtained from a complete finite-element simulation would be even larger, and therefore above the target value of 10,000 cycles.

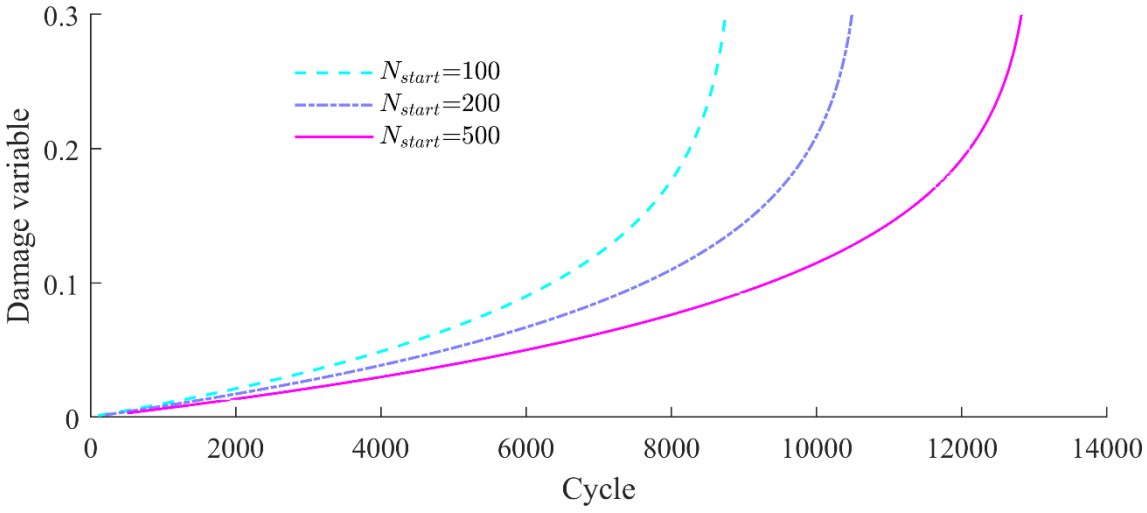

Figure 6.13 – Total damage evolution in the critical element for different values of the starting cycle number N_{start}

These results show that the postprocessor is not the ideal tool for estimating the lifetime, as the variability is significant depending on the chosen reference cycle number. However, the approach is conservative in this case as the estimated lifetime increases with increasing values of N_{start}. It can therefore be a sufficient tool for the validation of

the tube receiver design or for a pre-design step. Generally, the post-processor is not always conservative. Indeed, in a case where the surface temperature of the tube remains low (typically below 600°C, where there is little to no relaxation), the stress could increase with cycles, leading to an accelerated damage evolution. In such a case, the post-processor would not be conservative, and a more reliable approach would be necessary to compute the lifetime of the tube.

2.3 CYCLE-JUMP APPLICATIONS

2.3.1 Validation of the cycle-jump method

To validate the cycle-jump approach, the loading case defined in Table 6.1 of Section 1.2 is used with the 300-element mesh. The cycle-jump procedure was run for 5,000 cycles and the results were then compared to the results obtained with the full finite-element simulation. Figure 6.14 and Figure 6.15 show the comparison between the full finite-element calculation and the cycle-jump, respectively for the stresses and for the damage variable in the critical element. The cycle-jump procedure was started after 100 cycles, to avoid making jumps at the beginning of the loading where the variations from one cycle to another are large due to the significant stress relaxation (see Figure 6.9 and Figure 6.12). Figure 6.14 and Figure 6.15 show that there is a good correspondence between the full computation and the simulation with cycle jumps. The error on the total damage measured at cycle 5,000 is about 0.85%, which is negligible.

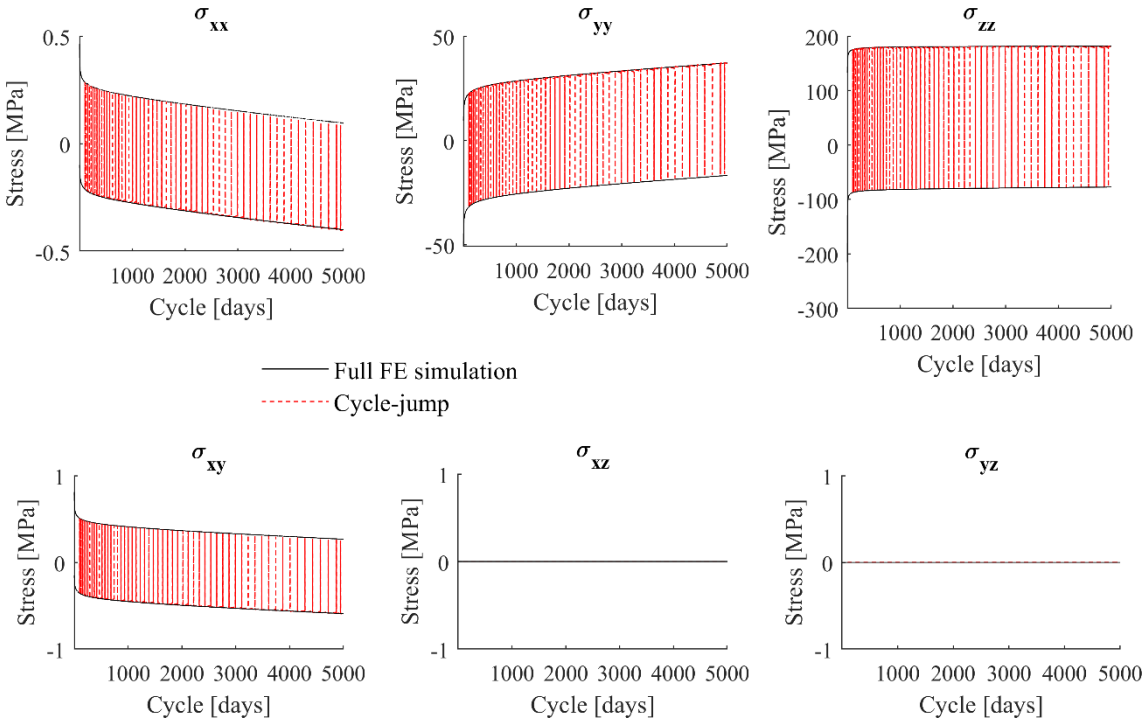

Figure 6.14 – Comparison between the evolution of stress components over 5000 cycles obtained with a full finite-element computation (black curves) and using the cycle-jump procedure (red dashed line)

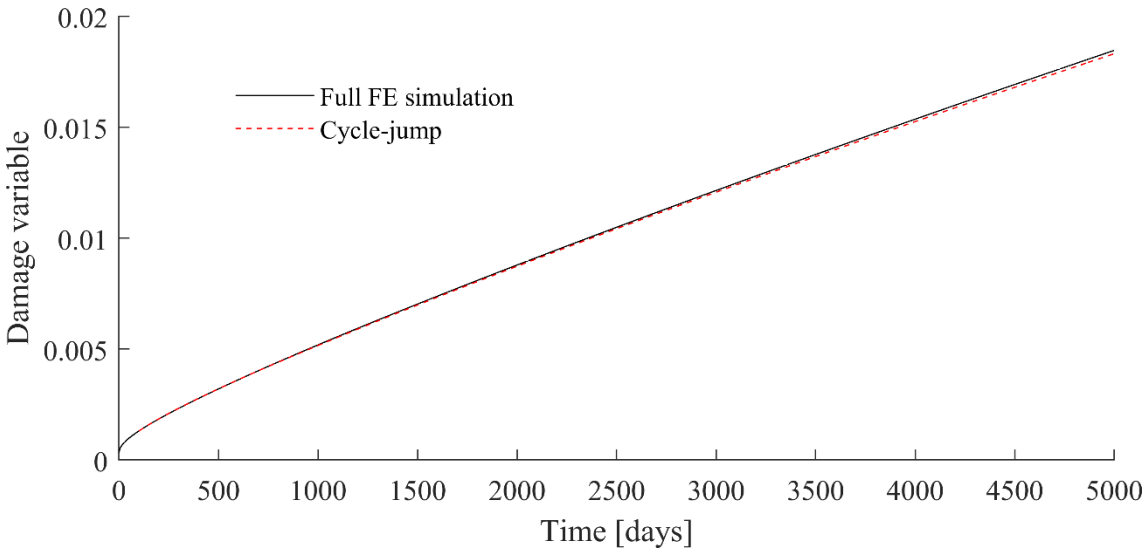

Figure 6.15 – Damage evolution over 5,000 cycles calculated using a full finite-element simulation and the cycle-jump procedure

The difference regarding computational time is, however, significant. The CPU time for the full computation in the finite-element code is about 4 days and 8 hours, while the computation with cycle-jump took only 11 hours (counting the 100 first cycles). The computation time is divided by a factor 10 using the cycle-jump procedure, while the results remain accurate (less than 1% error).

2.3.2 Lifetime calculation

The cycle-jump simulation was continued in order to obtain the lifetime – i.e., the cycle number where the total damage D reaches the value D_{crit}. The simulation stopped after 36,900 cycles due to convergence issues. As can be seen in Figure 6.16, a numerical problem occurred in the simulation at around cycle 31,000. This sudden change in the peak von Mises stresses is likely due to a small numerical error that was multiplied during a jump. It led to a significant decrease in the daytime peak stress and an increase in the night-time peak stress. This is problematic because the daytime peak stress is in large part responsible for the creep damage. Underestimating the von Mises stress level during daytime means underestimating creep damage, and therefore overestimating the lifetime. The numerical error could probably be avoided by lowering the number of jumped cycles N_j during the cycle-jump procedure, but this could not be done in this thesis due to a lack of time.

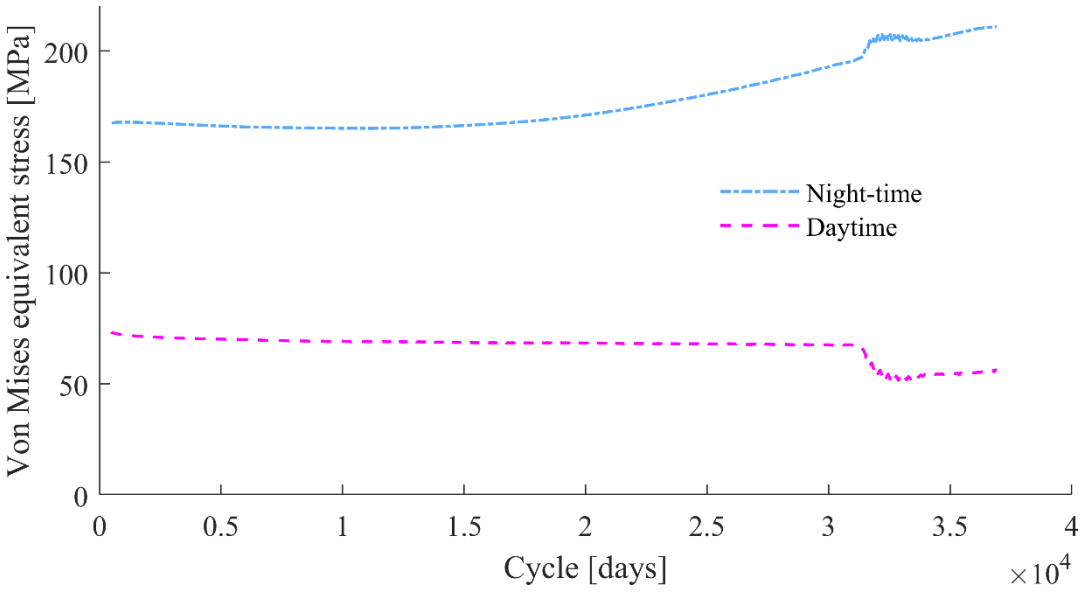

Figure 6.16 – Evolution of the peak von Mises equivalent stress during daytime and night-time for the critical element of the tube

Figure 6.17 shows the evolution of fatigue damage and creep damage over 36,900 cycles, as calculated using the cycle-jump method. Creep damage is largely predominant, with fatigue damage remaining close to 0 during the whole simulation. At 30,000 cycles, the value of creep damage is around 0.07, which is still far from the critical value ($D_{crit} = 0.3$). As can be seen, the evolution of creep damage suddenly slows down after around 31,000 cycles due to numerical error observed in Figure 6.16.

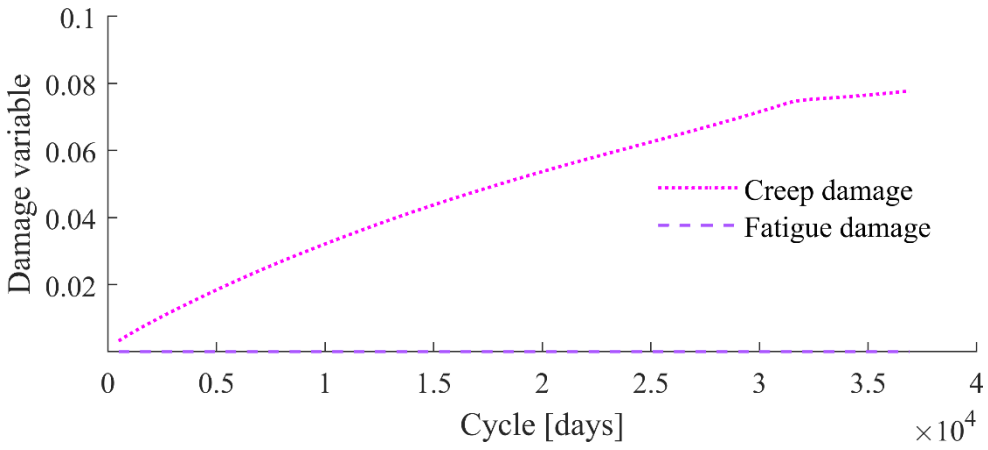

Figure 6.17 – Evolution of fatigue and creep damages in the critical element

Although the total lifetime could not be obtained using the cycle-jump method, it shows that the target value is largely exceeded.

2.3.3 Comparison with the postprocessor

To compare the performances of the two methods (postprocessor and cycle-jump), several criteria can be considered: the CPU time, the precision, and the capacity to converge (robustness). To measure the precision, the relative error on the value of total damage at

5000 cycles was computed based on the full finite-element simulation. Table 6.2 gives the values of the different criteria for the four tested configurations. The postprocessor is faster than the cycle-jump method and always converges; however, it is highly unreliable since the errors are above 200% in the three tested cases.

Table 6.2 – Comparison of the two computation methods

Method	Parameters	CPU time (to 10,000 cycles)	Error at cycle 5000	Convergence to lifetime
Postprocessor	$N_{start} = 100$	2h 15min	2956%	✓
	$N_{start} = 200$	4h 20min	540%	✓
	$N_{start} = 500$	10h 35min	251%	✓
Cycle-jump	$N_i = 4$ $N_j = 36$	20h 40min	0.04%	✗

The major drawback of the cycle-jump method is that it is likely to stop because of convergence issues and therefore it can be difficult to obtain a value for the lifetime.

To obtain a value of the lifetime based on available results of the cycle-jump calculation, the postprocessor was used, starting from 10,000 cycles and from 30,000 cycles. Figure 6.19 shows the damage evolution in the critical element obtained using the postprocessor with starting points 100, 200, 500 (full FE calculations) as well as 10,000 and 30,000 (cycle-jump simulations). The damage computed by the postprocessor increases exponentially, while the slope of the curve corresponding to the cycle-jump simulation (solid black line) seems to decrease with increasing number of cycles. This can be explained by the relaxation that keeps taking place cycle after cycle. As can be seen in Figure 6.18, the peak daytime von Mises stress keeps decreasing as the simulation progresses, causing smaller creep damage increments.

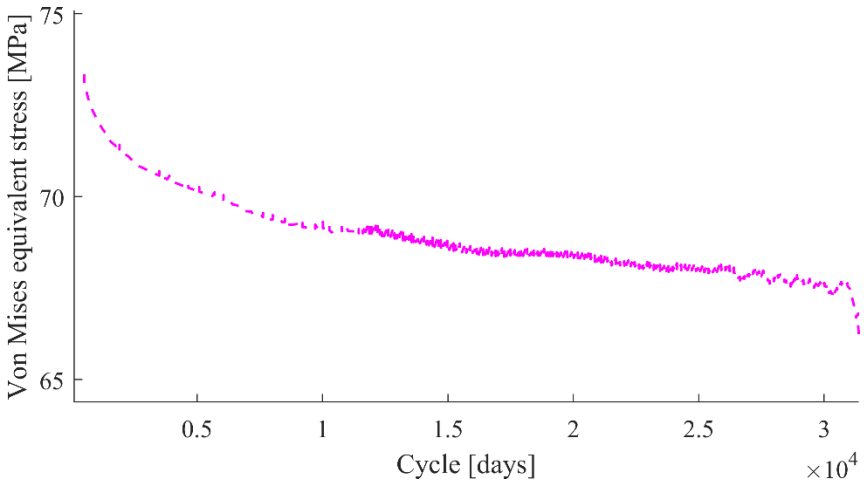

Figure 6.18 – Daytime peak von Mises stress

The lifetime estimated starting from 10,000 cycles is around 33,900 days (92 years) while the lifetime estimated from 30,000 cycles is around 65,800 days (180 years). However, these results should be considered with caution, as the damage model does not take proper consideration of thermal ageing, as explained in Chapter 3, Section 3.4. As can be seen in Figure 6.17, the fatigue damage remains close to zero during the whole simulation due to very low stresses at daytime. At night-time, the tensile stress in the critical element remains below the room temperature yield stress, leading to no damage at all. In reality, it is likely that thermal ageing would lower the elasticity limit at room temperature and cause fatigue damage during the night phases.

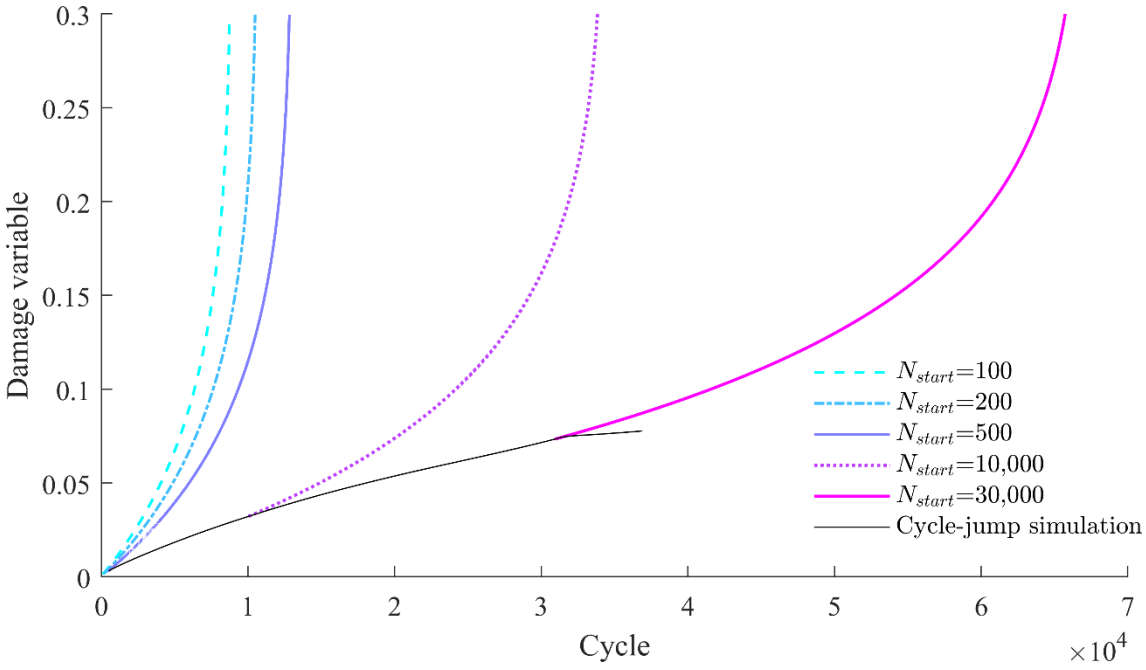

Figure 6.19 – Comparison of the damage computed by the postprocessor for the critical element using different starting points and the cycle-jump simulation

2.4 INFLUENCE OF CORROSION

In this section, the influence of uniform corrosion damage on the tube is evaluated. It is important to note that this study does not provide an extensive review of the influence of environmental damage in general, as local corrosion, erosion due to the salt flow, or the oxide properties are not taken into account due to limited experimental data.

To simulate corrosion damage, the model proposed in Section 3.1 of Chapter 4 is used. The mesh of the tube is the same as the one used in the previous sections; however, the inner layer of elements includes corrosion damage. Corrosion is only modelled as a depletion of the material, which corresponds to a loss of stiffness of the element in the model.

The tube receiver is designed to allow one third of the thickness to be taken away by corrosion. In the model, complete disintegration of an element corresponds to $D = 1$. However, values of damage close to 1 lead to convergence problems in the model, since the effective stress is equal to $\frac{\sigma}{1-D}$. The critical damage in the inner layer of elements is therefore set to 0.9 to avoid convergence issue. The critical damage in the rest of the elements, which are not affected by corrosion, remains at 0.3.

The simulation with corrosion was carried out using the cycle-jump method. Similarly to the simulation without corrosion, it stopped due to convergence issues after around 30,000 cycles.

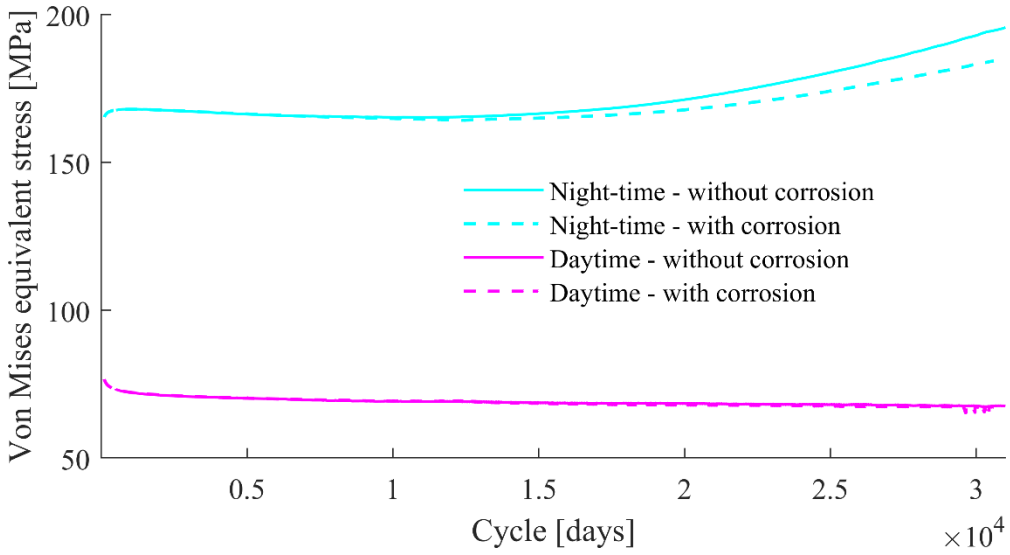

Figure 6.20 – Comparison of the evolution of the peak von Mises stress with corrosion and without corrosion

Figure 6.20 shows the daytime and night-time peak von Mises stresses for the critical element in the case with corrosion and in the case without corrosion (previous simulation). On the first 10,000 cycles, there is little to no difference between the two cases. From cycle 10,000 to 30,000, the daytime peak stress is more or less the same for both simulations, while the night-time peak stress becomes smaller for the simulation with corrosion. This could be explained by the fact that with corrosion, the stiffness of the whole structure is reduced and therefore the stresses are smaller.

Figure 6.21 shows the corrosion damage distribution at cycle 10,000 (i.e., after around 25 years). Most of the corrosion damage occurs at the front of the tube, where the temperature is maximal. The maximum value of corrosion damage at 10,000 cycles is around 0.161 which corresponds to approximately 80,5 µm of reduction for an element with an initial thickness of 0.5 mm. At the back of the tube where the temperature of the metal is lower, the corrosion damage reaches around 0.03, corresponding to a material loss of 15 µm. The corroded thickness obtained with the model is largely below the design value of one third of the total thickness.

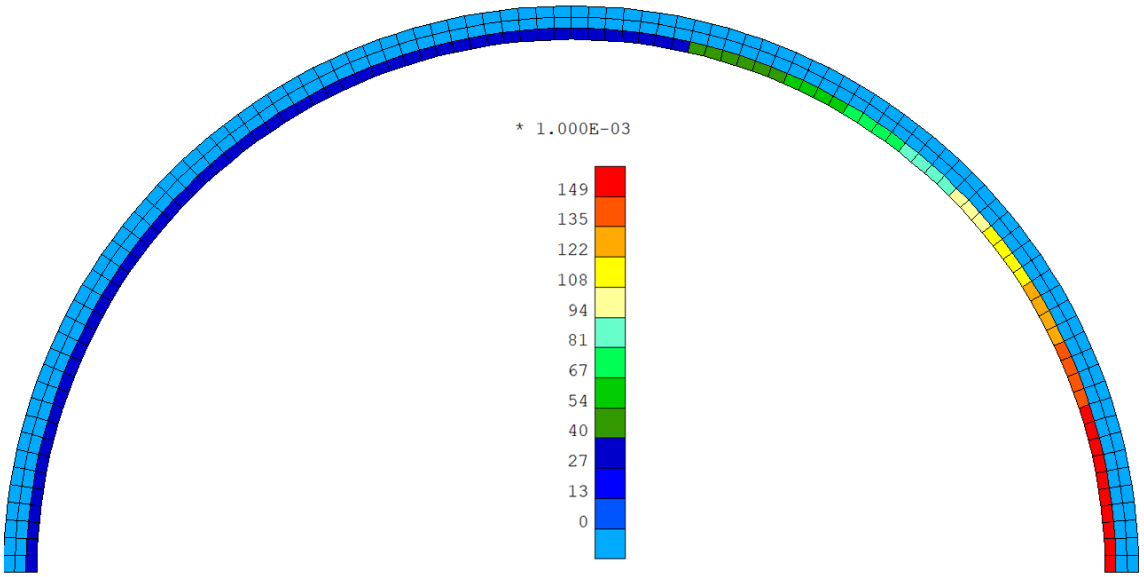

Figure 6.21 – Corrosion damage distribution at cycle 10,000

Figure 6.22 shows a comparison between the von Mises stress distribution obtained with or without corrosion damage. It can be noted that for the model with corrosion, the stress is slightly lower in the inner layer of elements at the front of the tube. This is due to the relatively high corrosion damage which lowers the stiffness of the inner layer of elements. Apart from that, the stress distribution is globally identical in both cases and no significant stress redistribution occurs.

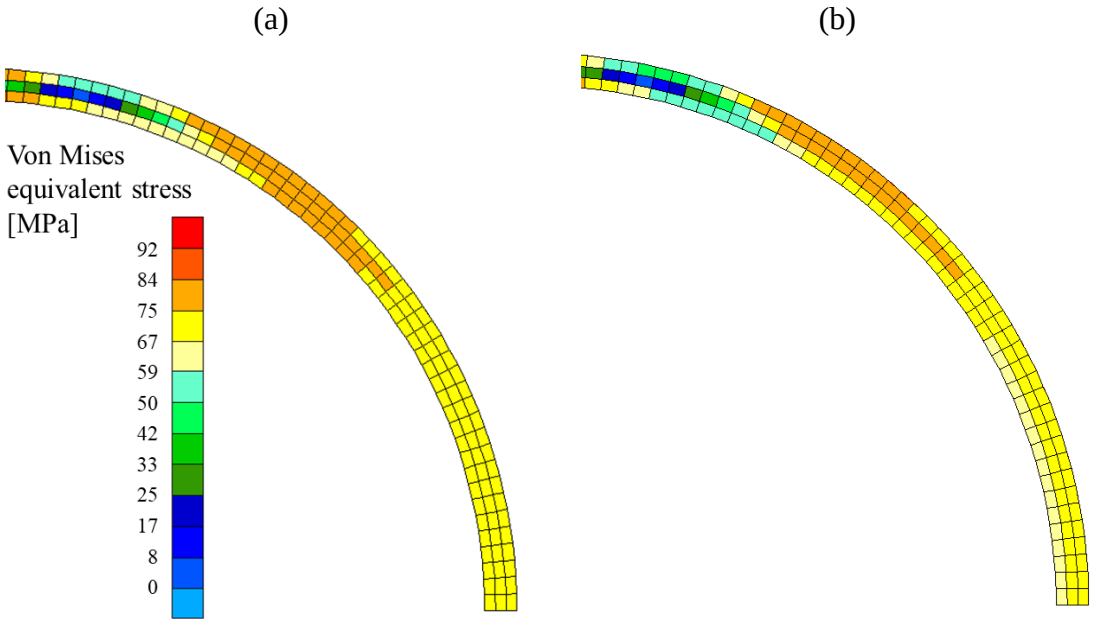

Figure 6.22 – Equivalent von Mises stress distribution at cycle 10,000 (daytime) (a) without corrosion damage and (b) with corrosion damage

This analysis of the influence of corrosion is based on the hypothesis of a parabolic law of corrosion obtained from static corrosion tests and will have to be confirmed to validate the model or disproven by experimental data from dynamic tests planned in the Solar

Gnext project. Based on this hypothesis, corrosion has little influence on the receiver tube behaviour within the target lifetime. However, there is a strong possibility that corrosion could be accelerated by erosion from the salt flow or by cracking of the oxide layer under thermal cycling. The influence of corrosion depicted in this study should therefore be considered as a primary analysis only, and not used as a validation of the model.

3 CONCLUSION

In this chapter, the tube receiver was modelled for a specific loading case, using different methods and configurations.

The results given by the behaviour model are consistent with the theoretical analysis of the tube: during the day when solar radiation hits the receiver, the front of the tube is under compressive stress in the axial direction while the back is under tensile stress.

The lifetime of the tube was estimated using the postprocessing tool and the cycle-jump method detailed in Chapter 5. Both methods show that the predicted lifetime is above the target value of 10,000 cycles. The results from postprocessor show a high variability depending on the initial cycle chosen for the calculation. The cycle-jump method is more accurate, but it is sensitive to numerical issues during the jump phases. This chapter shows that the complete model (behaviour, damage, and corrosion) is functional but has some limitations when using methods to improve computational efficiency.

Finally, the influence of uniform corrosion was evaluated based on the model developed in Chapter 4. Using this model and data from static corrosion tests, it appears that corrosion has little influence over the lifetime of the tube. However, further experimental data are necessary to validate this corrosion model, particularly regarding the effects of erosion due to salt flow, cracking of the corrosion layer due to thermal cycling, and the possible appearance of pitting corrosion.

A complete design of the receiver can be achieved by modelling, among other things:

- Different slices of the tube (corresponding to different heights).
- Tubes from a different panel (with other values of the salt temperature and the solar flux).
- The effect of a temporary excess of the solar flux on the tube.

4 REFERENCES

[1] S. Winand, “CSP Atacama 1 - Main Components Lifetime Calculation,” 2016.

Conclusions and perspectives

1 GENERAL CONCLUSIONS

In this thesis, a comprehensive behaviour and damage model was developed for the modelling of solar receiver tubes undergoing thermomechanical loading combining creep, fatigue, and corrosion.

Chapter 1 focuses on the properties and the behaviour of alloy 230, a nickel-based alloy used for the tube receivers. The macroscopic thermomechanical behaviour of this material was studied through an extensive experimental campaign led by the Centre de Recherches Métallurgiques (CRM Group) including tensile, fatigue, creep, relaxation, and creep-fatigue tests at various temperatures. A microscopic analysis of some of the tested samples was performed by the Metallurgy and Materials Science (MMS) lab of the University of Liège to better understand the damage mechanisms at play at the microstructural level. This analysis showed that mechanical tests at 700°C resulted in significant carbide precipitation, both at grain boundaries and inside grains. The cracking mode was transgranular for both fatigue and creep-fatigue tests with compressive hold times, although creep-fatigue tests have much shorter lifetimes and creep is normally associated with intergranular cracking. The reduction of lifetime with the addition of compressive hold times could be due to thermal ageing rather than creep.

The thermomechanical tests showed that alloy 230 displays good mechanical resistance up to 700°C, above which its mechanical properties (yield strength, Young modulus) start to degrade sharply. The experimental campaign put in light several aspects of the cyclic behaviour of alloy 230:

- Significant cyclic hardening occurs at temperatures between 400°C and 700°C.
- For creep-fatigue tests at high temperature, the Young modulus tends to decrease with increasing number of cycles.
- The addition of a compressive hold time in the cyclic loading significantly reduces the lifetime of the sample.

In Chapter 2, a model was chosen and implemented for modelling the behaviour of alloy 230 at different temperatures. This model is based on the Chaboche model framework and was originally developed by Ahmed [1]. It contains multiple features such as viscoplasticity, isotropic and kinematic hardening, cyclic hardening, static recovery, mean stress evolution, and influence of the temperature history. The model was implemented in the Lagamine finite-element code developed at the University of Liège. A large sensitivity analysis was conducted on the model parameters to get a better

understanding of the impact of each parameter and feature. A specific formulation was developed for the temperature-dependence of the parameter to avoid discontinuities in the behaviour that can occur when linear interpolation is used between two sets of parameters corresponding to two different temperatures.

Chapter 3 focuses on the modelling of mechanical damage, and more specifically fatigue and creep damage. A model based on the Lemaitre model was developed for alloy 230. This model contains two damage variables for the modelling of fatigue and creep damage, respectively. Two versions of the model were implemented in the Lagamine code:

- A non-coupled version, in which damage has no effect on the material behaviour.
- A coupled version, in which increasing damage tends to lower the stiffness of the element. The coupling is achieved through the use of the effective stress.

The model gave good results on fatigue and creep tests; however its validity varies on creep-fatigue tests. In particular, the model does not seem well-adapted for time-dependent effects such as thermal ageing which could play an important role in the rupture behaviour of alloy 230. Further developments of the damage model would be necessary to include time-dependent effects more accurately.

In Chapter 4, the effect of corrosion on alloy 230 was studied, using mostly sources from the scientific literature. Based on the limited information known on corrosion of alloy 230 in molten salts, a simplified uniform corrosion model was developed and implemented in the finite-element code. The model uses a corrosion damage variable, similar to the mechanical damage variables. As a consequence, corrosion is modelled as a loss of stiffness of the element to simulate the material loss that normally occurs. Additional experimental research is required to further improve the model.

Chapter 5 details two methods that were implemented to improve the computational efficiency of the model. Indeed, modelling a whole receiver tube requires a large number of finite elements, which make calculations slow. The first and simplest method developed to obtain fast results is a postprocessing tool that computes the evolution of damage based on the last results obtained from a finite-element simulation (stresses, plastic strain, temperature, etc.). This postprocessing tool is limited to the uncoupled model (i.e. damage does not influence the behaviour). The main limitation of this method is that its validity is conditioned to the stability of the material behaviour after a given number of cycles. Another drawback of the postprocessor is that the influence of damage on stress levels is not taken into account (uncoupled approach), and so it does not account for the impact of corrosion on the tube lifetime. A second method was therefore developed to include corrosion. This second method is called the ‘cycle-jump’ method and consists in replacing parts of the finite element calculation by simple linear extrapolations of

selected variables. This method significantly reduces the computation time while giving results that are very close to a complete finite-element simulation.

Finally, Chapter 6 dealt with the modelling of the receiver tubes. A specific case study was selected and modelled using the finite-element code. The lifetime was estimated using the postprocessor and the cycle-jump method. With both methods, the lifetime for the chosen loading case was found to be larger than the industrial target lifetime of 25 years (10,000 cycles). The postprocessor largely underestimated the lifetime, especially when started from a small number of cycles. The impact of corrosion was also assessed by comparing a simulation with corrosion to a simulation without corrosion. It appears that uniform corrosion does not have a significant influence on the tube lifetime. This conclusion, however, is only valid for a corrosion phenomenon that conforms to static corrosion tests (i.e., uniform corrosion with no influence of the stress state or flow rate), which is likely to not be the case in the receiver tubes.

The work done in this thesis contributed to the progress of thermo-mechanical modelling of industrial applications in many ways:

- The model developed and based on previous work is highly flexible and can be adapted to many materials.
- The introduction of a new formulation for the temperature dependence of the parameters proved efficient in improving the continuity of the results on anisothermal cases, improving robustness, and reducing the total number of parameters.
- The parameters of the model were identified for alloy 230 at temperatures ranging from 20°C to 850°C based on an extensive experimental campaign.
- Despite its complexity, the model was designed for an industrial application, and a particular attention was given to robustness and computational efficiency, with the study of Newton-type methods and the implementation of two methods for reducing computational times.
- A metallurgical analysis of the material after testing was done to verify the validity of the model hypothesis on damage.

2 PERSPECTIVES

The model is already functional and has already been used by John Cockerill to develop a monitoring tool that computes on-site the damage caused to the receiver tubes depending on the thermal loading applied. However, there is always room for improvement.

The robustness of the model, and particularly of the cycle-jump method could still be improved by an extensive study of the influence of the different parameters and the extrapolation methods.

Regarding mechanical damage, more investigation is required on the topic of thermal ageing and its influence at various temperatures to fully validate or modify the damage model. The use of a multilevel finite-element model, that is, a model where the macroscopic behaviour is derived from the evolution of the microstructure, would be the most accurate way of modelling thermal ageing. Another simpler way to include thermal ageing in the model could be to introduce a dependence of fatigue and creep damage parameters to the temperature history.

For future improvements of corrosion modelling, ongoing experiments on the corrosion of alloy 230, and more specifically corrosion under fatigue loading and corrosion in flowing salt should bring more insight on the corrosion phenomena to be expected in the receiver tubes. With the current model, this would require adapting the corrosion law to the corrosion kinetics observed experimentally and adding a damage variable for stress-assisted corrosion if needed. From a modelling point of view, models that include the diffusion of chemical elements using an additional degree of freedom seem more reliable as they simulate the actual physical phenomenon at the origin of corrosion. Another advantage is that they also model the diffusion of corrosive elements through the structure, which is not the case for the current model. This type of model could not be developed in this thesis due to limited time and the fact that the model had to be portable to another FE code, but it could be an interesting perspective for later work on the corrosion of nickel alloys in molten salts.

Curriculum Vitae

Education

2016−2019	PhD in Engineering Sciences	University of Liège (Belgium)
2014-2016	Master's in civil engineering	University of Liège (Belgium)
2012-2014	1st and 2nd year of Engineering School	École des Mines d'Alès (France)
2010-2012	Classes Préparatoires aux Grandes Écoles (Preparatory Classes to Engineering School)	Lycée Saint-Louis (Paris, France)

Publications

Morch, H., Tchuindjang, J. T., Duchêne, L., Novello, F., Harzallah, R., Mertens, A., Habraken, A.M. (2022) 'Effect of tensile and compressive hold times on the rupture behavior of nickel-based alloy 230 at 700°C', *To be published*

Morch, H.,Yuan, S., Duchêne, L., Harzallah, R., Habraken, A. M. (2022) 'A review of higher order Newton type methods and the effect of numerical damping for the solution of an advanced coupled Lemaitre damage model', Finite Elements in Analysis and Design, vol. 209, no. June, p. 103801. https://doi.org/10.1016/j.finel.2022.103801

Morch, H. et al., Duchêne, L., Harzallah, R., Tuninetti, V., Habraken, A. M. (2021) 'Efficient temperature dependence of parameters for thermo-mechanical finite element modeling of alloy 230', European Journal of Mechanics, A/Solids, 85. https://doi.org/10.1016/j.euromechsol.2020.104116

Morch, H., Duchene, L. and Habraken, A. M. (2018) 'Identification method of an advanced constitutive law for nickel-based alloy Haynes 230 used in solar receivers', Journal of Physics: Conference Series, 1063(1). https://doi.org/10.1088/1742-6596/1063/1/012149